Excited-State Dynamics of Semiconductor Nanocrystals: Trapped-Hole Diffusion and Electron-Transfer Kinetics in CdS and CdSe Nanorods

by

James Keller Utterback

B.S., Physics, University of Oregon, 2011

A thesis submitted to the

Faculty of the Graduate School of the

University of Colorado in partial fulfillment

of the requirement for the degree of

Doctor of Philosophy

Department of Chemistry and Biochemistry

2018

This thesis entitled:

Excited-State Dynamics of Semiconductor Nanocrystals:

Trapped-Hole Diffusion and Electron-Transfer Kinetics in CdS and CdSe Nanorods

written by:

James Keller Utterback

has been approved for the Department of Chemistry and Biochemistry by:

_____

Gordana Dukovic

_____

Joel D. Eaves

Date _____

The final copy of this thesis has been examined by the signatories, and we find that both the content and the form meet acceptable presentation standards of scholarly work in the above mentioned discipline.

Utterback, James Keller (Ph.D., Chemistry)

Excited-State Dynamics of Semiconductor Nanocrystals:

Trapped-Hole Diffusion and Electron-Transfer Kinetics in CdS and CdSe Nanorods

Thesis directed by Associate Professor Gordana Dukovic

Abstract

Colloidal semiconductor nanocrystals have many remarkable properties—such as exceptionally tunable excited states and surface chemistry—that have led to an enthusiastic interest in using them for optoelectronic applications such as solar-energy conversion. Such technologies require control over the generation, separation, and extraction of photoexcited electrons and holes. However, the interpretation of experimentally measured excited-state decay curves is challenging because they typically exhibit complicated shapes that are elusive to simple kinetic models. To understand the principles that govern electron and hole relaxation dynamics in these complex systems, models rooted in fundamental physical phenomena are needed. This dissertation describes efforts to understand the dynamics of recombination, charge carrier trapping, trapped holes, and charge transfer in photoexcited Cd-chalcogenide nanocrystals using a combination of ultrafast spectroscopy and kinetic modeling. The first part of this dissertation focuses on studying the spatial dynamics of trapped holes. In CdS and CdSe nanocrystals, photoexcited holes rapidly and efficiently trap to localized states on the surface. We demonstrate evidence that trapped holes are mobile in CdS nanorods, CdSe nanorods, and CdSe/CdS and ZnSe/CdS dot-in-rod heterostructures, and that they likely undergo a diffusive random walk between trap sites on the nanocrystal surface. The second part of the dissertation focuses on modeling charge-transfer kinetics in heterogeneous ensembles of donor–acceptor complexes. In complexes of CdS nanorods and [FeFe] hydrogenase, electron transfer is the key step for photochemical H_2 production. By accounting for the distributions in the numbers of electron traps and enzymes adsorbed, we determine the rate constants and quantum efficiencies for electron transfer. The relatively simple analytical models developed here establish a detailed conceptual and quantitative picture of the rich carrier dynamics in these systems, providing important insights for the design of semiconductor nanocrystals for light-driven applications.

Acknowledgements

To Gordana: Thank you for training me to be a careful and thoughtful scientist, driven by questions. You gave me the freedom and independence to follow my curiosities while refining my investigative approach and science communication. You have been a great example as an advisor for your brilliant vision of the research program, your rigorous standards, your efficiency and effectiveness, and thorough coaching of your students. You invested a great deal of time and energy into my education as a researcher and you granted me ample opportunities and responsibilities so that I could grow—I thank you sincerely for that. You always believed in me, which made me believe in myself. You pushed me to realize my full potential. I am glad to have had you as my mentor, and I am grateful to have spent five years working with you.

To Joel: While not formally my co-advisor, you informally functioned as my mentor in many ways. You took me under your wing and helped to bring me up to be the scientist I am now. In class you held me to a high expectation. In discussions of research you always gave innovative insights and helpful suggestions of what to try next; I would walk away from every conversation inspired and reinvigorated about science. In discussions of careers you gave me a great deal of support. In discussions of life you encouraged me to pursue my passions and spoke candidly with me about sensitive issues. I have thoroughly enjoyed working with you over the years.

To Niels: You played a key role in my being at CU Boulder. Thank you for your time and patience during the visit weekend, and for your guidance and encouragement during my years abroad preceding graduate school.

To Garry, David and Paul: Thank you for serving on my dissertation committee. Each of you played an important role in my education and it is an honor to have each of you be involved in this milestone in my life.

To My Labmates and Collaborators: To the Dukovic Group, thank you for being a great team to work with. Amanda, it was thanks to your mentorship that I climbed the learning curve of our field so quickly. Your prior work was key in kick-starting my project. It was a joy to work closely with you for several years. Orion. I learned a lot from you. You inspired me as a scientist. My best conversations about science over the last five years were had with you. Your musings invigorated me. Amanda and Orion collectively, walkies kept me sane and inspired many antics that became some of my favorite memories of grad school, including the bubble wrap and owl messengers. Dr. Molly Wilker, it was pleasure to work together. Your willingness to share data and ideas greatly helped to accelerate my progress. I owe much of my success to being able to stand upon the shoulders of a giant. You played a key role in my first publication, and I was happy to give back by helping you to bring the ligand length project to a close. Dr. Kyle Schnitzenbaumer, for being a wealth of information about fundamental photophysics. Thank you Hayden Hamby, for your inspiring doggedness, genuine conversation, and the things you taught me while we were co-mentors. Jesse Ruzicka, for reminding me to be enthusiastic and eager about pursuing science. Leah and Marta, for joyful breaks from work. Kristina Vrouwenvelder, for amusing sarcasm as well as genuine moral support. Nicholas Pogranichniy, I enjoyed the opportunity to be your mentor. Tais, for discussions of fundamental photophysics. Dr. Pornthip Tongying, for fun conversation and climbing. Many thanks also go to other group members and visiting scientists, past and present, with whom it has been a pleasure to do research: Kyureon Lee, Katherine Shinopoulos, Chi-Hung Chuang, Yinggang Lu, Shelby Beer, Jeremiah Duncan, Nelly Couzon and Helena Keller.

I am grateful to have worked with many talented collaborators as well. Peyton Cline, for having the courage to base your project off my work—that was more motivating than I ever said.

Steve Strong, for your excellent example as a co-mentor. Paul King, Kate Brown, David Mulder, Cara Lubner and the rest of the NREL team, for interesting discussions and for making much of my electron transfer research possible. Ryan Dill, for making my dream experiment (cryo-TA on nanocrystals) come true. Daniel Weingarten and Sean Shaheen, for a neat opportunity to leave the world of nanocrystals and think about organic photovoltaics.

There are also many people from the chemistry department who I would like to thank. Eric Carlson, Jasmine Wallas, Milena Jovanović, Alyssa Landin, José Luis Falla, Nick Johnson, Steve Fatur, Peter Foster, and the other students in my cohort for a great first year of classes, cumes, barbeques and commiserating. Sam Shepard, for providing a regular source of inspiration and amusement in the department. Thomas Carey, for getting me into the mountains and running a great D&D campaign. Anna Curtis, for making the department a nicer place and for helping me get a head start with cumes. Austin Cano, for good discussions and perspectives of science. Kayla Jones, for your inspiring competence and work in helping the department run smoothly, as well as for making the department a brighter place. And to the many other people in the department that brought fruitful conversations and a good community: Andrea Marton, Jordan Hernandez, Sam Park, Dmitry Baranov, Brett Fiedler, Joe Ryerson, Dave Zywotko, Julia Bakker-Arkema, Erin McDuffie, Franklin Maharaj, and more.

I also want to recognize those who helped get me to grad school in the first place by reading my application essays, inspiring me to pursue my ambitions, and hearing my endless questions: Jay McCarty, Jasper Cook, Erin Darlington, Akemi Kunibe, Eric Senning, Geoff Lott, Patrick Blower and Andy Marcus.

To My Friends: To all my friends, thank you for making Boulder a good place to be. Hari Mitar Singh Khalsa, for being the best man I know and a constant inspiration for how to be in this world. Atma Kaur Khalsa, for showing me how to treat all of Boulder as an adventure. Siri Radha Kaur Khalsa, for keeping me healthy and keeping it weird. Colin Gabrielson, for helping me to remember who I am. Jasper Cook, for taking this great step in life just ahead of me and making my transition smoother. I am grateful you introducing me to the department and advising me through finding a research group, cumes, classes and this dissertation. I was glad for another four years of friendship, building computers, frisbee golf, silly 10k's, and quirky shows and video games. Amanda Grennell—you thought I was finished after the labmates section—thank you for being such a good friend inside and outside of the lab. You taught me a great many things about health, politics, books, taxes, and not to mention science. I value our connection on movies, food, fantasy novels and mead. Drew Grennell, for being the hilarious man I wish I could be. Sean Ryan, for getting me to climb. The Pizza Night crew, for giving me an outlet of fun and friendship early on in grad school. Nuria Cirilo Gonzalez, for an easier transition moving to Boulder and fun in my early days here. Mick Tresemer, Jessie Porterfield, Steve Gardner and Jaime Dumont for music nights. Jackson, Ray Chen, Kate Macri and David Protter, for inspiring/forcing me to play Frisbee (Kate especially, for allowing me to be your baggage). Laura Johnson, for introducing me with the Boulder ultimate community and involving me with a wonderful team. Luke Erickson, Nate Kenyon, Tristan Weber and Marek Slipski, for running great frisbee teams. Emma Carr, for sharing your love of music and silly games, and for showing me Colorado. Hiking Club, for a wonderful community of the silliest people I could hope to surround myself with. Armerhouse, for youthful fun and a hilarious D&D campaign. Tristan, for music and soulful conversation. Emily Gallegos, for bringing life to my final years of graduate school.

To My Family: Mom and dad, how can I possibly thank you for all of your wonderful support, both academic and personal. From the first time you sat me down at the kitchen table to introduce me to the concept of homework and I cried, to your financial and emotional support in undergrad and in grad school, you have always encouraged to pursue my dreams and gave me the resources to do so without worry. You fostered in me a curiosity for the world and that was formative to my wonder of Nature and scientific questions. I am where I am today because of how you raised me. Danny, thank you for helping to raise me into the person I am today and for being an academic inspiration since I was young. Katie—my favorite sister—thank you for being a wonderful support while living in Colorado. You provided me with love and support; you fed me, you truly helped my transition to Colorado, you were a home base, and you were a source of relaxation, humor and inspiration. My family, I love you, and will always appreciate the support you have given me that began long before graduate school.

Funding: Finally, the pursuit of science would not be possible with funding. I am grateful to have been and National Science Foundation Graduate Research Fellowship Program (NSF GRFP) Fellow, under Grant No. DGE 1144083. The research presented in this dissertation was also supported by US Department of Energy, Office of Basic Energy Sciences, Division of Materials Sciences and Engineering under Award DE-SC0010334, the Air Force Office of Scientific Research under AFOSR award No. FA9550-12-1-0137, and National Science Foundation under CAREER Award No. CHE-1151151 and Award No. DMR-1410215. Thank you, Gordana, for acquiring funding so that we could focus on research and for your critical guidance in writing fellowship applications.

Table of Contents

List of Tables

List of Figures

Copyright

"In its encounter with Nature, science invariably elicits a sense of reverence and awe. The very act of understanding is a celebration of joining, merging, even if on a very modest scale, with the magnificence of the Cosmos… When we recognize our place in an immensity of light years and in the passage of ages, when we grasp the intricacy, beauty and subtlety of life, then that soaring feeling, that sense of elation and humility combined, is surely spiritual…The notion that science and spirituality are somehow mutually exclusive does a disservice to both."

– Carl Sagan

Chapter 1

Introduction

1.1 Motivation

Harvesting sunlight for the production of useful electrical and chemical energy is a promising application of nanomaterials. An exciting application of nanomaterials is the harvesting of solar energy to produce useful electrical and chemical energy. The research presented in this dissertation is largely motivated by the application of semiconductor nanocrystals to solar energy conversion. While fundamental in nature, the discoveries presented here may eventually provide the framework for future research into commercial device integration.

The field of nanoscience has seen an extraordinary rise in enthusiasm since its birth in the 1980s.[1-3] It is a highly interdisciplinary field of research, drawing on knowledge and expertise from many disciplines including physics, chemistry, engineering, and biology. Today, nanomaterials are employed for a wide range of technological applications including solar energy conversion,[4-8] nanobiology,[9-12] nanomedicine,[9] lighting and displays,[13] and sensing.[9,14] Nanoscience has even made its way into popular culture, featuring in everything from art to science fiction stories.[15,16]

The world currently relies primarily on fossil fuels to meet global energy demands. However, fossil fuels are an inherently limited resource and the burning of fossil fuels produces harmful air pollution as well as greenhouse gases that have been linked to anthropogenic climate change.[17-19] Solar energy harvesting is uniquely suited to address global energy needs by producing renewable energy with minimal environmental impact as the amount of solar energy

hitting the Earth's surface in two hours is more than the global energy use in one year.[20] The conversion of solar energy into electrical or chemical energy can be accomplished with photovoltaics or artificial synthesis, where photovoltaics directly convert solar energy into electricity and artificial photosynthesis mimics Nature's ability to generates fuels that can be stored for later use.[21] Both of these applications rely on the efficient absorption of light and subsequent transport or transfer of photoexcited charges. Semiconductor nanocrystals in particular have been intensely studied for these applications because they are strong light absorbers, have highly tunable properties, and exhibit efficient charge transfer.[4-6,8,22-34] Research on these applications of semiconductor nanocrystals continues to grow, and this dissertation represents my contributions towards achieving more effective solar energy conversion using these systems.

From a fundamental standpoint, we have much to learn about the behavior of photoexcited charge carriers in nanomaterials. Nanocrystals have unique properties as their nanoscale dimensions introduce quantum mechanical effects that can be synthetically controlled, and they interact strongly with their environment compared to bulk materials.[2] Ensembles of nanocrystals are complex, heterogeneous systems where every nanocrystal is unique in terms of size, crystallinity, the number and type of defects, the degree of coverage of surface ligands, etc.[26,35,36] This heterogeneity gives rise to distributions in optical and chemical properties that have important implications for the application of semiconductor nanocrystals. The dynamics of excited states are convoluted in such systems, as electrons and holes can undergo a variety of relaxation pathways with different efficiencies in each particle.[36,37] A large portion of this dissertation is dedicated to resolving the intricate details of nanocrystal excited-state dynamics using both theory and experiment and finding intuitive models to describe them

The work presented in this dissertation offers new discoveries about the behavior of electrons and holes in nanocrystals after the absorption of light, extending our basic understanding of nanocrystal photophysics by providing detailed physical pictures and theoretical models rooted in the analysis of experimental data. These fundamental advances to the field may help benefit optoelectronic applications of nanocrystals such as solar energy conversion.

1.2 Background

1.2.1 Colloidal semiconductor nanocrystals

Semiconductor nanocrystals (NCs) are a class of materials that bridge the gap between individual molecules and bulk crystalline semiconductors. NCs are typically 1–10 nm in size, being composed of 1,000–10,000 atoms (Figure 1.1). When a semiconductor absorbs a photon having an energy greater than or equal to that of the material's band gap, an electron is excited from the valence band to the conduction band, leaving behind a positively charged hole in the valence band (Figure 1.1). Electron–hole pairs known as excitons are formed from the Coulombic interaction between opposite charges.[38] In a bulk semiconductor, photoexcited charge carriers have delocalized wavefunctions. However, in a semiconductor NCs of small enough size, the exciton is confined by the small spatial dimensions of the material. This quantum confinement leads to a size-tunable band gap and the emergence of discrete, particle-in-a-box-like states in the valence and conduction bands (Figure 1.1).[1-3,39] Nanocrystals can be synthesized to have many different morphologies, such as spherical "quantum dots," cylindrical "nanorods," and planar "nanoplatelets." Each gives rise to different optical properties as the confinement effects are applied in 1 to 3 dimensions.[33-35,40]

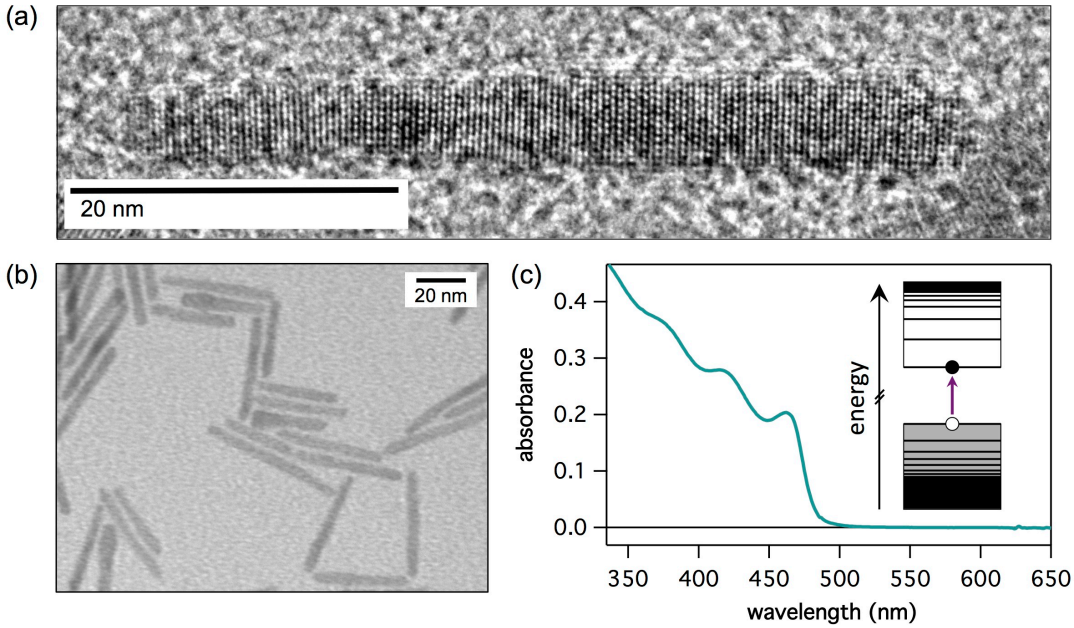

Figure 1.1. Transmission electron microscopy images and absorption spectrum of CdS nanorods. (a) High-resolution transmission electron microscopy (TEM) image of a 5 nm × 52 nm CdS nanorod with resolved wurtzite lattice structure due to regular columns of atoms. (b) TEM image of a sample of CdS nanorods that are 4 nm × 37 nm on average. (c) UV-visible absorption spectrum of the CdS nanorod sample from (b). The absorption spectrum exhibits discrete peaks due to quantum confinement in the radial direction of the cylindrical nanorod. Inset: Schematic depiction of absorption of a photon promoting an electron (filled circle) into the conduction band manifold (white region), leaving a hole (open circle) in the valence band manifold (grey region). Each band is composed of discrete states, and absorption to/from different states give rise to the distinct features in the absorption spectrum.

The surface of a colloidal semiconductor NC is a rich landscape of chemical and structural disorder where atoms can be undercoordinated.[26] As the size of a NC decreases, the ratio of its surface area to volume increases, so that a significant percentage of the NC's atoms lie at the surface—this number is about 40% in the systems studied here, for example. Because of these large surface-to-volume ratios, the NC's optical properties of the NCs are extremely sensitive to their surface chemistry and the surrounding environment.[41] Thus, control of the NC surface structure and chemistry grants the ability to tune the electronic, optical and chemical properties of colloidal semiconductor NCs, making them exceptionally versatile systems.

At the surface the inorganic crystal lattice is disrupted and interfaces with the molecular ligands and the solvent. Semiconductor NCs can be solubilized as colloidal suspensions through the use of surface-capping ligands, which promote the solubility of the NCs in a given solvent. Organic ligands, which bind to surface atoms through their binding functional groups while the rest of the molecule interacts with the solvent, can both passivate some surface defects of the NC and enable solubility in a wide range of nonpolar, polar and aqueous solvents.[8,26]

This dissertation will focus on colloidal semiconductor NCs made of Cd-chalcogenides (i.e., CdS and CdSe). This class of materials has been intensely studied for the past four decades because they have several characteristics that make them promising for use in optoelectronic applications such as solar energy harvesting.[3-8] Nanoscale materials are attractive as light absorbers for such applications because the photoexcited carriers have immediate access to the surface where they can by extracted or utilized. Extensive research has led to precise synthetic control over Cd-chalcogenide NC shape, size and surface chemistry.[26,32-34] CdS, CdSe and CdTe NCs absorb visible light, and do so strongly with molar absorptivities in the range of 10^5–10^7 M^{-1} cm^{-1},[25] which is up to 100 times more than the molecular dyes used for the most efficient dye-sensitized solar cells.[42] The bulk redox potentials of the conduction-band edges of these materials all provide sufficient driving force to carry out various reduction reactions, such as H^+ reduction to H_2, [8,43-47] and size tunability provides fine control over this driving force.[4,31] CdS, in particular, has the appropriate band alignment to potentially carry out water splitting. Finally, the surfaces of Cd-chalcogenide NCs can be modified to promote the interaction with a large host of acceptors and catalysts and to control the strength of electronic coupling to the environment.[5,8,26-30]

1.2.2 Non-exponential relaxation of photoexcited nanocrystals

Optoelectronic applications of semiconductor NCs require control over the generation, separation, and extraction of photoexcited electrons and holes.[6,8,22-24] To this end it is essential to understand the fundamental excited-state dynamics in these systems. Following excitation of a NC by light, a variety of relaxation pathways are available to both the electron and hole, as depicted in Figure 1.2. If the NC is exited with an energy above the band gap, the electron and hole will temporality occupy "hot" excited states that rapidly undergo intraband relaxation—or "cooling"—to the band edges on a sub-picosecond timescale.[26,48-50] Band-edge electrons and holes can undergo radiative and non-radiative decay over a vast range of timescales, including recombination and trapping to surface defects.[23,35-37,51-60] In the absence of charge transfer, photoexcited NCs ultimately decay by recombination between the electron and hole, whether from the band edges or trap states.[23,36,37,41,56,61]

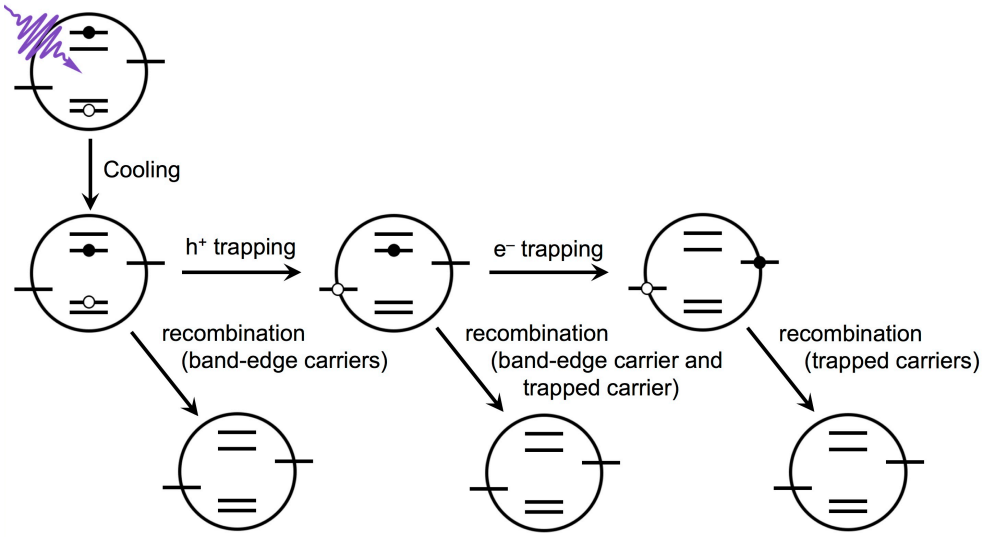

Figure 1.2. Schematic depiction of excited-state relaxation pathways in semiconductor nanocrystals. Photoexcitation of the NC with a photon having an energy above the band gap produces hot carriers that cool to the band edge. Electrons and holes can trap to defect sites within the lattice or at the surface, but can do so independently and on different timescales. Recombination can occur between two band-edge carriers, between a band-edge carrier and a trapped carrier, or between two trapped carriers. Figure is based on Knowles *et al*.[37]

In an ensemble of colloidal semiconductor NCs, structural and environmental heterogeneities lead to distributions in the rates of the various decay pathways. Therefore, NC excited-state decay curves are typically complex non-exponential functions that are sensitive to many factors such as sample preparation, composition, concentration, surface stoichiometry, ligands, temperature and light intensity.[36,37,62-66] The complicated shapes of experimentally measured excited-state decay curves often cannot be described by simple kinetic models.[36,37] While average carrier lifetimes in NC ensemble samples are straightforward to calculate,[24] these lifetimes do not provide the intrinsic rate constants for the underlying excited-state decay processes. They do not take into account the origins of the non-exponential behavior, such as sample heterogeneity. One of the goals of the research described in this dissertation is to understand the principles that govern electron and hole relaxation dynamics using models based on fundamental physical phenomena.

1.2.3 Nature and behavior of trap states in Cd-chalcogenide nanocrystals

Achieving a detailed picture of the nature and behavior of surface-trapped charge carriers in nanocrystals remains a major challenge in nanoscience. Our understanding of surface states—which typically have weak transition dipole moments—is much less developed than that of core exciton states, as surface states are more difficult to study experimentally. However, charge-carrier traps are pervasive in nanostructures: a better understanding of them would benefit a wide range of NC-based optoelectronic applications.

Surface traps are typically associated with undercoordinated surface atoms or redox-active ligands.[26,52,62,67-75] Surface traps in CdS and CdSe NCs have been intensely studied, and will be the subject of several chapters of this dissertation. Electron traps are typically associated

with undercoordinated Cd species on the NC surface, but can be passivated effectively with organic surface-capping ligands that saturate the Cd atoms, typically resulting in very small electron-trap densities in ensemble colloidal samples.[26,35,75-77] Hole traps on the other hand, which are associated with undercoordinated chalcogen species (S or Se),[52,68,69,74,76] are more pervasive and often cause fast and efficient nonradiative relaxation in spite of adequate ligand coverage. Hole trapping occurs on a picosecond timescale in both CdS and CdSe NCs,[23,37,52-60] leading to a localized holes at surface chalcogen species that are thermodynamically trapped.[74,76,78,79]

While a considerable understanding of the nature of trapped carriers has been achieved, their dynamic behavior has remained more elusive because of the optically forbidden nature of surface states. Still, important insights have been gained about trapped-carrier dynamics through indirect measurements, elucidating hole-detrapping kinetics, surface-state emission, and the transfer of trapped holes to molecular acceptors.[80-83] The conventional picture is that trapped holes, being energetically trapped and spatially localized, are stationary. However, my work presented here demonstrates that trapped holes may actually be mobile at room temperature, undergoing a diffusive random walk amongst surface trap states.

Charge-carrier traps have a fundamental impact on the electronic structure and excited-state dynamics on NCs, affecting various processes including photoluminescence (PL),[68,76,80,81] charge transfer,[65,82-85] Auger recombination,[86,87] blinking,[88] charge transport,[89] and optical gain.[90,91] The ability to mitigate trapping in NCs by surface passivation is relatively well understood—for example, through the growth of inorganic shells around the nanocrystal core.[92-94] However, the resulting reduction in electronic coupling between NCs and their environment can be detrimental to optoelectronic applications that rely on the transfer of photoexcited charge

carriers to acceptors.[5,70,95-98] Thus, it is critical to understand the nature of surface traps and the dynamic behavior of trapped carriers.

1.2.4 Nanocrystals for photochemistry

Coupling colloidal semiconductor NCs to redox catalysts is an emerging strategy to photochemically drive fuel-generating reactions such as H_2 production.[24,30,31,44,99-105] While photoexcited NCs may have the appropriate band alignment to drive such reactions, they are typically inefficient at accomplishing multi-electron chemistry alone and instead require redox cocatalysts to make efficient fuel-producing systems.[106] These NC–cocatalyst systems integrate the tunable electronic structure, strong light absorption, and surface chemistry of NCs with a variety of tailored cocatalysts. Photochemical reactions of NC–cocatalyst complexes proceed through a sequence of steps: light absorption in the nanocrystals, transfer of photoexcited electrons to the cocatalysts where they participate in catalysis, and hole scavenging by sacrificial electron donors (Figure 1.3).[24,30,101]

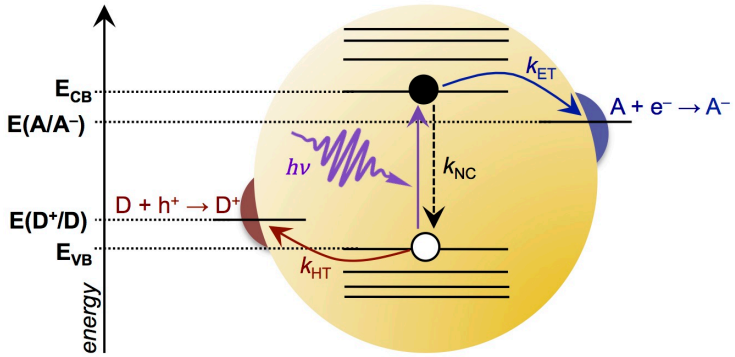

Figure 1.3. Schematic representation of photochemical reactions mediated by a semiconductor NC–cocatalyst complex. Photons with energy $h\nu$ excite the NC, placing an electron in the conduction band and a hole in the valence band with energies E_{CB} and E_{VB}, respectively. Photoexcited electrons can reduce electron acceptors (A) at an energy of $E(\mathrm{A/A^-})$, transferring with rate constant k_{ET}, and holes oxidize electron donors (D) at an energy of $E(\mathrm{D^+/D})$, transferring with rate constant k_{HT}. These processes compete excited-state decay of the NC, which in a single-exponential decay model has a total rate constant of k_{NC}. The electron acceptors and donors can be either reactants or intermediates in a multi-electron reaction. Figure is based on Wilker *et al*.[8]

The kinetics of electron transfer (ET) from the nanocrystal to the catalyst play a crucial role in the overall photochemical reactivity. The quantum efficiency of ET (QE_{ET}) determines the upper limit on the quantum yield of fuel generation. QE_{ET}, in turn, depends on how the rate constant of ET compares to the rate constants of competing excited-state decay processes in the nanocrystal, such as recombination and carrier trapping. In a simple case of single exponential relaxation kinetics in a homogeneous system, QE_{ET} can be formulated as

$$QE_{ET} = \frac{k_{ET}}{k_{NC} + k_{ET}}, \quad (1.1)$$

where k_{ET} is the rate constant of ET and k_{NC} is the total rate constant of decay on the NC.

When driving multi-electron reactions in many NC–cocatalyst complexes, the photochemical yield is limited by recombination or back-ET after the electron(s) have been transferred but before the product is formed.[107-113] This motivates the integration of semiconductor NCs with redox enzymes, which offer superior reaction selectivity and intermediate stability compared to molecular and inorganic catalysts. CdS–enzyme complexes have been used to photochemically drive several multi-electron reduction reactions with relatively high efficiency, including H_2 production, CO_2 reduction, and N_2 fixation.[8,24,44-46,65] In some such systems the quantum yield of fuel production is thought to be dominated by QE_{ET},[61] and thus is controlled by the competition between ET and NC relaxation. Therefore, it is critical to be able to measure the rate constants of these competing pathways, understand what factors determine QE_{ET}, and then control the rate constants of the competing pathways in order to improve the quantum yield of fuel production in such systems. In this dissertation we address each of these points in complexes of CdS nanorods with [FeFe] hydrogenase I from *Clostridium acetobutylicum*, which photochemically reduces $2H^+$ to H_2.[44]

1.2.5 Transient absorption (TA) spectroscopy

In order to experimentally probe excited-state dynamics and electron transfer in Cd-chalcogenide nanocrystals we primarily used TA spectroscopy throughout the work presented in this dissertation. TA spectroscopy is a powerful technique for measuring time-resolved dynamics of photophysical and photochemical processes.[26,114,115] This is a pump–probe technique in which a pump pulse of monochromatic light is used to photoexcite a fraction of particles in the sample (Figure 1.4). This pulse is followed some time later by a broadband, "white light" probe pulse that measures changes in the absorption spectrum in response to excitation by the pump pulse. The difference absorption spectrum, ΔA, is calculated by comparing the probe absorption with and without excitation of the sample by the pump, subtracting out contributions of the ground-state signal and therefore selectively monitors the photoexcited particles in the sample. Varying the time delay between the pump and probe pulses allows one to monitor the time evolution of the photoexcited states resolved in the probe spectrum, yielding both the spectral and temporal evolution of the sample: $\Delta A(t, \lambda)$ (here t is the pump–probe time delay and λ is the wavelength) Since photoexcited states in most colloidal semiconductor NC systems can evolve over a range of picoseconds to microseconds, we use a combination of complementary experimental setups—one that uses spatially-delayed pump and probe pulses that are ~100 fs in duration and another that uses an electronically-controlled probe pulse that is ~100 ps in duration—that, when used in conjunction, allow us to monitor spectral signals throughout the visible region over a time window of 100 fs–0.4 ms.[116]

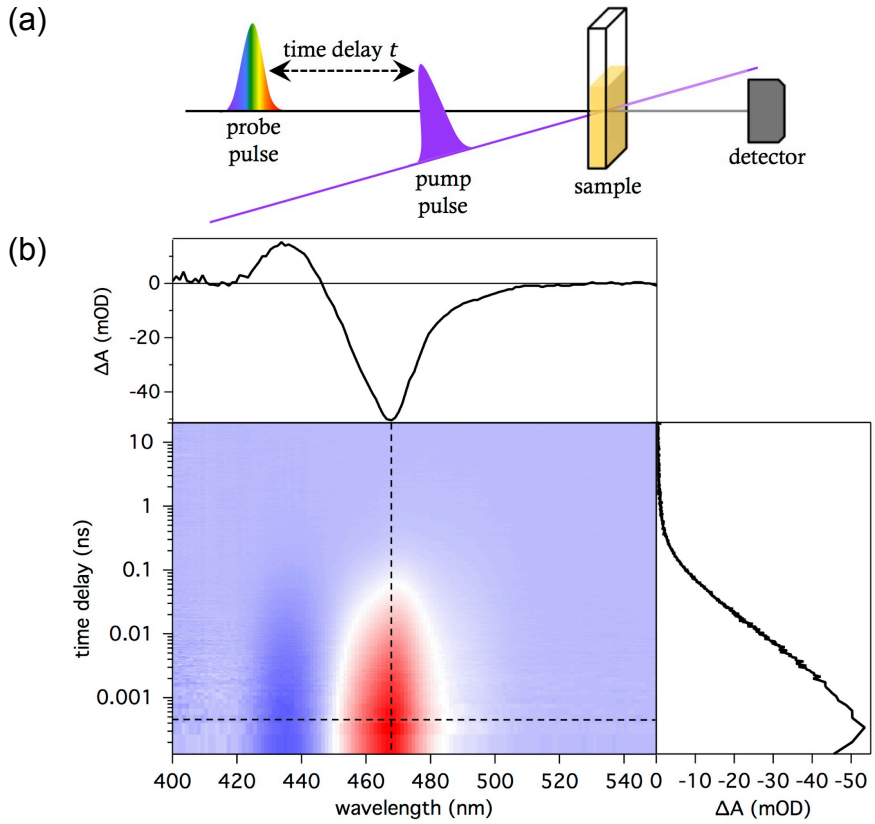

Figure 1.4. Transient absorption spectroscopy. (a) Pump–probe geometry used in TA spectroscopy. The monochromatic pump pulse excites the sample and the remaining beam is dumped. After a time delay t a white light probe pulse passes through the sample and is then focused onto a detector. (b) Representative TA spectroscopy data of CdS nanorods. The main panel shows $\Delta A(t, \lambda)$, where red and blue correspond to negative and positive ΔA amplitudes, respectively. The TA spectrum at a given time (top panel) or TA time trace at a given wavelength (right-hand panel) can be extracted by taking slices (dashed lines in main panel) of the TA spectroscopy data.

In general, a TA spectrum is comprised of various processes that lead to positive or negative ΔA signals:[115]

(1) ground-state bleach, wherein the excitation leads to a decreased ground-state population, decreases the amount of probe light absorbed and thus contributes a negative signal at the bleached transition;

(2) stimulated emission, wherein photons degenerate with the excited transition stimulate excited-state decay by photon emission, leads to an increase of light intensity of the

detector due to the presence of excited particles and thus contributes a negative signal at the bleached transition;

(3) excited-state absorption, which is where the probe light is absorbed by an excited particle, causing a transition to a higher-laying excited state, contributes a positive signal;

(4) product absorption, where a photochemical process occurs leading to the formation of a new species and therefor new spectral features that are not seen in the ground state absorption spectrum.

In Cd-chalcogenide NCs, the amplitudes of the TA bleach signals are dominated by the occupation of electrons in excited states within in the conduction band manifold, and are effectively independent of excited hole populations.[114,117] An example of this can be seen in Figure 1.4, which shows a bleach peak centered at the band-edge transition (468 nm) due to the presence of a photoexcited electron at the band edge, even though the hole has trapped to the surface. Though other features, such the positive feature seen in Figure 1.4, will be important for some analyses, the work in this dissertation we will focus on the evolution of the band-edge bleach. Most importantly for this dissertation, the amplitude of the band-edge bleach is directly proportional to the population of electrons at the conduction-band edge, and by monitoring the time evolution of this peak (Figure 1.4) we are directly measuring the number of electrons at the conduction-band edge over time.[114,118] In this way we can learn a great deal about the relaxation dynamics of Cd-chalcogenide NCs.

1.3 Summary and goals

In this dissertation we seek to find robust physical descriptions of the complex photophysical and photochemical behavior of Cd-chalcogenide nanocrystals. Combining advanced experimental

techniques, theoretical modeling, and extensive data analysis can lead to deeper insights than when any one approach is used alone. Here, we use ultrafast spectroscopy to monitor the dynamics of photoexcited electrons and holes, theoretical modeling rooted in physical phenomena to gain qualitative and quantitative information about the underlying dynamics, and rigorous data analysis to extract subtle features within the data. Ultimately, this dissertation extends our fundamental understanding of the behavior of trapped holes at the surfaces of Cd-chalcogenide NCs as well as electron-transfer kinetics in NC–electron acceptor complexes.

This dissertation is structured as follows. The research efforts in this dissertation are broken in two parts. Part I (Chapters 3–6) focuses on the dynamics of trapped holes while Part II (Chapters 7–9) concentrates on the kinetics of electron transfer in nanocrystal–acceptor complexes. After a description of the experimental methods used throughout this dissertation in Chapter 2, Chapter 3 details the discovery of trapped-hole diffusion on the surfaces of CdS nanocrystals. Using a combination of transient absorption spectroscopy and theoretical modeling, we present evidence that trapped holes in CdS nanorods are mobile and execute a random walk at room temperature. Chapter 4 extends the study of trapped-hole diffusion to CdSe/CdS and ZnSe/CdS dot-in-rod heterostructures, showing that the behavior of electrons is similar in several CdS nanorod-based nanostructures, and that hole trapping and nanoparticle morphology ultimately drive electron dynamics in such systems. Chapter 5 shows that trapped-hole diffusion also occurs in CdSe nanorods, suggesting that it is a general phenomenon in Cd-chalcogenide nanocrystals. Chapter 6 describes temperature dependence studies of trapped-hole diffusion in CdS and CdSe nanorods that rule out alternative mechanisms for experimental observations, rounding off the trapped-hole diffusion work by leaving diffusion as the most consistent model for the data. Chapter 7 turns to the kinetic modeling of electron transfer and competing relaxation

pathways in complexes of CdS nanorods and [FeFe] hydrogenase. Chapter 8 explores at the role of ligand length on the electron transfer and H_2 production in the CdS nanorod–hydrogenase system. Chapter 9 concerns the exact calculation of electron-transfer quantum efficiency from measurements on heterogeneous ensembles of nanocrystal–acceptor complexes that exhibit non-exponential relaxation, featuring CdS nanorod–hydrogenase as a case study. Finally, Chapter 10 provides an overview of the work presented in this dissertation and offers and outlook for future work.

Chapter 2

Methods

2.1 Nanocrystal synthesis

2.1.1 Synthesis and purification of non-uniform CdS nanorods (NRs)

We synthesized CdS NRs according to previously reported methods.[119,120] Synthesis was done under inert argon at ~620 Torr (atmospheric pressure in Boulder, CO). In a typical synthesis, 1.6 mmol cadmium oxide (CdO; Sigma Aldrich, ≥99.99% trace metals basis), 3.2 mmol n-octadecylphosphonic acid (ODPA; PCI Synthesis), and 8.6 mmol trioctylphosphine oxide (TOPO; Sigma Aldrich, *ReagentPlus*®, 99%) were stirred under vacuum at 120 °C and then heated under Ar to 320 °C for 1 hr. The mixture was then brought down to 120 °C, stirred under vacuum for 1 hr, and reheated under Ar to 320 °C. Then, 5.4 mmol tri-n-octylphosphine (TOP; Strem Chemicals, min. 97%), and 3.2 mmol trioctylphosphine sulfide (TOP:S) were injected. TOP:S was prepared by mixing TOP and elemental S (Aldrich, 99.998%) in a 1:1 molar ratio in an Ar glovebox and stirred for 48 hr at room temperature. After TOP:S injection, nanocrystals were grown at 315 °C for 45 min. The reaction mixture was then cooled to 80 °C, and the NRs were precipitated using a toluene:acetone (1:2 volume ratio) mixture. The CdS NRs were purified under Ar through sequential re-dispersion/precipitation steps using toluene/octylamine/acetone, chloroform/nonanoic acid/isopropanol, and hexane/isopropanol mixtures. Sequential precipitation steps using increasing amounts of isopropanol were used to separate the mixture into fractions of different mean lengths with narrow size distributions before

re-dispersing and storing in toluene.[116] This synthetic procedure results in batches of CdS NRs in which a significant fraction (~50%) of nanostructures are non-uniform in diameter.

2.1.2 Seeded synthesis of CdS nanorods (NRs)

The CdS NRs synthesis was adapted from a published procedure for a seeded-growth method and carried out in an argon atmosphere.[46,121] CdS seeds were synthesized from an initial mixture of 0.100 g cadmium oxide (CdO, 99.99% Aldrich), 0.603 g octadecylphosphonic acid (ODPA, 99%, PCI Synthesis), and 3.299 g trioctylphosphine oxide (TOPO, 99%, Aldrich). At 320ºC, a sulfur stock solution (0.179 g hexamethyldisilathiane ($(TMS)_2S$, synthesis grade, Aldrich) in 3 g of tributylphosphine (TBP, 97%, Aldrich)) was quickly injected. Nanocrystal growth proceeded for 7.5 minutes at 250ºC. The reaction was stopped by removing the heating mantle and injecting 4 mL of anhydrous toluene. The CdS seeds were washed by precipitation with methanol and the final product was dissolved in trioctylphosphine (TOP, 97%, Strem). The CdS seeds had their lowest-energy exciton peak at 408 nm. The rods were synthesized from a starting solution of 0.086 g CdO, 3 g TOPO, 0.290 g ODPA, and 0.080 g hexylphosphonic acid (HPA, 99%, PCI Synthesis). The solution was heated to 350ºC then 1.5 mL of TOP was injected into the solution. When the temperature of the Cd-containing solution stabilized at 350°C, the seed-containing sulfur injection solution (0.124 g of sulfur (S, 99.998%, Aldrich) in 1.5 mL of TOP mixed with 8 $\times$ 10^{-8} mol CdS QD seeds) was quickly injected. Nanocrystal growth proceeded for 8 minutes, after which the solution was cooled and the particles were purified using size-selective precipitation

2.1.3 Synthesis and purification of CdS quantum dots (QDs)

We synthesized and purified CdS QDs following the method of Peterson et al.[122] Cadmium oleate was produced by heating 0.128 g of CdO, 6.85 mL of 1-octadecene (ODE; Sigma Aldrich,

90%), and 3.2 mL of oleic acid (OA; Sigma Aldrich, 90%) to 250 °C under Ar in a 3-neck round-bottom flask. Once the solution turned clear, the heat source was removed and the solution is allowed to cool to 60 °C. 4 mL of cadmium oleate solution was transferred into a separate round-bottom flask containing 3 mL of degassed ODE, and this solution is heated to 260 °C. Once reaction temperature was reached, 1 mL of 0.10 M elemental S dissolved in ODE was injected and the solution allowed to cool to 220 °C. After 3 min, 0.5 mL of S precursor was injected using a cannula under positive pressure. Six subsequent 0.5 mL additions of Cd or S precursors were performed at 1 min intervals. After the final cadmium oleate injection, the solution was cooled in a room temperature oil bath. The crude reaction mixture was moved into an Ar-filled glovebox.

CdS QDs were purified from the reaction mixture using a liquid-liquid extraction with a 3:1 ratio of methanol to reaction mixture, with several drops of isopropanol added to encourage mixing. The QDs were then purified further using precipitation/dispersion steps using acetone/toluene and methanol/toluene. The size distribution was further narrowed using a sequential precipitation in isopropanol.[116] The sizes of the CdS QDs used in Chapter 3 were determined from a published tuning curve to be 5 nm in diameter.[25]

2.1.4 Synthesis of ZnSe/CdS and CdSe/CdS dot-in-rod heterostructures

The materials used in the synthesis of ZnSe/CdS and CdSe/CdS dot-in-rod heterostructures were tri-n-octylphosphine (TOP, Strem Chemicals, min. 97%), sulfur (99.9%, Aldrich), selenium (99.9%, Aldrich), trioctylphosphine oxide (TOPO, 99%, Aldrich), n-octadecylphosphonic acid (ODPA, 99%, Polycarbon), cadmium oxide (CdO, Sigma Aldrich, ≥99.99% trace metals basis), octadecylamine (ODA, 99%, Aldrich), diethylzinc (Et_2Zn, 52% wt% in toluene, Aldrich), anhydrous toluene (99.8% Sigma Aldrich), anhydrous acetone (≥99.9%, Sigma Aldrich),

octylamine (99%, Aldrich), anhydrous chloroform (≥99.9%, Sigma Aldrich), nonanoic acid (96%, Sigma Aldrich), anhydrous isopropanol (99.5%, Sigma Aldrich), anhydrous hexanes (mixture of isomers, ≥99%, Sigma Aldrich), anhydrous methanol (99.8%, Sigma Aldrich), 3-mercaptopropionic acid (3-MPA, ≥99%, Sigma Aldrich), and tetramethylammonium hydroxide pentahydrate salt (TMAH, 97%, Sigma Aldrich). Materials were used as purchased.

Synthesis of ZnSe Seeds. Synthesis of monodisperse wurtzite ZnSe nanocrystals was adapted from previous work.[123] All reactions were conducted under argon using standard Schlenk techniques at atmospheric pressure (~620 Torr in Boulder, CO). Trioctylphosphine sulfide (TOP:S) and trioctylphosphine selenide (TOP:Se) were prepared by stirring TOP and either elemental sulfur or selenium, respectively, at room temperature in Ar atmosphere for 48 h.26 mmol of ODA was heated under vacuum at 130 °C for 1.5 h. The ODA was heated to 300 °C under Ar. Maintaining this temperature, 2.4 mL of 0.32 M TOP:Se solution was added to the ODA, followed by a rapid injection of 1 mL of a ~10% by weight solution of Et_2Zn (0.8 mmol) in toluene. The nanocrystals were then grown at 265 °C for 1 h. The reaction mixture was cooled to 80 °C in an oil bath, then 20 mL of ethanol and 4 mL of toluene, both at 75 °C, were added to precipitate the nanocrystals. Purification was done by repeated precipitation and re-dissolution using ethanol and toluene until the solution was clear at room temperature. The ethanol, toluene, and nanocrystal mixture were kept at 75 °C during purification to prevent solidification of the ODA. The final product was stored in toluene.

Synthesis of ZnSe/CdS dot-in-rods (*DIRs*). Growth of CdS rods on ZnSe seeds was adapted from previous work.[124,125] An injection solution containing ZnSe seeds was made by drying 211 μL of purified ZnSe seeds solution to remove the toluene, then dissolving the dried nanocrystals in 0.5 g TOP. The volume of ZnSe seed solution (211 μL) dissolved in TOP was

chosen so that the product of the absorbance at 360 nm and solution volume was in the range of 30-40 mL. The ZnSe seeds in TOP were then mixed with 0.65 g of 2.06 M TOP:S to make the final injection solution. Next, 1.61 mmol CdO, 9.18 mmol TOPO, and 3.23 mmol ODPA were heated to 150 °C while stirring and then kept under vacuum at that temperature for 1 h. Under Ar, the mixture was heated to 280 °C and held there for 10 min. The temperature was reduced to 160 °C and the mixture was held under vacuum for 2 h. The mixture was then heated to 300 °C under Ar, 1.81 mL of TOP was injected, and the temperature was allowed to recover. The injection solution, containing ZnSe seeds and TOP:S, was then rapidly injected into the reaction flask. The temperature of the reaction mixture dropped to 290 °C, and was slowly raised to 315 °C over the course of 50 min. The reaction mixture was held at 315 °C for 20 min, then cooled to 60 °C in an oil bath. 7 mL of toluene were added to prevent solidification, and the nanocrystals were purified by repeated precipitation and re-dissolution with mixtures of toluene/octylamine/acetone and chloroform/nonanoic acid/isopropanol (~3:1:3 volume ratio). The nanocrystals were suspended in hexane as the remaining impurities precipitated overnight, then re-dispersed in toluene.

Synthesis of CdSe seeds. We followed a previously reported synthesis of CdSe seeds.[121,125] 8.2 mmol TOPO, 0.84 mmol ODPA, and 0.46 mmol CdO were mixed and heated to 150 °C under Ar, then held under vacuum for 1 h at that temperature. The reaction mixture was heated to 300°C under Ar and held there for 20 min. The temperature was then reduced to 150 °C and the mixture was held under vacuum for 1.5 h. Under Ar, the temperature was increased to 300 °C and 1.5 g of TOP was injected in the flask. The temperature was increased to 365 °C and 0.418 g of TOP:Se was rapidly injected. The reaction was quenched after 3 min by removing the heating mantle and cooling to 60 °C in an oil bath. Purification was performed by

precipitation and re-dissolution using methanol and toluene. The final product was re-dispersed in TOP.

Synthesis of CdSe/CdS DIRs. The growth of CdS rods on CdSe seeds has been previously described and we followed those published procedures.[121,125] 1.61 mmol CdO, 9.18 mmol TOPO, and 3.23 mmol ODPA were heated to 150 °C while stirring and then held under vacuum for 1 h at that temperature. Under Ar, the mixture was heated to 280 °C and held there for 10 min. The temperature was reduced to 150 °C and the mixture was held under vacuum for 2 h. Under Ar, the mixture was heated to 300 °C, 1.81 mL of TOP was injected and the temperature was allowed to recover. A TOP:S/CdSe injection solution was made by mixing 7.24×10^{-4} mmol of CdSe seeds (285 μL of stock CdSe seeds in TOP) in 0.5 g of TOP and mixing this with 0.65 g of 2.06 M TOP:S. The reaction mixture was brought to 255 °C and the TOP:S/CdSe solution was rapidly injected. The temperature of the reaction mixture dropped to 340 °C after injection, and was held here for a 45 min during nanocrystal growth. The heating mantle was removed to quench the reaction and the mixture was cooled to 60 °C in an oil bath and 7 mL of toluene were added to prevent solidification. Purification was done by repeated precipitation and re-dissolution with mixtures of toluene/octylamine/acetone and chloroform/nonanoic acid/isopropanol (~3:1:3 volume ratio). The nanocrystals were suspended in hexane as the remaining impurities precipitated overnight. The final product was re-dispersed in toluene.

2.1.5 Synthesis and purification of CdSe nanorods (NRs)

This synthesis was adapted from a previously reported procedure.[126] Into a 25 mL flask equipped with a condenser and temperature probe, 3.1783 g trioctylphosphine oxide (TOPO, 99%, Aldrich), 140.1 mg hexylphosphonic acid (HPA, 99%, PCI), 681.4 mg tetradecylphosphonic acid (TDPA, 99%, PCI), and 207 mg cadmium oxide (CdO, 99.99%, Aldrich) were added. This

mixture was heated to 120°C with stirring under Ar and then degassed for 1 hour under vacuum. Under Ar the solution was heated to 320°C for 15 minutes and then cooled to room temperature by removing the heating mantle. The solution turned from clear and colorless to cloudy and white at room temperature. Once cooled, the flask was opened to air and allowed to age overnight in a vent hood. After at least 24 hours of aging, the flask was resealed, placed under Ar, and heated to 120°C. The mixture liquefied and remained cloudy and white. The flask was switched to vacuum and degassed for 1 hour. Under Ar, the flask was heated to 320°C and the Se precursor [250 mg of 25% w/w Se:TBP (Se shot, 99.99%, Aldrich; tri-n-butylphosphine, 97%, Aldrich) dissolved in 1.444 g tri-n-octylphosphine (TOP, 97%, Strem) and 301 mg toluene] was injected. The temperature controller was set to 300°C and the nanocrystals were allowed to grow for 8 minutes. After growth, the flask was cooled to 80°C using an oil bath, and the solution was placed in an air-free vial containing 5 mL methanol to induce precipitation. The vial was centrifuged for 15 min at 3500 rpm to separate the nanocrystals from unreacted precursors and residual solvent. The vial was then pumped into the glovebox for purification.

Centrifugation produced a clear, colorless supernatant with a compact brown precipitate at the bottom of the vial. The supernatant was poured off and the precipitate was washed by successive acid and base washes whereby the additions of either Chloroform/Nonanoic Acid/Ethanol or Toluene/Octylamine/Methanol were followed by centrifugation for 5 minutes at 4400 rpm. The final product was redissolved in 4 mL Hexane and stored in the glovebox for at least 24 hours, after which the solution was centrifuged for 1 hour at 3500 rpm to remove any remaining impurities. The nanocrystals were precipitated by the addition of a 2:1 mixture of Isopropanol:Methanol followed by centrifugation for 15 minutes at 4400 rpm. The final product was dissolved in toluene.

2.1.6 Ligand exchange

Many experiments in this dissertation were performed on nanocrystals for which the native surface-capping ligands were replaced with 3-mercaptopropanoic acid (3-MPA) and suspended in an aqueous buffer solution. In those cases, ligand exchange to 3-MPA ligands was carried out following a previously reported procedure.[44,107] The ligand exchange procedure is the same for all nanocrystals used here since all have CdS surfaces with their native, organic surface-capping ligands. A 70 mM solution of 3-MPA (Sigma Aldrich, ≥99%) in methanol was prepared and its pH was raised to 11 with tetramethylammonium hydroxide pentahydrate (Sigma, ≥97%). The as-synthesized, organic-capped nanocrystals in toluene were precipitated using methanol, and then vigorously mixed with just enough 3-MPA solution so that the mixture was no longer cloudy. Toluene was added to precipitate the 3-MPA-capped nanocrystals and the resulting particles were collected and re-dissolved in an aqueous buffer solution (50 mM Tris-HCl, pH 7). For CdSe NRs the native nanocrystal surface ligands were exchanged for 3-MPA ligands according to previously published work on CdS NRs[44] and were dispersed in 12.5 mM Tris Buffer at pH 7.

2.1.7 H_2ase Purification, Characterization, and Coupling to CdS NRs

The [FeFe] hydrogenase from *Clostridium acetobutylicum* (CaI) was expressed and purified from *Escherichia coli* as previously described with some modifications.[127] For expression, cells were grown in a 10 L fermenter (Sartorius Stedim Biotech) at 37°C with 250 rpm stirring and 0.9 L/min air bubbling. For induction, 1.5 mM Isopropyl β-D-1-thiogalactopyranoside (IPTG) was added, along with 4 mM ammonium iron (III) citrate, 2 mM cysteine, 0.5% glucose, and 10 mM sodium fumurate. The stirring was adjusted to 75 rpm, temperature to 30°C, and air bubbling was switched to N_2 bubbling (0.3 L/min). The anaerobic induction proceeded overnight and the next morning the cells were collected using an in-line centrifuge (Eppendorf, 3000 rpm) under

N_2 atmosphere. The centrifuge cell was transferred to a glovebox (Coy Laboratories, 3% H_2 atmosphere), the cells were washed with buffer A (50 mM Tris pH 8, 5 mM NaCl, 5% glycerol, 5 mM NaDT), and frozen at -80°C. For purification, all steps were carried out under strict anaerobic conditions with initial cell lysis in a Coy chamber (3% H_2 atmosphere) and subsequent chromatography steps in an Mbraun glove-box (N_2 atmosphere). For cell lysis, 30 µL Benzonase (Sigma-Aldrich), lysozyme (Sigma-Aldrich), 2 EDTA-free protease inhibitor tablets dissolved in 1 mL buffer A (Roche), and 2 mM DTT were added to the cell suspension. A microfluidizer (M-110S, Microfluidics) under Ar pressure was used to break the cells. After centrifugation (15,000 rpm, 45 min, 4°C) the cell-free-lysate was first purified over DEAE resin (GE Healthcare) and eluted by a 4 column volume gradient to buffer B (50 mM Tris pH 8, 1M NaCl, 5% glycerol, 5 mM NaDT). Fractions were collected and analyzed for protein content by SDS-PAGE and hydrogenase activity assay (10 mM NaDT, 5 mM methyl viologen) with H_2 evolution measured by GC chromatography (Agilent Technologies). The active fractions were combined and concentrated to ~30 mL using a 30 kDa MWCO membrane and Amicon concentrator cell under Argon gas pressure. The concentrated fraction was purified over 25 mL Strep-Tactin Superflow High Capacity resin (IBA) and eluted into 50 mM Tris pH 8, 200 mM NaCl, 5% glycerol, 5 mM NaDT for the final purification step. Protein concentration was determined by Bradford assay (±10%) using Hemoglobin as the standard,[128] and the H_2 evolution activity (1,700 µmol H_2/min/mg) was measured as described above. FTIR spectroscopy was also used to verify incorporation of the active site H-cluster. Mixtures of CdS NRs and H_2ase were prepared in buffer C (12.5 mM Tris-HCl, 5mM NaCl, 5% glycerol, pH 7) under an anaerobic Ar environment.

2.2 Spectroscopy

2.2.1 UV-visible absorption spectroscopy

UV-visible absorption spectra were recorded using an Agilent 8453 spectrophotometer utilizing tungsten and deuterium lamps at room temperature sealed under Ar in 2 mm quartz cuvettes.

2.2.2 Steady state photoluminescence spectroscopy

The photoluminescence spectra were obtained using a SLM AMINCO 8000C Spectrofluorometer (SLM Instruments, Inc.) with an Ushio UXL-450S-0 xenon short arc lamp and Hamamatsu R928P PMT operating at −850 V, DC. The sample was sealed under Ar in a 1 cm x 1 cm quartz cuvette with a concentration of 18 nM. The sample was excited at 370 nm and emission was recorded at 90° relative to the excitation with a 390 nm longpass filter to reduce scattered light. The emission spectrum was corrected for wavelength dependence of the instrument response.

2.2.3 Transient absorption (TA) spectroscopy

Femtosecond TA spectroscopy measurements in the 100 fs to 3 ns time window were performed using a regeneratively amplified Ti:sapphire laser (Solstice, Spectra-Physics, 800 nm, 100 fs, 1 kHz, 3.5 mJ/pulse), an optical parametric amplifier (TOPAS-C, Light Conversion), and a HELIOS spectrometer (Ultrafast Systems, LLC). A fraction of the 800 nm Solstice output was used to pump the TOPAS-C in order to produce the 400 nm pump beam used for sample excitation. The pump pulse was directed through a series of neutral density filters, a depolarizer and a synchronized 500 Hz chopper, then focused into the sample with a beam waist of ~240 μm with a pulse energy of ~10 nJ/pulse. Another fraction of the 800 nm Solstice output was used to generate a white-light continuum (450–800 nm) with a sapphire plate to be used as the probe pulse. The pump-probe time delay was controlled with a motorized delay stage. The probe beam

was split into probe and reference channels, with the probe beam being focused onto the sample and overlapped with the pump pulse. The probe and reference beams were focused into optical fibers coupled to multichannel spectrometers with CMOS sensors. The transient change in absorbance (ΔA) was found using the probe intensities with and without excitation.

Nanosecond TA spectroscopy (0.3 ns to 10 μs) was performed using an EOS spectrometer (Ultrafast Systems, LLC). The 400 nm pump pulse was generated and treated as described above with the exception of not being chopped. The white-light probe beam (400–900 nm, 0.3 ns, 2 kHz) was generated by a Nd:YAG laser focused into a photonic crystal fiber and the pump-probe delay was controlled by an electronic delay generator (CNT-90, Pendulum Instruments). The probe was split into probe and reference channels and detected as described above.

Samples for TA spectroscopy experiments were generally prepared such that the optical density at the band-edge transition was ~1. The samples were sealed under Ar in 2 mm quartz cuvettes equipped with Kontes valves. A magnetic stirrer continuously stirred samples during data collection. The pump power was chosen so as to be in a regime where the nanocrystal decay kinetics were independent of pump power, ensuring that the signal originated primarily from nanocrystals excited by single photons.[114] Experiments were conducted at room temperature, unless otherwise noted.

2.2.4 Photoluminescence upconversion spectroscopy

PL upconversion spectroscopy was performed using a Halcyone MC multichannel fluorescence upconversion spectrometer with ~150 fs temporal resolution (Ultrafast Systems). The pump pulse was produced using the TOPAS-C while a fraction of the Ti:sapphire laser output was used as a gate pulse. The pump polarization was rotated to magic angle using a half-wave plate. PL

was collected in the forward propagating direction, collimated using an off-axis parabolic mirror, passed through a long-pass filter to filter out excitation light, and then focused using a second off-axis parabolic mirror into a 0.5 mm Type II BBO crystal cut at 46.2 degrees where it was overlapped with the delayed gate pulse. The resulting upconverted photons were selected using a broad UV bandpass filter, directed into a spectrograph, and spread onto the pixels of a CCD camera. While the system is capable of spectrally resolving the decay by rotating the upconversion crystal during data acquisition, the crystal was held fixed to maximize the signal.

2.3 Transmission electron microscopy (TEM)

2.3.1 Low-resolution TEM

Transmission electron micrograph (TEM) samples were prepared by drop-casting as-synthesized nanocrystals (CdS NRs, ZnSe/CdS DIRs and CdSe/CdS DIRs) with native ligands onto TEM grids. TEM images were taken using a Phillips CM100 TEM at 80 kV with a bottom-mounted 4 megapixel AMT v600 digital camera. Samples prepared for this microscope used 300 mesh copper grids with carbon film from Electron Microscopy Science.

For CdSe NRs, TEM samples were prepared by drop-casting CdSe NRs with native ligands onto TEM grids (300 mesh copper grids with carbon film, Electron Microscopy Science). TEM images were taken on a FEI Tecnai Spirit BioTwin operating at 120 kV and equipped with a side-mount AMT (2k × 2k) CCD.

The dimensions of NRs were determined by measuring about 200 particles in TEM using ImageJ software.[129]

2.3.2 High-resolution TEM

High-resolution TEM images were taken using a FEI Tecnai F20 FEG TEM operating at 200 kV with a bottom-mounted 4k × 4k Gatan Ultrascan 895 CCD camera while binning by 2. Samples prepared for this microscope used ultrathin carbon film supported by a lacey carbon film on a 400 mesh copper from Ted Pella, Inc.

2.4 Temperature dependence studies

2.4.1 Cryostat

Temperature dependence studies were carried out using a Janis STVP-100 continuous flow optical cryostat with quartz windows equipped with a home-built 1 cm cuvette holder. The cuvette was cooled under flowing nitrogen vapor and the temperature was controlled with a LakeShore 335 temperature controller connected to two thermocouple/heating element pairs, one at the head of the sample holder and the other in the vaporizer assembly located at the bottom of the cryostat. Experiments were carried out on nanocrystals that were capped with 3-mercaptopropionic acid ligands and dispersed in a 4:1 ethanol:methanol (v/v). The sample was held in 1 cm cryogenic cuvette from FireflySci (type 66FL) with a screw cap. Samples were prepared under Ar then immediately moved to the cryostat, which was promptly purged with nitrogen.

Part I

Trapped-Hole Diffusion in Cd-chalcogenide nanocrystals

Chapter 3

Observation of Trapped-Hole Diffusion on the Surfaces of CdS Nanorods*

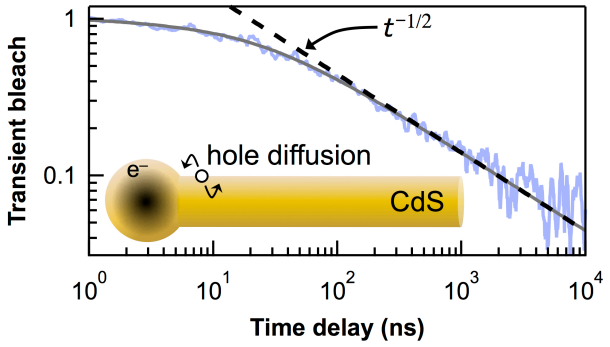

3.1 Abstract

In CdS nanocrystals, photoexcited holes rapidly trap to the particle surface. The dynamics of these trapped holes have profound consequences for the photophysics and photochemistry of these materials. Using a combination of transient absorption spectroscopy and theoretical modeling, we demonstrate that trapped holes in CdS nanorods are mobile and execute a random walk at room temperature. In CdS nanorods of non-uniform width, we observe the recombination of spatially separated electrons and trapped holes, which exhibits a $t^{-1/2}$ power-law decay at long times. A one-dimensional diffusion-annihilation model describes the time-dependence of the recombination over four decades in time with a single adjustable parameter. We propose that diffusive trapped hole motion is a general phenomenon in CdS nanocrystals, but one that is normally obscured in structures where the wavefunctions of the electron and trapped hole

*Adapted with permission from Utterback, J. K., Grennell, A. N., Wilker, M. B., Pearce, O. M., Eaves, J. D., and Dukovic, G. *Nat. Chem.*, **2016**, *8*, 1061–1066. (Copyright © 2016, Springer Nature)

spatially overlap. This phenomenon has important implications for the oxidation photochemistry of CdS nanocrystals.

3.2 Introduction

Many novel properties of semiconducting nanostructures emerge through the confinement of electronic wavefunctions to small regions of space.[32] Cadmium-based chalcogenide nanocrystals are some of the most widely studied and used systems in nanoscience because synthetic control over particle shape and size allows one to manipulate both electronic energies and wavefunctions.[32-34] Because of this tunability, there has been a growing interest in using colloidal Cd-chalcogenide nanocrystals for optoelectronic applications such as solar energy conversion.[4-8] Such technologies require control over the generation, separation, and extraction of photoexcited electrons and holes.[6,8,22-24] The dynamics of these two carriers can differ substantially.[23,36,37,56,57] To understand the principles that govern electron and hole relaxation dynamics in these complex systems, models based on fundamental physical phenomena are needed. However, the complicated shapes of experimentally measured excited state decay curves are often elusive to simple kinetic models.[36,37]

In CdSe and CdS nanocrystals, photoexcited holes rapidly and efficiently trap to localized states on the surface.[23,26,37,56,57] In nanoscale CdS in particular, hole trapping occurs on a picosecond timescale with >99% efficiency, so electrons primarily recombine with trapped, rather than delocalized, holes.[23,56,57,82] Consequently, trapped holes play an integral role in excited state dynamics,[23,36,56,80] and the ability to harvest them is critical for applications such as photovoltaics and solar photochemistry.[82] Despite their importance, remarkably little is known about the nature of the trap states and the dynamics of trapped holes.[23,56,80,82] The prevailing view

is that the trapped holes are spatially localized, suggesting that delocalized electrons recombine with stationary holes.[26,80,82,130] There has not, however, been direct evidence in support of this picture of recombination. If the energetically trapped holes were instead spatially mobile, the governing picture of their relaxation dynamics would fundamentally change.

Here, using transient absorption (TA) measurements on the sub-picosecond to microsecond timescale, in conjunction with theoretical modeling, we provide evidence that trapped holes on CdS nanorod surfaces are not stationary. Instead, they execute a diffusive random walk at room temperature. In CdS nanorods (NRs) of non-uniform width, excitation wavelengths can be chosen such that photoexcited electrons dissociate from trapped holes and localize to larger-diameter regions of the NRs with lower quantum confinement. TA experiments probing the relaxation of these localized electrons show a $t^{-1/2}$ power-law decay over several decades in time, suggesting a nonexponential recombination mechanism. In contrast, in CdS *quantum dots* (QDs) and CdS NRs when the electron and trapped hole are not spatially separated, the electron-hole recombination is exponential. These observations motivate an analytical model for one-dimensional diffusion-limited electron-hole recombination in the non-uniform NRs that fits the electron decay over four decades in time, from one nanosecond to ten microseconds, with only one adjustable parameter. We propose that the diffusive motion of trapped holes is a general phenomenon in CdS nanocrystals that is normally obscured in structures where electron and trapped-hole wavefunctions remain spatially overlapped during the measurement of their recombination dynamics. Finally, we illustrate how this fundamentally different picture of the behavior of trapped holes may impact the photochemistry of CdS nanostructures.

3.3 Methods

3.3.1 Synthesis, preparation and characterization of CdS NRs and QDs

Details of nanocrystal synthesis, preparation and characterization are provided in Chapter 2. Previously published procedures were used to synthesize CdS NRs[44,116,119,120] and CdS QDs.[122] Unless otherwise noted, all experiments were performed on nanocrystals that were functionalized with 3-mercaptopropanoic acid (3-MPA) to replace the native ligands and suspended in an aqueous buffer solution (50 mM Tris-HCl, pH 7). TEM samples were prepared by drop-casting as-synthesized nanocrystals onto TEM grids. The dimensions of the CdS NRs were determined by measuring over 200 particles in TEM (Table 3.1) and the sizes of the CdS QDs were determined from a published tuning curve[25] to be about 5 nm in diameter.

3.3.2 Transient absorption spectroscopy

The complete experimental setup for TA measurements has been previously described.[116] The concentration of CdS NRs used for TA experiments was about 0.7 μM and CdS QDs were about 3 μM. Concentrations were determined from UV-visible absorption spectra and the molar absorptivities.[25,116] TA measurements were done on samples sealed under Ar in 2 mm quartz cuvettes at room temperature (293 K). Solutions were stirred continuously with a magnetic stirrer. The pump pulse was passed through a depolarizer and the power was controlled with neutral density filters. The pump beam had a beam waist of ~240 μm, pulse duration of ~150 fs, and pulse energy of ~10 nJ/pulse for 405 nm excitation of the NRs, ~200 nJ/pulse for 510 nm excitation of the NRs, and ~10 nJ/pulse for 400 nm excitation of the QDs. The pump powers in all cases were chosen such that the TA decay trace shapes were independent of pump power so that the signal originated primarily from nanocrystals excited by a single photon.[114] TA traces were smoothed using a Savitzky-Golay filter because this method preserves higher order

moments of the signal.[131] Fitting was performed on raw data and the data was smoothed for presentation only.

3.3.3 Sample characterization

To determine the size distributions of the rod and bulb and the fraction of non-uniform nanorods in each sample, we adopted the criterion that a nanorod has a bulb when it has a large enough variation in width such that the electron can be localized in the larger diameter region at room temperature (293 K). This occurs when the confinement energy of the electron in the bulb is at least $k_{\mathrm{B}}T = 25$ meV less than that of the rod, and thus the electron does not have sufficient thermal energy to significantly occupy the rod. While we treat the smaller diameter rods as perfect cylinders, the bulbs can be either cylindrical or spherical in shape. The confinement energies can be calculated for spherical and cylindrical confinement. The confinement energies of each charge carrier in the lowest energy excited state of a cylindrical and spherical potentials are[2]

$$E_{\mathrm{c}}^{\mathrm{cyl}} = \frac{\alpha_{10}^2 \hbar^2}{2ma_{\mathrm{cyl}}^2}; \tag{3.1}$$

$$E_{\mathrm{c}}^{\mathrm{sph}} = \frac{\pi^2 \hbar^2}{2ma_{\mathrm{sph}}^2}, \tag{3.2}$$

where $\alpha_{10} \approx 2.40$ is the first root of the radial Bessel function, m is the effective mass of the charge carrier in CdS, and a_{cyl} and a_{sph} are the radii of a cylindrical and spherical structure, respectively. The electron and hole effective masses in bulk CdS are 0.2 and 0.7 times the electron mass, respectively, and the bulk Bohr exciton radius is 2.8 nm.[2,132]

TEM images of each nanorod sample were used to measure the size distributions of rods and bulbs. In these measurements we judged whether each bulb was cylindrical or spherical, approximating bulbs in structures such as those in Figure 3.4a and c as perfect cylinders and

bulbs such as those in Figure 3.1 and Figure 3.4b as perfect spheres. Nanorods in which the width variations did not give energy offsets larger than $k_B T$ were considered to be uniform, only consisting of a rod. Size distributions and fractions of nanorods with bulbs for the three NR samples appear in Table 3.1.

Table 3.1. Size distributions of non-uniform CdS nanorods

NR sample	Length (nm)	Rod Diameter (nm)	Bulb Diameter (nm)	Fraction With Bulbs
22 nm NRs	22 ± 5	4.4 ± 0.4	5.2 ± 0.5	32%
37 nm NRs	37 ± 8	4.2 ± 0.4	5.2 ± 0.8	59%
68 nm NRs	68 ± 14	4.3 ± 0.5	5.1 ± 0.7	65%

The energy offsets depicted in Figure 3.1 were approximated using the locations of the center of the rod and bulb bleach peaks in the TA spectra for the transition energies and Equation (3.1) for the contribution from confinement. The different energy offsets for the electron and hole are due to their different effective masses. These are approximate offsets that do not account for Coulomb interactions.

The absorption spectrum in Figure 3.1 was fit with two Gaussian peaks for the lowest energy rod and bulb transitions. The photoluminescence spectrum (Figure 3.5) was fit with three Gaussian peaks to account for rod, bulb and trap emission. Fit functions were of the form $f(\lambda) = \sum_i A_i/\sqrt{2\pi\sigma_i{}^2}\exp\left[-\left(\lambda-\lambda_{0,i}\right)^2/2\sigma_i^2\right]$. Fit parameters appear in Table 3.2.

Table 3.2. Absorption and photoluminescence fit parameters

Feature	Absorption Spectrum[a]			Photoluminescence Spectrum[b]		
	A^c	λ_0 (nm)	σ (nm)	A^c	λ_0 (nm)	σ (nm)
rod	13.2 ± 0.1	465 ± 1	8.6 ± 0.1	1.03 ± 0.04	473.4 ± 0.1	7.4 ± 0.1
bulb	1.00 ± 0.05	480 ± 1	13.0 ± 0.6	1.00 ± 0.04	488.0 ± 0.9	19.9 ± 0.5
trap	–	–	–	20.8 ± 0.1	753.2 ± 0.5	76.4 ± 0.4

[a] From Figure 3.1.
[b] From Figure 3.5.
[c] Amplitudes are normalized relative to bulb amplitude.

3.4 Results and discussion

3.4.1 Electronic structure of non-uniform CdS nanorods

When a photoexcited electron is delocalized over an entire CdS nanocrystal, upon hole trapping, recombination behavior is insensitive to the location of the trapped hole. To experimentally examine whether trapped holes can move on nanocrystal surfaces, we use nanostructures with excited states that exhibit spatial electron-hole separation and compare them to structures in which the photoexcited electron and hole are not separated. Synthesis of rod-shaped CdS nanocrystals results in a mixture of nanorods with uniform and non-uniform widths along their lengths.[130] Non-uniform CdS NRs provide a region where a photoexcited electron can localize (Figure 3.1, Figure 3.2, Figure 3.3, Figure 3.4).[130] Wu *et al.* have examined these structures in detail and showed that non-uniform CdS NRs exhibit two morphological features assigned to the spatially and spectrally distinct electronic states depicted in Figure 3.1: a long, narrow cylinder (*rod*) that is similar in size to CdS nanorods of uniform width, and a short, wider component (*bulb*).[130] Although most bulbs have roughly spherical or cylindrical shapes, they only need to be wider than the rod to produce the spectral features and decay dynamics described here (Figure 3.4). For simplicity, we schematically represent them as spherical (Figure 3.1b). Decreased quantum confinement in the bulb relative to the rod causes the bulb to have a lower transition energy (Figure 3.1c). As a result, it is energetically favorable for the electrons to localize in the bulb. To estimate the fraction of our CdS sample composed of non-uniform nanostructures, we consider only structures in which the bulb electron state has a lower energy than the rod state by at least the thermal energy at room temperature. By this criterion, 59% of nanorods in the sample shown in Figure 3.1 are non-uniform, as determined by TEM measurements (Figure 3.3). The NRs shown in Figure 3.1 have an average length of 37 ± 8 nm, rod diameter of 4.2 ± 0.4 nm, and bulb diameter of 5.2 ± 0.8 nm.

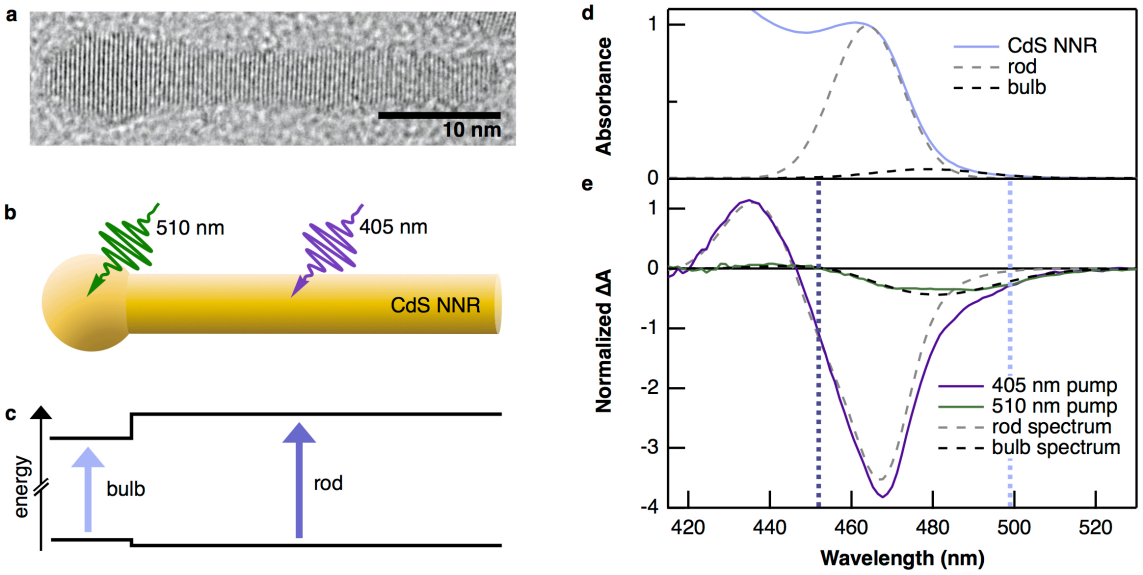

Figure 3.1. Relationship between CdS NR morphology and TA spectra. (a) Representative TEM image of a non-uniform CdS NR showing rod and bulb components. (b) Schematic depiction of a non-uniform CdS NR. 405 nm light primarily excites the rod while 510 nm photons selectively excite the bulb. (c) Energy level diagram as a function of position along the NR, relative to (b). The bulb has a larger diameter than the rod, resulting in a lower transition energy. Energy offsets are drawn to scale for 70 meV and 20 meV electron and hole offsets, respectively, which are based on the centers of the rod and bulb bleach peaks in (e). (d) Absorption spectrum of a sample of CdS nanorods that are, on average, 37 nm long and 4.2 nm wide with 5.2 nm bulbs (Table 3.1), fit to two Gaussian peaks for the lowest energy rod and bulb transitions (Table 3.2). (e) TA spectra of CdS NRs recorded 1 ns after excitation with 405 nm and 510 nm pulses. Spectra are normalized to have the same amplitude at 499 nm. Vertical lines mark 452 nm and 499 nm, the wavelengths that isolate the rod and bulb signals of these CdS NRs, respectively.

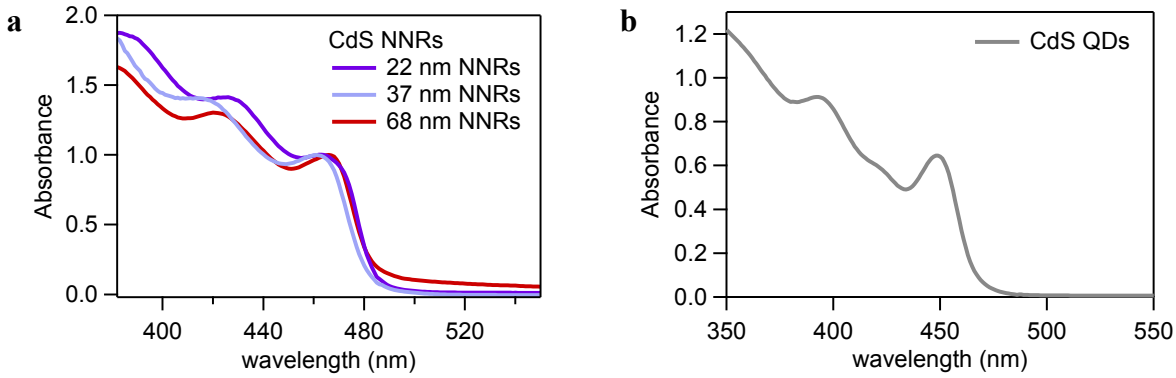

Figure 3.2. UV-visible absorption spectra. UV-visible absorption spectra of (a) CdS nanorod samples of varying lengths normalized at the lowest-energy rod transition, and (b) CdS QDs.

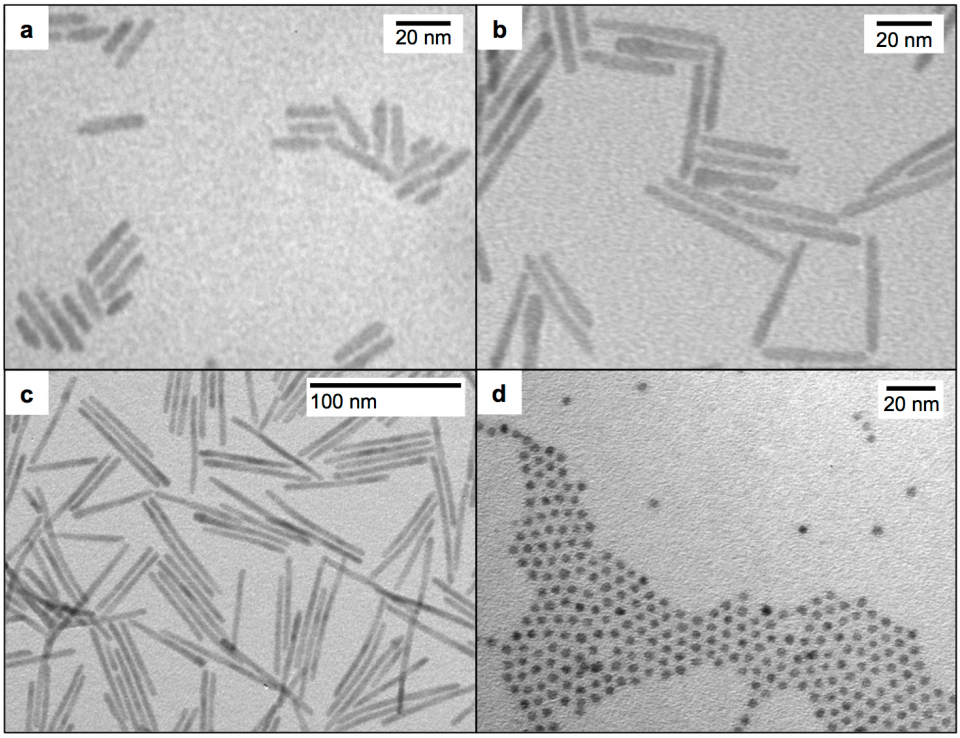

Figure 3.3. TEM images. Representative TEM images of (a) 22 nm CdS nanorods, (b) 37 nm CdS nanorods, (c) 68 nm nanorods, and (d) CdS QDs.

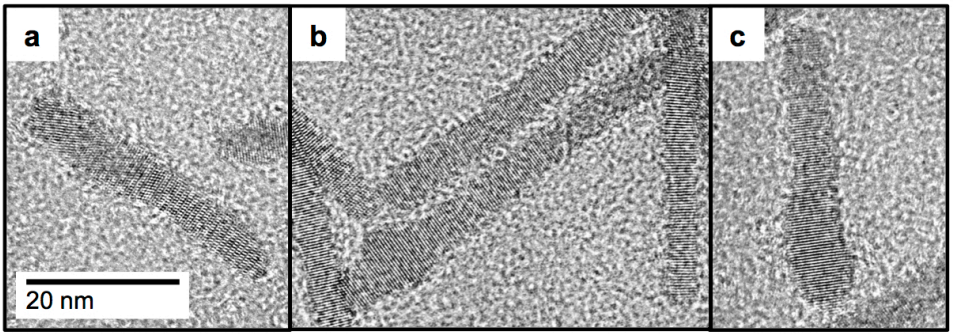

Figure 3.4 High-resolution TEM images. Selected TEM images of 37 nm CdS NRs showing bulbs. In addition to manifesting as a spherical bulb at the end of the nanorod as in Figure 3.1, bulbs can have various shapes including (a) a cylindrical region of uniform but larger diameter than the more narrow rod, (b) a spherical bulb located some distance from either end of the nanorod, and (c) irregular shapes of larger diameter.

Wu *et al*. showed that the bulb structural motifs in non-uniform CdS NRs exhibit clear signatures in the absorption (Figure 3.1d), photoluminescence (Figure 3.5), and TA spectra (Figure 3.1e) that cannot be attributed to sub-band gap transitions such as an Urbach tail.[130] In

the TA spectra of CdS nanostructures, photoexcitation leads to transient bleach signals that reflect the time-dependent populations of excited electrons.[23,114] Figure 3.1e shows the TA spectra of a sample of CdS nanorods recorded 1 ns after excitation at 405 nm and 510 nm, with pump fluences chosen to avoid multiple excitations of individual nanocrystals. 405 nm pump pulses primarily excite the rod transition because it comprises the majority of the volume of the nanostructure.[25,133] Electrons initially generated in the rod of non-uniform NRs localize to the bulb as they relax to a lower energy state.[130] The resulting TA spectrum 1 ns after excitation therefore consists of two overlapping bleach features due to rod and bulb electron populations (Figure 3.1e, Figure 3.6). 510 nm pulses selectively excite the bulbs without sufficient energy to populate the rod.[130] This localizes both the electron and hole in the bulb, yielding the pure bulb TA spectrum (Figure 3.1e, Figure 3.6). The individual contributions of the rod and bulb to the TA spectrum after 405 nm excitation are shown in Figure 3.1e (analysis appears in following section). The rod and bulb bleach features are centered at 467 nm (2.66 eV) and 482 nm (2.57 eV), respectively. The resulting energy offsets for the electron and hole are 70 meV and 20 meV, respectively. The rod and bulb spectra have significant overlap in the TA spectrum excited at 405 nm. For the analysis that follows, it is critical to isolate their individual contributions. As described in the following section, the pure bulb bleach appears at longer wavelengths where the rod amplitude is negligible (499 nm), whereas the pure rod signal can be extracted at a wavelength where the bulb signal contribution is zero (452 nm).

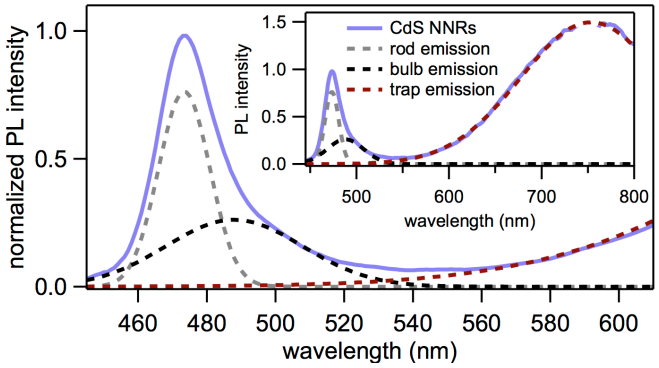

Figure 3.5. Photoluminescence spectrum. Photoluminescence spectrum under 370 nm excitation of the 37 nm long CdS nanorod sample from Figure 3.1. Inset: Expanded view showing trap emission that peaks near 750 nm. The data around 740 nm was removed because it contained second order diffraction of the excitation light. The spectrum was fit with three Gaussian peaks representing rod, bulb and trap emission. Fit parameters appear in Table 3.2.

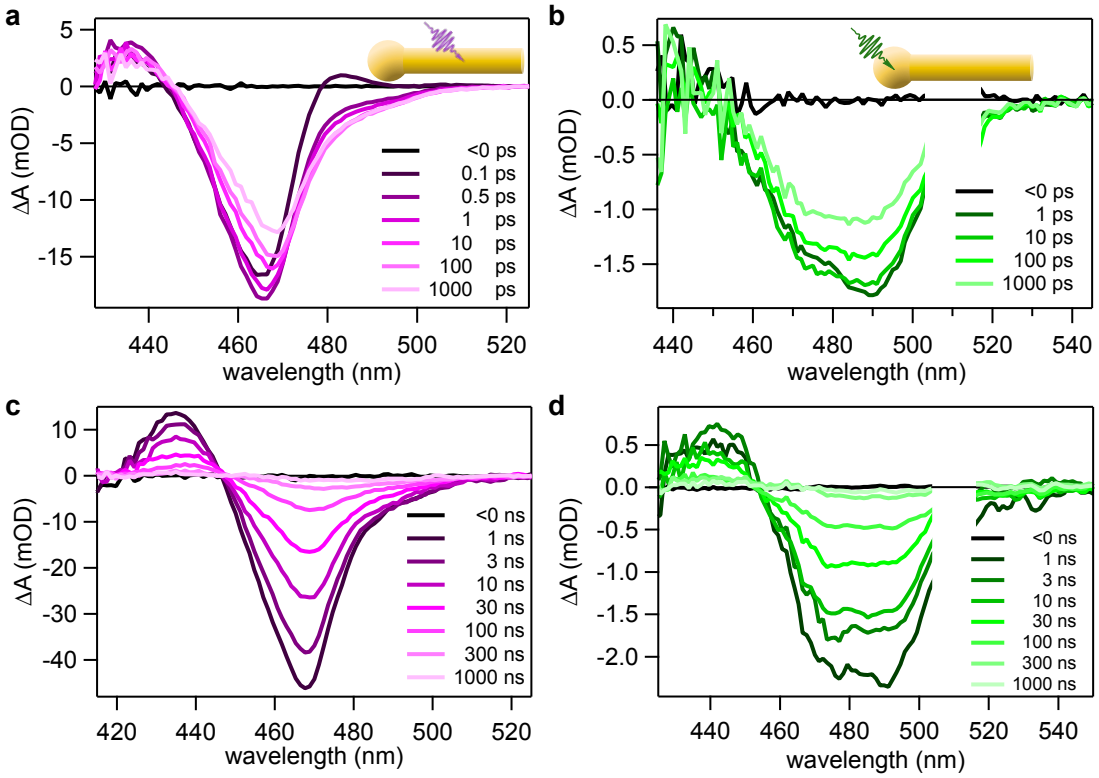

Figure 3.6. TA spectra over time. TA spectra of CdS NRs over 0.1 ps to 1 μs after excitation at 405 nm (a,c) and 510 nm (b,d). The TA spectra after 405 nm excitation undergo an apparent redshift over time, which originates from the relative amplitude changes of the overlapping rod and bulb bleach peaks. In the first few hundred ps (a) the rod bleach decays while the bulb bleach has a corresponding rise. For times around 1 ns and longer (c) both bleaches decay but the bulb signal decays more slowly than the rod. In contrast, the spectral shape of NRs excited by 510 nm light (b,d) does not change over time because only a single electronic state, the bulb, is populated for all times.

3.4.2 Isolation of rod and bulb dynamics

Because the rod and bulb signals spectrally overlap in the TA data of non-uniform CdS NRs, it is important to rigorously separate them in order to isolate the dynamics of the electron in the rod and the bulb. This is especially important in this system because the two electron states spectrally overlap but decay with distinct dynamics. Here we explain how we separate the signals of the two features.

Excitation with a 510 nm pump (Figure 3.6) excites only the bulb feature of the NRs because the photons do not have sufficient energy to excite the rod. Normalization of the TA spectra after 405 nm and 510 nm excitation shows that the spectra overlap for wavelengths of 499 nm and longer (Figure 3.1). Thus, the TA spectrum after 405 nm excitation is dominated by the bulb bleach there, and the decay at any wavelength in this range can be used to represent the decay of the electron in the bulb. This is confirmed by the fact that the decays observed at wavelengths of 499 nm and longer are identical with a long-time $t^{-1/2}$ decay, only increasing in noise level at longer wavelengths. Furthermore, based on the rod spectrum found by global fitting (described below) we find that the amplitude of the rod bleach at 499 nm at early times is sufficiently negligible (<0.1%) to isolate the bulb signal. Thus 499 nm was chosen to represent bulb dynamics.

To isolate the rod signal we utilize the fact that the bulb spectral shape has a "magic" wavelength at which its amplitude is zero, occurring when the bulb's bleach and photoinduced absorption contributions cancel each other. In addition to the main bleach peaks for the rod and bulb, each state has a corresponding positive photoinduced absorption (PA) peak on its higher energy side. This can be clearly seen in the TA spectra both after 405 nm and 510 nm excitation (Figure 3.6). In each case this feature follows the same decay as the corresponding lower energy

bleach, and for the rod this feature has been assigned to the interaction between electron population of the lowest energy excited state with a higher energy state excited by the probe pulse.[23,134] Thus, the rod PA signal reflects the population of the lowest energy excited state of the rod, just like the rod bleach itself. Similarly, the PA feature that corresponds to bulb, resolved by 510 nm excitation, reflects the population of electrons in the lowest energy state of the bulb with a decay that is identical to that of the bleach. The magic wavelength at which the bulb spectrum goes through zero can be directly observed in the TA spectra after 510 nm excitation. Examining the spectra over the 1 ns–10 μs time window (Figure 3.6) yields 452 ± 4 nm for the magic wavelength. Monitoring the TA decay at this wavelength isolates the dynamics of the rod. This analysis assumes that the bulb spectrum does not shift over time, which is consistent both with the observation that there is no shift over 0.1 ps–10 μs when the bulb is resonantly excited (Figure 3.6), as well as our global fitting results described below.

Electron population in CdS nanorods is often analyzed via the decay of the bleach maximum, which in Figure 3.1 appears at 466 nm.[23,65] In our data the decay of bleach maximum contains contributions from both the rod and bulb, which we can show by reconstructing the bleach maximum decay using the decay traces at 452 nm and 499 nm. As shown in Figure 3.7, the decay of the bleach maximum (466 nm) can be reproduced by taking a weighted sum of the decay traces for the rod at 452 nm and the bulb at 499 nm. This shows that the decay of the bleach maximum is dominated by the rod signal at early times and then the bulb signal at long times.

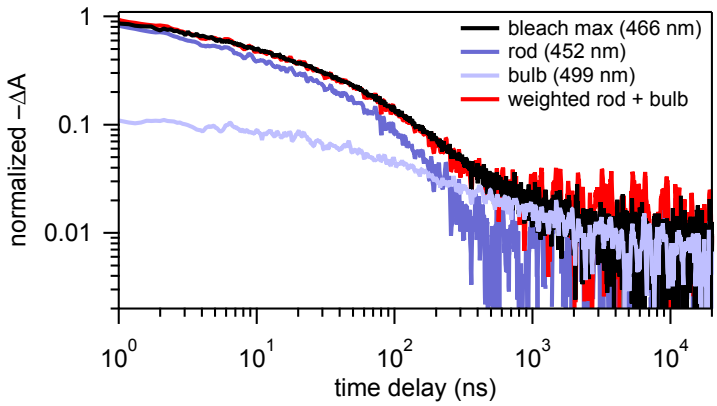

Figure 3.7. Isolation of rod and bulb dynamics. TA decay of the 37 nm long CdS NRs after 405 nm excitation monitored at the bleach maximum at 466 nm, the rod at 452 nm, and the bulb at 499 nm. The decay traces for the rod and bulb were normalized to match the bleach maximum trace at 1 ns and 200 μs, respectively. Taking the weighted sum of the rod and bulb decays at these normalizations generates the red trace. These normalization amplitudes are also consistent with the amplitudes of each spectrum at 466 nm after 1 ns found by global fitting (Figure 3.1 and Figure 3.8). Data is smoothed for presentation.

Global fitting of the TA spectra after 405 nm excitation serves to confirm the spectral contributions of the rod and the bulb to the total TA spectra, and demonstrates that they do not shift or broaden over time. The TA spectra after 405 nm excitation can be globally fit over time with only two spectral contributions that originate from the rod and the bulb (Figure 3.1 and Figure 3.8). The bleach and PA peaks composing each spectral shape were approximated as Gaussian peaks. The rod spectrum required one peak for its PA feature and two peaks for its bleach in the wavelength window examined, while the bulb spectrum required only one peak for each. This simple model is meant to qualitatively capture the shape and decay of each spectrum in this wavelength window and does not reflect the physical origin of features composing each spectral line shape.[23]

Global fitting was performed on TA spectra of the 37 nm long CdS NRs after 405 nm excitation from 1 ps – 10 μs, after spectral features due to hot carriers have decayed.[23] Fit parameters for peak positions, peak widths and the relative amplitudes of each bleach and their respective PA peaks were optimized as common parameters for all spectra over time, only

allowing the amplitudes of the fixed rod and bulb spectra to vary independently over time. We note that even when allowed to, the fitted peak positions do not systematically shift over time. TA spectra with their corresponding fits are shown in Figure 3.8. The individual contributions of the rod and bulb to the total TA spectrum presented in Figure 3.1 were constructed using the global fit results at 1 ns. While global fitting automatically gives the amplitudes of rod and bulb signals as a function of time, we choose not to use these extracted fit values to represent the true decays because they are subject to systematic error. We note however that the decay shapes of rod and bulb signals extracted from global fitting qualitatively agree with those observed at 452 nm and 499 nm, exhibiting multiexponential (Equation (3.3)) and power-law decays (Equation (3.20)), respectively.

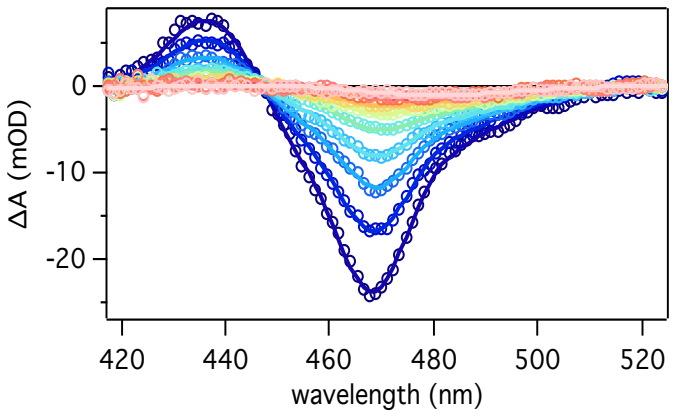

Figure 3.8. Global fitting of TA spectra. Selected TA spectra after 405 nm excitation (circles) and corresponding global fits over 10 ns–1 μs (lines). The TA spectra are globally fit by two spectral components, originating from the rod and the bulb, that do shift or broaden over a wide time window (1 ps–10 μs). Globally fit spectra confirm the isolation of rod and bulb signals using their representative wavelengths.

A general implication of this analysis is that the TA spectra can be well fit with two spectral shapes, arising from the rod and the bulb, that do not shift or broaden over an extensive time window. This confirms that decay traces taken at the single wavelengths stated above

represent the populations of each electron state over time. This also shows that the apparent redshift of the bleach peak after 405 nm excitation (Figure 3.6c) can be accounted for by changes in the relative amplitudes of the overlapping rod and bulb bleach peaks, which occur because the bulb decays much more slowly than the rod. Global fitting also provides approximate spectra for the rod and bulb, which can be used to examine their overlap and verify that 452 nm and 499 nm probe wavelengths isolate their contributions to the TA signal. The bulb spectrum obtained from global fitting to the TA spectra after 405 nm excitation is in excellent agreement with the TA spectra after 510 nm excitation (Figure 3.1), suggesting that the shape of the bulb spectrum does not change when CdS NRs are excited with 405 nm light. This confirms that the bulb spectrum crosses zero at 452 nm, validating the use of 452 nm as the magic wavelength to isolate rod dynamics. Similarly, the global fits allow us to examine the rod spectrum (Figure 3.1). According to the global fits, the amplitude of the rod spectrum at 499 nm contributes <0.1% to the signal after hot carrier cooling, supporting the identification of this wavelength to represent the bulb dynamics. Finally, the normalizations of the rod and bulb decay traces used to reconstruct the bleach maximum decay in Figure 3.7 are consistent with the amplitudes of each feature at 466 nm after 1 ns found from global fits.

3.4.3 Power-law decay of spatially separated carriers

After excitation of the rod at 405 nm, electron localization from the rod to the bulb causes a partial decay of the rod bleach and a simultaneous rise of the bulb bleach (Figure 3.9a), consistent with prior findings.[130] In our samples, this partial decay makes up 54% of the total rod decay, in agreement with the TEM measurements of the non-uniform NR fraction in the sample. The timescale of electron localization[130] was estimated by finding the average lifetime with multiexponential fits to the rod and bulb TA traces within the time window of electron

localization (0–300 ps), which includes the complete rise of the bulb signal (Figure 3.9a). The partial decay of the rod was fit with $\sum_i a_i e^{-t/\tau_i}$ and the rise of the bulb was fit with $A\left(1 - \sum_i a_i e^{-t/\tau_i}\right)$. The average lifetime is defined as $\overline{\tau} = \sum_i a_i {\tau_i}^2 / \sum_i a_i \tau_i$. Three exponentials ($i = 1$ to 3) were used to fit this time window for each signal. We treat this as an empirical fit and do not ascribe meaning to individual decay components. The average lifetimes for the partial rod decay and the bulb rise were 34 ± 5 ps and 26 ± 7 ps, respectively. We take the weighted average of these two values to represent the average lifetime for electron localization from the rod to the bulb, giving 31 ± 4 ps. Since hole trapping occurs on a ~1 ps timescale in CdS nanocrystals,[23,56,82] and because the hole energy difference between the rod and the bulb is not sufficient to localize most holes, the trapped hole can remain on the rod as the electron localizes to the bulb, resulting in spatial separation of the two carriers. Further evidence for this spatial separation is presented in a control experiment described later in the text. Well after electron localization is complete (>1 ns), the decays of the bleach signals reflect their individual recombination pathways without further population transfer.[130]

As shown in Figure 3.9b, the rod and bulb electron populations decay with drastically different functional forms. The rod signal fits a previously reported kinetic model (Equation (3.3)) that describes the competition between exponential decay pathways for the electron (Figure 3.9b, Table 3.3).[65,84,135,136] In this model the survival probability of electrons follows

$$S(t) = S_0 \exp\left[-t/\tau_0 + \langle N_{\mathrm{tr}} \rangle \left(e^{-t/\tau_{\mathrm{tr}}} - 1\right)\right], \tag{3.3}$$

where S_0 serves as a normalization factor, τ_0 is the electron-hole recombination lifetime, $\langle N_{\mathrm{tr}} \rangle$ is the average number of electron traps per nanorod in the ensemble, and τ_{tr} is the electron trapping time constant. The complete derivation of this model is described in Chapter 7. The key assumption in this kinetic model is that the probability of for recombination is a constant per unit

time. This can only be true if the trapped hole and electron wavefunctions share the same region of space. This model is ultimately a multiexponential fit where the relative amplitudes and time constants have direct physical meaning. The fit of Equation (3.3) to these signals is shown in Figure 3.9b, c and d, and appear on a linear-log scale in Figure 3.10 below. Fit parameters for these fits are summarized below in Table 3.3. We note that a double exponential also gives a satisfactory fit in this time window.

In stark contrast, the bulb signal decay follows a power law, $t^{-1/2}$, from 100 ns to 10 μs (Figure 3.9b). This long-time power-law behavior is reproducible, appearing in three CdS NR samples with an average power-law exponent of –0.49 ± 0.01 (Table 3.4). Directly exciting the lowest energy rod transition at 472 nm yields rod and bulb decays similar to those in Figure 3.9b (Figure 3.11), indicating that the power-law behavior of the bulb does not depend on excess energy of hot carriers produced with 405 nm excitation. The different functional forms of the rod and bulb electron decays indicate that the dynamics of recombination of an electron with a trapped hole originate from distinct microscopic mechanisms.

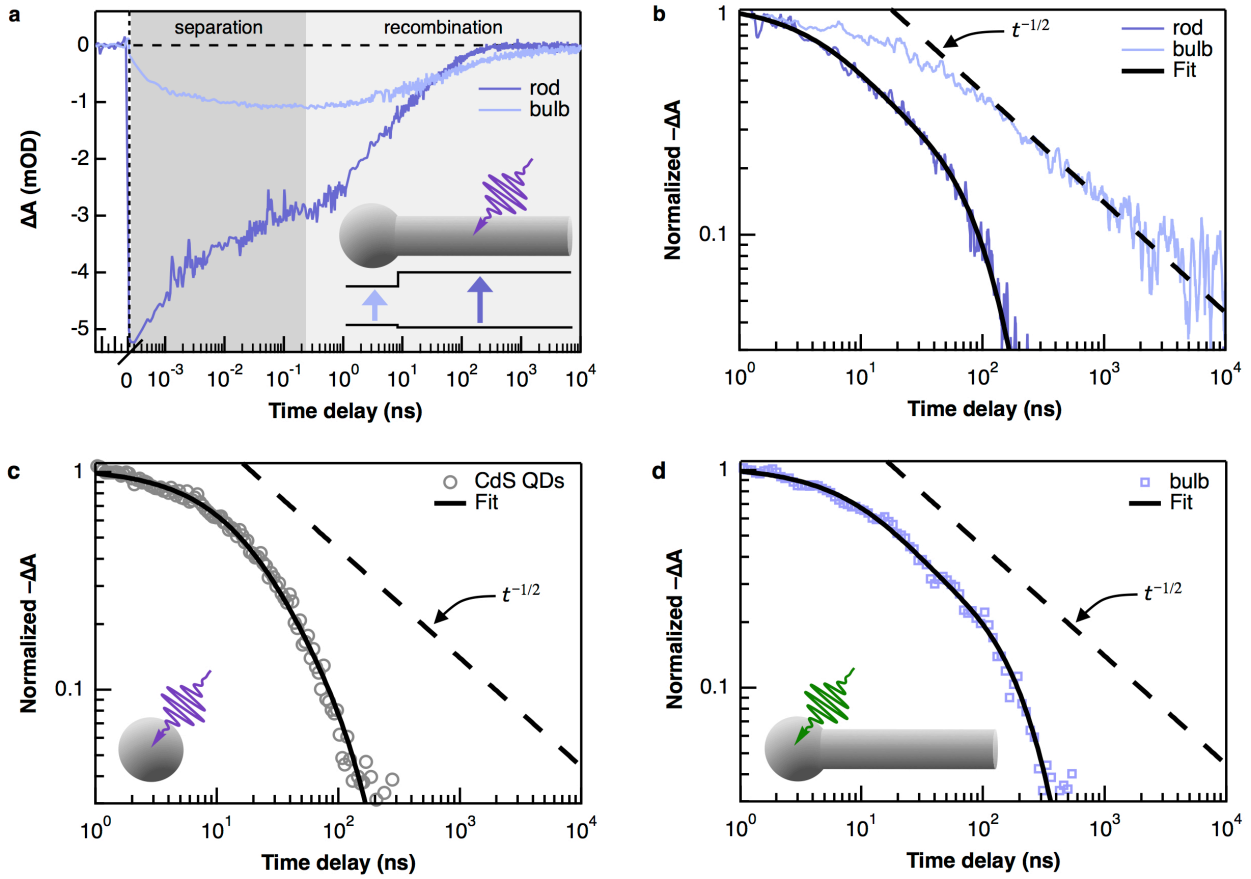

Figure 3.9. TA bleach decay of electrons in CdS nanocrystals. (a) TA decays after 405 nm excitation for the sample shown in Figure 3.1, monitored at the rod transition (452 nm) and the bulb transition (499 nm). The decays are plotted with a split time axis that is linear for the first 250 fs and logarithmic thereafter. The shaded regions indicate time windows dominated by electron-hole separation and recombination. The inset color-codes which morphological feature is being excited and probed. (b) TA decays from (a) in the 1 ns – 10 µs time window, normalized at 1 ns, plotted on a log-log scale. The rod decay fits Equation (3.3), while the bulb feature decays as a $t^{-1/2}$ power law (dashed black line) after 100 ns. (c) TA decay of CdS QDs excited at 400 nm. (d) TA decay of CdS NRs when the bulb is pumped at 510 nm. The data in (c) and (d) are fit with Equation (3.3) and have no power-law decay (dashed black line). Fit parameters appear in Table 3.3 and linear-log scale plots appear in Figure 3.10.

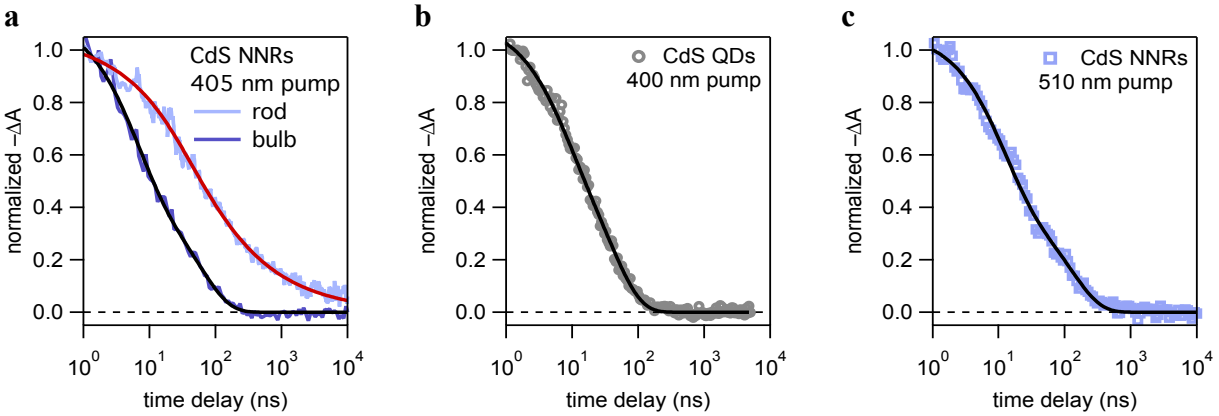

Figure 3.10. Fits to TA decays on linear ΔA scale. Data and fits from (a) Figure 3.9b and Figure 3.13d, (b) Figure 3.9c, and (c) Figure 3.9d, presented with a linear scale for ΔA and logarithmic scale for time. The fit to the bulb decay of CdS NRs pumped at 405 nm is Equation (3.20) (red curve) and the other three fits are to Equation (3.3) (black lines).

Table 3.3. Summary of fitting parameters for fits to Equation (3.3)

Sample *Feature and conditions* (Corresponding Figure)	τ_0 (ns)	$\langle N_{tr} \rangle$	τ_{tr} (ns)	$\overline{\tau}$ (ns)
CdS NRs *rod decay after 405 nm excitation* (from Figure 3.9b)	57 ± 2	0.89 ± 0.03	7.4 ± 0.6	51
CdS QDs *bleach decay after 400 nm excitation* (from Figure 3.9c)	61 ± 2	1.03 ± 0.05	22 ± 1	48
CdS NRs *bulb decay after 510 nm excitation* (from Figure 3.9d)	140 ± 20	1.0 ± 0.1	21 ± 4	120

Table 3.4. Diffusion characteristics of multiple CdS NR samples.

NR sample	α^a	τ^b (ns)
22 nm NRs	−0.54 ± 0.02	13 ± 7
37 nm NRs	−0.47 ± 0.01	55 ± 2
68 nm NRs	−0.49 ± 0.01	16 ± 1

[a] Power law exponent from fits to $S(t) \sim t^{\alpha}$.
[b] Decays in Figure 3.13d fit to Equation (3.20) over 1 ns–10 μs

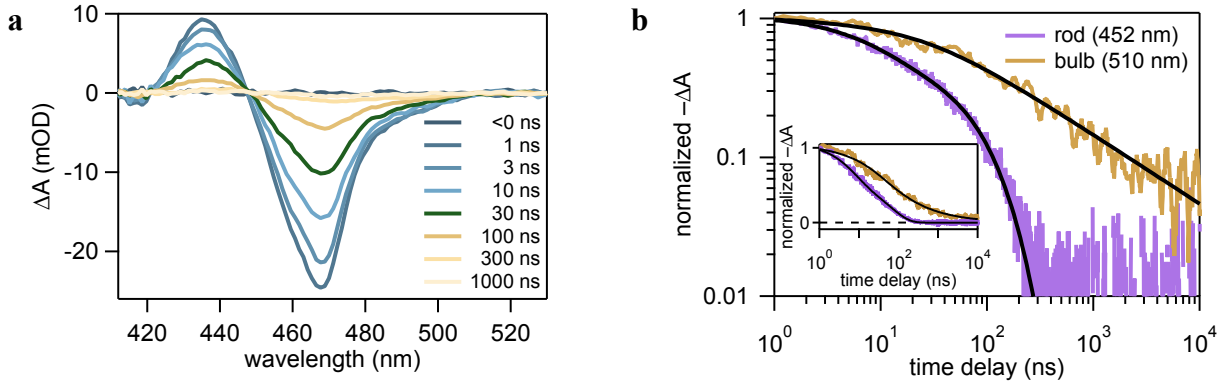

Figure 3.11. Relaxation dynamics after resonantly exciting the rod transition. (a) TA spectra of CdS NRs over 1–1000 ns after 470 nm excitation (resonant with the rod transition). (b) Normalized TA decays of CdS NRs after 470 nm excitation from 1 ns to 10 μs monitored for the rod at 452 nm and for the bulb at 510 nm. The inset shows the same data on a linear ΔA scale. The rod decay fits Equation (3.3) with $\tau_0 = 69 \pm 1$ ns, $\langle N_{tr} \rangle = 0.70 \pm 0.01$ and $\tau_{tr} = 11 \pm 1$ ns while the decay of the bulb fits Equation (3.20) with $\tau = 59 \pm 7$ ns. Thus, resonantly exciting the CdS NRs rod transition results in relaxation dynamics that are very similar to when exciting higher lying states at 405 nm.

The $t^{-1/2}$ power-law decay of the TA signal has not been reported in prior studies of CdS nanocrystals, suggesting that, after excitation of the rod and electron localization to the bulb, the bulb electrons decay by a previously undiscovered mechanism. The decay of the TA signal from roughly spherical CdS QDs (Figure 3.2, Figure 3.3, Figure 3.12) does not exhibit the $t^{-1/2}$ power law (Figure 3.9c), implying that the nanorod geometry is responsible for this functional form. Additionally, the power law is absent when the bulbs of CdS NRs are directly excited at 510 nm, co-localizing the electron and the trapped hole in the bulb (Figure 3.9d). In both of these cases, the photoexcited electron and trapped hole are localized in the same region of a nanostructure with overlapping wavefunctions, and the time-dependence reported in Figure 3.9c and d can be described by the kinetic model of Equation (3.3). Because the bulb signal in NRs after excitation of either the rod (405 nm) or the bulb (510 nm) corresponds to the same electron state in both cases, the drastic difference in decay dynamics shown in Figure 3.9 must be due to the trapped hole, and in particular, to where the trapped hole originates. Together with the

timescales of hole trapping and electron localization discussed above, the control experiments shown in Figure 3.9c and d support the idea that excitation of the rod produces a spatially separated state in which the electron is localized in the bulb and the hole is trapped on the rod surface.

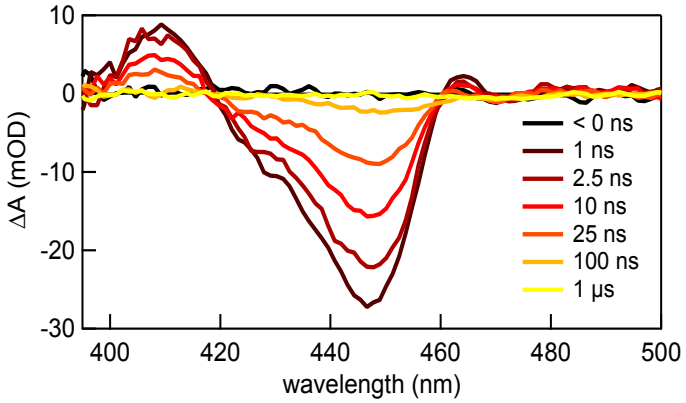

Figure 3.12. TA spectra of CdS QDs. TA spectra of CdS QDs after 400 nm excitation from 0 to 1 μs. The spectral shape does not change over time because CdS QDs do not have different electron states underlying the lowest energy bleach.

The $t^{-1/2}$ power law is a universal feature of diffusion-annihilation reactions and signifies a dynamical mechanism that, in contrast to a kinetic process, cannot be described with an average time or rate.[137] Because the power law appears only in the case where the carriers are spatially separated in non-uniform NRs, we pursue a theoretical model of recombination based on diffusion-annihilation. Our experimental observations favor this approach rather than descriptions based on distributed trap depths, spectral diffusion, or the power-law statistics of blinking, because those processes exhibit the same behavior for both zero-dimensional QDs and one-dimensional nanorods alike.[138-140]

3.4.4 Analytical Model for Diffusion-Limited Recombination

To describe how the spatially separated carriers recombine in non-uniform CdS NRs, we developed an analytical model for one-dimensional diffusion-limited recombination between a diffusing trapped hole and a stationary electron localized in the bulb. The derivation of the model is outlined briefly here and the detailed derivation follows. In this model, the hole undergoes an unbiased random walk on the surface of the rod, with diffusion coefficient D, until it comes within the recombination zone centered at the stationary electron in the bulb (Figure 3.13a). The TA bleach signal is proportional to the survival probability of the electron in the bulb, $S(t)$, which is the fraction of bulb electrons remaining in the sample at a given delay time t after excitation. We consider times after hole trapping and electron localization are complete (>1 ns) and only allow the electron to decay through recombination with the trapped hole, which makes the electron and trapped hole survival probabilities equivalent. Because the diffusion equation is linear, the distribution of initial hole positions in the ensemble, $p(z_0)$, determines the diffusive hole dynamics and the functional form of the survival probability. The power-law decay implies that the trapped holes start out so close to the bulb electrons that only a negligible fraction of holes encounter the other end of the nanorod on the timescale of the experiment.[137] Furthermore, we find that the initial distribution $p(z_0)$ must have a finite width to fit the data in the 1 ns to 10 μs time window. Our model approximates $p(z_0)$ to be uniform for $0 < z \leq \ell$, where ℓ is a length smaller than the length of the random walk, L (Figure 3.13b). The diffusion theory models both the time-dependent probability density of observing a hole at time t, $p(z,t)$, and the survival probability, which are related by $S(t) = \int dz\, p(z,t)$.

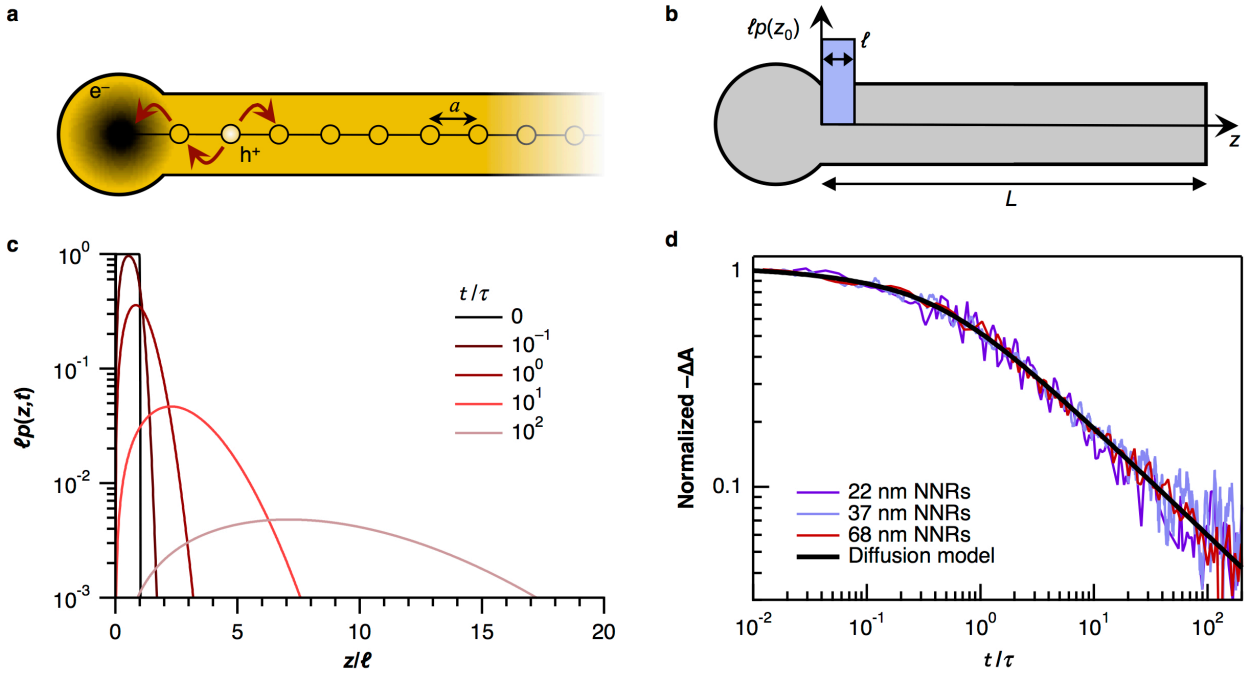

Figure 3.13. Recombination of a localized electron and trapped hole as a diffusion–annihilation process. (a) Schematic representation of trapped-hole diffusion along the rod of a CdS NR. The hole moves with diffusion coefficient D along the rod in a series of steps of length a (red arrows) until it encounters the electron, which is stationary in the bulb, and recombines with it. (b) Schematic overlay of the initial hole distribution on a NR, where $\ell \ll L$. (c) Probability density of the trapped-hole distribution as a function of time, $\ell p(z,t)$, from the diffusion model (Equation (3.21)). Using the mean NR length as an estimate of L, the NRs in this study satisfy $L > 20\ell$. (d) Decay of the bulb signal after 405 nm excitation for three CdS NR samples of different mean nanorod lengths fit to the diffusion model of Equation (3.20). Consistent with the predictions of the model, the data from different samples collapse to a master curve when plotted against t/τ.

We treat the recombination as a first-passage problem in which the hole starts from some position z_0 on the rod and diffuses according to a random walk in one dimension, along the nanorod with length L, until it reaches the stationary electron localized in the bulb at the origin where it recombines. In this model, L is the length over which the hole can execute a random walk. More accurately, L is the length of the rod segment (Figure 3.13b) in which the electron and hole are prepared by the pump pulse.

First we show that the hole diffusing on the nanorod surface reduces from diffusion on a cylinder to one-dimensional diffusion on a line. The behavior of a hole undergoing an unbiased

random walk can be described by the probability density, $p(\vec{r},t)$, where $p(\vec{r},t)d^3\vec{r}$ is the probability for finding the hole in a differentially small volume $d^3\vec{r}$ around position $\vec{r}$ at time t. The probability density obeys the diffusion equation,

$$\frac{\partial}{\partial t}p(\vec{r},t) = D\nabla^2 p(\vec{r},t), \tag{3.4}$$

where D is the diffusion coefficient and ∇^2 is the Laplacian. This treatment assumes a coarse-graining in both space and time so that the jump lengths in the random walk are much smaller than the spatial variations in $p(\vec{r},t)$. Cylindrical coordinates are the natural coordinates for trapped-hole motion on a nanorod, and in these coordinates, the probability density is $p(\vec{r},t) = p(r,\phi,z,t)$, where r is the radial coordinate, ϕ is the azimuthal angle, and z is the coordinate along the length of the rod, relative to the electron which has the edge of its recombination zone at $z = 0$. Because the hole is constrained to the surface of the nanorod,[23,26,56,76] the probability must be a constant function of r, and $p(\vec{r},t) = p(\phi,z,t)$. We assume that the electron density in the bulb reflects the shape of the bulb, and therefore the recombination rate of the electron with the hole, once the hole is inside the recombination zone, is independent of ϕ. This assumption leads to separable boundary conditions in ϕ and z. Specifically, the solution is periodic in ϕ and so solutions must be of the form $p(\phi,z,t) = \sum_{m=-\infty}^{\infty} e^{im\phi}p_m(z,t)$. The time-evolution of the probability density is trivial in the ϕ direction. The marginal probability density is $p(z,t) = \int_0^{2\pi} d\phi\ p(\phi,z,t) = p_0(z,t)$. Upon integration over ϕ only the constant mode at $m = 0$ survives. Thus the problem reduces to the one-dimensional diffusion equation. This reduced dimensionality reflects the symmetry of the system. Motion around the waist of the nanorod does not bring the hole closer to the electron, and therefore does not contribute to recombination. The survival probability therefore cannot depend on ϕ. Thus, although a hole localized on the rod

surface may undergo motion on a cylinder, diffusion around the circumference of the rod does not lead to recombination, so the one-dimensional motion of the hole along the length of the rod in the z-direction governs the survival probability (Figure 3.13a and b).

Denoting the initial position of the hole z_0 and using the composition property of the probability density, $p(z,t) = \int dz_0 p(z_0) p(z,t|z_0)$, we can solve Equation (3.4) for an arbitrary initial hole distribution by employing Green's function methods. The Green's function is the conditional probability density $p(z,t|z_0)$, which is the probability that the hole is at position z at time t given that it started at position z_0 at time $t = 0$. Let the distribution of initial hole positions be $p(z_0)$. Nondimensionalizing by defining $Z = z/L$ and rescaling time by $T = Dt/L^2$ gives

$$\frac{\partial}{\partial T} p(Z,T|Z_0) = \frac{\partial^2}{\partial Z^2} p(Z,T|Z_0). \tag{3.5}$$

To model the diffusion-annihilation process, the boundary conditions are absorbing at the origin, $Z = 0$, and reflecting at the end of the rod, $Z = 1$. These considerations give the inner boundary condition,

$$p(0,T|Z_0) = 0, \tag{3.6}$$

the outer boundary condition,

$$\frac{\partial}{\partial Z} p(Z,T|Z_0)\Big|_{Z=1} = 0, \tag{3.7}$$

and the initial condition,

$$p(Z,T=0|Z_0) = \delta(Z - Z_0). \tag{3.8}$$

The absorbing boundary condition ensures that whenever a trapped hole finds an electron, it leaves the system. The survival probability is the integral over all space, $S(T) = \int_0^1 dZ\, p(Z,T)$, or equivalently,

$$S(T) = \int_0^1 dZ \int_0^1 dZ_0\, p(Z_0)p(Z,T|Z_0). \tag{3.9}$$

We note in passing that one can solve for the survival probability directly using the backwards Fokker-Planck equation, but because we want to visualize $p(z,t)$, we do not choose this path. Using an eigenfunction expansion to solve Equation (3.5) and integrating over the initial distribution gives[137]

$$p(Z,T) = \sum_{n=0}^{\infty} c_n \sin[(n+1/2)\pi Z]\, \mathrm{e}^{-(n+1/2)^2\pi^2 T}, \tag{3.10}$$

where the expansion coefficients, $c_n = 2\int_0^1 dZ_0 p(Z_0)\sin[(n+1/2)\pi Z_0]$, with $n = 0, 1, 2, \cdots$ are the projections of the initial hole distribution onto the Fourier sine component for mode n. Integrating over Z yields the survival probability (Equation (3.9)),

$$S(T) = \sum_{n=0}^{\infty} \frac{c_n}{(n+1/2)\pi} \mathrm{e}^{-(n+1/2)^2\pi^2 T}. \tag{3.11}$$

The spectrum of the expansion coefficients, c_n, determines both $p(Z,T)$ and $S(T)$ in their entirety, and shows that these two functions depend uniquely on $p(Z_0)$. While the experimental measurement depends entirely upon $p(Z_0)$, this distribution is not directly measurable, and so finding this distribution from the experimental data requires the solution of an inverse problem. There are two ways to proceed. One can either extract the spectrum c_n from the experimental data by inverse Laplace transform methods, or take a simple, physically motivated and parameterized form for $p(Z_0)$ and fit the parameters from the data. We choose the latter, but verify that the TA decays in the experiment are not sensitive to the detailed form of $p(Z_0)$, so an approximate analysis that highlights the general features of the initial condition is sufficient. Indeed, the method we choose is likely to be more accurate than the inverse Laplace approach. As we will show in Chapter 5, allowing a finite recombination time with the hole by making the

inner boundary condition an imperfectly absorbing boundary introduces another parameter that only leads to small, quantitative changes in the predicted behavior, and so we leave the inner boundary condition absorbing.

Reaction-diffusion in a finite system: asymptotics and pre-asymptotics

At long times ($T \gg 1$, or $t \gg L^2/D$) only the slowest mode $n = 0$ survives and the decay is exponential: $S(T) \propto c_0 \mathrm{e}^{-\pi^2 T/4}$. Thus, for a any finite system, the decay at the longest times asymptotically approaches this exponential function.[137] An exponential decay is clearly not consistent with the experimental data for the long-time decay of the electron in the bulb of CdS NRs. However, note that the time required to achieve the longest time behavior depends on the shape of $p(Z_0)$, and that time can be very long indeed. If the initial distribution $p(Z_0)$ is broad, c_0 carries a significant amplitude and the decay becomes exponential rather quickly. If $p(Z_0)$ is constrained close to $Z_0 = 0$ then the asymptotic behavior takes a long time to appear and a pre-asymptotic $t^{-1/2}$ power law dominates the decay of $S(T)$.[137]

Exact solution for a broad and uniform distribution of holes

Because the hole can trap quickly,[23,56,57] it is natural to assume that the probability for having a trapped hole anywhere along the nanorod is uniform. However, with this initial distribution the pre-asymptotic power-law behavior does not appear. For a broad and uniform initial distribution, $p(Z_0)$ is unity for $0 < Z_0 \leq 1$. Evaluating c_n in Equation (3.11) for this case gives[137]

$$S(T) = 2\sum_{n=0}^{\infty} \frac{1}{(n+1/2)^2\pi^2} \mathrm{e}^{-(n+1/2)^2\pi^2 T}. \tag{3.12}$$

While this survival probability has no closed-form solution, its time derivative, which is the first passage time distribution $f(T) = -dS(T)/dT$, does. Differentiating Equation (3.12) with respect to time and multiplying by –1 gives

$$f(T) = 2\sum_{n=0}^{\infty} \mathrm{e}^{-(n+1/2)^2\pi^2 T}. \tag{3.13}$$

After making the substitution $q = \mathrm{e}^{-\pi^2 T}$ this series converges to the Jacobi theta function,

$$f(q) = \vartheta_2(0, q). \tag{3.14}$$

From here the survival probability follows from integration of the first passage distribution,

$$S(T) = \int_T^{\infty} dT' f(T') = \int_{\mathrm{e}^{-\pi^2 T}}^{\infty} dq f(q) \frac{dT'}{dq} = \frac{1}{\pi^2} \int_0^{\mathrm{e}^{-4\pi^2 T}} dq \frac{\vartheta_2(0, q)}{q} \tag{3.15}$$

This integral is over the interval $0 \leq q \leq 1$ and is trivial to evaluate numerically. The result is that the survival probability for a uniform distribution rapidly becomes exponential with no discernable power-law behavior at any point in the decay. One can examine the pre-asymptotic behavior of $S(T)$ by expanding $\vartheta_2(0, q)$ in a series for small q and then integrating, in which case Equation (3.15) becomes a multiexponential rather than a power law. These results are consistent with the expectation that, for a distribution of holes with a width comparable to the length of the nanorod, the survival probability should be exponential for all times. This prediction is, however, inconsistent with the data, suggesting that the hole does not trap along the length of the rod with equal probability when the electron localizes to the bulb.

Initial hole distribution near the electron: requirements for a pre-asymptotic power law

From the arguments above, we expect that we are probing a pre-asymptotic regime, where trapped holes begin undergoing a random walk close to the electron but have not had enough time to encounter the end of the nanorod ($t < L^2/D$). For a finite one-dimensional system in

which the diffusing particle starts very close to the absorbing boundary, the survival probability does display $t^{-1/2}$ behavior, just like a random walk with an open outer boundary and an absorbing inner boundary.[137] This power-law decay holds until an appreciable number of particles reach the outer boundary. The longest observable timescale is still $\sim L^2/D$, but the pre-asymptotic behavior is determined by the initial distribution. Thus the observation of a power law in our data tells us that trapped holes must start out very close to the electron localized in the bulb.

To demonstrate how the pre-asymptotic power law can emerge in a finite system, we examine the exact solution for the survival probability as the hole starts progressively closer to the electron. For a hole that starts with the initial position Z_0 with a sharp distribution, we can write $p(Z_0) = \delta(Z - Z_0)$. For this $p(Z_0)$ Equation (3.11) becomes

$$S(T) = 2\sum_{n=0}^{\infty} \frac{\sin[(n+1/2)\pi Z_0]}{(n+1/2)\pi} \mathrm{e}^{-(n+1/2)^2\pi^2 T}. \tag{3.16}$$

As $Z_0 \to 1$ the initial electron-hole separation is comparable to the length of the nanorod, whereas a small value of Z_0 corresponds to the case when the hole starts close to the electron. Plots of Equation (3.16), running the sum until convergence, for different values of Z_0 illustrate that as the initial separation (z_0) becomes significantly smaller than L, a pre-asymptotic $t^{-1/2}$ power-law develops (Figure 3.14). The transition to the pre-asymptotic power-law decay begins around $t = z_0^2/4D$ and the asymptotic exponential sets in around $t = 4L^2/\pi^2 D$. Within this pre-asymptotic time window the system behaves like an infinite system because a negligible fraction of holes have had time to encounter the end of the nanorod opposite to the electron. This demonstrates how we observe a pre-asymptotic regime for the survival probability in our TA

experiments. We expect that the asymptotic exponential decay does occur in this system, but that it does not develop until some time after 10 μs.

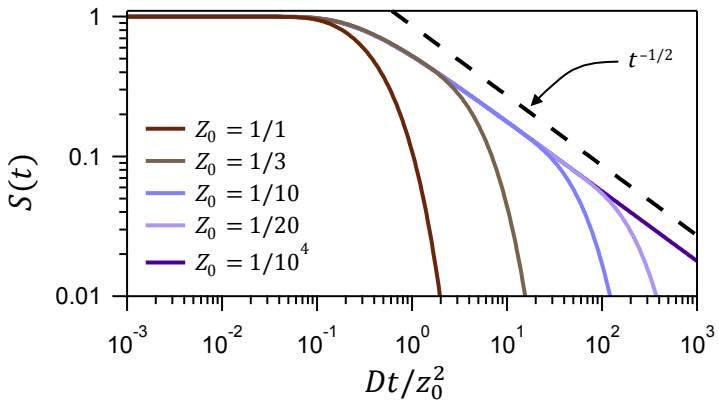

Figure 3.14. Exact solution to diffusion model. Plots of Equation (3.16), with time scaled by z_0^2/D, for $Z_0 = z_0/L =$ 1/1, 1/3, 1/10, 1/20 and $1/10^4$, to show the emergence of a pre-asymptotic power-law behavior as z_0 becomes smaller than L. A $t^{-1/2}$ power-law decay is shown for comparison. The transition from power-law to exponential decay occurs at $t \sim L^2/D$.

Analytical solution for the pre-asymptotic regime

Because we do not observe the turnover to an exponential decay in the time window of our TA data, we can focus on the pre-asymptotic regime to obtain a closed-form analytical expression to describe that regime. Mathematically, we can ignore the outer boundary and solve Equation (3.5) on the entire line subject to the delta function initial condition, $p(z_0) = \delta(z - z_0)$, using Fourier transforms, restrict the solution to the semi-infinite half line $[0, \infty)$, and enforce the absorbing boundary condition at the origin using the method of images,[137,141]

$$p(z,t|z_0) = \frac{1}{\sqrt{4\pi Dt}}\left[e^{-(z-z_0)^2/4Dt} - e^{-(z+z_0)^2/4Dt}\right], \tag{3.17}$$

for $z > 0$. Integrating over z between 0 and ∞ gives the conditional survival probability for the delta function initial condition,[137]

$$S(t, z_0) = \text{erf}\left(\frac{z_0}{\sqrt{4Dt}}\right), \tag{3.18}$$

where $f(x) = \text{erf}(x)$ is the error function. By expanding the error function for small arguments, one can show that it has the behavior $S(t) \propto 1/\sqrt{t}$ at long times, which agrees with our experimental data at the longest times with the correct exponent for the power law. While the long-time behavior of Equation (3.18) is consistent with the data, this function does not quite match the bulb decay at early times. The transition to the power-law tail is too sharp to describe the data, suggesting that the TA decays measured in the experiment are sensitive to whether or not $p(z_0)$ has a finite width. This reflects the idea that the initial electron-trapped hole separation has some distribution in the ensemble. We model $p(z_0)$ for the ensemble as a uniform distribution that goes from the origin to some distance ℓ with a constant probability (Figure 3.13b). This form for $p(z_0)$ gives a simple analytical expression for $S(t)$, but as Figure 3.13c shows, the experiment is not likely to be sensitive to the detailed form of $p(z_0)$ because the distribution quickly forgets its initial shape. It is only important that $p(z_0)$ has a mean close to the electron and that it has a finite width.

Integrating Equation (3.18) over the uniform distribution from ϵ to ℓ and then taking the limit $\epsilon \to 0^+$ gives the form that leads up to the model that will be used,

$$S(t) = \sqrt{4Dt/\pi\ell^2}\left(e^{-\ell^2/4Dt} - 1\right) + \text{erf}\left(\sqrt{\ell^2/4Dt}\right). \tag{3.19}$$

Without knowing the value of either the diffusion coefficient of the trapped hole D or the width of the initial hole distribution ℓ we cannot use these variables as independent parameters. We can only obtain $\tau = \ell^2/4D$ from fits to the TA data. After substituting for τ and introducing a normalization factor S_0 to account for the early time dynamics not in the diffusion model, we get

$$S(t) = S_0\left[\sqrt{t/\pi\tau}\left(e^{-\tau/t} - 1\right) + \text{erf}\left(\sqrt{\tau/t}\right)\right]. \tag{3.20}$$

This simple model describes the TA decay of the bulb in CdS NRs well (Figure 3.13d).

The probability density for this initial condition can be found by averaging Equation (3.17) from 0 to ℓ, giving

$$\ell\, p(z,t) = \mathrm{erf}\left[\frac{z}{\ell}\sqrt{\frac{\tau}{t}}\right] - \frac{1}{2}\mathrm{erf}\left[\left(\frac{z}{\ell}-1\right)\sqrt{\frac{\tau}{t}}\right] - \frac{1}{2}\mathrm{erf}\left[\left(\frac{z}{\ell}+1\right)\sqrt{\frac{\tau}{t}}\right], \tag{3.21}$$

for $z > 0$. This function was used to generate the plots in Figure 3.13c. As the plots for $p(z,t)$ in Figure 3.13c show, the distribution function forgets its initial shape quickly, so the experiment is not likely to be sensitive to the detailed form of $p(z_0)$.

The closed-form analytical expression of Equation (3.20) fully describes the early and pre-asymptotic decay regimes up until the exponential cutoff, which is sufficient to fully describe our experimental data. The exact solution for the complete decay, including the asymptotic exponential tail, can be found by calculating Equation (3.11) when $p(Z_0)$ is the flat distribution with support from 0 to $\ell \leq L$:

$$S(T) = \frac{4L}{\ell}\sum_{n=0}^{\infty}\frac{\sin^2[(n+1/2)\pi\ell/2L]}{(n+1/2)^2\pi^2}\mathrm{e}^{-(n+1/2)^2\pi^2 T}. \tag{3.22}$$

Equation (3.22) introduces a second fit parameter compared to Equation (3.20), which is only relevant when the asymptotic exponential is present in the experimental time window. This function behaves qualitatively like Equation (3.16) in Figure 3.14. For ℓ/L close to 1, the survival probability is dominated by an exponential decay. As ℓ/L becomes much smaller than 1, the pre-asymptotic $t^{-1/2}$ power-law decay develops. The solution of Equation (3.20) is equivalent to the case where $\ell/L \ll 1$ in Equation (3.22), and mathematically can be obtained by taking an integral approximation of Equation (3.22).

Equation (3.20) is an excellent fit to the bulb decay of CdS NRs in the 1 ns – 10 μs time window with only a single adjustable parameter, τ (Figure 3.13d). The ability to describe the TA

decay with one adjustable parameter is remarkable in light of the fact that excited-state decays of nanocrystals normally require multi-exponential fits with several parameters to adequately describe the data.[24,36,37] While τ is a fitting parameter, Equation (3.20) predicts that the survival probability is only a function of t/τ. The data in Figure 3.13d are consistent with this prediction: the decays for non-uniform CdS NR samples with mean lengths from 22 to 68 nm all collapse to a master curve when each decay is plotted as a function of t/τ. The extracted values of τ do not correlate with nanorod length (Table 3.4), reinforcing the conclusion that, in the time window measured, the diffusion-limited recombination dynamics are independent of the nanorod length and are governed instead by the initial distribution of electron-hole separations.

The timescales associated with the diffusion model provide insights into trapped-hole motion on the CdS surface. While we cannot uniquely determine the value of either ℓ or D from fitting Equation (3.20) to our TA data, we can estimate an upper bound for each. As in any finite-sized system, when $t \sim L^2/D$, the power law will transition to an asymptotic exponential decay as the hole population encounters the far end of the NR (Figure 3.14).[137] In this model, the transition from the pre-asymptotic power-law decay to the asymptotic exponential decay would occur at $t = 4L^2/\pi^2 D$. Because we do not observe this asymptotic behavior on the timescale of our measurement we can only find an upper bound for D based on the longest time measured here, 10 μs, and the shortest non-uniform NRs used, 22 nm, as an upper bound for L. In this way we estimate the upper limit of D to be ~10^{-7} cm^2/s. This value is orders of magnitude smaller than the diffusion coefficient for band-like hole transport in bulk CdS.[132] It is, however, in the range of values of diffusion coefficients reported for trapped carrier diffusion in semiconductors such as TiO_2 (10^{-8}–10^{-4} cm^2/s).[142,143] With the estimated value for D, the fit value of τ (55 ns) places an upper bound on ℓ of 2 nm using $\tau = \ell^2/4D$, which is both an order of magnitude

larger than the inter-atomic spacing and an order of magnitude smaller than the length of the NR. The diffusion approach taken here is a continuum approximation to an underlying discrete random walk (Figure 3.13a), and to be consistent, the step length must be smaller than the smallest length scale in the model (ℓ). This suggests that the step length in the random walk of the trapped hole is on the order of inter-atomic distances. This is consistent with the view that hole trap states in CdS nanocrystals originate from surface S atoms.[26,56,76,80] CdS NRs studied here are capped with thiol-based surface capping ligands (3-MPA), which can provide additional hole traps from the S atoms of the ligand.[26] However, when CdS NRs are passivated with the native phosphonate ligands, the bulb electron decay fits the diffusion-annihilation model as well (Figure 3.15), demonstrating that diffusion does not require thiol-based ligands.

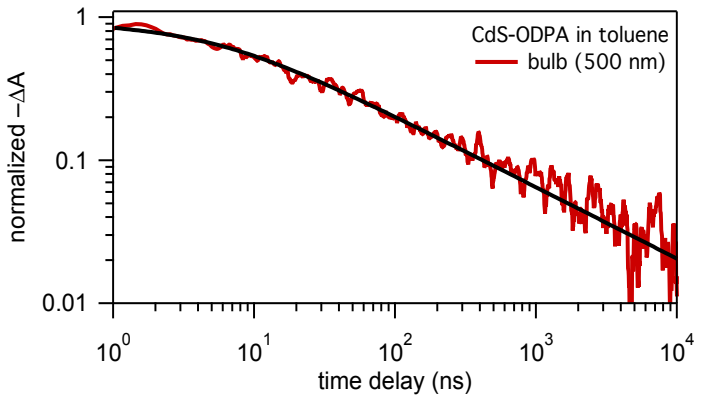

Figure 3.15. Power-law decay in CdS nanorods with native ligands. TA decay of the bulb signal after 405 nm excitation of 37 nm long CdS NRs with native octadecylphosphonic acid (ODPA) ligands in toluene. The decay has a clear $t^{-1/2}$ power-law tail and can be fit with Equation (3.20) ($\tau = 14 \pm 1$ ns). Fitting was done on raw data and the data was smoothed for presentation only.

3.4.5 Implications of Trapped-Hole Diffusion.

While the morphology of the non-uniform CdS NRs provides a way to observe diffusive trapped-hole motion, the origin of surface hole traps should be independent of particle shape.[35] Thus, it is likely that the diffusion of trapped holes is a general phenomenon in CdS nanocrystals, but is

only revealed when the recombination of the electron and the trapped hole is diffusion-limited. In most structures, trapped-hole motion is obscured because the wavefunctions of the electron and trapped hole remain spatially overlapped on the timescale of recombination, as is the case in CdS QDs (Figure 3.9c), rods (Figure 3.9b), and bulbs excited at 510 nm (Figure 3.9d). The $t^{-1/2}$ signature reported here arises from a one-dimensional diffusion-limited recombination mechanism, but the specific functional form will depend on the particle geometry and effective dimension. For example, in a two-dimensional structure, the survival probability would decay as $1/\ln(t)$ at long times.[137] Similar to CdS, CdSe nanocrystals have hole trap states associated with surface Se atoms.[26,68] Therefore, it is likely that trapped holes are mobile in CdSe nanostructures as well.

The diffusion of trapped holes on the surfaces of CdS nanorods has important implications for the photochemistry of CdS nanostructures. Reduction of adsorbed catalysts by photoexcited electrons in CdS nanorod-based structures and subsequent H_2 production has been studied in a variety of systems, and the behavior of photogenerated holes in these systems strongly influences H_2 generation.[7,44,107,111,144-146] Spatial separation of electrons and holes in nanoheterostructures improves H_2 production by slowing down recombination.[107,144] Furthermore, the rate of hole transfer out of the nanocrystal by oxidation of an electron donor can limit the rate of H_2 production.[111,145,146] Efficient hole removal also enhances photostability of CdS nanorods, making photodegradation less pervasive than in bulk CdS.[145,146] Trapped holes in particular can have a strong influence on electron transfer from CdS nanorods to H_2 generation catalysts,[147] and can themselves transfer to hole acceptors on the nanorod surface.[82] The next challenge in nanocrystal photochemistry is to use photoexcited holes to oxidize water rather than sacrificial electron donors.[148] In water splitting, the four-electron oxidation half reaction is more

difficult to catalyze than the two-electron reduction reaction that generates H_2,[116,148,149] and surface-trapped holes must transfer from CdS to water oxidation catalysts.[82] At the low surface catalyst concentrations appropriate for multi-electron redox chemistry,[24] the efficiency of hole transfer to the catalyst would be negligible if the trapped holes were stationary. High rates and efficiencies of trapped-hole transfer from CdS nanorods to molecular hole acceptors and water oxidation catalysts have indeed been observed at low surface coverages,[82,116] which is inconsistent with a stationary hole picture. Trapped-hole diffusion explains these earlier observations as it provides a mechanism in which the hole samples the nanocrystal surface to find an adsorbed molecule. Our results suggest that in order to control CdS nanocrystal oxidation photochemistry, it is not sufficient to only tune properties such as driving force, electronic coupling, and reorganization energy that normally dictate rates of charge transfer. Rather, the key to enhancing rates and efficiencies of processes such as photochemical water oxidation may lie in manipulating trapped-hole diffusion to enable trapped holes to encounter catalysts before they recombine with electrons.

3.5 Conclusions

Our work reveals that energetically trapped holes are mobile on the surfaces of CdS nanorods on timescales from nanoseconds to tens of microseconds. Taken together, the experimental measurements and theoretical model reported here provide a detailed conceptual and quantitative picture of carrier dynamics in CdS nanorods on timescales relevant for optoelectronic applications. While the carrier relaxation dynamics are complex and nonexponential, they are rooted in the simple physical phenomenon of trapped-hole diffusion on the nanocrystal surface. Trapped-hole diffusion is likely to be a general phenomenon in CdS and CdSe nanocrystals and

should occur in structures of any morphology. The ability of trapped holes to diffuse on nanocrystal surfaces at room temperature may have wide-ranging consequences for the photophysics and photochemistry of semiconductor nanocrystals.

Chapter 4

Relationships between exciton dissociation and slow recombination within ZnSe/CdS and CdSe/CdS dot-in-rod heterostructures†

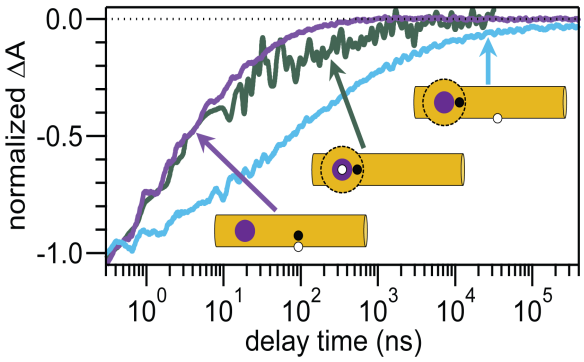

4.1 Abstract

Type-II and quasi type-II heterostructure nanocrystals are known to exhibit extended excited-state lifetimes compared to their single material counterparts because of reduced wavefunction overlap between the electron and hole. However, due to fast and efficient hole trapping and non-uniform morphologies, the photophysics of dot-in-rod heterostructures are more rich and complex than this simple picture. Using transient absorption spectroscopy, we observe that the behavior of electrons in the CdS "rod" or "bulb" regions of non-uniform ZnSe/CdS and CdSe/CdS dot-in-rods is similar regardless of the "dot" material, which supports previous work demonstrating that hole trapping and particle morphology drive electron dynamics. Furthermore, we show that the longest lived state in these dot-in-rods is not generated by the type-II or quasi

---

†Adapted with permission from Grennell, A. N.; Utterback, J. K.; Pearce, O. M.; Wilker, M. B.; Dukovic, G. *Nano Lett.* **2017**, *17*(6), 3764-3774. (Copyright © 2017 American Chemical Society). This publication is based on a previously published thesis chapter: Grennell, A. N. Photophysics and Electron Transfer Dynamics of Type-II and Quasi Type-II Heterostructure Nanocrystals. *University of Colorado Boulder, Chemistry & Biochemistry Graduate Theses & Dissertations*, **2017**.

type-II band alignment between the dot and the rod, but rather by electron–hole dissociation that occurs due to fast hole trapping in the CdS rod and electron localization to the bulb. We propose that specific variations in particle morphology and surface chemistry determine the mechanism and efficiency of charge separation and recombination in these nanostructures, and therefore impact their excited-state dynamics to a greater extent than the heterostructure energy level alignment alone.

4.2 Introduction

Heterostructure nanocrystals (NCs), in which two or more semiconductor domains are attached epitaxially, have attracted considerable attention due to their capacity for spatial control over electron and hole wavefunctions governed by the relative energy levels of the component materials.[112,113,150-153] So-called type-I heterostructures are designed to funnel the photoexcited electron and hole into one semiconductor domain. This approach has been remarkably successful in enhancing photoluminescence (PL) quantum yields of NCs.[41,150,151,154,155] On the other hand, type-II heterostructures are designed to spatially separate the photoexcited electron and hole across the interface of two semiconductor domains in order to impede charge recombination.[113,152,153,156-164] Quasi type-II structures are similar in function, except that one carrier (usually the electron) delocalizes over the two domains, while the hole is confined to one domain.[133,165-174] The extended excited-state lifetimes in (quasi) type-II heterostructures benefit applications such as photochemical fuel production.[4,5,8,47,107,109,111-113,175] CdSe/CdS dot-in-rod (DIR) heterostructures in particular have shown nearly 100% efficiency of electron transfer in some cases, and enhanced charge separation that leads to light-driven fuel-production rates higher than those of CdS nanorods alone.[47,82,107,109,118,144] The dynamics of photoexcited carriers

in type-II and quasi-type-II nanocrystals are central to their performance in applications and the physical picture of these intricate excited-state dynamics continues to evolve.[36,37,64,80,133,160,161]

Wavefunction engineering via energy level structure is a compelling concept that has been successful in controlling heterostructure excited states in core/shell motifs.[41,113,150-153,156,159] However, recent studies demonstrated that excited-state dynamics in heterostructures that contain CdS nanorods (NRs) are more complex than what might be expected from energy level structure alone.[89,133,160] CdS NR samples often contain structures that are non-uniform in width, containing narrow and wide regions referred to as the "rod" and "bulb," respectively.[130] The bulb has a lower energy transition compared to the rod because of a lower degree of quantum confinement, giving rise to two spatially distinct electronic states (rod and bulb) that can be spectrally resolved, and making non-uniform NRs type-I structures.[130] ZnSe/CdS and CdSe/CdS DIRs also can contain CdS bulbs, or shells, which typically grow around the seed material (ZnSe and CdSe) during synthesis.[133,160,173] Such DIR heterostructures exhibit three distinct excitons that reside within with the rod, bulb and interface regions (see Figure 3.1).[133,160] The rod and bulb excitons are comprised of an electron and a hole in the CdS rod or CdS bulb region, respectively. The exciton at the interface between the two materials exists with the hole localized in the seed and the electron either located in the bulb (type II) or delocalized across both the seed and bulb (quasi type II).

Another signature feature of CdS NRs is fast (~1 ps) and efficient trapping of photoexcited holes to the surface.[23,26,37,56,57,82] Photoexcited electrons are influenced by the energy level landscape of the nanostructure and tend to dissociate from the trapped hole to localize to the less quantum confined bulb when initially generated in the rod.[64] This can result in a long-lived charge-separated state in which the hole is trapped on the rod and the electron is

localized in the bulb.[64] The subsequent recombination is slow with a power-law decay at long times. Because their surface is the same as that of CdS NRs, hole trapping on the CdS surface is also fast in ZnSe/CdS and CdSe/CdS DIR heterostructures and competes with hole localization to the seed.[23,82,89,133,160,176] If the hole traps instead of localizing to the seed, excited states ultimately consist of a hole trapped on the CdS surface and a conduction band electron in the CdS rod, the bulb (in type-II structures), or across the bulb and seed (in quasi type-II structures). While much progress has been made in understanding the electronic transitions and carrier localization dynamics of ZnSe/CdS and CdSe/CdS DIRs,[112] the effects of this electron–hole dissociation on recombination dynamics have not yet been elucidated.

In this work, we investigate how the charge-separated state created by hole trapping on the CdS rod surface and electron localization to the bulb impacts the excited-state dynamics of ZnSe/CdS and CdSe/CdS DIRs when compared with CdS NRs of similar dimensions. Using transient absorption (TA) spectroscopy, we directly populate either the rod or the interface of ZnSe/CdS and CdSe/CdS DIRs and observe the evolution of different excited states on timescales from 160 fs to 400 μs. We find that, in all three materials, when the CdS rod is directly populated, holes trap with a <1 ps timescale and excited electrons in the rod have similar kinetics. Electrons that localize to the bulb and interface in non-uniform structures dissociate from the hole trapped on the CdS rod, leading to a charge-separated state that undergoes slow recombination with a power-law tail. On the other hand, when the interface state is directly populated in ZnSe/CdS and CdSe/CdS DIRs, holes are localized in the seed rather than trapped on the CdS rod and thus spatially overlap with the electron to a greater extent. Under those conditions, the interface and bulb electron populations decay on a similar timescale as an electron in the CdS rod. Notably, this decay is faster than the decay of the charge-separated

stated created after the rod is populated. Additionally, we isolate the electron–hole recombination dynamics in uniform structures, which do not have bulbs, and compare them with results for non-uniform structures. Together, these experiments show that charge separation induced by fast hole trapping on the CdS rod surface and electron localization to the bulb can yield states that are significantly longer lived than the interfacial states deriving from type-II and quasi type-II energy level alignment between the dot and the rod in the DIR nanostructure. We discuss the origin and impact of this additional layer of complexity that governs the excited-state dynamics in nanocrystal heterostructures. Because this work relies on comparisons of TA data examining multiple transitions in three different materials with two different pump wavelengths for each, to facilitate readability we first describe the results in their entirety and then discuss how they relate to each other to reach general conclusions about excited-state dynamics in these systems.

This work represents a close collaboration between Dr. Amanda Grennell and myself, as we contributed equally as co-first-authors of the published article on which this chapter is based.[177] Dr. Amanda Grennell carried out the nanocrystal synthesis TA spectroscopy experiments and data analysis. I contributed to data analysis, experimental design and physical interpretation. This work also appears in her dissertation.[178]

4.3 Methods

4.3.1 Synthesis, preparation and characterization of nanocrystals

The synthesis and preparation of all materials is described in Chapter 2. Unless otherwise noted, all nanocrystals studied here were capped with 3-mercaptopropionic acid ligands and dispersed in 12.5 mM Tris-HCl buffer at pH.

4.3.2 Transient absorption spectroscopy

The setup of the transient absorption (TA) experiment has been described previously and in Chapter 2.[116] Samples were prepared in airtight 2 mm path length quartz cuvettes sealed under Ar with a Kontes valve and stirred during data collection. Nanocrystal concentrations of ~560–650 nM were used, prepared in a 12.5 mM Tris-HCl buffer at pH 7. TA kinetics of ZnSe/CdS and CdSe/CdS DIRs pumped with 405 nm light were measured at various pump powers to identify the regime in which kinetics are independent of pump power. When pumping samples with 570 nm light, the pump energy was scaled to account for the lower absorption of the sample at this wavelength compared to 405 nm. The energies of 405 nm and 570 nm pump pulses were ~6 nJ and ~50 nJ per pulse, respectively, with beam diameters of ~250 μm. An instrument response function was measured with a solvent at each pump wavelength, and was used to correct for chirp of the white light probe.

4.3.3 Sample characterization

Dilute (~0.1 μM) samples of NCs with native ligands in toluene were drop cast onto carbon coated 300 mesh copper TEM grids (Electron Microscopy Science) and dried. Particle dimensions for ZnSe seeds, CdS NRs, CdSe/CdS DIRs, and ZnSe/CdS DIRs were determined by measuring over 150 particles using ImageJ software.[129] Sizes of CdSe seeds were determined from published tuning curve to be 2.8 nm in diameter.[25] Size distributions of particles appear in Figure 4.1 and average sizes and standard deviations appear in Table 3.1.

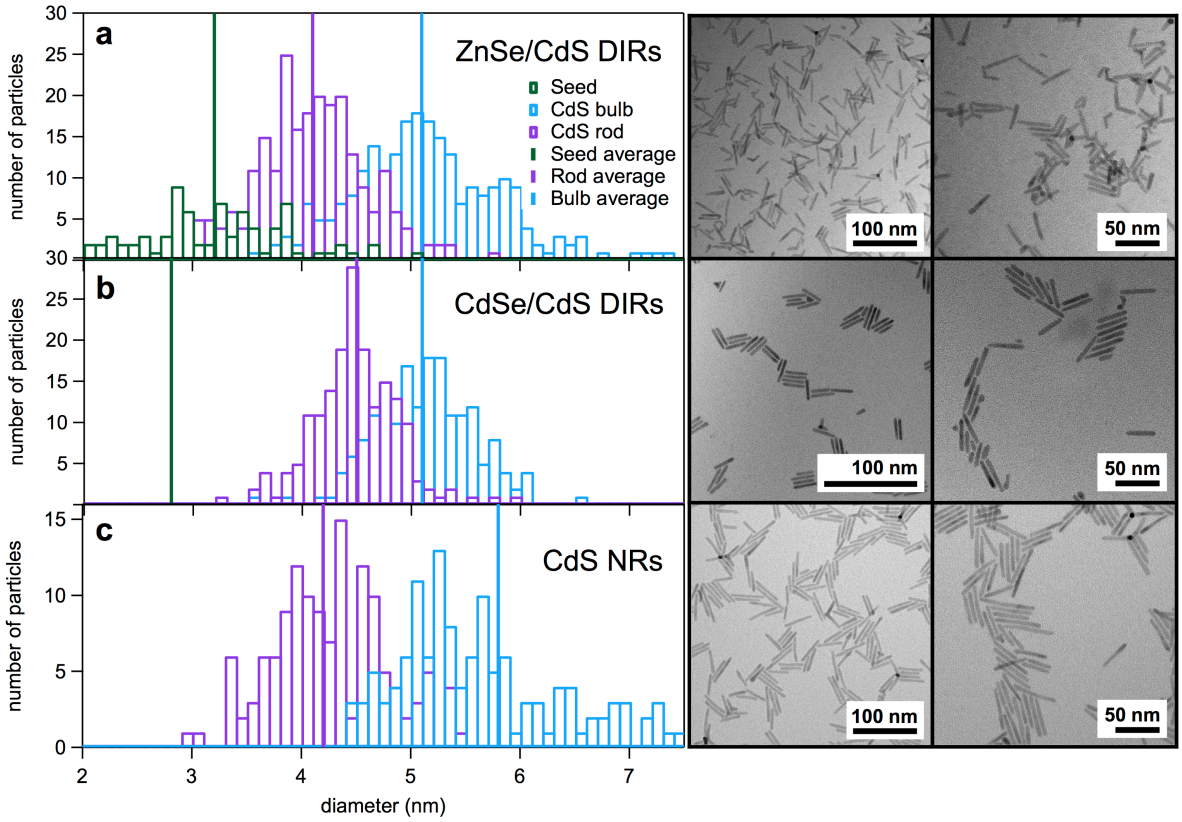

Figure 4.1. Histograms of particle width measurements and TEM images. Row (a) ZnSe/CdS DIRs, row (b) CdSe/CdS DIRs, row (c) CdS NRs.

Table 4.1. Nanocrystal component sizes measured by TEM

Sample	Seed diameter (nm)	Bulb diameter (nm)	Rod diameter (nm)	Rod length (nm)
CdS	—	5.8 ± 0.9	4.2 ± 0.5	37 ± 8
CdSe/CdS	2.8	5.1 ± 0.6	4.5 ± 0.4	30 ± 8
ZnSe/CdS	3.2 ± 0.7	5.1 ± 0.7	4.1 ± 0.6	31 ± 6

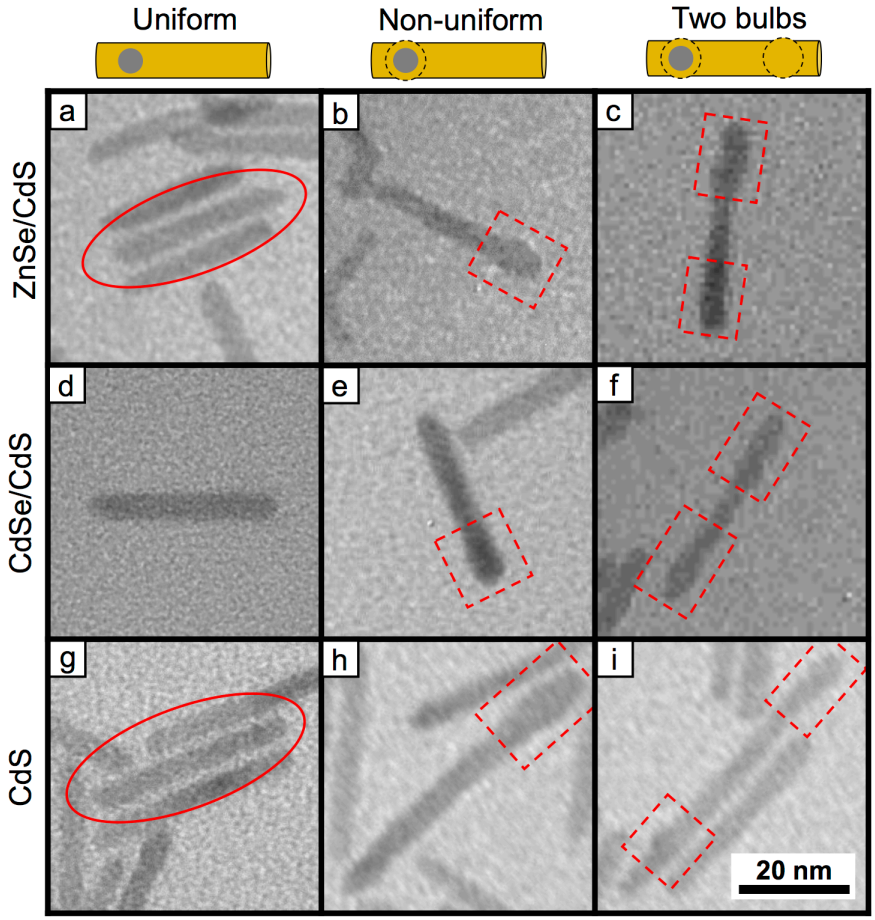

Figure 4.2. Selected TEM images of CdS nanorods, ZnSe/CdS DIRs, and CdSe/CdS DIRs showing uniform particles, non-uniform particles with one bulb, and non-uniform particles with two bulbs. (a) Uniform ZnSe/CdS DIR (center particle, circled). (b) Non-uniform ZnSe/CdS DIR with one bulb. (c) Non-uniform ZnSe/CdS DIR with two bulbs. (d) Uniform CdSe/CdS DIR. (e) Non-uniform CdSe/CdS DIR with one bulb. (f) Non-uniform CdSe/CdS DIR with two bulbs. (g) Uniform CdS NR (center particle, circled). (h) Non-uniform CdS NR with one bulb. (i) Non-uniform CdS NR with two bulbs. Bulbs are outlined in dashed boxes.

UV-visible absorption spectra were obtained at room temperature using an Agilent 8453 spectrophotometer with tungsten and deuterium lamps. Samples for TA spectroscopy were prepared at ~600 nM concentration and were sealed under Ar in 2 mm path length quartz cuvettes with Kontes valves. Molar absorptivity was found by comparison of UV-vis absorption with Cd^{2+} ion concentrations found by elemental analysis (ICP-OES) after acid digestion. These samples had concentrations in the range ~10–100 nM and were prepared in 1 cm x 1 cm quartz cuvettes, sealed under Ar. TEM measurements were used to determine the number of Cd^{2+} ions

per nanocrystal (NC). The molar absorptivity per NC estimated by this method was ~2 × 10^7 M^{-1} cm^{-1} at 350 nm for each NC sample.

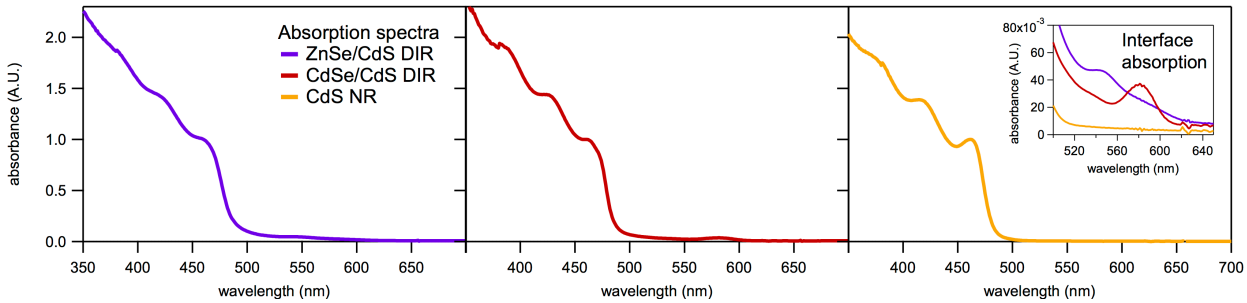

Figure 4.3. UV-visible absorption spectra of ~600 nM TA samples of the three types of NCs studied. Inset shows absorption at the interface, which is approximately ten times weaker than the lowest-energy CdS rod absorption.

In the energy level diagrams in Figure 4.4, the lower quantum confinement in the bulb is reflected in the lower-lying conduction band and higher-lying valence band edges. The offsets between the bulb and rod energy levels are shown to scale, as determined by calculating the confinement energies of the electron and hole using their effective masses and the transition energies determined by absorption spectra (Figure 4.3).[64] In ZnSe/CdS and CdSe/CdS DIRs, the bulb is located around the seed material, and the bulb electron has been shown to share a state with the interface electron.[133,160] The valence band offset between the seed and bulb can be determined by taking the difference between the bulb and interface transition energies.

4.4 Results and Discussion

4.4.1 Electronic transitions and TA spectra of non-uniform DIR heterostructures

CdS NRs, ZnSe/CdS DIRs and CdSe/CdS DIRs were synthesized according to previously reported methods.[44,121,123,124] ZnSe and CdSe seeds had diameters of 3.2 nm and 2.8 nm, respectively, and all three structures had similar CdS rod dimensions: they are about 4.5 nm in diameter and 30 nm in length (Figure 4.1, Figure 4.2 and Table 4.1. Nanocrystal component sizes measured by TEM). Additionally, all particles studied here have the same surface-capping ligands (3-mercaptopropionic acid) and are dispersed in aqueous buffer solution at pH 7.[44] See Chapter 2 for a detailed description of synthesis and sample preparation. Optical spectra of ZnSe/CdS and CdSe/CdS DIRs include two spectral features that have been assigned to CdS (rod and bulb) and one due to the interface between the seed and CdS (interface) (Figure 4.3, Figure 4.4).[133,160] The presence of the bulb is common for CdS NRs, CdSe/CdS DIRs, and ZnSe/CdS DIRs,[124,130,133,160,165,173,179,180] and can be seen in transmission electron micrograph (TEM) images of our samples (Figure 4.2). In Figure 4.4a-c, the quantum-confined energy levels of the conduction band and valence band of each material are shown along with a schematic representation of the corresponding structure, and are labeled with the transition energies of the rod, bulb, and interface excitons. These diagrams depict the relationship between the excitation energy and the location of the corresponding exciton. A description of how the band offsets were determined appears in the Methods section above. The bulb exciton has a lower energy transition than the rod because the bulb is wider in diameter and therefore experiences less quantum confinement.[130] Because the quantum-confined energy levels depend on size, in this work we compare the excited-state dynamics of structures with similar CdS rod dimensions (Table 4.1). The interface feature is lower in energy than either of the parent materials, as seen in the steady-

state absorption spectra (Figure 4.3). The energy of this transition is determined by the energy-level alignment at the interface, as depicted in Figure 4.4a-c.[121,124,133,179] The interface exciton is thought of as a hole localized in the seed (either ZnSe or CdSe) and an electron in the surrounding CdS.[133,160,165-172,181,182] In ZnSe/CdS, the interface/bulb electron is confined to the surrounding CdS due to the very high conduction band energy of the ZnSe seed, making them type-II heterostructures.[160,181,182] In CdSe/CdS, there is a small conduction band offset and the electron wavefunction is thought to extend over both CdSe and CdS, making them quasi type-II heterostructures.[133,165-172] Figure 4.2 shows that our samples also contain structures of uniform width and the contributions from both the uniform and non-uniform structures to the excited state dynamics observed in these samples will be discussed throughout the chapter.

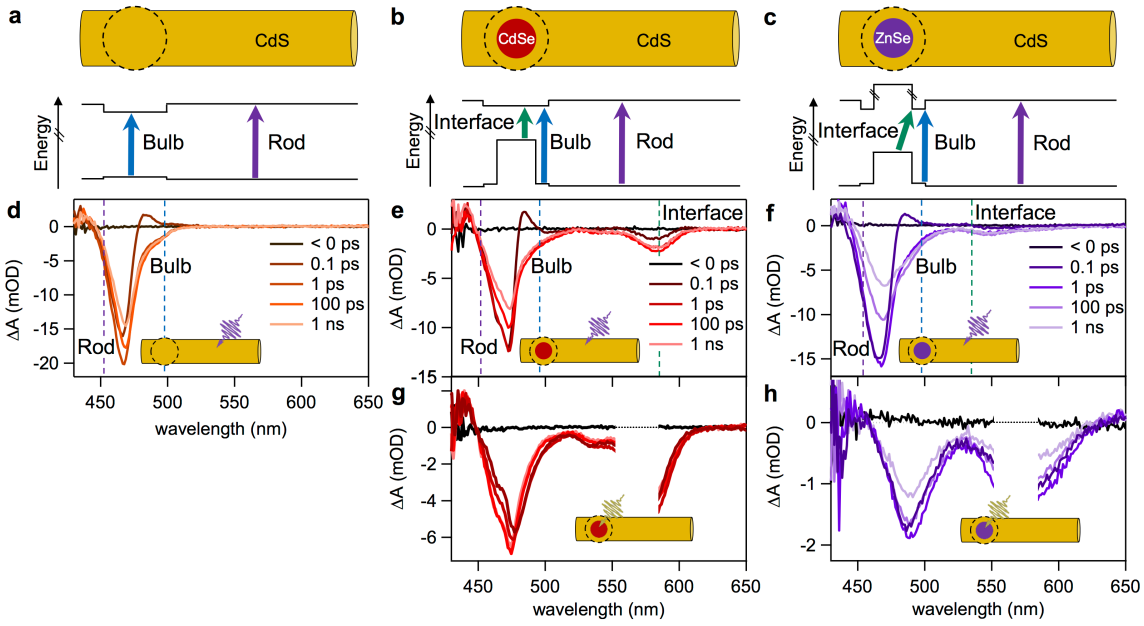

Figure 4.4. Relationship between non-uniform morphology, electronic structure and TA spectra. (a–c) Schematic representations of (a) CdS, (b) CdSe/CdS, and (c) ZnSe/CdS NCs depicting the non-uniformities in the structure as a spherical bulb along the rod. Energy level diagrams show the locations of rod, bulb, and interface excitons in each structure. Energy level offsets are drawn to scale. (d–f) Evolution of TA spectra for each type of NC studied after excitation of the rod at 405 nm. Dotted lines show the wavelengths chosen to isolate the rod, bulb, and interface signals. (g–h) Evolution of TA spectra of CdSe/CdS and ZnSe/CdS DIRs after excitation of the interface transition at 570 nm. Pump scatter (552–585 nm) has been removed. TA spectra from 1 ns to 50 μs appear in Figure 4.5.

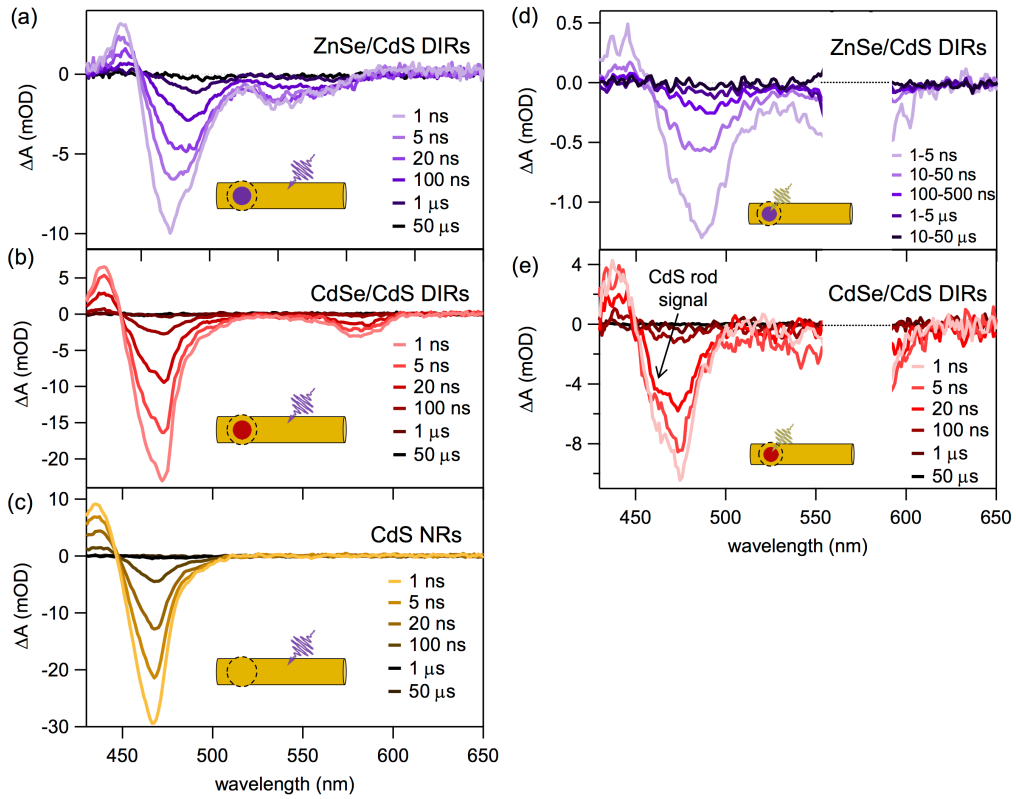

Figure 4.5. TA spectra from 1 ns to 50 μs. TA spectra from 1 ns to 50 μs of ZnSe/CdS DIRs, CdSe/CdS DIRs, and CdS NRs when pumped at 405 nm (a–c) and of ZnSe/CdS and CdSe/CdS DIRs when pumped at 570 nm (d–e). After 570 nm excitation, the TA spectra of ZnSe/CdS DIRs (d) contain a bulb bleach centered at 489 nm which do not have a shoulder on the blue side, indicating that no rod signal is present. Alternatively, in the TA spectra of CdSe/CdS DIRs when the interface is pumped at 570 nm (e), the bulb bleach centered at ~475 nm contains a clear shoulder on the blue side, indicating that rod signal is present. Pump scatter from 552-585 nm has been removed in (d) and (e).

To examine the formation and decay dynamics of the rod, bulb, and interface signals in ZnSe/CdS and CdSe/CdS DIRs we use TA spectroscopy on timescales from 160 fs to 400 μs. Further details on the TA experiment appear in Chapter 2. In all of the TA experiments described below, low pump fluences were chosen to avoid multiple excitations per nanocrystal. A conduction band electron located in a particular region of the nanostructure will give rise to bleach peaks corresponding to that region (Figure 4.4d–f). The magnitude of the TA bleach signal of each feature in these structures, ΔA, reflects the time-dependent populations of excited

electrons in each state, regardless of whether the hole is trapped or even located in a different region of the nanostructure.[23,114,133,160] By measuring these signals as a function of pump–probe delay time, we can compare the dynamics of the rod, bulb, and interface electrons.[23,114,133,160] In DIRs, rod and bulb bleach peaks are observed at nearly identical energies as in CdS NRs, and the interface bleach (530–600 nm) appears at a lower energy, as expected from the energy level alignment Figure 4.4d–h, Figure 4.5).

As has been shown previously, excitation of non-uniform CdS NRs, ZnSe/CdS DIRs, and CdSe/CdS DIRs with 405 nm pulses primarily excites the rod part of the structure due to its much larger volume than the seed and bulb regions.[130,133,160,165] Following 405 nm excitation, hot carriers cool to the band edge in under 1 ps, as evidenced by the fast decay of the photoinduced absorption peak at ~480 nm.[23,114] After cooling in CdS NRs and in both types of DIRs, electrons in the non-uniform structures undergo localization to the bulb,[82] and the TA spectrum contains overlapping bleach features corresponding to both the rod and the bulb (Figure 4.4d–f). To compare the dynamics of the rod and bulb electrons, it is important for their signals to be isolated by choosing wavelengths at which the pure bulb and rod spectra equal zero, respectively.[64] The wavelengths that correspond to the different signals are shown as dotted vertical lines in Figure 4.4d–f. While extracting the signals in this manner is critical to isolating the decay shapes of the rod or bulb components, there is a compromise in the signal-to-noise ratio as the pure rod and bulb kinetics occur at wavelengths where the signal is ~1/5–1/3 of the maximum bleach amplitude. 570 nm light directly excites the interface transition of ZnSe/CdS and CdSe/CdS DIRs, with an electron in the bulb and a hole in the seed, as those photons are the too low in energy to be absorbed by either the rod or the bulb (Figure 4.6). The bulb and interface signals both appear instantaneously (Figure 4.4g and h), which demonstrates the existence of the bulb

feature and is consistent with the assignment that the bulb and interface transitions share an electron state.[133,160]

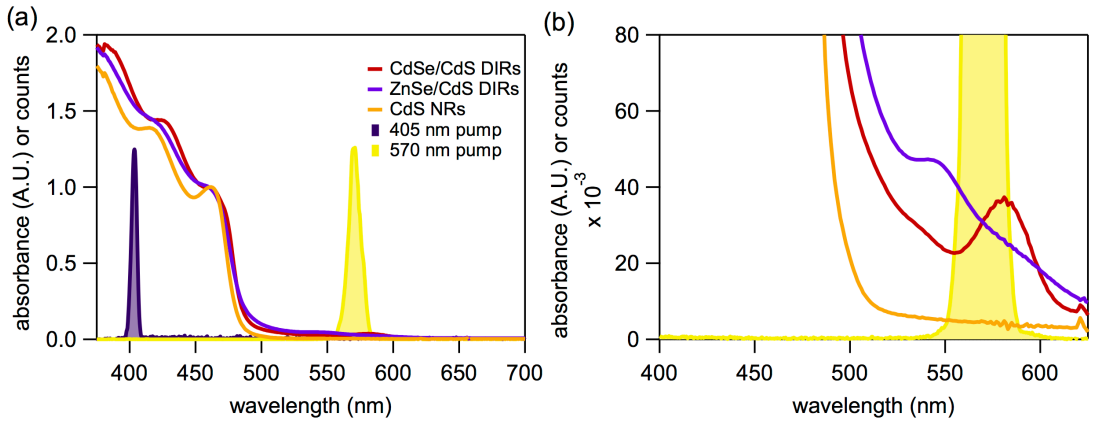

Figure 4.6. Spectra of pump pulses for TA experiments. (a) Overlay of UV-visible absorption of TA samples with both 405 and 570 nm pump spectra. (b) Overlay of UV-visible absorption of TA samples with 570 nm pump spectra, shown in the region of DIR interface absorption. Pump spectra are normalized.

4.4.2 Comparison of carrier dynamics in CdS, ZnSe/CdS, and CdSe/CdS after rod excitation

To understand the similarities and differences in excited-state behavior between CdS, ZnSe/CdS, and CdSe/CdS structures, we first examine the processes of hole trapping in the CdS rod, electron localization from the rod to the bulb, and the subsequent electron relaxation in the CdS regions (rod and bulb) of the three samples. The TA spectra of each of the three samples studied here exhibit a broadband photoinduced absorption feature that appears at wavelengths to the red of the band-edge bleach features (Figure 4.7). This feature has been assigned to trapped holes in CdS nanorods.[23] The kinetics of hole trapping to the CdS rod surface can thus be directly probed in CdS nanorod-based structures by examining the rise of this broadband photoinduced absorption feature.[23,82,89] The formation kinetics were fit to an exponential rise, convoluted with

a Gaussian IRF (160 fs FWHM). The time constants for hole trapping for CdS NRs, CdSe/CdS DIRs, and ZnSe/CdS DIRs are 0.9 ± 0.2 ps, 0.7 ± 0.3 ps, and 0.9 ± 0.3 ps, respectively. These hole trapping time constants are consistent with previous reports of hole trapping in CdS NRs and CdSe/CdS DIRs.[23,82,89]

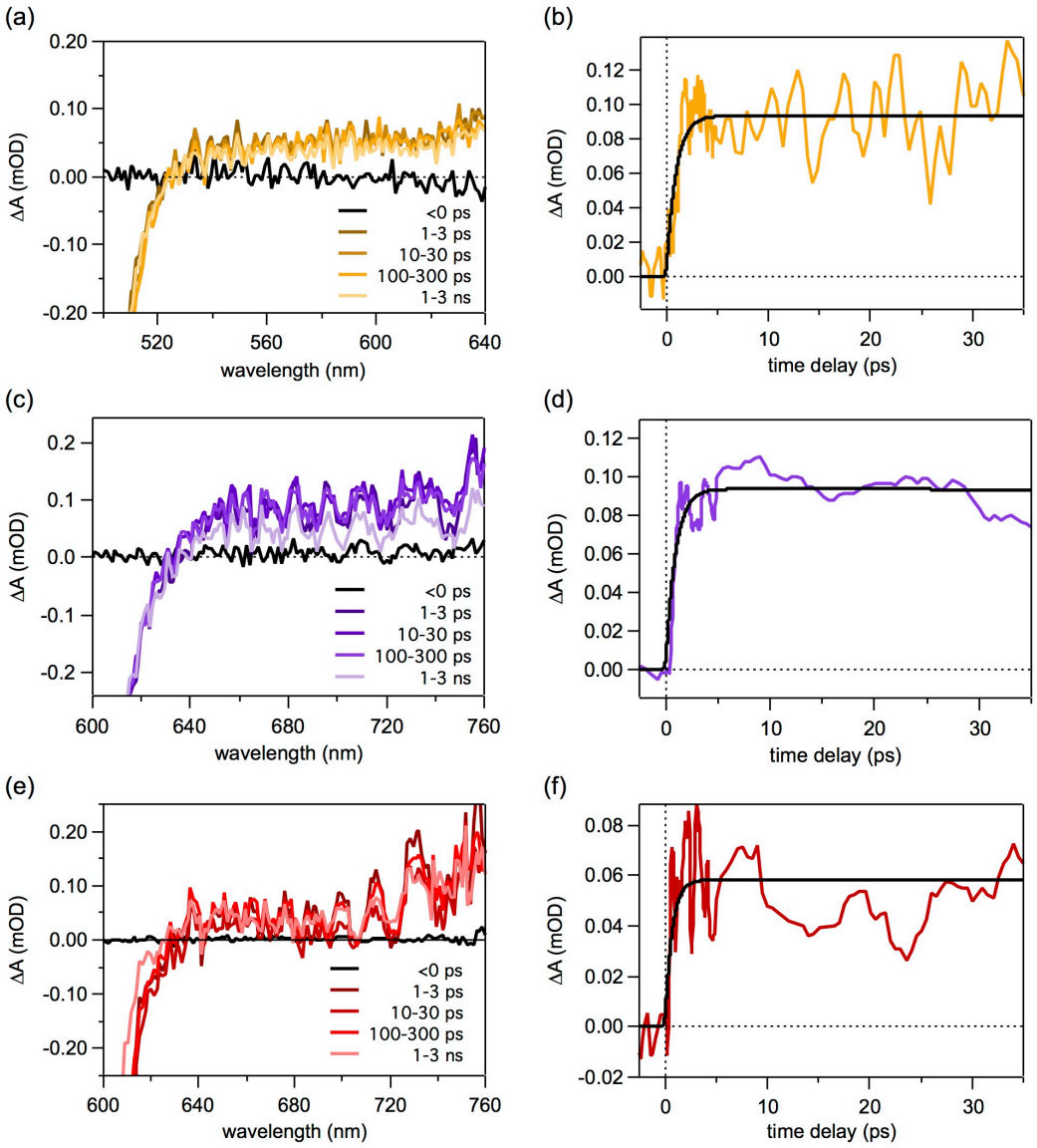

Figure 4.7. Hole trapping kinetics. TA spectra and formation kinetics of the PA feature in (a, b) CdS NRs, (c, d) ZnSe/CdS DIRs, and (e, f) CdSe/CdS DIRs. The TA spectra were averaged over the indicated time ranges in order to increase the signal-to-noise ratio. The time traces of (b) CdS NRs, (d) ZnSe/CdS DIRs and (f) CdSe/CdS DIRs were averaged over the spectral ranges of 550–620 nm, 650–750 nm and 650–750 nm, respectively. Fits were performed on raw data and the data were smoothed for presentation only.

Figure 4.8 shows the normalized TA time traces of the rod and bulb bleach signals for all three samples after the rod is pumped with 405 nm pulses. Upon excitation at this wavelength, the rod signal undergoes a rapid partial decay (Figure 4.8b) while the bulb signal has a corresponding rise (Figure 4.8d). These two behaviors correspond to the electrons leaving the CdS rod to become localized in the CdS bulb.[64,89,130,133,160] Electron localization continues even after the hole has trapped and is complete by about 100 ps in these structures, suggesting that the electron dissociates from the trapped hole when it localizes to the bulb.[64] Although there is a Coulomb attraction between the electron and a trapped hole,[130,133,147,160,176,183] the driving force for electron localization appears to drive this charge separation.[64] A comprehensive discussion of the evidence for this charge separation can be found later in the text.

It has been shown in non-uniform CdS nanorods that, as long as the energy difference in conduction bands between the bulb and rod is $>k_{\mathrm{B}}T$, virtually all rod electrons localize to the bulb (Figure 4.4).[64] Therefore, rod signal after localization is due primarily to structures that are effectively uniform in width. Uniform structures do not have bulbs for electrons to localize to and therefore do not contribute to the initial decay of the rod signal. Using this logic, we can estimate the fraction of structures that are non-uniform in each sample using the partial decay of the rod bleach because the amplitude of the initial rod decay is equal to the fraction of non-uniform structures in the sample. This amplitude is different for each of the samples studied here; in CdS, the initial decay is 54% of the total, in ZnSe/CdS it is 69%, and in CdSe/CdS it is 41%, while the remaining signal is due to structures that are uniform in width. Because there is a separation of timescales between electron localization (<1 ns) and intrinsic decay processes such as electron trapping and charge recombination (>1 ns),[35,64,65,84] we can isolate the rod decay due to localization in non-uniform nanostructures by subtracting the rest of the decay after electron

localization is complete. This reveals that the localization kinetics overlap for all three samples (Figure 4.8b inset) indicating that the decay shapes, and thus the underlying kinetics of electron localization, are the same in all three structures. Similarly, the rise of the bulb signal also has the same kinetics in all three types of NCs (Figure 4.8d). These results show that the energetics of the seed do not play a significant role in the kinetics of electron localization, consistent with previous findings.[89]

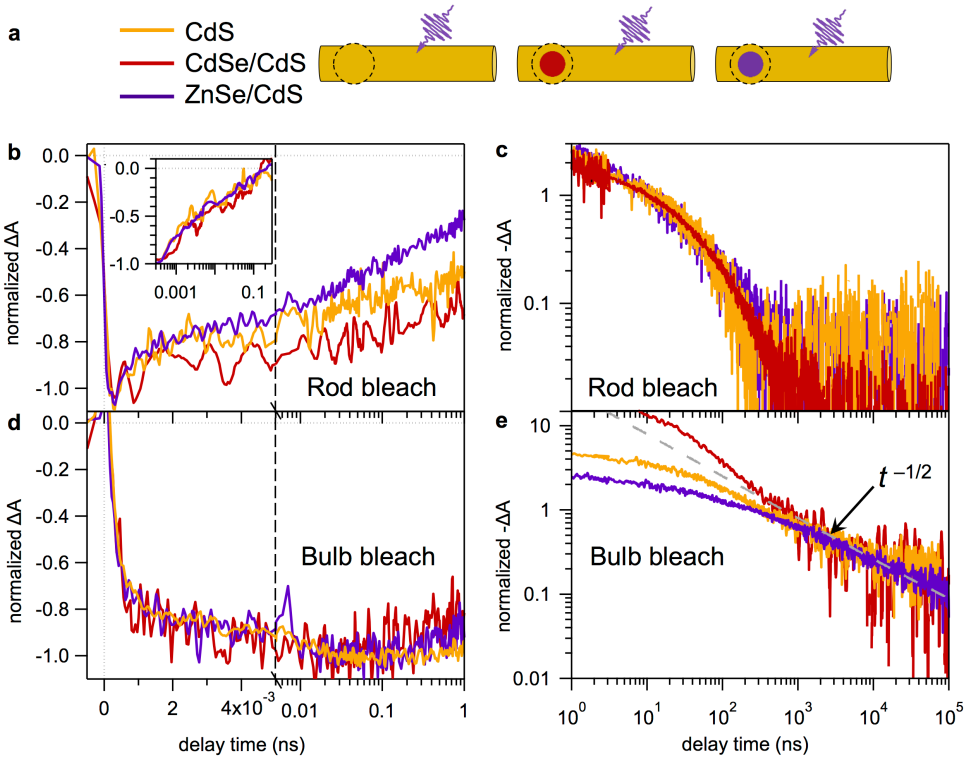

Figure 4.8. Comparison of rod and bulb bleach kinetics in all three types of NCs after 405 nm excitation. (a) Key for (b–e): CdS (yellow), CdSe/CdS (red), and ZnSe/CdS (purple). Schematic representation of each NC shows the rod being excited at 405 nm. (b) The rod bleach signals (~452 nm) for each NC from 0 to 1 ns, normalized at their maximum amplitudes. Decays are plotted on a split-time axis that is linear for the first 5 ps and logarithmic thereafter. The inset shows the same data after subtraction of the post-localization kinetics. (c) The rod bleach signals (~452 nm) for each NC from 1 ns to 400 μs, shown as positive signal on a log-log scale. Decays are normalized at 3 ns, after which time all three nearly overlap. (d) The bulb bleach signals (~498 nm) for each NC from 0 to 1 ns, normalized at their maximum amplitudes. Decays are plotted on a split-time axis that is linear for the first 5 ps and logarithmic thereafter. (e) The bulb bleach signals (~498 nm) for each NC, shown as positive signal on a log-log scale and normalized at 1.5 μs. Decays all have the same $t^{-1/2}$ power law over the range of 1 to 400 μs. For (c) and (e), bleach signals are normalized to a positive value so the y-axis can be logarithmic. Data have been smoothed for presentation.

Figure 4.8c shows the decay of the rod bleach of all three NCs after electron localization has occurred (i.e., signal from uniform structures), shown as a positive signal on a log-log scale to examine the functional form of the decay shape. In order to compare the NC kinetics after localization, these decays are normalized well after that process is complete. This comparison reveals that all three types of NCs have the same long-time decay kinetics of rod electrons, as the three traces nearly overlap. Thus electrons in the CdS rod region of uniform structures relax in a way that is not strongly influenced by the seed. The decay of CdS rod electrons in this time window can be described with a multi-exponential kinetic model in which the electron can decay by recombination with the trapped hole or trapping on the surface.[35,65,84,135,136]

Figure 4.8e shows the bulb decays after electron localization is complete, also shown as positive signals on a log-log scale. Normalization reveals that the long-time bulb decays overlap. Each sample exhibits a slow $t^{-1/2}$ power-law tail that is easily distinguished from the exponential tail of the rod decay. In non-uniform CdS NRs, the $t^{-1/2}$ power-law decay of the bulb electron was described as a signature of trapped-hole diffusion-limited recombination wherein the trapped hole diffuses along the rod until it encounters the localized bulb electron.[64] The bulb decays of ZnSe/CdS and CdSe/CdS after rod excitation exhibit power-law tails with the same exponent of –1/2, and only the amplitude of this tail varies between structures. Thus it is reasonable to expect that the formation of a charge-separated state followed by trapped-hole diffusion-limited recombination occurs in the DIR heterostructures in a manner similar to CdS NRs.

A quantitative comparison of the rod (Figure 4.8c) and bulb (Figure 4.8e) lifetimes in CdS, ZnSe/CdS, and CdSe/CdS is rendered problematic by the presence of the power-law tails in

the bulb decays. While the rod decay fits a model that is based on exponential pathways of recombination and trapping, systems that exhibit power laws cannot be described by a characteristic timescale. However, at any time, the instantaneous rate of decay of the bulb power-law decay is slower than the exponential decay of the rod. This prolongs the excited state of the bulb well beyond that of the rod. In this sense bulb electrons are "longer lived" than rod electrons in all structures. Because we cannot compare lifetimes per se for exponential and power law decays, in the analysis that follows we opt to simply point out where these power-law tails occur with the understanding that such behavior makes the decay longer lived than exponential decays such as the rod decays.

4.4.3 Comparison of rod, bulb, and interface electron dynamics in ZnSe/CdS DIRs as a function of excitation wavelength

We now turn to comparing the temporal evolution of rod, bulb, and interface signals for each type of heterostructure (ZnSe/CdS and CdSe/CdS). We first examine ZnSe/CdS DIRs. Figure 4.11 shows the time-resolved rod, bulb, and interface signals of ZnSe/CdS DIRs when pumped at 405 nm (Figure 4.11a, b), which primarily excites the rod, and 570 nm (Figure 4.11c, d), which generates an interface exciton (Figure 4.6). We showed above (Figure 4.8) that in ZnSe/CdS DIRs, when the rod is pumped at 405 nm, electron localization is observed as a fast partial decay in the rod signal corresponding to a rise of the bulb signal, which then decays with a different functional form than the rod. With the 405 nm pump, the interface signal also rises with the same kinetics as the bulb signal (Figure 4.11a), and exhibits a $t^{-1/2}$ power-law tail (Figure 4.11b, Figure 4.9a). Because the bulb and the interface are thought to share an electron state,[133,160] it is unsurprising that their rise kinetics overlap. However, the bulb and the interface signals do not have overlapping decays (Figure 4.11b). Although they both have power-law tails at long times,

the bulb signal decays considerably slower with a larger contribution of the power-law tail (Figure 4.8e, Figure 4.9a, Figure 4.10). As we discuss later in the text, these differences can be explained by the presence of both uniform and non-uniform structures in the sample.

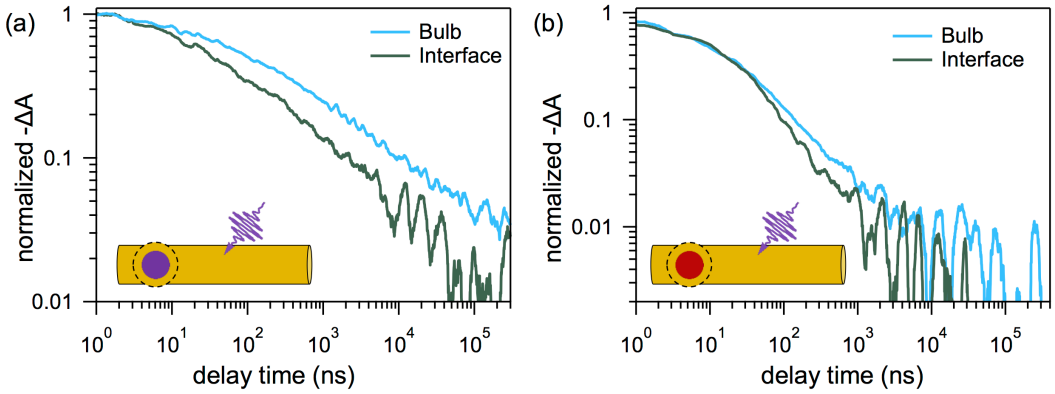

Figure 4.9. Bulb and interface decays in ZnSe/CdS and CdSe/CdS DIRs. Decay of (a) ZnSe/CdS and (b) CdSe/CdS bulb and interface signals when the rod is pumped (405 nm), from 1 ns to 400 μs. Bleach time traces are shown as positive signals to plot on a log-log scale to examine the functional form of the decay. The tails of each decay follow a $t^{-1/2}$ power law. Data were smoothed for presentation.

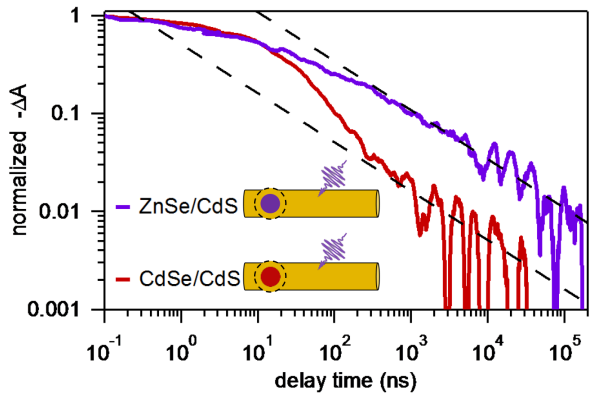

Figure 4.10. TA decays of ZnSe/CdS and CdSe/CdS DIRs interface signals after 405 nm pump. The bleach time traces are plotted with positive signal on a log-log scale to show the power law present in the tail of the interface decays. Data were smoothed for presentation.

Absorption of the 570 nm pump generates the interface exciton, with an electron in the bulb and a hole in the seed. As we would expect under these conditions, no rod signal is observed (Figure 4.4h, Figure 4.5d). The bulb and interface signals appear instantaneously

(Figure 4.11c), consistent with the assignment that these transitions share the electron state.[160] The subsequent decays of the two signals overlap after 1 ns (Figure 4.11d). The decays of the interface and bulb signals when rod-pumped and when interface-pumped are directly compared in Figure 4.12. These comparisons show that the interface-pumped bulb and interface signals decay faster than when the rod is pumped, even though the 570 nm excitation directly pumps the interface state created by the type-II energy level alignment (Figure 4.4c). Thus charge separation due to dissociation between a bulb-localized electron and rod-trapped hole can enhance the electron lifetime well beyond what is achieved with the type-II band alignment of the interface.

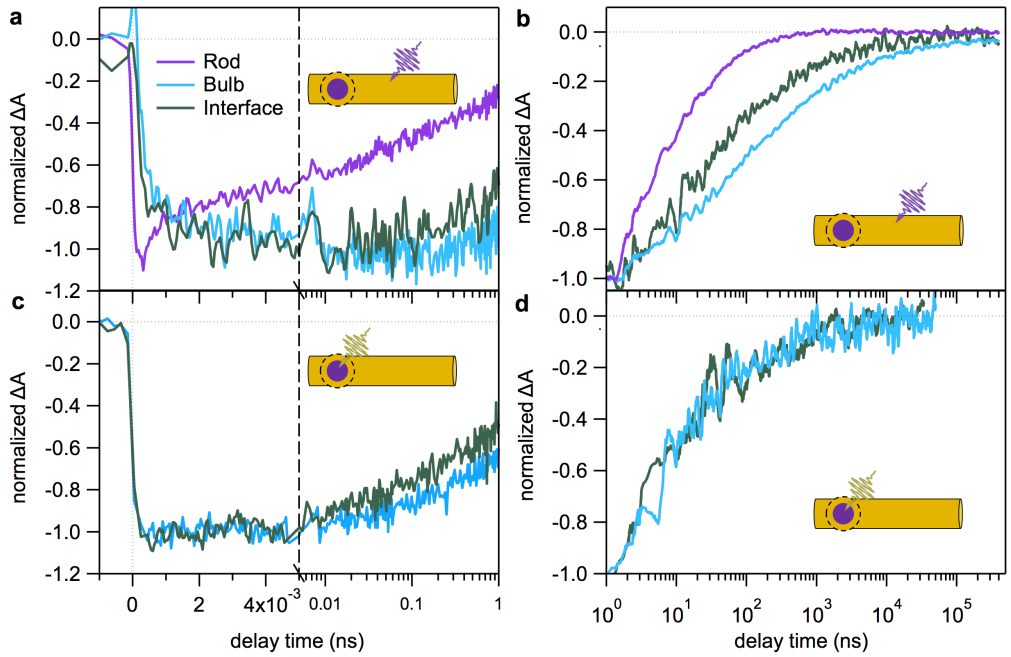

Figure 4.11. TA time traces of ZnSe/CdS DIR bleach signals after rod and interface excitation. (a) Rise of ZnSe/CdS rod (456 nm), bulb (498 nm) and interface (535 nm) bleach features when the rod is pumped at 405 nm. Data are normalized at the maximum signal of each transition. (b) Decays of rod, bulb, and interface signals when rod is pumped, normalized at 1 ns, after electron localization is complete. (c) Rise of ZnSe/CdS bulb (489 nm) and interface (535 nm) signals when the interface is pumped at 570 nm. Data are normalized at the maximum signal of each transition. No signal is observed at the rod transition. (d) Decays of bulb and interface signals when interface is pumped, normalized at 1 ns. No signal is observed at the rod transition (c). Interface data in (a) and all data in (b) and (d) were smoothed for presentation.

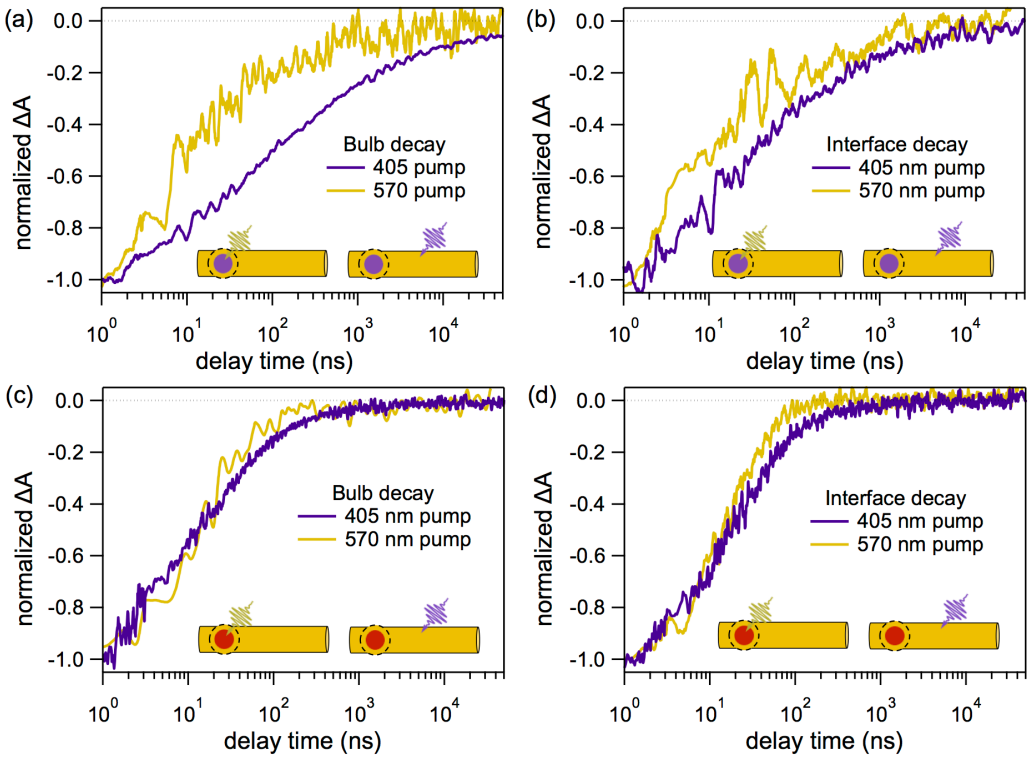

Figure 4.12. Comparison of bulb and interface decays of ZnSe/CdS and CdSe/CDS DIRs for different excitation wavelengths. Decay of bulb signal (a) and interface signal (b) of ZnSe/CdS when rod-pumped (405 nm) and when interface-pumped (570 nm). Decay of bulb signal (c) and interface signal (d) of CdSe/CdS when rod-pumped (405 nm) and when interface-pumped (570 nm). The bulb and interface electron states for both ZnSe/CdS and CdSe/CdS DIRs are shorter lived when interface-pumped than when rod-pumped. The rod-pumped DIRs are longer lived because electron-hole dissociation occurs, leading to decays with power-law tails, which are fairly pronounced in ZnSe/CdS but relatively small in CdSe/CdS (Figure 4.10). Data were smoothed for presentation.

4.4.4 Comparison of rod, bulb, and interface electron dynamics in CdSe/CdS DIRs as a function of excitation wavelength

Next, we compare the rod, bulb, and interface decays in the CdSe/CdS DIRs as a function of excitation wavelength. In Figure 4.13, CdSe/CdS DIRs are pumped at the rod (405 nm) and interface (570 nm) transitions. Just like ZnSe/CdS DIRs and CdS NRs, when the rod is pumped at 405 nm, electron localization is observed as a partial decay in the rod signal and a corresponding rise in both the bulb and the interface signals (Figure 4.8b, d, Figure 4.13a).[133,160] As in the ZnSe/CdS case, the bulb and interface transitions grow in together. Figure 4.13b shows

the decay of the rod, bulb, and interface signals after localization is complete (~100 ps). Although the decays of the three signals appear to be similar, their functional forms are notably different at long times, as they are in the case of ZnSe/CdS. We showed in Figure 4.8 above that the rod decay has an exponential tail while the bulb decays more slowly with a power-law tail. The interface also exhibits a power-law decay at long times (Figure 4.9, Figure 4.10). We again see evidence of a long-lived charge-separated state in which the electron localizes to the bulb while the trapped hole is left behind on the rod. The bulb and interface decays do not quite overlap at long times (Figure 4.9b). This is similar to the case of ZnSe/CdS (Figure 4.11b, Figure 4.9a), but not as pronounced, and again is likely due to the presence of both uniform and non-uniform CdSe/CdS DIRs in the sample as discussed later in the text.

When the CdSe/CdS DIR sample is pumped at 570 nm, only the interface transition is low enough in energy to be excited (Figure 4.6). Yet, in addition to the expected instantaneous rise of the bulb and interface signals (which share an electron state), we also observe a bleach signal from the rod transition (Figure 4.4g, Figure 4.13c, d, Figure 4.5e). The rod signal appears quickly and then undergoes a slow rise until ~100 ps. Concurrent with this rise the bulb and interface signals undergo a partial decay (Figure 4.13c). The partial decay of bulb and corresponding rise of the rod suggests that population transfer from the bulb to the rod occurs in this sample. This behavior has been previously observed in TA of CdSe/CdS DIRs.[89,133,165] When pumped at the interface, the decays of the rod, bulb, and interface signals are close to overlapping after 1 ns (Figure 4.13d), and are somewhat shorter lived than their respective decays when the rod is pumped (Figure 4.12). Like the case of ZnSe/CdS, electron–hole dissociation enhances the electron lifetime to a greater extent than the reduced wavefunction overlap induced by the quasi type-II band alignment of the interface.

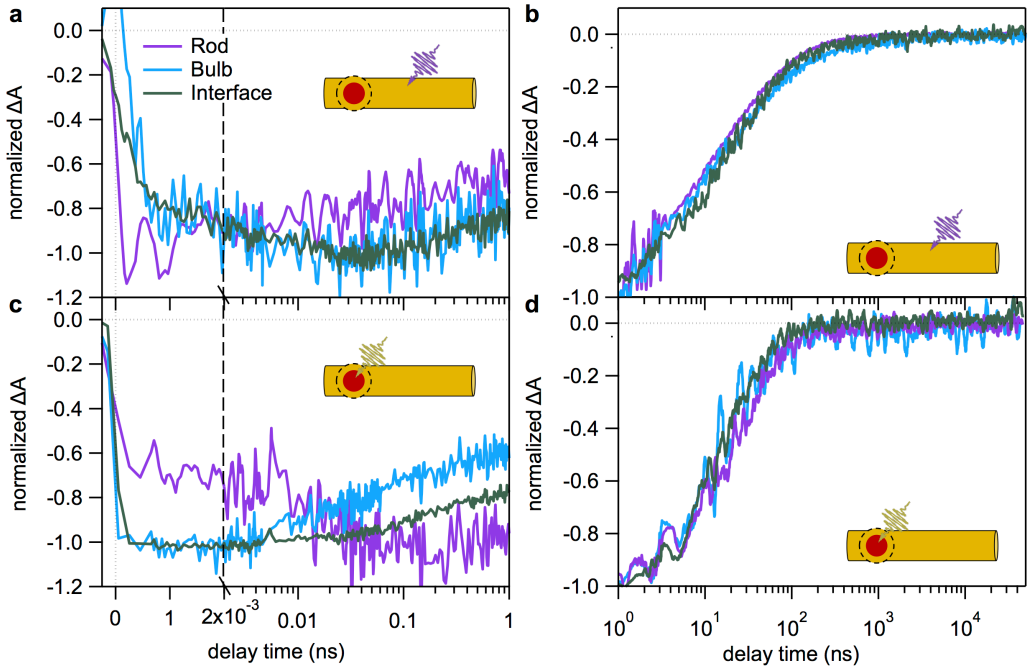

Figure 4.13. TA time traces of CdSe/CdS DIR bleach signals after rod and interface excitation. (a) Rise of CdSe/CdS rod (451–457 nm), bulb (495 nm), and interface (585 nm) bleach features when the rod is pumped at 405 nm, normalized at the maximum signal of each transition. (b) Decays of rod, bulb, and interface signals when rod is pumped, normalized at 1 ns. (c) Rise of CdSe/CdS rod (451–457 nm), bulb (495 nm), and interface (590 nm) bleach features when the interface is pumped at 570 nm, normalized at the maximum signal of each feature. (d) Decays of rod, bulb, and interface when interface is pumped, normalized at 1 ns. Rod data in (a) and (c) and all data in (b) and (d) were smoothed for presentation.

4.4.5 Summary of results

Before proceeding, we summarize the results that are most pertinent to the following discussion of the excited-state dynamics in the three types of NCs studied here. (i) In all three structures (non-uniform CdS NRs, ZnSe/CdS and CdSe/CdS DIRs), when the rod is excited at 405 nm, the rod signal undergoes a partial decay (Figure 4.8b) while the bulb and interface signals rise on the same timescale (Figure 4.8d, Figure 4.11a, Figure 4.13a), corresponding to localization of the electron from the rod to the bulb. The electron localization process observed here is slower than the timescale of hole trapping to the surface of the CdS rod (<1 ps). (ii) After localization, the

decays of the rod signal in the recombination time window follow the same exponential tail for all samples (Figure 4.8c) while the bulb and interface (in the case of ZnSe/CdS and CdSe/CdS) features exhibit a $t^{-1/2}$ power-law tail at long times (Figure 4.8e, Figure 4.9). Surprisingly, the bulb and interface decays do not overlap when the rod is pumped (Figure 4.11b, Figure 4.13b, Figure 4.9, Figure 4.10), but are similar when the interface is pumped (Figure 4.11d, Figure 4.13d). Of all the features, the bulb displays the longest-lived excited state with the largest contribution of this power-law tail in both materials. (iii) In both ZnSe/CdS and CdSe/CdS DIRs, when the interface is pumped, both the bulb and interface lifetimes shorten relative to when the rod is pumped (Figure 4.12), decaying about as quickly as the rod decay (Figure 4.14).

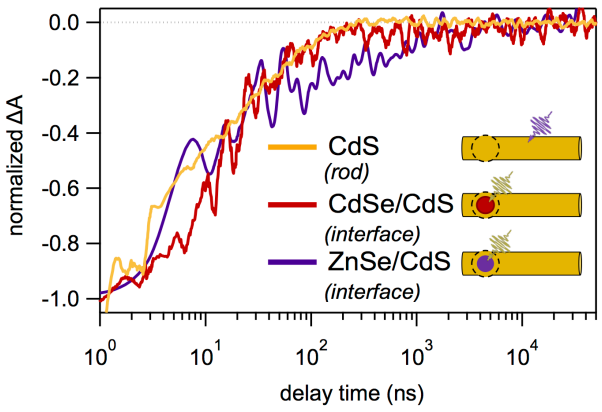

Figure 4.14. Comparison of CdS rod decay when pumped directly with ZnSe/CdS and CdSe/CdS interface decays when the interface is directly pumped. All decays are fairly similar, demonstrating that the lifetime of the interface exciton is not significantly enhanced compared to the recombination of a conduction-band electron with a trapped hole when they are overlapping in the same region of the nanostructure (i.e., in the rod). While the interface exciton of ZnSe/CdS DIRs here decays slightly slower than the other nanocrystals around 100 ns, the charge separation between a rod-trapped hole and bulb-localized electron still leads to an exceptionally long-lived state that overshadows what is achieved with the staggered band alignment of the interface. Data were smoothed for presentation.

4.4.6 Critical role of electron–hole dissociation in the photophysics of CdS, ZnSe/CdS, and CdSe/CdS samples

Our examination of the excited-state dynamics of the CdS regions of CdS NRs and ZnSe/CdS and CdSe/CdS DIRs revealed remarkable similarities in the kinetics of electron localization and recombination in all three samples, after excitation of the CdS rod (Figure 4.8). For both the initial partial rod decay and the corresponding rise of the bulb, the TA kinetics, and therefore electron dynamics, are nearly the same in all three structures Figure 4.8b, d). This indicates that electron localization from the rod to the bulb in these structures is not strongly affected by the differences in the energy levels of the seed. This is consistent with the previous finding in CdSe/CdS DIRs that the efficiency of exciton localization to the bulb does not depend on the details of the seed and bulb energetics, but rather the rod length and hole-trapping rate.[89] The kinetics of electron trapping and recombination with a trapped hole in the uniform rods are also nearly identical in all three samples, as demonstrated by the overlapping rod decays in Figure 3.2c. This indicates that when the hole is trapped on the rod surface, the behavior of an electron in the conduction band of the CdS rod is not strongly influenced by the seed. Finally, the bulb decays for the different materials exhibit the same $t^{-1/2}$ power-law tail (Figure 4.8e). This suggests the same non-exponential decay mechanism in CdS NRs and the DIRs alike, namely trapped-hole diffusion limited recombination.[64] Taken together, these findings show that the dynamics of charge carriers in the CdS components of the DIR heterostructures after the rod is excited are similar regardless of the composition of the seed. This points to the critical role of hole trapping, which competes with localization of the hole to the seed, as well as nanostructure morphology, in determining the photophysical behavior of these structures. Below, we elaborate

on the role of hole trapping and morphology in the dynamics of the CdS components in the three materials.

We first elaborate on the evidence for the dissociation of electrons from trapped holes in non-uniform DIR heterostructures. When the rod is pumped, a slowly decaying $t^{-1/2}$ power-law tail is observed for both the interface and bulb signals in all three samples (Figure 4.8e, Figure 4.9, Figure 4.10). This long-lived state has previously been reported in non-uniform CdS NRs when a charge-separated state forms due to the electron localizing to the bulb while the hole stays trapped at the rod surface.[64] We expect similar behavior to occur in the DIRs because the composition, dimensions, non-uniform morphology, and surface chemistry of the CdS components are similar in all structures. The electron localizes to the bulb over tens of picoseconds and the process is not complete until 100 ps in these structures,[64] much slower than the <1 ps hole trapping we observe, suggesting that electron–hole dissociation occurs in these DIRs. This charge separation picture is further supported by the remarkably long-lived bulb state formed after rod excitation, compared to interface excitation (Figure 4.12). The difference between these two excitation wavelengths is only in the resulting location of the hole, as shown in Figure 4.15.[64] This scheme shows the excited-state configurations that impact the dynamics of DIRs. For simplicity, the carriers are shown as filled and empty circles for electrons and holes, respectively, with the understanding that, unless trapped on the surface, they are delocalized over the region that they occupy in the structure.

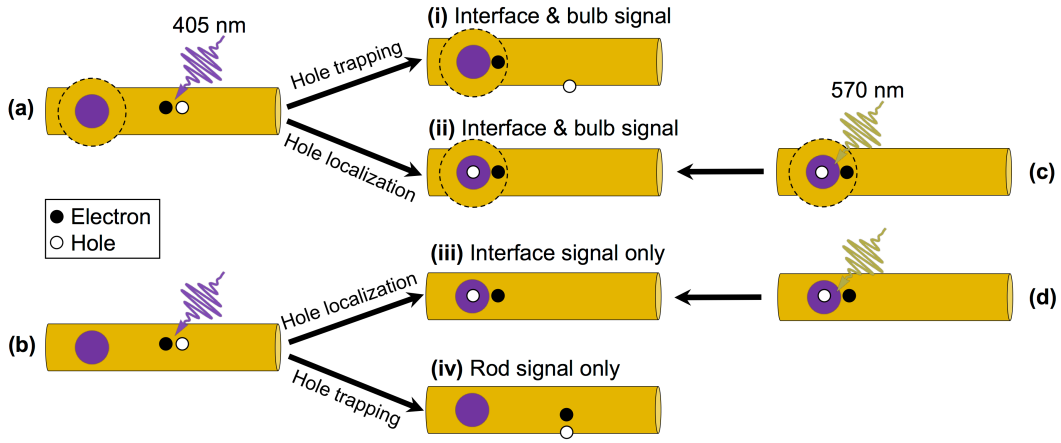

Figure 4.15. Schematic depiction of excited states in non-uniform dot-in-rod heterostructures. Configurations of electrons and holes in DIR heterostructures of both uniform and non-uniform morphologies when (a–b) pumped at the rod (405 nm) or (c–d) pumped at the interface (570 nm).

Exciting the rod can lead to electron–hole dissociation (Figure 4.15i) in non-uniform structures, while exciting the interface produces an interface exciton with small but still significant overlap of the electron and hole wavefunctions (Figure 4.15ii). The observed difference in bulb decay kinetics between the case of rod-pumping and interface-pumping (Figure 4.11b, d, Figure 4.13b, d, Figure 4.12), coupled with the fast hole trapping measured in all samples and relatively slower electron localization, strongly suggests that dissociation occurs, just like in CdS NRs. We note that the excited state shown in Figure 4.15ii can also contribute to the bulb decay, but will not have a $t^{-1/2}$ power-law tail. When charge separation occurs with high efficiency, we expect a strong contribution from the power-law, as is the case in the ZnSe/CdS DIRs here (Figure 4.8e, Figure 4.9). If instead the electron and hole co-localize in the seed/bulb in a significant fraction of the nanostructures, we expect a smaller amplitude of the power-law tail and a larger contribution from exponential recombination, as is the case in the CdSe/CdS DIRs studied here (Figure 4.8e, Figure 4.9). The CdSe/CdS structures have larger bulbs (Figure 4.1) and a significant contribution from direct absorption into the bulb may explain the smaller power-law contribution. The slow power-law decay is also observed in the interface

signal after the rod is pumped (Figure 4.9, Figure 4.10). This is because in non-uniform DIRs the interface and bulb share an electron state, so the interface signal that arises after the rod is excited reports on the recombination of the bulb electron with the trapped hole on the CdS rod. This analysis leads us to propose that it is the charge-separated state (Figure 4.15i) that causes the interface signal of these DIRs to be long lived following rod excitation, rather than the reduced wavefunction overlap caused by band alignment at the interface. Altogether, our data suggest that features such as non-uniform morphology and fast hole trapping in NRs can yield lifetime enhancement well beyond what is achieved with staggered band alignment at the interface of these DIR heterostructures.

4.4.7 Factors that determine charge-carrier dynamics in DIRs

While the bulb and interface features in both ZnSe/CdS and CdSe/CdS DIRs have been shown to share the same electron state, they can exhibit different recombination dynamics, as observed here.[133,160] The TA signal is sensitive only to the electron population, so no matter how the bulb and interface electron population changes—by electron localization from the rod, recombination with a trapped hole, recombination with a seed hole, or trapping—the dynamics of the interface and bulb TA decays should be identical. This is only true, however, if every seed is enclosed by a corresponding bulb. Previous investigations of DIR heterostructures have revealed bulb and interface decays that are very different in some cases and the same in others. In the case of CdSe/CdS DIRs, when pumped at the rod, the half-life of the bulb was about twice as long as the interface.[133] But, when pumped at the interface, the bulb and interface had identical decays. In contrast, a different study on ZnSe/CdS DIRs showed that when the rod was pumped, the bulb and interface decayed with the same lifetime.[160] In the samples studied here, the bulb is longer lived than the interface in both ZnSe/CdS and CdSe/CdS DIRs after the rod is excited. However,

both in this study and in previously published work, when the interface is directly pumped, the bulb and interface always have the same decay in both ZnSe/CdS and CdSe/CdS, and are always shorter lived than when the rod is pumped.[133]

We can explain the differences between the bulb and interface decays in ZnSe/CdS and CdSe/CdS DIRs after the rod is pumped with the following hypothesis: because both uniform and non-uniform DIRs are present in the sample, the measured decay behavior is a combination of the behavior of the two populations (Figure 4.15). From the partial decay of the rod signal during the time window of localization (Figure 4.8b), we estimated that 69% of ZnSe/CdS DIRs and 41% of CdSe/CdS DIRs are effectively non-uniform. Just like uniform CdS NRs, uniform DIRs (Figure 4.15b) do not have a bulb for the electron to localize to, and therefore cannot dissociate to form the charge-separated state shown in Figure 4.15i. However, while hole trapping to the CdS rod surface can occur in uniform structures (Figure 4.15iv), it competes with hole localization to the seed, which can cause the electron to localize to the interface due to Coulomb attraction (Figure 4.15iii).[133,160] So, in uniform structures, interface electrons predominantly recombine with seed-localized holes (Figure 4.15iii), but in non-uniform structures interface electrons may recombine with either trapped holes (Figure 4.15i) or seed-localized holes (Figure 4.15ii), the former giving power-law dynamics, the latter yielding a faster decay. The interface decay is therefore shorter lived than the bulb decay when the rod is pumped (Figure 4.11b, Figure 4.13b) because the interface signal in the ensemble measurement includes both uniform and non-uniform structures (Figure 4.15i, ii, and iii), whereas the bulb signal includes only non-uniform structures (Figure 4.15i and ii). However, when the interface is pumped (Figure 4.15c, d), holes are generated directly in the seed, and recombination of a seed hole with a bulb or interface electron should be nearly the same in uniform and non-uniform

DIRs alike. Therefore, the bulb and interface decays are the same when the interface is pumped (Figure 4.11d, Figure 4.13d).

We isolate the contribution of interface decay from uniform structures with further analysis of the TA data. Since the interface and bulb share the same electron state in non-uniform DIRs, we assume that the decay of the interface signal in non-uniform DIRs is identical to the decay of the bulb signal, both of which are primarily due to recombination between the charge-separated carriers and have power-law tails when the rod is excited. In terms of Figure 4.15, the total interface signal after rod excitation is composed of the structures in Figure 4.15i, ii, and iii, while the bulb signal is composed of only the structures in Figure 4.15i and ii. Therefore subtracting the bulb signal from the interface signal leaves only signal from structure Figure 4.15iii—the interface signal of uniform DIRs. To isolate this signal, the bulb and interface decays after 405 nm excitation were normalized to overlap around 1–400 μs, the time window in which the long-lived charge separated state dominates the signal compared to interface excitons. Then the bulb decay was subtracted from the interface decay to yield the interface decay of uniform DIRs. The resulting decay traces of the interface signal of the uniform structures are plotted in Figure 4.16 and compared to the decays of the bulb and interface after interface excitation. The uniform interface signal after rod excitation should have similar decay kinetics to the bulb and interface decays after interface excitation because in both cases the electron and hole should not dissociate; an interface exciton should form both after excitation of the interface in non-uniform DIRs (Figure 4.15a to Figure 4.15ii) and after rod excitation in uniform DIRs (Figure 4.15d to Figure 4.15iii). The extracted decays of the interface electron in uniform structures in Figure 4.16 are in excellent agreement with the DIR decays after interface excitation for both ZnSe/CdS and CdSe/CdS. This analysis demonstrates that the origin of the

differing decay kinetics of the bulb and interface after rod excitation are due to different morphological subpopulations in the ensemble of DIRs.

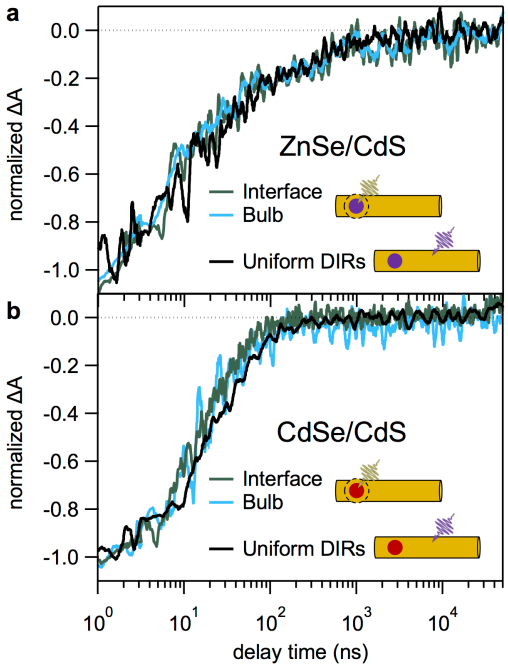

Figure 4.16. Extracted decay kinetics of the interface electron in uniform DIRs of **a** ZnSe/CdS and **b** CdSe/CdS compared to bulb and interface decay traces after interface excitation (570 nm pump). Decay traces are shown for the 1 ns to 50 μs time window on a logarithmic time axis and normalized at 1 ns. Data are smoothed for presentation.

It is also possible that the differing bulb and interface decays originate in part from a subpopulation of nanostructures in which there are bulbs that do not surround a ZnSe or CdSe seed. DIRs with at least two bulbs are apparent in the TEM images (Figure 4.2). Such DIRs would give rise to different bulb and interface electron states within the same structure; therefore, they do not need to have the same decay kinetics. These structures may also contribute to the differing bulb and interface dynamics we observe in a way that is similar to the contributions from uniform DIRs explained above. The current experiments cannot distinguish between these two scenarios, and Figure 4.16 is consistent with this second hypothesis as well. It is likely that

all of the subpopulations (uniform, non-uniform with one bulb, and non-uniform with multiple bulbs) contribute to the decay as they are all present in the TEM images.

Finally, we consider the structural factors that contribute to the recombination dynamics observed in each particular sample. The non-uniform width of the structures described here is commonly observed for CdS NRs, and CdSe/CdS and ZnSe/CdS DIRs.[124,130,133,160,165,173,179,180] Having both uniform and non-uniform structures in a sample opens up the possibility for the bulb and interface decays to be different when the rod is excited; in non-uniform structures the bulb and interface share an electron state while in uniform structures there is only the interface state. If hole localization to the seed is efficient, then bulb and interface decays will be similar because in both uniform and non-uniform structures the interface/bulb electron will primarily recombine with a seed-localized hole (Figure 4.15ii and iii). If hole trapping to the rod is more efficient, as in our work, the structure in Figure 4.15i will dominate the decay of the non-uniform structures, resulting in a slow $t^{-1/2}$ power-law. However, the structure in Figure 4.15iii will still contribute to the interface decay, making the interface decay occur more quickly than the bulb. Thus the observed excited-state dynamics depend on both the competition between hole trapping to the rod and hole localization to the seed and the relative fractions of non-uniform and uniform DIRs. More broadly, the exact behavior of a particular sample is determined by particle morphology, the fraction of uniform and non-uniform structures in the sample, rod length (which determines localization rate),[89] the relative volume of the bulb and rod, and ligand properties and coverage (which govern hole trapping), all of which may vary from sample to sample. For example, when our ZnSe/CdS and CdSe/CdS DIR samples are passivated with the native phosphonic acid ligands, the bulb and interface signals decay somewhat differently than in the thiol-capped samples described in this chapter (Figure 4.17). The power-law tail is still present in

each of the decays but exhibits different relative amplitudes with the different ligands. Furthermore, compared to the efficient electron–hole dissociation observed in our structures, samples with shorter rod lengths or different surface-capping ligands could have more efficient hole localization to the seed and thus the power-law component may not be as prominent.[89,133,160] Overall, our work suggests that each sample of these types of heterostructures can exhibit different excited-state relaxation behavior depending on the structural details of these complex nanostructures. However, the intricate dynamics that manifest for a given sample can be broken down and understood in terms of the relaxation pathways described here. The specific morphological distributions and surface chemistry of a particular sample only determine the relative contributions of each relaxation pathway.

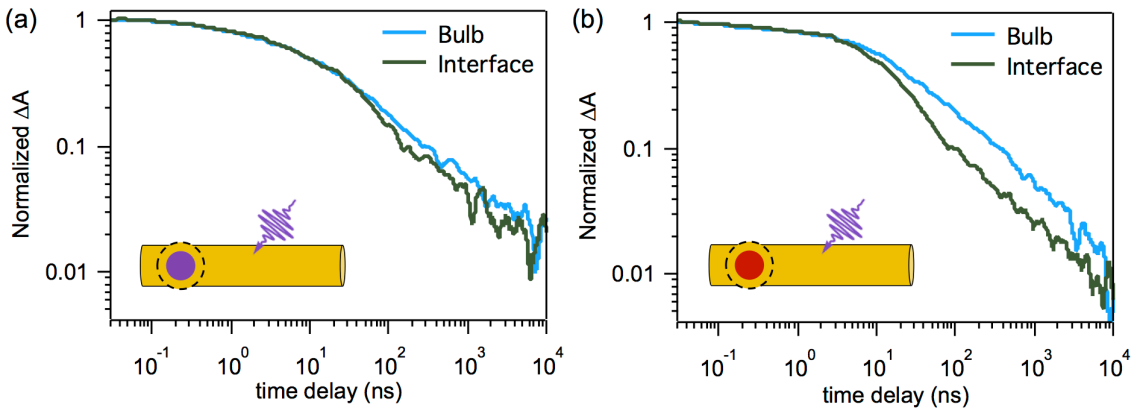

Figure 4.17. TA time traces with native ligands. TA time traces of the bulb and interface decays of (a) ZnSe/CdS DIRs and (b) CdSe/CdS DIRs with native octadecylphosphonic acid (ODPA) ligands after excitation at 405 nm. Data are normalized at the maximum signal of each transition and presented on a log-log scale from 30 ps to 10 μs. (a) For ZnSe/CdS, the bulb and interface signals were probed at 492 nm and 535–545 nm, respectively. (b) For CdSe/CdS, the bulb and interface signals were probed at 499–503 nm and 585 nm, respectively. Data were smoothed for presentation.

4.4.8 Implications of long-lived charge separation for photophysics and photochemistry

Semiconductor heterostructure NCs are designed to control the locations of the photoexcited electron and hole within a NC, and thus control their excited-state dynamics, via energy level alignment. In type-II and quasi type-II structures, staggered band alignment is designed to separate charges so that the photoexcited electron localizes in the conduction band of one semiconductor and the hole resides in the valence band of the other. This can extend the excited-state lifetime of the interface transition because the electron and hole wavefunction overlap is reduced. Core/shell heterostructures of this type have been shown to exhibit extended excited-state lifetimes at room temperature (40–400 ns) compared to the lifetimes of structures that have more significant wavefunction overlap, such as bare quantum dots or type-I heterostructures (1–20 ns).[96,113,152,153,156,158,159,161,164,184] However, in CdS NR-based structures, hole trapping is fast and efficient and the electron can dissociate from the hole and localize to the bulb, leading to a variety of excited state configurations (Figure 4.15). Even without dissociation, such as the case of electrons in CdS rods, hole trapping intrinsically leads to extended lifetimes (~60 ns) caused by reduced wavefunction overlap between a delocalized conduction-band electron and a trapped, rather than valence band, hole.[23,65] So, there is reduced electron–hole wavefunction overlap both in the case shown in Figure 4.15iv (surface trapped hole and rod electron) and for the interface excitons in Figure 4.15ii and iii. Thus, when the hole is prepared in the seed by directly pumping the interface transition, the lifetime of the interface decay is similar to the rod decay of CdS NRs (Figure 4.14), which in turn overlaps the rod decay of ZnSe/CdS and CdSe/CdS DIRs (Figure 4.8c). Significantly, neither the rod electron nor the interface exciton is the longest-lived state in either DIR sample. Instead, it is the electron–hole dissociation between a rod-trapped hole and a

bulb-localized electron that produces the longest-lived, charge-separated excited state (Figure 4.15i).

DIR nanoheterostructures, particularly CdSe/CdS, have demonstrated superior quantum yields when used in nanocrystal–catalyst complexes for solar-fuel production compared to CdS NRs, CdSe/CdS core/shell QDs, and bare CdSe or CdS seeds.[47,107-109,111] When electron transfer (ET) to an electron acceptor or a reduction catalyst is much faster than the electron–hole recombination in the nanocrystal, increases in the NC lifetime by use of heterostructures will not significantly improve the ET efficiency.[47,111] However, heterostructures still excel in their photochemical activity compared to single-component nanostructures because of the slower rate of recombination that occurs after ET, i.e., the recombination between the electron in the acceptor with the hole in the nanocrystal.[47,111] In DIRs, this recombination becomes inefficient when holes localize to the seed, spatially separating from the electron in the acceptor.[47,107,111,112,118,144,180,185] Therefore, in systems where recombination after ET needs to be mitigated, the primary consideration is to have the hole efficiently localize a large distance from the acceptor. However, in systems with relatively slow ET, such as complexes of NCs with enzymes for photochemical H_2 production and N_2 fixation,[24,44-46,65] ET directly competes with electron–hole recombination, and nanostructures should be designed to have the longest excited state possible in order to achieve efficient ET. As we show here, the separation of charges after rod excitation caused by hole trapping to the rod surface and electron localization to the bulb provides remarkably long-lived excited states. In this regard, the modest lifetime enhancement granted by the type-II band alignment is overshadowed by the long-lived charge-separated state that occurs intrinsically in the non-uniform nanostructures studied here (Figure 4.15i). However, while the electrons localized in the bulb are longer-lived than the rod electrons, they are also

lower in energy and sample less of the NC surface and therefore have lower proximity to electron acceptors. It remains to be seen how this tradeoff between lower driving force for ET, reduced acceptor proximity, and slower electron–hole recombination affects the overall ET efficiency and photochemical quantum yields.

4.5 Conclusions

We have examined the excited-state dynamics of ZnSe/CdS and CdSe/CdS heterostructure DIRs compared to their single-material counterpart, CdS NRs. The fact that the dynamics of electrons in the CdS rod and bulb regions do not strongly depend on the seed material in these samples points to the critical role of hole trapping and morphology as the drivers of charge carrier dynamics. The timescale of recombination of an interface exciton in DIRs is notably similar to electron–hole recombination on the CdS rod. While both of these excited states are longer lived than excited states in bare quantum dots or type-I core/shell heterostructures, the type-II or quasi type-II band alignment between the dot and the rod does not significantly extend the excited-state lifetime compared to the single component CdS NRs. Instead, the electron–hole dissociation caused by fast trapping of the hole to the CdS rod surface and electron localization to the bulb generates the longest-lived charge-separated state in these structures. We propose that the features critical to achieving such long-lived excited states are the surface chemistry and non-uniform morphology, which together can cause hole trapping in the rod to out-compete hole localization to the seed and drive the electron to dissociate and localize to the bulb. Therefore, the excited-state behavior of a particular DIR sample is governed by structural features of the particles including, but not limited to band alignment. These features offer multiple layers of

control for tailoring the excited-state dynamics of nanostructures and their use in photochemical systems.

Chapter 5

Trapped-hole diffusion in photoexcited CdSe nanorods‡

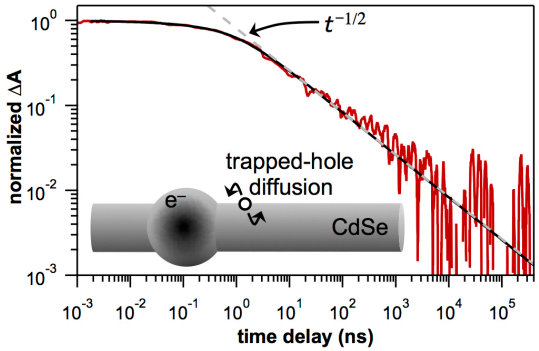

5.1 Abstract

Surface charge-carrier traps are ubiquitous in colloidal semiconductor nanocrystals and fundamentally impact excited-state relaxation, making it critical to understand both their nature and their dynamics. Here, using photoluminescence upconversion and transient absorption spectroscopy, we study hole trapping and the dissociation between electrons and trapped holes in non-uniform CdSe nanorods and monitor their subsequent recombination dynamics. The recombination following spatial separation of an electron and a trapped hole is described well with a diffusion–annihilation model wherein the trapped hole undergoes a random walk on the nanocrystal surface until it encounters the electron. This model fits the non-exponential excited-state decay over more than seven orders of magnitude in time with a single adjustable parameter. The observation of trapped-hole diffusion in CdSe nanostructures extends our fundamental understanding of excited-state dynamics in this important class of materials by revealing the spatial dynamics of trapped holes. The surface motion of trapped holes may have important implications for optoelectronic applications that rely on charge transport and charge transfer.

---

‡Adapted with permission from Utterback, J. K., Hamby, H., Pearce, O. M., Eaves, J. D., and Dukovic, G. *J. Phys. Chem. C*, **2018**, *122*, 16974-16982. (Copyright © 2018, American Chemical Society)

5.2 Introduction

The surfaces of colloidal semiconductor nanocrystals (NCs) are complex environments where atoms can be under-coordinated and the NC core interfaces with surface-passivating ligands and the solvent. NC excited-state relaxation is extremely sensitive to their surface coordination and the surroundings.[41] Surface traps, typically associated with under-coordinated surface atoms or redox-active ligands, are ubiquitous in semiconductor NCs.[26,52,62,67-75,186] In CdS and CdSe NCs, hole traps are associated with undercoordinated chalcogen species (S or Se) and are particularly pervasive.[52,68,69,74,76] Hole trapping is often a dominant relaxation pathway that occurs on the timescale of picoseconds in both CdS and CdSe NCs,[23,37,52-60] leading to localized holes at surface chalcogen species.[74,76,78,79] Trapped holes play important roles in the photophysics and photochemistry of these materials, affecting, for example, photoluminescence (PL) dynamics and hole transfer to electron donors on the NC surfaces.[68,76,79-83,85,98] Even when a shell of CdS decreases the extent of hole trapping in a CdSe NC, oxidation of a surface-adsorbed species can be mediated by hole traps on the surface of the CdS shell.[83,85,98] Thus, it is important to better understand the nature and behavior of trapped holes in this class of nanocrystals. In particular, because trapped holes are associated with localized sites on the surface, rather than delocalized in the nanostructure, it is desirable to experimentally probe the spatial aspects of their dynamics.

Recently, we presented evidence that trapped holes undergo a diffusive random walk on the surfaces of CdS nanorods (NRs) at room temperature, and hypothesized that these holes hop with a step size on the order of inter-atomic distances.[64] This conclusion arose from modeling of dynamics of recombination between spatially separated electrons and trapped holes, measured by transient absorption (TA) spectroscopy, as a one-dimensional diffusion-annihilation process. Subsequent theoretical work on CdS has found direct evidence in support of this model, where

holes form small polarons located in the orbitals of surface-exposed S atoms that then undergo diffusion by thermally-activated hopping.[186] The nature of hole trap states in CdSe NCs is similar to those in CdS NCs in that they are localized on under-coordinated chalcogenide atoms,[52,68,74,76] have similar energetics,[69,79] and the surfaces in both materials have similar geometries, lattice structure and atomic spacing. This, together with previous observations that hole trapping occurs with similarly fast rates and high efficiencies in both materials,[64] prompted us to examine whether the trapped-hole diffusion occurs in CdSe NCs as well.

In this chapter, we show evidence that trapped holes in CdSe NRs are indeed mobile. Using femtosecond PL upconversion and ultrafast TA spectroscopy, we study the excited-state dynamics of CdSe NRs on the timescales of ~100 fs to ~100 μs. In CdSe NRs that are non-uniform in diameter, we find that holes trap on a ~1 ps timescale and electrons dissociate from them in under 20 ps as they localize to wide-diameter regions of the nanostructures with lower quantum confinement. The resulting spatially-separated state, monitored by TA spectroscopy, decays as an inverse square-root in time over five orders of magnitude in time. In the absence of charge separation, on the other hand, electrons and trapped holes recombine with an exponential tail. We model the recombination of the charge-separated state as a one-dimensional diffusion–annihilation process wherein the trapped hole diffuses along the length of the NR until it encounters the electron. This model fits the TA signal decay over more than seven orders-of-magnitude in time and four orders-of-magnitude in amplitude, with a single adjustable parameter related to the diffusion coefficient. The experimental data and model point to a slow diffusion process, with a diffusion coefficient within range of what is seen for trapped carrier motion in other semiconductors.[64,142,143] The details of the diffusion model suggest that the motion occurs with small steps, on the order of interatomic distances, consistent with recent theoretical

predictions in CdS.[186] The motion of trapped holes described here is a potential pathway for transporting trapped charges in light-driven applications.

5.3 Methods

5.3.1 Nanocrystal preparation and characterization

This synthesis was adapted from a previously reported procedure and is described in Chapter 2.[126] The native nanocrystal surface ligands were exchanged for 3-mercaptopropionic acid (MPA) ligands according to previously published work on CdS NRs.[44] MPA-capped particles were dispersed in 12.5 mM Tris Buffer at pH 7. Transmission electron micrograph (TEM) samples were prepared by drop-casting CdSe NRs with native ligands onto TEM grids (300 mesh copper grids with carbon film, Electron Microscopy Science). TEM images were taken on a FEI Tecnai Spirit BioTwin operating at 120 kV and equipped with a side-mount AMT (2k × 2k) CCD. The dimensions of the CdSe NRs were determined by measuring about 200 particles in TEM using ImageJ software.[129]

5.3.2 Spectroscopy

The sample used for UV-visible absorption and PL spectroscopy contained CdSe NRs capped with MPA ligands, dispersed in buffer solution at an optical density of 0.1 at the absorption band edge, and were sealed under Ar in a 1 cm x 1 cm quartz cuvette. The photoluminescence spectrum was collected by exciting the sample at 600 nm and the emission was recorded at 90° relative to the excitation. The emission spectrum was corrected for wavelength dependence of the instrument response.

The TA experimental setup was previously described in detail and in Chapter 2.[116] TA experiments were performed on a sample of CdSe NRs with MPA ligands in 12.5 mM Tris-HCl

buffer (pH 7) at an optical density of ~1 at the absorption band edge. The samples were sealed under Ar in 2 mm quartz cuvettes equipped with Kontes valves at room temperature. A magnetic stirrer continuously stirred samples during data collection. The pump was focused into the sample with a beam waist of ~250 μm with a pulse energy of 7 nJ/pulse for 600 nm excitation and 150 nJ/pulse for the 745 nm excitation. The pump power was chosen so as to be in a regime where the CdSe NR decay kinetics were independent of pump power and did not have signals from excitation of multiple electron-hole pairs.[114]

PL upconversion spectroscopy was performed using a Halcyone MC multichannel fluorescence upconversion spectrometer as described in Chapter 2. PL upconversion experiments were performed on a sample of CdSe NRs with MPA ligands in 12.5 mM Tris-HCl buffer (pH 7) at an optical density of ~1.2 at the absorption band edge. The sample was excited at 600 nm and the emission was passed through a 660 nm long-pass filter. The samples were sealed under Ar in 2 mm quartz cuvettes equipped with Kontes valves. A magnetic stirrer continuously stirred samples during data collection. The pump beam was focused onto the sample with a beam waist of ~23 μm and the pump power of 1 nJ/pulse. While the system is capable of spectrally resolving the decay by rotating the upconversion crystal during data acquisition, the crystal was held fixed to maximize the signal. Still, the PL upconversion spectrum is in good agreement with the steady-state emission spectrum, indicating that both rod and bulb emission peaks were collected.

5.4 Results and Discussion

5.4.1 Electronic structure and spectra of non-uniform CdSe nanorods

The synthesis of rod-shaped nanocrystals often results in particles that are non-uniform in diameter.[64,130,133,160,173,177] The impact of such non-uniform diameters on electronic structure and excited-state dynamics has been described in detail for CdS nanorods and dot-in-rod heterostructures.[64,130,133,160,173,177] These non-uniform nanostructures are described as having two morphological features along their lengths: narrow-diameter cylindrical rods and wide-diameter spherical bulbs.[64,160,177] The larger diameter of the bulb causes a decrease in quantum confinement, resulting in lower transition energy compared to the rod. Wu *et al*. performed a systematic study on CdS NRs with varying degrees of non-uniformity and showed that the rod and bulb constitute distinct electronic states that can both be observed in steady-state absorption, PL and TA spectra.[130] Moreover, they established that the bulb electronic state could not be attributed to sub-band gap transitions, such as an Urbach tail. In prior work, we used non-uniform CdS nanorods to probe the spatial dynamics of trapped holes.[64] To examine trapped-hole dynamics in CdSe nanostructures, we synthesized CdSe nanorods of non-uniform width using a procedure described in Chapter 2. Transmission electron microscopy (TEM) images of the resulting sample show a mixture of structures that are effectively uniform and non-uniform (Figure 5.1a). The rods of uniform and non-uniform NRs have average diameters of 8.1 ± 0.8 nm while the bulbs of the non-uniform NRs have average diameters of 9.6 ± 1.2 nm. The average lengths of the NRs in the sample are 39 ± 4 nm. Due to the difference in quantum confinement in the radial direction, the non-uniform structures effectively have a type-I band alignment where the carrier energies are lower in the bulb (Figure 5.1b). Similar to non-uniform CdS nanorods,[64,130] neither the lowest-energy absorption transition nor the band-gap PL spectrum

(Figure 5.1c) can be fit with a single Gaussian peak and instead both exhibit an additional lower-energy peak underlying the primary peak (Figure 5.2). These spectral features, as well as the dynamics of electrons in this state discussed below, are analogous to the case of non-uniform CdS NRs, and thus we adopt the assignment of the high- and low-energy peaks in CdSe NRs to transitions in the rod and bulb, respectively.

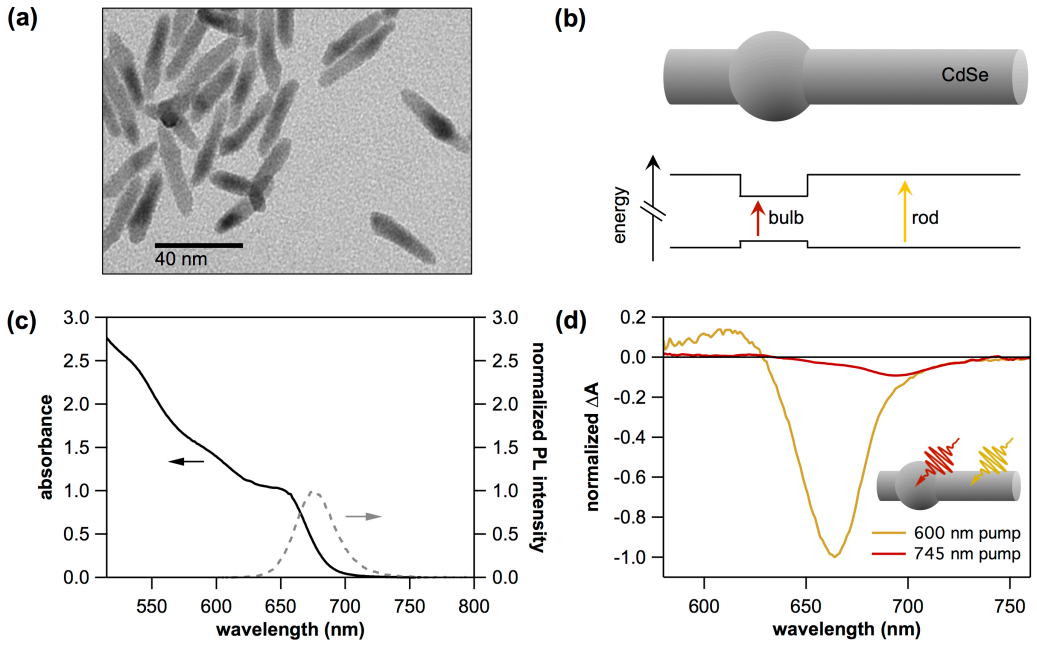

Figure 5.1. Non-uniform CdSe nanorod morphology and optical properties. (a) Representative TEM image of CdSe NRs featuring structures with non-uniform diameters. (b) Schematic depiction of a non-uniform CdSe NR, showing the rod and bulb components and energy-level diagram as a function of position along the NR. The larger diameter of the bulb compared to the rod results in a lower transition energy for the bulb. Energy offsets for the electron (top) and hole (bottom) are drawn to scale for their different effective masses. (c) Absorption and PL spectra of the CdSe NR sample. The PL spectrum was collected under 600 nm excitation. (d) TA spectra of CdSe NRs recorded 1 ns after excitation by 600 nm and 745 nm light. The 745 nm excitation isolates the TA spectrum of the bulb, while the sample excited with the 600 nm pump has both the rod and the bulb features. Spectra are normalized to have the same amplitude at 705 nm.

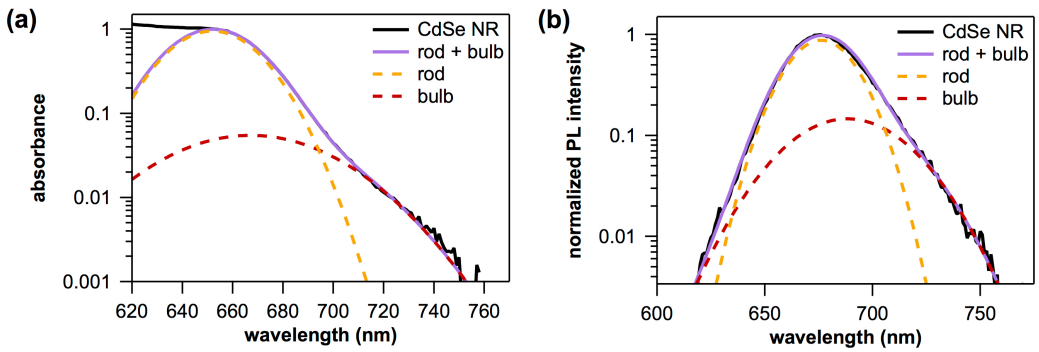

Figure 5.2. Contributions of the rod and bulb transitions to the band-gap absorption and photoluminescence of non-uniform CdSe nanorods. (a) Absorption spectrum and (b) emission spectrum from Figure 5.1 on semi-log axes, fit to the sum of two Gaussian peaks for the lowest-energy rod and bulb transitions. In the absorption spectrum, the rod and bulb peaks are centered at 652 nm and 675 nm, respectively, with a full-width half maximum (FWHM) of 39 nm and 71 nm respectively. In the PL spectra, the rod and bulb peaks are centered at 667 nm and 691 nm, respectively, with a FWHM of 32 nm and 52 nm, respectively.

While the bulb spectral signal can be seen in the absorption and PL spectra of the samples containing non-uniform NRs (Figure 5.2), its presence is most definitively identified in the TA spectra of non-uniform NRs.[64,130] The amplitude of the transient bleach signals of Cd-chalcogenide NCs is proportional to the population of electrons in the conduction band.[114] In this study, we focus on the bleach of the lowest-energy transition of the CdSe NRs, which reports on electron dynamics at the band edge.[40,97,187-190] Optical excitation of CdSe NRs above the band gap at 600 nm primarily excites the rod rather than the bulb because the rod comprises a larger volume fraction of the nanostructure.[25,133,191] The energy offset between the rod and bulb provides a driving force for photoexcited carriers to localize to the bulb. Thus, while the rod transition dominates the absorption spectrum, photoexcited electrons undergo population transfer from the rod to the bulb in non-uniform nanostructures, giving rise to a shoulder from the bulb

signal centered at 694 nm in the TA spectra 1 ns after excitation (Figure 5.1d).[64,130] Alternatively, the bulb can be selectively excited using 745 nm light,[64] which is too low in energy to excite the rod, yielding the pure bulb spectrum (Figure 5.1d). The evolution of the TA spectra over time is shown in Figure 5.3. While the TA spectra collected after 600 nm excitation exhibit a red-shift due to energetically downhill population transfer from the rod to the bulb over time, the TA spectra resulting from direct population of the bulb with 745 nm excitation do not shift, indicating that electrons do not have sufficient thermal energy to undergo uphill transfer from the bulb to the rod.

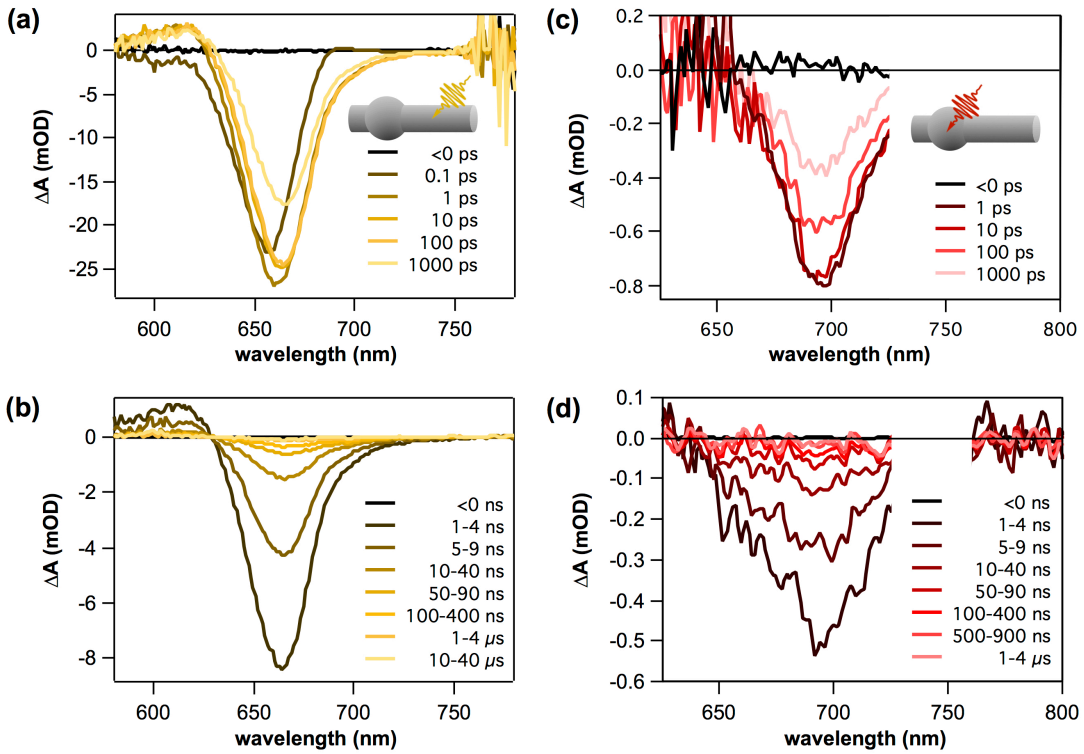

Figure 5.3. TA spectra of CdSe nanorods over 0.1 ps to 40 μs after excitation at 600 nm (a,b) and 745 nm (c,d). Insets show which morphological feature is being excited at each wavelength. The TA spectra after 600 nm excitation undergo an apparent redshift over time, which originates from the relative amplitude changes of the overlapping rod and bulb bleach peaks. In the first few hundred picoseconds, the rod bleach decays while the bulb bleach has a corresponding rise (a). For times around 10 ps and longer (b) both bleach peaks decay but the bulb signal decays more slowly than the rod. In contrast, the spectral shape of CdSe nanorods excited by 745 nm light (c,d) does not change over time because only a single electronic state, the bulb, is populated at all times.

5.4.2 Excited-state dynamics in non-uniform CdSe nanorods

The relative timescales of hole trapping and rod-to-bulb electron localization in non-uniform CdSe NRs allow for charge separation to occur after excitation. Hole trapping in CdSe NCs is known to occur on a picosecond timescale.[52-56,58,59] Because hole trapping dynamics for CdSe nanorods have not been reported in the literature, we directly measured the rate of hole trapping in our CdSe NRs using femtosecond PL upconversion. While the TA bleach signal of Cd-chalcogenide NCs is proportional only to the electron population, band-edge PL can decay because of relaxation of either the electron or hole and therefore it reports on the dynamics of the shorter-lived carrier.[52,56,57] CdSe NRs were excited at 600 nm and the intensity of the upconverted emission, collected over the rod and bulb transitions, was monitored over time (Figure 5.4a). The PL decay is dominated by a 1.0 ± 0.2 ps component. Similar behavior has previously been observed in PL upconversion studies of CdSe quantum dots and the ~1 ps component was assigned to hole trapping.[52-55] Our data are consistent with that assignment.

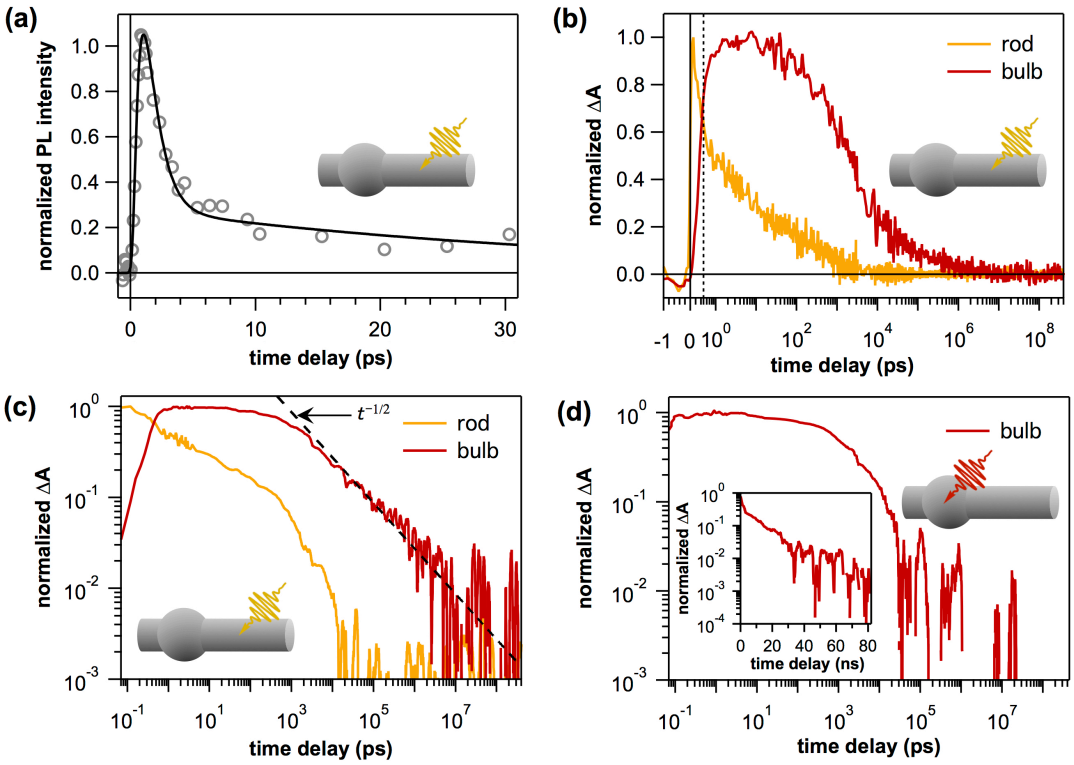

Figure 5.4. Excited-state dynamics in non-uniform CdSe nanorods. (a) PL upconversion signal of CdSe NRs excited with 600 nm light and detected across the band-gap emission spectrum. The PL decay is fit with a double exponential function with time constants of 1.0 ± 0.2 ps (86 ± 3 %) and 37 ± 6 ps (14 ± 3 %). (b) TA time traces of CdS NRs after 600 nm excitation, monitored at the rod (631 nm) and bulb (707–725 nm) bleach transitions. Traces are normalized to have maximum amplitudes of 1. The time axis is linear for the first 0.3 ps and logarithmic thereafter. (c) TA time traces from (b) plotted on a log-log scale, demonstrating the presence of the $t^{-1/2}$ power-law decay of the bulb signal. (d) TA time traces of CdSe NRs when the bulb is selectively excited at 745 nm. The power-law decay is not present when the bulbs are excited directly. The inset shows the same data on a log-linear scale to show the exponential tail. Data have been smoothed for presentation.

We obtain information about relaxation processes occurring after hole trapping from TA spectroscopy. As in the case of CdS nanorods, the dynamics of electrons in the rod and bulb states can be isolated from each other through judicious choice of wavelengths monitored in the TA spectra.[64] We isolate the pure bulb bleach signal by monitoring the low-energy side of the spectrum (707–725 nm) and we extract the pure rod bleach signal at a wavelength where the bulb TA spectrum crosses zero (631 nm). In Figure 5.4b the time-dependent populations of electrons

in the rod and bulb after 600 nm excitation are shown out to 400 μs. All of the bleach time traces in Figure 5.4 are normalized to positive values. The rod and bulb states exhibit different excited-state dynamics. The rod signal undergoes an initial partial decay while the bulb signal has a corresponding rise. This behavior reflects electron population transfer from the rod to the bulb, much like rod-to-bulb localization in non-uniform CdS NRs and CdS NR-based dot-in-rod heterostructures, as well as branch-to-core localization CdSe tetrapods.[64,89,130,133,160,177,191] The remaining rod signal is composed primarily of uniform NRs. The rise of the bulb signal has an average lifetime of 3 ± 1 ps and does not appear to be complete until ~20 ps. The combination of the TA and PL upconversion results suggests that photoexcited holes can trap before they reach the bulb and that charge separation occurs when the electron localizes to the bulb. Further evidence for this charge separation comes from the excitation-wavelength dependent decay dynamics, as discussed below.

After electron localization is complete (>20 ps), the decays of the electron populations are dominated by recombination with trapped holes for both the rod and bulb states (Figure 5.4b,c). The electron populations in these two states decay with drastically different functional forms (Figure 5.4c). The rod signal decays faster than the bulb signal and exhibits an exponential tail (Figure 5.4c). In contrast, the bulb decay after charge separation follows a power law with an exponent of –1/2 for over five orders of magnitude in time (Figure 5.4c). The power law is not present when the bulb is selectively excited at 745 nm (Figure 5.4d) and the electron and trapped hole are co-localized in the bulb. Instead, the decay has an exponential tail, seen as a linear decay on a log-linear plot (Figure 5.4d inset), similar to the decay of uniform NRs in Figure 5.4c. Because the bulb signal in non-uniform NRs corresponds to the same electron state for both excitation wavelengths, the difference in decay dynamics must result from the difference in

where the hole traps (rod vs. bulb). This, together with the timescales of hole trapping and electron localization after rod excitation, indicates that charge separation between a bulb-localized electron and a rod-trapped hole causes the slow power-law decay. Below we describe the physical picture of recombination in these scenarios that is consistent with the observed excited-state dynamics.

5.4.3 Mechanisms of electron–hole recombination

The different functional forms of the electron decays in the uniform and non-uniform NRs indicate distinct microscopic mechanisms of recombination when the electron and trapped hole are either co-localized or spatially separated. When the electron and trapped hole are both located in the same region of the nanostructure, as is the case in uniform NRs (Figure 5.5a) and in non-uniform NRs when the bulb is directly excited (Figure 5.5b), the spatially overlapping carriers can recombine directly. This results in decays with exponential tails as is commonly observed in CdSe NRs[189,190,192,193] as well as other Cd-chalcogenide NCs.[35,37,58,64,72] In contrast, when the electron and trapped hole are spatially separated, recombination occurs more slowly with a $t^{-1/2}$ power-law tail, where t is the time delay (Figure 5.5c). This behavior mirrors what has previously been found in non-uniform CdS NRs, where the $t^{-1/2}$ power law was identified as a signature of trapped-hole diffusion-limited recombination.[64] Thus our data on CdSe NRs support the following picture in non-uniform structures: after photoexcitation of the rod of a non-uniform CdSe NR, electron–hole dissociation within the nanostructure occurs because of fast hole trapping and morphology-induced band alignment, leaving the hole trapped on the rod and the electron localized in the bulb (Figure 5.5c). After this spatial separation, slow diffusion of the trapped hole along the length of the rod occurs until it encounters the stationary electron in the bulb and recombines with it.

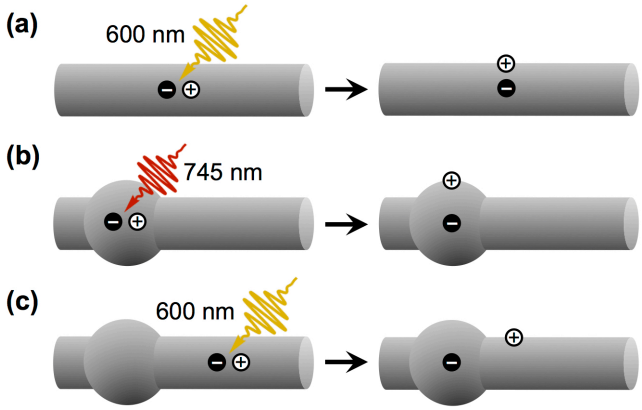

Figure 5.5. Schematic of carrier spatial distribution in photoexcited CdSe nanostructures. In the left-hand column the photons depict which regions of the nanostructure are initially excited and where the charge carriers are generated. The right-hand column depicts the state achieved ~20 ps after excitation but before recombination. (a) Rod excitation of a uniform NR leads to a state in which the electron and trapped hole are both located in the same region of the nanostructure (i.e. the rod). (b) Bulb excitation of a non-uniform NR leads to a state in which the electron and trapped hole are both located in the same region of the nanostructure (i.e. the bulb). (c) Rod excitation of a non-uniform NR leads to a charge-separated state in which the electron is localized in the bulb while the hole is trapped on the rod.

The dynamics of recombination of the bulb electron with a hole trapped on the rod—including the $t^{-1/2}$ power-law tail—can be modeled as trapped-hole diffusion-limited recombination. This diffusion–annihilation model has been described previously and applied to CdS NRs (Chapter 3).[64] Briefly, the trapped hole starts near the bulb and then undergoes an unbiased random walk along the length of the rod, with diffusion coefficient D, until it encounters the electron in the bulb and recombines with it. In that model, the conditional probability density of the trapped hole—the probability of finding it at a distance z from the bulb at time t given that it started at z_0—satisfies the one-dimensional diffusion equation:

$$\frac{\partial}{\partial t}p(z,t|z_0) = D\frac{\partial^2}{\partial z^2}p(z,t|z_0). \tag{5.1}$$

The TA spectroscopy experiment measures the survival probability of the electron in a given state. The conditional survival probability—the probability that the trapped hole has lived for a

time t given that it started at position z_0 such that $p(z,0|z_0) = \delta(z - z_0)$—is obtained by integrating the probability density over space: $S(t|z_0) = \int dz\, p(z,t|z_0)$. We assume that the electron does not decay by any pathway other than recombination and thus the survival probabilities of the electron and the trapped hole are identical. The survival probability used to fit the bulb electron signal was found by solving the diffusion equation on a semi-infinite half line $[0,\infty)$ with a perfectly absorbing boundary condition at the origin ($p(0,t|z_0) = 0$), then finding the conditional survival probability, and then averaging over the initial distribution of trapped holes, $p(z_0)$, which was approximated to be uniform on $0 \leq z \leq \ell$.[64] This model leads to the following formula for the survival probability of electrons in the bulb:[64]

$$S(t) = S_0\left[\sqrt{t/\pi\tau}\left(e^{-\tau/t} - 1\right) + \mathrm{erf}\left(\sqrt{\tau/t}\right)\right], \tag{5.2}$$

where S_0 is a normalization constant and $\tau = \ell^2/4D$. For $t \gg \tau$ this expression follows the $t^{-1/2}$ tail that is the universal asymptotic behavior of one-dimensional diffusion-limited recombination.[137] Figure 5.6 shows a fit of Equation (5.2) to the bulb signal in CdSe NRs after rod excitation and charge separation. The trapped-hole diffusion-limited recombination model fits the data remarkably well for over seven orders of magnitude in time (20 ps to 400 μs) with only a single adjustable parameter, τ (2.15 ± 0.01 ns). In contrast, a fit to the same data using a sum of exponentials requires four exponentials with eight adjustable parameters to yield a comparable reduced chi-squared value, and even then there are clear unphysical oscillations in the residual.

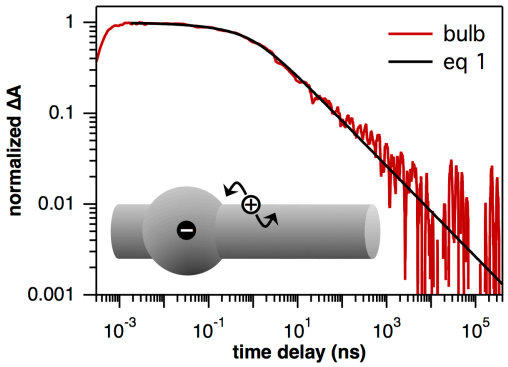

Figure 5.6. Recombination of a bulb-localized electron and a trapped hole modeled as diffusion–annihilation. TA time trace monitored at the bulb transition (707–725 nm) after 600 nm excitation, reproduced from Figure 5.4c. Raw data was fit to the diffusion–annihilation model of Equation (5.2). Data were smoothed for presentation only.

The parameter τ contains key information about trapped-hole diffusion. In terms of the bulb electron decay, τ is approximately equal to the half-life and is a measure of the timescale when the decay transitions into the power-law tail. For the diffusing hole, it is the time at which its mean-squared displacement is $\ell/\sqrt{2}$. In the diffusion–annihilation model of Equation (5.2), τ is determined by the width of the initial hole distribution ℓ and the trapped-hole diffusion coefficient D. While we do not have independent measures of ℓ and D, we can estimate their upper bounds. The finite length of a NR imposes an exponential cutoff to the power-law decay on a timescale of $\sim L^2/D$, where L is the length of the random walk between the bulb and the end of the rod.[64] If ℓ were comparable to L, the survival probability would decay exponentially rather than algebraically.[64] We do not observe this exponential cutoff on the timescale of the measurement ($\sim 10^{-4}$ s) (Figure 5.6), so we can take this time to be a lower bound for L^2/D. Using the mean length of these CdSe NRs (39 nm) as an upper bound for L, we estimate the upper bound of D to be $\sim 10^{-7}$ cm^2 s^{-1}. The estimated upper bound for D and the measured value for τ in turn place an upper bound of ℓ on the order of ångströms. These values are similar to those of CdS NRs.[64] The value of τ for this sample of CdSe NRs (2 ns) is smaller than that of

CdS NRs, which was found to range from about 10 to 100 ns.[64] Functionally, this means that the bulb decay in CdSe NRs transitions to the power-law tail at an earlier time. Without more information, we cannot determine whether τ is smaller for CdSe NRs than for CdS NRs because of differences in ℓ, D, or both.

The diffusion–annihilation model of Equation (5.2) employed an absorbing boundary condition such that the recombination occurs whenever the trapped hole reaches the electron in the bulb. If, instead, a finite number of holes re-engage in the random walk after encountering the bulb at the origin, the boundary is partially absorbing, which is known as the radiation boundary condition of the diffusion–annihilation equation, $\partial p(z,t|z_0)/\partial z|_{z=0} = \kappa p(0,t|z_0)$.[137,194] This boundary condition introduces a new adjustable parameter, κ, with units of inverse length. The left-hand side of this equation is the diffusive flux of the trapped holes out of the bulbs while the right-hand side is the current of recombination with the electron. This is a steady-state condition that accounts for a finite recombination rate by matching these two currents, with κ defining their ratio.[137,194] When $\kappa \to \infty$, one recovers the absorbing boundary.

The conditional survival probability for the partially absorbing boundary is[194]

$$S(t|z_0) = S_0 \left[\mathrm{erf}\left(\sqrt{{z_0}^2/4Dt}\right) + e^{\kappa z_0} e^{D\kappa^2 t} \mathrm{erfc}\left(\sqrt{{z_0}^2/4Dt} + \sqrt{D\kappa^2 t}\right)\right]. \tag{5.3}$$

Equation (5.3) can be reduced to a two-parameter model by substituting $\tau_0 = {z_0}^2/4D$ (not to be confused with $\tau = \ell^2/4D$ from Equation (5.2)) and $\tau_\mathrm{r} = 1/D\kappa^2$:

$$S(t|z_0) = S_0 \left[\mathrm{erf}\left(\sqrt{\tau_0/t}\right) + e^{\sqrt{4\tau_0/\tau_\mathrm{r}}} e^{t/\tau_\mathrm{r}} \mathrm{erfc}\left(\sqrt{\tau_0/t} + \sqrt{t/\tau_\mathrm{r}}\right)\right]. \tag{5.4}$$

Note that while it is tempting to think of τ_r as the electron–hole recombination time constant, it includes the spatial aspect of recombination and there is no direct relationship between this and the "well mixed" recombination time constant one would compute or measure from a spatially

uniform distribution of electron and hole populations. Incorporating the partially absorbing boundary into the model affects the pre-asymptotic decay but not the long-time behavior: Equation (5.4) exhibits a $t^{-1/2}$ power-law tail at long times just like Equation (5.2).

When applying Equation (5.2) to bulb decay after charge separation in Figure 5.6, the value of the Pearson correlation coefficient between τ_0 and τ_r is large at $\rho = 0.9$ and the reduced chi-squared value is not significantly improved. This indicates that including a finite κ, even if ignoring the initial distribution of hole positions, leads to a model that overfits the data. Including a distribution in the initial positions of trapped holes in addition to the radiation boundary, as in the model of Equation (5.2),[64] does not quantitatively change this situation, again giving a two-parameter model with a high correlation between fit parameters. Thus the experimental data are not sensitive to a finite electron–hole recombination rate at room temperature, but are sensitive to the width of the initial distribution function for hole positions, $p(z_0)$. The one-parameter fit of Equation (5.2) to the experimental data is remarkably good, so we interpret this model as describing the essential physics of the recombination dynamics in our experiments. Describing the data with more complex models with more parameters is unlikely to improve the fit compared to the diffusion–annihilation model in Equation (5.2), making it difficult to justify them under our experimental conditions.

5.4.4 Implications of trapped-hole diffusion

The observation of recombination dynamics that can be described with the diffusion–annihilation model in CdSe nanorods contributes to the mounting evidence of trapped-hole diffusion in II-VI nanocrystals. Similar recombination behavior with a $t^{-1/2}$ power law has been observed in numerous CdS NRs samples with different surface-capping ligands,[64] as well as in CdS NR-based dot-in-rod heterostructures (CdSe/CdS and ZnSe/CdS dot-in-rods) when fast hole trapping

and non-uniform nanorod morphology led to a charge-separated state analogous to Figure 5.5c.[177] We have observed the power-law decay in over twenty different CdS NR samples from different synthesis batches with a reproducible, sample-independent power-law exponent of –1/2 within experimental uncertainty. The recurrence of the power-law exponent of –1/2 favors a model in which the fundamental microscopic behavior is robust to sample variation and composition, such as one-dimensional diffusion-limited recombination where the power-law exponent depends only on the effective dimensionality of the system. This is in contrast to models such as distributed trapping/detrapping rates, in which the power-law exponent can depend sensitively on sample properties.[195,196]

The observation of trapped-hole diffusion in both CdS and CdSe nanostructures can be rationalized by considering the similarities in their surface properties. In both types of nanocrystals, hole traps are thought to be associated with chalcogenide dangling bonds with similar trap depths.[13,26,69,74,76,79,186] Hole-trapping occurs on a picosecond timescale in both materials as well.[23,37,52-60] Given these similarities, it is not surprising that trapped holes exhibit similar fundamental dynamic behavior. An implicit feature of the diffusion–annihilation model is that the underlying discrete random walk occurs with small steps, on the order of interatomic distances, consistent with hole motion between neighboring chalcogen atoms on the surface.[64] Recent theoretical work on CdS surfaces supports this picture, and proposes that hole hopping is a thermally-activated process between weakly coupled trap states on S atoms.[186] This picture of weak coupling is consistent with the upper limits on D for CdS and CdSe in our experimental data ($\sim 10^{-7}$ cm^2 s^{-1}), which are orders of magnitude smaller than band-like carrier transport in bulk Cd-chalcogenides, but are in the range of diffusion coefficients for trapped-carrier diffusion in other semiconductors.[132,142,143] We note that non-uniform particle morphology is not what

causes trapped-hole diffusion. Rather, it is the charge separation followed by diffusion-limited recombination that reveals the underlying behavior. Theoretical work suggests that the trapped-hole diffusion is a property of the surface.[186] One would not observe it in TA experiments on structures like uniform nanorods and quantum dots, in which the electron and the trapped hole remain spatially overlapped, because their recombination is not limited by the motion of the hole.[64]

The diffusion of trapped holes on the surfaces of CdS and CdSe NCs may have important implications for optoelectronic applications, such as photon energy conversion. Such applications require control over the transport and transfer of photogenerated charges.[6,8,22-24] For example, in NC arrays photoexcited electrons and holes need to be transported through and between NCs,[6] while in light-driven chemistry charge carriers often must transfer to catalysts located on the NC surface to participate in redox photochemistry.[8,112] In both of these applications trapped-hole diffusion could provide a charge transport mechanism that gives rise to efficient trapped-hole transfer.[64,197] The low values of the trapped-hole diffusion coefficient we observe suggest that finding ways to increase the rate of hole hopping could be beneficial for such applications.

5.5 Conclusions

Achieving a detailed picture of the nature and behavior of surface-trapped charge carriers in nanocrystals remains a major challenge in nanoscience. Our understanding of surface states is much less developed than that of core exciton states due to a limited number of ways to probe them. Yet, charge-carrier traps are pervasive in nanostructures, and a better understanding of them will benefit a wide range of NC-based optoelectronic applications. Through monitoring

optical signals of electrons after charge separation, we have probed the spatial dynamics of trapped holes CdSe nanostructures and showed that trapped holes are able to diffuse among traps. This extends our fundamental understanding of excited-state dynamics in these nanostructures by revealing the spatial dynamics of trapped holes.

Chapter 6

Temperature dependence of trapped-hole diffusion in CdS and CdSe nanorods

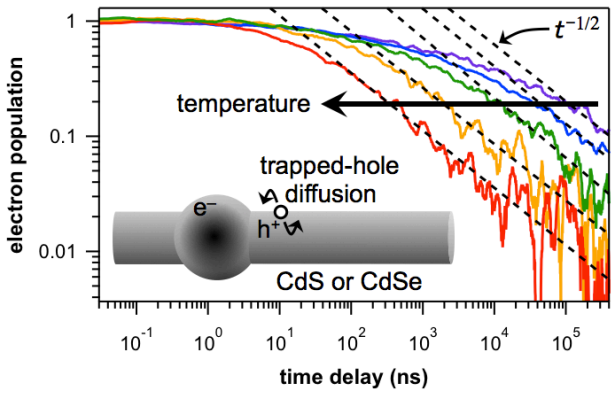

6.1 Abstract

We have previously demonstrated evidence that trapped holes diffuse on the surfaces of CdS and CdSe nanorods. The excite-state decay due to the recombination of spatially separated electrons and trapped holes in non-uniform nanorods exhibits a power-law decay with an exponent of –1/2, which was modeled as diffusion-annihilation in one dimension. However, power-law dynamics have been reported in Cd-chalcogenide nanocrystals and have been interpreted in terms of other microscopic models. By carrying out transient absorption spectroscopy over a range of temperatures from 160 to 294 K in CdS and CdSe nanorods, we find that the power law is independent of temperature. This observation rules out activated processes as the origin of the power in these nanostructures, leaving trapped-hole diffusion-limited recombination as the most consistent model for our data.

6.2 Introduction

The preceding chapters of Part I have discussed evidence that trapped-holes on the surfaces of CdS and CdSe nanorods (NRs) undergo a diffusive random walk at room temperature.[64,177] In nanorods of non-uniform diameter, intrinsic charge separation occurs because hole trapping is fast and electrons transfer to large-diameter regions so that recombination must occur between spatially separated electrons and trapped holes. This removes the typical pathway of recombination—direct recombination of overlapping carriers—making recombination rely on the electron and trapped hole reaching each other in some way. Electrons in this spatially-separated state decayed following a power law with an exponent of –1/2, which was modeled as diffusion-limited recombination in one dimension. In this interpretation, trapped holes undergo a diffusive random walk along the length of the NR, likely between undercoordinated chalcogen species on the surface, until it reaches the electron.[64] Subsequent theoretical work carried out by our colleagues corroborated this phenomenon, suggesting trap-to-trap hopping occurs by thermally activated hopping on a timescale that is in agreement with our experimental measurements.[186] However, the experimental evidence is indirect, relying on the power-law exponent being –1/2. Thus, it is important to consider that the origin of the power law can in principle be a different mechanism.

Power-law dynamics have been observed in many instances of semiconductor nanocrystal (NCs) excite-state dynamics. Power-law decays of photoexcited charge carriers can occur when there is a distribution in rate constants. For instance, power-law decays have been modeled in Cd-chalcogenide NCs as activated processes with exponential probability distributions in energy barriers where single particles obey an exponential rate process. Examples include electron trapping, where the power law originates from a distribution in

activation barrier heights,[195] charge-carrier detrapping, where the power law originates from a distribution in trap depths,[196,198] and blinking statistics, where the power-distribution in "on" and "off" times has been modeled in terms of many different mechanisms.[88,199,200] Unlike the diffusion–annihilation model, whose power-law exponent is uniquely determined by the geometry,[137] many of these other models involve thermally-activated processes that give temperature-dependent power-law exponents. Thus, examining the temperature dependence of the power-law decay in CdS and CdSe NRs can distinguish between models.

This chapter describes temperature-dependent transient absorption (TA) spectroscopy experiments performed on CdS and CdSe NRs. The temperature dependence of electron–trapped hole recombination following charge separation is investigated over 160–294 K. We find that the power-law exponent does not depend on temperature. We discuss how this observation rules out activated processes as the origin of the observed power law, leaving diffusion as the most consistent model for the data.

6.3 Methods

6.3.1 Synthesis, preparation and characterization of CdS and CdSe NRs

Details of CdS and CdSe NR synthesis, preparation and characterization appear in Chapter 2, where CdS NRs were prepared using the seeded synthesis procedure. All experiments were performed on nanocrystals that were functionalized with 3-mercaptopropanoic acid (3-MPA) and suspended in a glass-forming solvent mixture of 4:1 ethanol:methanol (v/v). TEM samples were prepared by drop-casting as-synthesized nanocrystals onto TEM grids. The dimensions of the non-uniform NRs were determined by measuring over 200 particles in TEM images.

6.3.2 Transient absorption spectroscopy

The complete experimental setup for TA measurements is described in Chapter 2. The concentration of CdS and CdSe NRs used for TA experiments was about 100 nM. The sample was held in 1 cm cryogenic cuvette from with a screw cap. Samples were prepared under Ar then immediately moved to the cryostat, which was promptly purged with nitrogen. The pump pulse was passed through a depolarizer and the power was controlled with neutral density filters. The pump beam had a beam waist of ~240 μm, pulse duration of ~150 fs, and pulse energy of 20 nJ/pulse for 400 nm excitation of the CdS NRs and 6 nJ for 600 nm excitation of the CdSe NRs. The pump powers in all cases were chosen such that the TA decay trace shapes were independent of pump power at both 294 K and 160 K so that the signal originated primarily from nanocrystals excited by a single photon.[114] Due to instrumental limitations of the cryostat, solutions were not stirred. However, at the pump power selected, no significant difference was observed between decay traces with and without stirring at room temperature. TA traces presented below were smoothed using a Savitzky-Golay filter because this method preserves higher order moments of the signal.[131] Fitting was performed on raw data and the data was smoothed for presentation only.

6.4 Results and discussion

6.4.1 Morphology and electronic structure of non-uniform Cd-chalcogenide nanorods

The synthesis of rod-shaped Cd-chalcogenide nanocrystals often results in particles that are non-uniform in diameter,[64,130,133,160,173,177] as can be seen the transmission electron microscope (TEM) images of the CdS and CdSe NRs studied here (Figure 6.1). The impact of such non-uniform diameters on electronic structure and excited-state dynamics in CdS and CdSe NRs has been described in detail (Chapters 3–5).[130,133] These non-uniform nanostructures can be modeled as

having two morphological features along their lengths: narrow-diameter cylindrical rods and wide-diameter spherical bulbs (Figure 6.2a,b). From measurements of the TEM images, we estimate that the CdS NRs studied have average rod diameters of 4.8 ± 0.4 nm, bulb diameters of 5.8 ± 0.8 nm, and lengths of 32 ±3 nm, while for the CdSe NRs the average rod diameters are 8.1 ± 0.8 nm, the bulbs are 9.6 ± 1.2 nm, and the lengths are 39 ± 4 nm. The rod and bulb morphological features give rise to distinct electronic states.[130] As depicted in Figure 6.2c, such structures effectively have a type-I band alignment were the rod has a higher transition energy than the bulb due to the differences in radial quantum confinement (Chapters 3–5).[64,130]

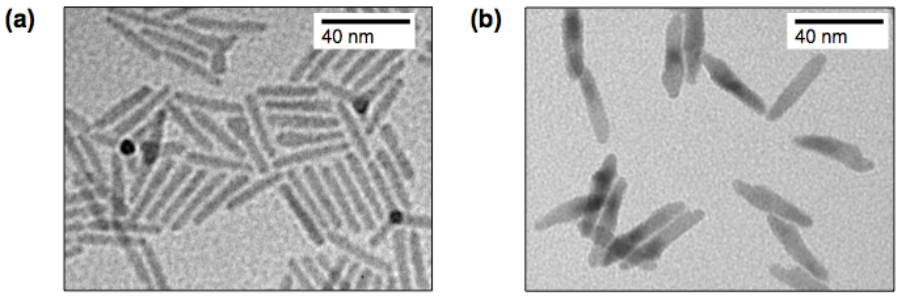

Figure 6.1. TEM images of CdS and CdSe nanorods. In these samples of (a) CdS nanorods and (b) CdSe nanorods studied here, many nanorods are non-uniform in diameter.

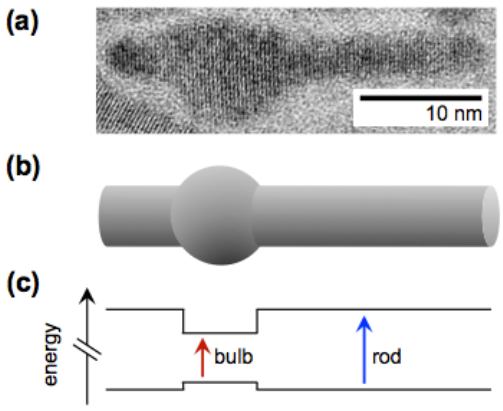

Figure 6.2. Morphology and electronic structure of non-uniform nanorods. (a) Selected TEM image of non-uniform CdS nanorod. (b) Schematic diagram of a non-uniform nanorod, depicting a simplified breakdown of rod and bulb components. (c) Energy-level diagram as a function of position along the nanorod, according to (b). The larger diameter of the bulb compared to the rod results in a lower transition energy for the bulb.

Figure 6.3 shows the TA spectra of CdS and CdSe NRs 1–3 ns after excitation at different temperatures in the range of 160–294 K. CdS NRs were excited at 400 nm while the CdSe NRs were excited at 600 nm. It has previously been demonstrated that the amplitude of the transient bleach signals of Cd-chalcogenide NCs is proportional to the population of electrons in the conduction band, independent of the population of holes in the valence band.[23,114,190] Optical excitation of CdS and CdSe NRs above the band gap primarily excites the rod rather than the bulb because it comprises a larger volume fraction of the nanostructure.[25,133,191] The energy offset between the rod and bulb provides a driving force for photoexcited charge carriers to localize to the bulb. Thus, while the rod transition dominates the absorption spectrum, photoexcited electrons undergo population transfer from the rod to the bulb over time in non-uniform nanostructures, giving rise to a substantial bulb signal in the TA spectra 1–3 ns after excitation (Figure 6.3). As the temperature is lowered, both the rod and bulb bleach peaks shift to higher energies and narrow, as is commonly observed in bulk and nanocrystalline semiconductors.[201,202] Accounting for the changes in transition energies and spectral shapes over this temperature range allows us to selectively monitor the spectral signals of the bulb at different temperatures.

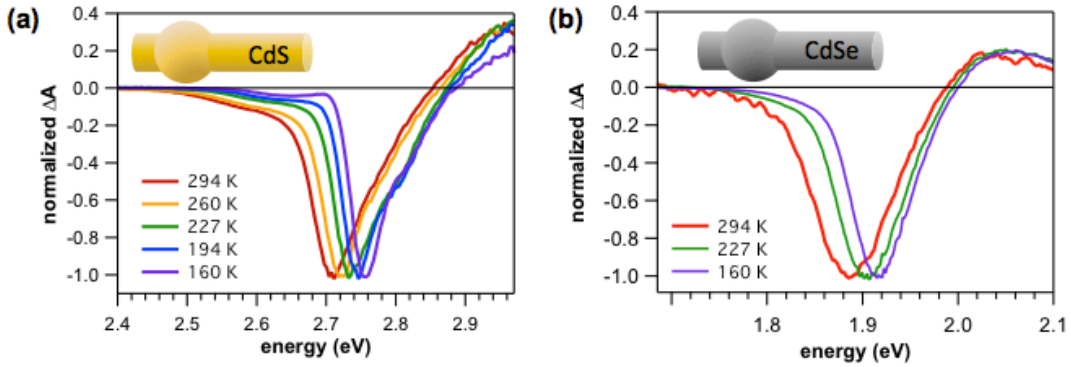

Figure 6.3. Temperature dependence of TA spectra of CdS and CdSe nanorods. (a,b) TA spectra, averaged over 1–3 ns and normalized and the bleach maximum, for (a) CdS NRs and (b) CdSe NRs at different temperatures between 160 K and 294 K. CdS NRs were excited with 400 nm pulses and CdSe NRs were excited with 600 nm pulses.

6.4.2 Temperature-dependent relaxation dynamics

We have previously studied hole trapping, charge separation and subsequent trapped-hole diffusion-limited recombination in non-uniform CdS and CdSe NRs in detail (Chapters 3–5). Hole trapping occurs on a picosecond timescale in both CdS and CdSe NCs (Chapters 3–5),[23,37,52-60] leading to localized holes at surface chalcogen species (i.e., S or Se) that are energetically trapped.[74,76,78,79] When the rod state is photoexcited, the hole is more likely to trap in rod. Driven by the lower excited-state energy within the bulb, the electron dissociates from the trapped hole and localizes in the bulb (Chapters 3–5). This spatial separation between the electron in the bulb and the trapped hole on the surface of the rod reduces the wavefunction overlap, temporarily delaying recombination. Recombination can only occur if the electron and hole reach each other in some way. This is in contrast to what occurs in an effectively uniform NC, where the electron and trapped hole remain in the same region of the nanostructure and undergo direct recombination. When monitoring the population of electrons in the bulb states after charge separation using TA spectroscopy at room temperature, a slow $t^{-1/2}$ power-law decay is seen that we previously assigned to trapped-hole diffusion-limited recombination.[64] Here we examine

on the temperature dependence of the decay of bulb electrons in non-uniform CdS and CdSe NRs in the time window after spatial separation.

Figure 6.4 shows the decays of the bulb population in CdS and CdSe NRs at different temperatures in the range 160–294 K. Bulb decay traces were obtained by spectral averaging over the bulb bleach peak, accounting for the spectral shift with changing temperature. At 294 K both materials exhibit power-law tails that are consistent with previous reports of bulb decay after spatial separation (Chapters 3 and 5).[64,203] As the temperature is lowered the bulb electron relaxation gets slower. Most importantly, a power-law tail persists at each temperature.

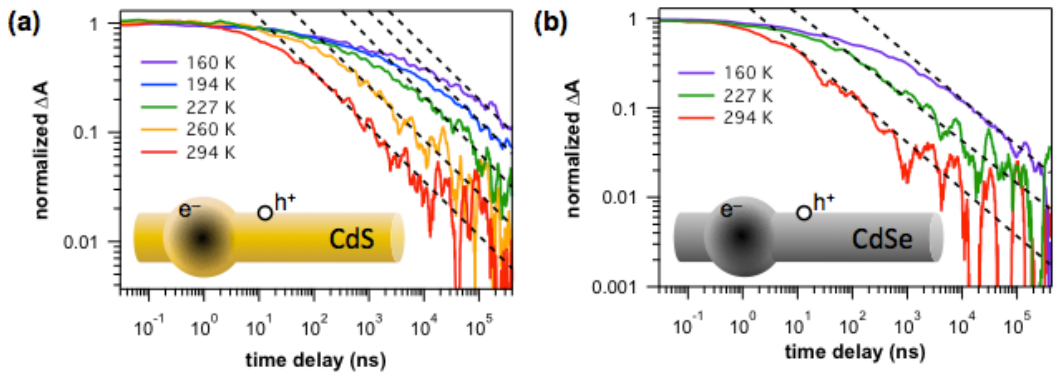

Figure 6.4. Temperature dependence of electron–trapped hole recombination in CdS and CdSe nanorods. TA time traces of bulb signal of (a) CdS NRs and (b) CdSe NRs. For CdS NRs, time traces of the bulb signal at 294, 260, 227, 194 and 160 K were obtained by averaging signal over the spectral windows 464–484, 467–476, 470–490, 478–488 and 480–490 nm, respectively. For CdSe NRs, time traces of the bulb signal at 294, 227 and 160 K were obtained by averaging signal over the spectral windows 665–675, 675–690 and 690–700 nm, respectively. Power-law tails were fit with a floating power-law exponent α (black dashed lines). Data are smoothed for presentation.

The power-law tails of each decay were fit to a power law function of the form

$$S_{\text{bulb}}(t) \sim t^{\alpha}. \tag{6.1}$$

The fit results appear in Table 6.1 and are plotted in Figure 6.5. In each case the power-law exponent, α, is consistent with –1/2, within error. The origin of the power-law tail and its temperature independence is discussed below.

Table 6.1. Power-law exponent as a function of temperature

T (K)	α	
	CdS	CdSe
294	– 0.50 ± 0.02	– 0.52 ± 0.04
260	– 0.49 ± 0.04	—
227	– 0.52 ± 0.04	– 0.47 ± 0.04
194	– 0.49 ± 0.04	—
160	– 0.49 ± 0.09	– 0.51 ± 0.03

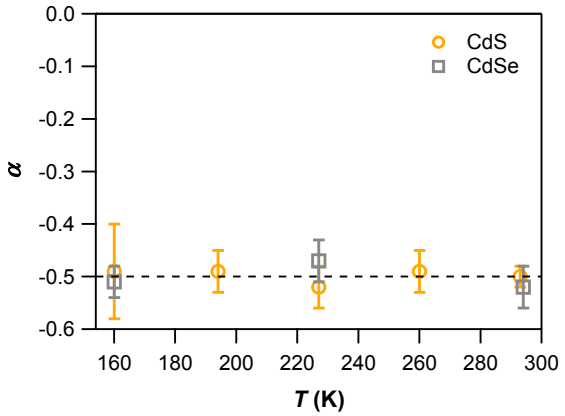

Figure 6.5. Power-law exponent of bulb decay in non-uniform CdS and CdSe NRs as a function of temperature.

6.4.3 Origin of the power law

Examining the temperature dependence of the bulb decay allows us to distinguish between different models for power-law decay, thereby telling us about the physical mechanism of electron decay. Here we discuss several possible mechanisms for recombination between the spatially separated electron in the bulb and trapped hole in the rod, considering how each one

might give rise to power-law dynamics, and looking at the temperature dependence of the power-law exponent in each case.

Firstly, we illustrate how power-law dynamics can arise in an ensemble decay due to a distribution of rate constants. We consider cases where an individual decay event of a single particle obeys an exponential rate process with rate constant κ:

$$S(\kappa, t) = Ae^{-\kappa t}. \tag{6.2}$$

Generally, a power law can arise in an ensemble of exponentially decaying particles when there is a power-law distribution in rate constants. This can happen when the rate constant is determined by a thermally activated process and there is an exponential distribution in activation energies. In this model, the rate constant is given by an Arrhenius equation,

$$\kappa(E_\mathrm{a}, T) = \kappa_0 e^{-E_\mathrm{a}/k_\mathrm{B}T}, \tag{6.3}$$

where κ_0 is the maximum rate constant, E_a is the height of energy barrier and $k_\mathrm{B}T$ is the thermal energy at temperature T. We can write the exponential ensemble distribution of activation energies as

$$P(E_\mathrm{a}) = ae^{-aE_\mathrm{a}}, \tag{6.4}$$

where a represents the inverse of the characteristic barrier height. The ensemble behavior is found by averaging the single-particle decay over the distribution in barrier heights:

$$S(T, t) = \int_0^\infty dE_\mathrm{a}\, P(E_\mathrm{a}) S(k(E_\mathrm{a}, T), t) \tag{6.5}$$

Focusing on the asymptotic behavior of the ensemble gives the long-time behavior: $S(T, t) \sim t^\alpha$, where $\alpha = -ak_\mathrm{B}T$ is the temperature-dependent power-law exponent.

One can conceive of several plausible scenarios in which the observed power-law decay of the bulb electron population is due to recombination mechanisms other than trapped-hole diffusion. First, recombination could occur by the electron transferring from the bulb back to the

rod via thermal activation, returning to the delocalized state of the rod that can recombine directly with the hole. In this case, a power-law decay could originate from an exponential distribution of rod–bulb energy offsets. This would follow the formalism above, where κ is the rate constant for bulb-to-rod population transfer, E_a is the energy difference between the rod and bulb due to different quantum confinement energies, and the distribution $P(E_a)$ originates from different relative rod and bulb radii in different NRs. Before considering the temperature dependence for this model, we note that this model can be dismissed based on previous experiments: we have previously shown that when the bulb state is selectively excited in CdS and CdSe NRs, rod electron signal was not observed (Chapter 3 and 5),[64] suggesting that the electrons do not transfer from the bulb to the rod on the timescale of recombination. Second, electrons could be trapping while the hole remains stationary on the rod. In this case the power-law decay of the electron population would reflect a distribution in trapping rates that could originate from a distribution in trapping activation barriers.[195] Here κ would be the rate constant for electron trapping in a given bulb, E_a is the height of the barrier the electron must overcome to trap, and the distribution $P(E_a)$ originates from a distribution in barrier heights. Finally, recombination could be limited by detrapping of the hole; while the hole is trapped it could be stationary, but eventually it returns to the valence-band edge and from there it would rapidly transfer to the bulb where it recombines. In this model, the power-law decay of the bulb electrons would originate from a power-law distribution of detrapping times, $1/\kappa$. This could occur if there were an exponential distribution in trap depths, $P(E_a)$.[199] However, this is inconsistent recent work by Kambhampati and coworkers that suggests there is a narrow distribution of trap depths.[79] It is also inconsistent with the low photoluminescence quantum yields typically observed in CdS and CdSe nanocrystals,[36,204,205] which imply that recombination of conduction

band electrons predominantly occurs with trapped holes rather than valence-band holes as this model demands.[23]

The temperature dependence study performed here is consistent with the model of trapped-hole diffusion and inconsistent with the above thermally-activated relaxation models. In all the alternative scenarios described above, the decay of electrons in the bulb occurs through a thermally activated pathway. Models for producing an ensemble power-law decay could be constructed based on Equations 6.2–6.5, but in each case the power-law exponent is temperature dependent: $\alpha = -ak_{\mathrm{B}}T$. If the power-law tails observed in CdS and CdSe NRs in Figure 6.4 were due to an activated mechanism then the magnitude of the power-law exponent would have changed by nearly a factor of 2 over the temperature range studied; because α = –0.50 at room temperature, 294 K, then decreasing the temperature to 160 K would have brought α to –0.27 were the an activated process dominating the decay. The lack of temperature dependence in the experimentally measured α (Figure 6.5) rules out the possibility of a distributed activated process as the origin of the power law. Moreover, even though the distributed activated models could give rise to a power-law decay, one would expect α to be highly sensitive to sample preparation, which is likely to cause significant changes in the value of a in the distributions of, for example, the relative sizes of the rods and bulbs, electron trapping barriers or the hole trap depths. Instead, the power-law exponent of –1/2 has proven to be robust, occurring in over twenty CdS nanorod samples to date, ZnSe/CdS and CdSe/CdS dot-in-rod heterostructures, and CdSe NRs (Chapters 3–5).[64,177] Thus the temperature dependence data and the reproducibility of α favor a model in which the fundamental microscopic behavior is robust to sample variation and composition, depending only on a universal property of these systems such as one-dimensional diffusion-limited recombination. However, it is worth noting that the present work

does not indicate that the above activated processes do not occur on some timescale, just that they do not dominate the mechanism behind the power-law decay of charge separated electrons and trapped holes in CdS and CdSe NRs.

6.5 Conclusions

This chapter provides strong support for the model of trapped-hole diffusion in CdS and CdSe nanocrystals. Alternative mechanisms for the power-law recombination dynamics of spatially separated electrons and trapped holes that rely on thermally-activated decay pathways can be ruled out by the observation of a temperature-independent power-law exponent. The notion that surface-trapped holes are mobile in these nanocrystals may provide a novel framework for the design of systems that seek to utilize trapped charge carriers for photovoltaic and photochemical applications. Further analysis of this data is ongoing in an effort to learn more about the nature of trapped-hole diffusion in CdS and CdSe nanocrystal.

Part II

Electron-transfer kinetics in nanocrystal–acceptor complexes

Chapter 7

Competition between electron transfer, trapping, and recombination in CdS nanorod–hydrogenase complexes[§]

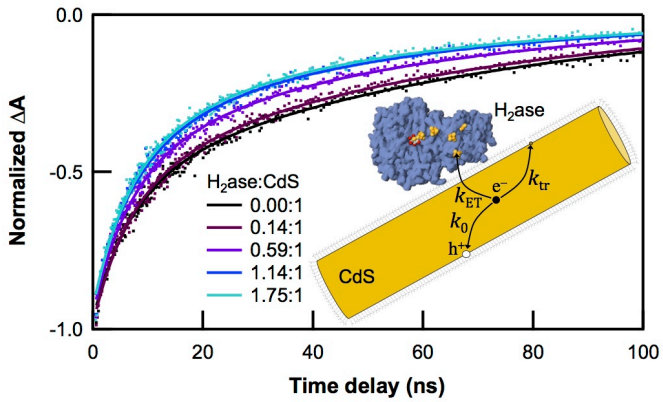

7.1 Abstract

Electron transfer from photoexcited CdS nanorods to [FeFe] hydrogenase is a critical step in photochemical H_2 production by CdS-hydrogenase complexes. By accounting for the distributions in the numbers of electron traps and enzymes adsorbed, we determine rate constants and quantum efficiencies for electron transfer from transient absorption measurements.

7.2 Introduction

Coupling semiconductor nanocrystals to redox enzymes is an emerging strategy to photochemically drive fuel-generating reactions such as H_2 production and CO_2 reduction.[24,30,31,44,99-103] These hybrid structures integrate the tunable electronic structure, strong

[§]Adapted from Utterback, J. K.; Wilker, M. B.; Brown, K. A.; King, P. W.; Eaves, J. D.; Dukovic, G. *Phys. Chem. Chem. Phys*. **2015**, *17*, 5538-5542 with permission from The Royal Society of Chemistry. (© Copyright 2015 The Royal Society of Chemistry)

light absorption, and surface chemistry of nanocrystals with the catalytic selectivity of enzymes. Photochemical reactions of nanocrystal-enzyme complexes proceed through a sequence of steps: light absorption in the nanocrystals, transfer of photoexcited electrons to the enzyme where they participate in catalysis, and hole scavenging by sacrificial electron donors.[24,30,101] The kinetics of electron transfer (ET) from the nanocrystal to the enzyme play a crucial role in the overall photochemical reactivity. The quantum efficiency of ET (QE_{ET}) determines the upper limit on the quantum yield of fuel generation. QE_{ET}, in turn, depends on how the rate of ET compares to the rates of competing excited state decay processes in the nanocrystal, such as radiative and nonradiative recombination and carrier trapping. We have recently measured electron decay kinetics in complexes of CdS nanorods (NRs) with [FeFe]-hydrogenase I from *Clostridium acetobutylicum* (H_2ase), which photochemically reduces $2H^+$ to H_2.[24] Transient absorption (TA) spectra recorded over a time window of 10^{-13}–10^{-4} s indicate that ET occurs on a similar timescale as the excited state decay of NRs.[24] Similar results were reported in complexes of CdTe quantum dots and H_2ase.[31]

Quantifying the interplay between ET and the competing relaxation processes is critical for increasing the photochemical efficiency of nanocrystal-enzyme hybrids. Understanding the kinetics of nanocrystal-enzyme ET is complicated by the fact the excited states of nanocrystals decay nonexponentially over many decades in time, even in the absence of catalysts.[36,37,206] These dynamics reflect the structural heterogeneities present in nanocrystal samples, some of which arise from variations in the number of carrier trapping sites on the nanocrystal surface.[36,80] Adsorption of enzymes further increases sample heterogeneity.[44] Average electron lifetimes in CdS NR and CdS–H_2ase ensemble samples can be determined from multiexponential and/or stretched exponential fits to TA data.[24] However, these lifetimes do not provide the intrinsic rate

constants for the excited state decay processes because they do not take into account the underlying sample heterogeneity, i.e., the number distribution of electron traps and enzymes per NR in the ensemble. Thus, to understand how electron decay processes in CdS NRs compete with ET to H_2ase, it is necessary to use a kinetic model that accounts for population heterogeneities.

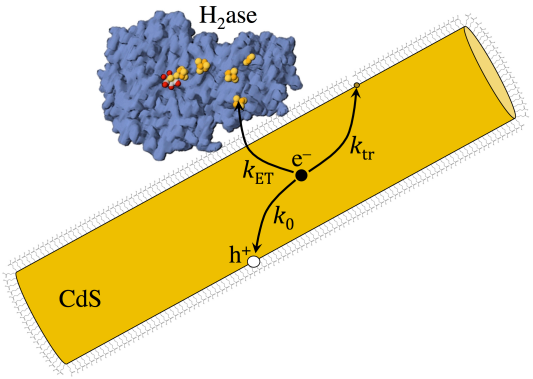

Figure 7.1. Schematic depiction of photoexcited electron decay pathways in a CdS–H_2ase complex, including electron-hole recombination (k_0), electron trapping (k_{tr}) and electron transfer (k_{ET}).

In this chapter, we employ such a model to analyze the decay of the electron population observed in the TA signal of CdS NRs and CdS–H_2ase complexes in the 1–100 ns time window. We determine the intrinsic rate constants, i.e. probabilities per unit time that a particular microscopic relaxation event occurs, for three electron decay processes: electron-hole recombination in CdS NRs (k_0), electron trapping (k_{tr}), and ET to H_2ase (k_{ET}) (Figure 7.1). In this model, the numbers of the electron trap sites and adsorbed H_2ase moieties follow independent Poisson distributions. We find k_0 to be 1.5×10^7 s^{-1}, and k_{tr} to be 7-fold larger (1.1×10^8 s^{-1}), with the average electron trap density ($\langle N_{tr}\rangle$) of 0.59 per NR. From a series of CdS–H_2ase samples with varying CdS:H_2ase molar ratios, we find that k_{ET} (2.4×10^7 s^{-1}) is within a factor of two of k_0. QE_{ET} in the ensemble sample is a function of both the ratios of the

intrinsic rate constants and of the average numbers of traps and enzymes. While it depends strongly on the ratio k_{ET}/k_0, the dependence on k_{tr}/k_0 is weak because $\langle N_{tr} \rangle$ is small, causing trapping to play a minor role in determining QE_{ET} for the ensemble. We find a quantitative agreement between ensemble QE_{ET} and the previously reported quantum yield of H_2 generation using CdS–H_2ase complexes.[44] Thus the key to more efficient photochemical H_2 generation lies in improving the efficiency of ET from CdS NRs to H_2ase by manipulating the individual contributions of k_{ET} and k_0. Finally, the model predicts that the fraction of CdS NRs that have no H_2ase adsorbed limits the maximum achievable value of QE_{ET} for the ensemble. The kinetic model that accounts for heterogeneity of CdS–H_2ase complexes provides quantitative insights into factors that play a critical role in photochemical H_2 generation.

7.3 Methods

7.3.1 Sample preparation and characterization

The synthesis of CdS NRs was carried out following previously reported methods that are described in Chapter 2.[44,116,119] CdS NR surfaces were functionalized, subsequent to NR synthesis, with 3-mercaptopropanoic acid (3-MPA) using a previously reported ligand exchange procedure.[44,107,116] This enabled aqueous solubility and an electrostatic interaction with H_2ase. The molar absorptivity of the CdS NRs was found by comparison of UV-visible absorption spectra with Cd^{2+} concentrations, found by elemental analysis (ICP-OES), after acid digestion of NR samples. The estimated molar absorptivity at 350 nm was 1.1×10^7 M^{-1} cm^{-1} for this sample. The expression and purification of H_2ase from *Escherichia coli* has been described elsewhere.[127] CdS–H_2ase complexes were prepared under Ar by mixing solutions of CdS NRs and H_2ase in buffer (50 mM Tris-HCl, 5 mM NaCl, 5% glycerol, pH 7) with no hole scavenger added.

7.3.2 Transient absorption spectroscopy

The complete experimental setup for the TA measurements has been previously described.[116] In all mixtures used for TA experiments, the concentration of CdS was held constant at about 0.7 μM, as determined from UV-visible absorption spectra and the molar absorptivity, and the concentration of H_2ase was varied relative to this in order to give different molar ratios H_2ase:CdS. Samples were sealed under Ar in 2 mm quartz cuvettes equipped with air-tight valves. TA samples were rapidly stirred and pumped with a beam that was ~240 μm in diameter with pulse energies of ~10 nJ. The pump power was low enough that TA decay kinetics were independent of power to prevent signal from multiple excitons[114] and isolate the kinetics of one electron transferring to H_2ase. TA kinetics were collected with a time resolution of 0.3 ns.

7.4 Results and discussion

7.4.1 Excited-state relaxation of CdS NRs

Details of the preparation and characterization of the CdS NRs and H_2ase have been described previously.[24,44] CdS NRs used in this study had an average length of 21.5 ± 5.2 nm and an average diameter of 4.4 ± 0.6 nm (Figure 7.2). The CdS NR surface was functionalized with 3-mercaptopropanoic acid (3-MPA), which enabled aqueous solubility and an electrostatic interaction with H_2ase. H_2ase binds to the CdS NRs via the attraction between the negatively charged carboxylate groups of deprotonated 3-MPA and a positively charged region on the surface of the enzyme (Figure 7.1).[44] This interaction is analogous to the *in vivo* binding of the electron-donating protein ferredoxin with the same positively charged region of the H_2ase protein surface.[30,44]

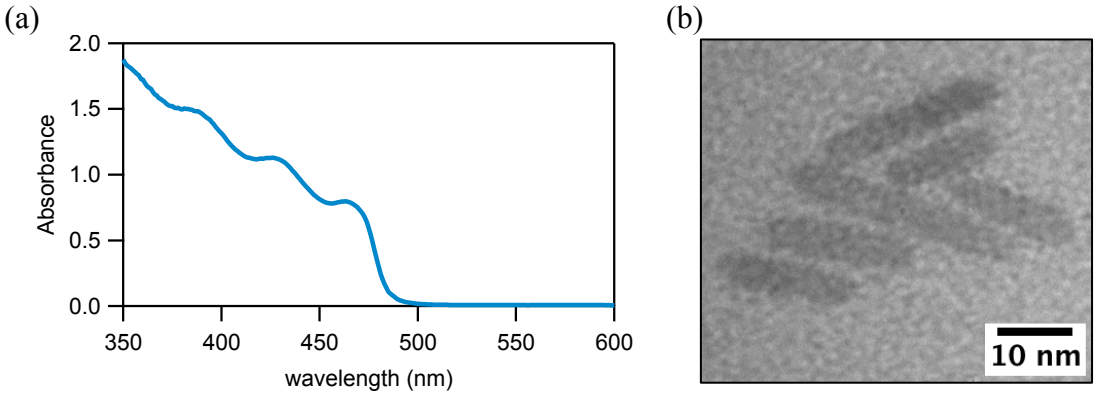

Figure 7.2. CdS NR characterization. (a) UV-visible absorption spectrum of CdS NRs in buffer. (b) TEM image of CdS NRs.

To monitor the relaxation kinetics of photoexcited CdS NRs with and without adsorbed H_2ase, we used TA spectroscopy. The laser setup has been described previously,[116] and relevant experimental details are described in the Methods section. Photoexcitation of CdS NRs at 400 nm gives rise to a transient bleach feature corresponding to the band gap at 471 nm (Figure 7.3). The magnitude of the bleach is proportional to the population of electrons filling the lowest lying $1\sigma_e$ electron level of CdS NRs and is independent of the valence band hole population.[114,207] Thus, the decay of the bleach signal for CdS NRs without H_2ase represents the kinetics of electrons depopulating the $1\sigma_e$ level by radiative and nonradiative recombination with the photoexcited hole and by electron trapping. We note that H_2ase does not have a detectable signature in the TA spectrum at the concentrations used here.

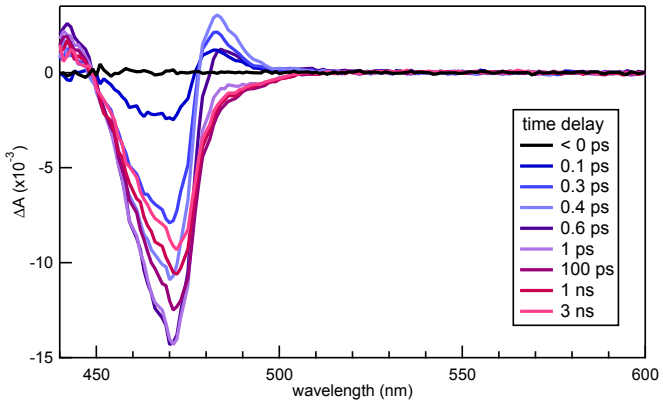

Figure 7.3. TA spectra of CdS NRs over time. Photoexcitation of CdS NRs at 400 nm gives rise to a transient bleach feature peaked at 471 nm in this particular sample, corresponding the band gap. Kinetic traces are obtained by monitoring the ΔA amplitude at 471 nm. The induced absorption feature at 485 nm is due to carrier cooling and is short lived (<1 ps).

The TA decay curve for CdS NRs has a complicated functional form. This is commonly observed with semiconductor nanocrystals[37,130] We observe three time windows of distinct decay shapes in the relaxation of the CdS NR bleach feature (Figure 7.4). 98% of the decay can be fit with a single exponential plus a stretched exponential fit:

$$f(t) = A_e e^{-t/\tau_e} + A_s e^{-(t/\tau_s)^{\beta}}. \quad (7.1)$$

The fast 1.8 ps single exponential decay component constitutes 12% of the overall decay and has been attributed to exciton localization to a part of the nanorod with the largest diameter, or weakest quantum confinement.[130] Most of the decay (86%) occurs in the intermediate time window and can be described with a stretched exponential with a time constant of 24 ns and a stretching exponent of 0.47. At short delay times, a fast (~1 ps) exponential decay component constitutes 12% of the overall decay and has recently been assigned to exciton localization.[130] Most of the decay occurs in the intermediate time regime and can be fit with a stretched exponential. At long delay times (>100 ns), with the amplitude down to 2% of the initial value, the kinetics change to a much slower decay and the stretched exponential fails to describe its shape. The decay in this region follows a $t^{-1/2}$ power-law decay that can be described by

trapped-hole diffusion-limited recombination in non-uniform NRs.[64] This decay is the subject of Chapter 3 and will not be addressed here. Although the decay of the CdS NR TA signal intensity occurs over a broad range of time, most of the change in the signal intensity upon addition of H_2ase occurs in the window of 1-100 ns.[24] Thus, the 1-100 ns time regime is the most relevant for understanding ET kinetics in this system and will be the focus for the remainder of this work.

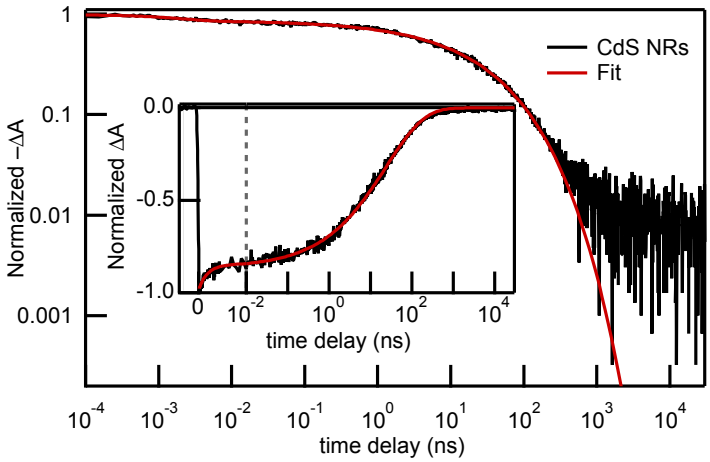

Figure 7.4. Nonexponential relaxation dynamics of CdS NRs. TA kinetics of the band gap feature in CdS NRs probed at 471 nm over a time window of 0.1 ps–30 μs with a time resolution of 150 fs. The signal is shown as –ΔA on log-log axes. The inset shows the same data on a split time axis that is linear for the first 10 ps and logarithmic thereafter. A fit function that includes a fast single exponential plus a stretched exponential is shown in red. The plots reveal the existence of three time windows with distinct functional forms.

To analyze the band edge bleach recovery of CdS NRs in the 1–100 ns time window, we use a kinetic model for excited state decay that explicitly includes the number distribution of electron trap sites per CdS NR in the ensemble sample. A similar model was developed for the study of quenching kinetics of luminescent probes in micellar systems,[208,209] and has more recently been employed to study the kinetics of carrier trapping in nanocrystals,[35,37] as well as energy,[210,211] hole[207] and electron transfer[212] in nanocrystal–acceptor complexes. The merit of this model is that it reveals the intrinsic rate constants for electron relaxation. The decay of the

TA signal can be modeled as the survival probability of the electron in the $1\sigma_e$ electron state, $P_{\mathrm{Cds}}(t)$, because $P_{\mathrm{Cds}}(t)$ is directly proportional to $\Delta A(t)$. This model assumes that, in this time window, trapping, recombination, and ET are not dominated by diffusion.

7.4.2 The kinetic model for excited state relaxation in NRs

For completeness, we present the derivation of the model of the CdS survival probability, $P_{\mathrm{Cds}}(t)$. Though this derivation closely follows previously published works,[84] it is a foundational part of our description for electronic relaxation in the presence of both traps and enzyme with and without rate constant fluctuations.

The TA signal is proportional to the number of electrons in the $1\sigma_e$ excited state at time t, which is the survival probability of the electron in excited state, $P_{\mathrm{Cds}}(t)$, multiplied by the total number of electrons excited at time zero. Thus the survival probability fully characterizes the time-dependent relaxation embodied in the TA signal, $\Delta A(t)$. The total survival probability, $P_{\mathrm{Cds}}(t)$, is related to the conditional survival probability for a NR that has a given number N_{tr} of traps, $P_{\mathrm{Cds}}(t, N_{\mathrm{tr}})$, by the law of total probability $P_{\mathrm{Cds}}(t) = \sum_{N_{\mathrm{tr}}=0}^{\infty} P(N_{\mathrm{tr}}) P_{\mathrm{Cds}}(t, N_{\mathrm{tr}})$. Because each NR is independent, one can view $P_{\mathrm{Cds}}(t, N_{\mathrm{tr}})$ as the total number of electrons in the excited state at time t divided by the total number of electrons that were excited at time zero for the subpopulation where N_{tr} is fixed. $P(N_{\mathrm{tr}})$ is the (time-independent) probability that one NR has N_{tr} traps and can be computed from equilibrium statistical mechanics. The equation of motion for $P_{\mathrm{Cds}}(t, N_{\mathrm{tr}})$ is the master equation,[213]

$$\frac{dP_{\mathrm{Cds}}(t, N_{\mathrm{tr}})}{dt} = -(k_0 + k_{\mathrm{tr}} N_{\mathrm{tr}}) P_{\mathrm{Cds}}(t, N_{\mathrm{tr}}). \tag{7.2}$$

Here k_0 is the sum of rate constants for radiative and nonradiative recombination of the electron with the hole, and k_{tr} is the rate constant for electron trapping. The factor of $k_{\mathrm{tr}} N_{\mathrm{tr}}$ is

the total probability, per unit time, that an electron reacts with *any* of the N_{tr} traps. The rate constant k_0 is the probability per unit time that the electron relaxes by any process other than trapping. This model assumes that the photophysics occurs in the "well-mixed" limit, i.e., that the electron samples the spatial extent of the NR on a timescale that is fast compared to the trapping time. This means that the time required for an electron to find a trap is not dominated by diffusion in this time window. The solution to Equation (7.2) is

$$P_{\mathrm{CdS}}(t, N_{\mathrm{tr}}) = P_{\mathrm{CdS}}(t_0, N_{\mathrm{tr}}) e^{-(k_0 + k_{\mathrm{tr}} N_{\mathrm{tr}})(t - t_0)}. \tag{7.3}$$

The survival probability decays in the short time window (0.1 ps – 10 ps) in a way that is independent of N_{tr} so that the initial condition becomes $P_{\mathrm{CdS}}(t_0, N_{\mathrm{tr}}) = P_{\mathrm{CdS}}(t_0)$, the amplitude at time t_0 after the relaxation of CdS between time 0 and t_0.

At low concentrations of traps, one can find $P(N_{\mathrm{tr}})$ using equilibrium statistical mechanics for non-interacting particles. We describe the distribution of electron trap sites, $P(N_{\mathrm{tr}})$, as an ensemble of NRs coupled to an ideal solution of traps that are noninteracting with one another but are at fixed chemical potential, temperature and volume so that the number of traps at equilibrium, N_{tr}, in a NR follows a Poisson distribution:

$$P(N_{\mathrm{tr}}) = \frac{\langle N_{\mathrm{tr}} \rangle^{N_{\mathrm{tr}}} e^{-\langle N_{\mathrm{tr}} \rangle}}{N_{\mathrm{tr}}!}. \tag{7.4}$$

where $\langle N_{\mathrm{tr}} \rangle$ is the average number of traps at thermal equilibrium. The decay of the ensemble of complexes, $P_{\mathrm{CdS}}(t)$, computed from probability theory is then equivalent to a thermal ensemble average,

$$P_{\mathrm{CdS}}(t) = \sum_{N_{\mathrm{tr}}=0}^{\infty} P(N_{\mathrm{tr}}) P_{\mathrm{CdS}}(t, N_{\mathrm{tr}}), \tag{7.5}$$

$$= P_{\mathrm{CdS}}(t_0)e^{-k_0 t}\left[\sum_{N_{\mathrm{tr}}=0}^{\infty} P(N_{\mathrm{tr}})e^{-k_{\mathrm{tr}}N_{\mathrm{tr}}t}\right], \tag{7.6}$$

$$= P_{\mathrm{CdS}}(t_0)\exp\left[-k_0(t-t_0) + \langle N_{\mathrm{tr}}\rangle\left(e^{-k_{\mathrm{tr}}(t-t_0)} - 1\right)\right]. \tag{7.7}$$

Because $k_0 t_0 \ll 1$ and $k_{\mathrm{tr}} t_0 \ll 1$, we simplify the fit equation by omitting t_0 and writing $P_{\mathrm{CdS}}(t_0)$ as the amplitude, A:

$$P_{\mathrm{CdS}}(t) = A\exp[-k_0 t + \langle N_{\mathrm{tr}}\rangle(e^{-k_{\mathrm{tr}}t} - 1)]. \tag{7.8}$$

This model allows for the simultaneous determination of k_0, k_{tr}, and $\langle N_{\mathrm{tr}}\rangle$.

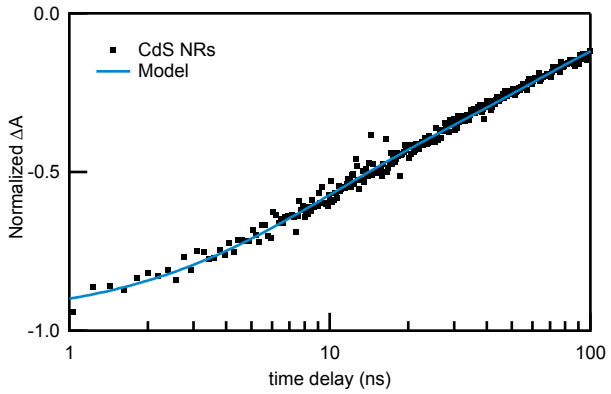

Figure 7.5. TA time trace of CdS NRs. TA time traces of CdS NRs in the time window of 1–100 ns showing the fit of the kinetic model (Equation (7.8)) in blue.

Figure 7.5 shows the TA decay of CdS NRs in the 1–100 ns time window with a fit to Equation (7.8). Equation (7.8) has an inherent correlation of parameters, meaning that different combinations of $\langle N_{\mathrm{tr}}\rangle$ and k_{tr}, for example, can give the same fit. We used the bootstrapping Monte Carlo method to determine the average value and corresponding 95% confidence interval for each parameter (see Error Analysis section). The resulting fit parameters are given in Table 3.1. The k_0 value of 1.5×10^7 s^{-1} describes electron-hole recombination pathways and is dominated by recombination of a $1\sigma_e$ electron with a surface-trapped hole because hole trapping is very fast (ps) in CdS NRs.[23] Electron trapping is 7-fold faster than recombination, with a rate

constant of 1.1×10^8 s^{-1}. The average number of traps is 0.59 in this sample, meaning that 33% of the NRs have one electron trap, and 55% have none. Because of the low electron trap density, the ensemble measurement of the excited state decay, and the associated average lifetime, is dominated by k_0. Similar trapping rates and trap densities have been previously determined for CdS NRs and CdSe QDs using the same kinetic model.[37,84]

Table 7.1. Electron decay parameters for CdS NRs and CdS–H_2ase complexes

H_2ase:CdS molar ratio	k_0 (10^7 s^{-1})[a]	$\langle N_{tr}\rangle$[a]	k_{tr} (10^8 s^{-1})[a]	$\langle N_{H_2ase}\rangle$[b]	k_{ET} (10^7 s^{-1})[b]
0.00:1	1.5 ± 0.1	0.59 ± 0.04	1.1 ± 0.2	–	–
0.14:1	1.5 ± 0.1	0.59 ± 0.04	1.1 ± 0.2	0.13 ± 0.02	2.4 ± 0.6
0.59:1	1.5 ± 0.1	0.59 ± 0.04	1.1 ± 0.2	0.42 ± 0.04	2.4 ± 0.6
1.14:1	1.5 ± 0.1	0.59 ± 0.04	1.1 ± 0.2	0.68 ± 0.05	2.4 ± 0.6
1.75:1	1.5 ± 0.1	0.59 ± 0.04	1.1 ± 0.2	0.76 ± 0.06	2.4 ± 0.6

[a]Values found by fitting CdS NR kinetic trace (Figure 7.5) with Equation (7.8).
[b]Result of global fit of data in Figure 7.6 to Equation (7.28) by holding k_0, k_{tr}, and $\langle N_{tr}\rangle$ fixed, defining k_{ET} as a global parameter between data sets containing H_2ase and allowing $\langle N_{H_2ase}\rangle$ to vary between data sets.
Uncertainties associated with each fit parameter are 95% confidence intervals.

Below we derive an expression that allows for fluctuations in k_{tr} at the level of second cumulant approximation, but find that they do not lead to a statistically better fit. Thus, a single value of k_{tr} is sufficient to describe the data.

7.4.3 Fluctuations in both numbers and intrinsic rate constants for traps and H_2ase

Here we derive an equation for the survival probability in the presence of fluctuations for the intrinsic rate constants. Fluctuations in the intrinsic rate constants can occur when there are additional sources of disorder in the system beyond the number fluctuations modeled above. For example, distributions in distances between the enzyme and the NR or conformational fluctuations of the enzyme might influence electron transfer rates. In this section we derive the

expression for the survival probability for electron trapping when there are fluctuations in the trapping rates. Suppose there are N_{tr} traps in a NR and that the rate constant for each trap is a random variable chosen from some distribution, $k_i = k_{\mathrm{tr}} + \delta_i$, where k_{tr} is the mean of the distribution and δ_i is the fluctuation away from the mean for a given trap, i. The distribution function for each δ_i, $p(\delta_i)$, in the set $\{\delta\} = (\delta_1, \dots, \delta_{N_{\mathrm{tr}}})$ is identical and has finite first and second moments.

The master equation for the survival probability $P_{\mathrm{CdS}}(t, N_{\mathrm{tr}}, \{\delta\})$ is

$$\frac{dP_{\mathrm{CdS}}(t, N_{\mathrm{tr}}, \{\delta\})}{dt} = -\left(k_0 + k_{\mathrm{tr}} N_{\mathrm{tr}} + \sum_{i=1}^{N_{\mathrm{tr}}} \delta_i \right) P_{\mathrm{CdS}}(t, N_{\mathrm{tr}}, \{\delta\}), \tag{7.9}$$

which is the survival probability for a given N_{tr} and a given realization of the random variable $\{\delta\}$. Solving the differential equation, and again omitting t_0 and replacing $P_{\mathrm{CdS}}(t_0, N_{\mathrm{tr}}, \{\delta\})$ in favor of the amplitude $P_{\mathrm{CdS}}(t_0)$ gives

$$P_{\mathrm{CdS}}(t, N_{\mathrm{tr}}, \{\delta\}) = P_{\mathrm{CdS}}(t_0)\, e^{-\left(k_0 + k_{\mathrm{tr}} N_{\mathrm{tr}} + \sum_{i=1}^{N_{\mathrm{tr}}} \delta_i\right) t} \tag{7.10}$$

Because the initial condition is independent of N_{tr}, it must also be independent of the values for the intrinsic rate constants. Thus, for a given N_{tr} we can average over the fluctuations in the intrinsic rates first, and then average over the number fluctuations,

$$\langle e^{-\sum_{i=1}^{N_{\mathrm{tr}}} \delta_i t} \rangle = \int_{-k_{\mathrm{tr}}}^{\infty} \prod_{i=1}^{N_{\mathrm{tr}}} d\delta_i p(\delta_i) e^{-\sum_{i=1}^{N_{\mathrm{tr}}} \delta_i t}, \tag{7.11}$$

$$= \int_{-k_{\mathrm{tr}}}^{\infty} \prod_{i=1}^{N_{\mathrm{tr}}} d\delta_i p(\delta_i) e^{-\delta_i t}, \tag{7.12}$$

$$= \left[\int_{-k_{\mathrm{tr}}}^{\infty} d\delta p(\delta) e^{-\delta t} \right]^{N_{\mathrm{tr}}}, \tag{7.13}$$

$$= \hat{p}(t)^{N_{\mathrm{tr}}}. \tag{7.14}$$

The simplification above comes from the fact that all δ_i are independent, identically distributed random variables chosen from the same distribution. $\hat{p}(t)$ above is the moment generating function for the distribution of trapping rate fluctuations, $\hat{p}(t) = \int_{-k_{\mathrm{tr}}}^{\infty} d\delta p(\delta) e^{-\delta t}$. Finally, averaging over the Poisson distribution in N_{tr} gives the survival probability in the presence of both sources of fluctuations,

$$P_{\mathrm{Cds}}(t) = \sum_{N_{\mathrm{tr}}=0}^{\infty} P(N_{\mathrm{tr}}) P_{\mathrm{Cds}}(t, N_{\mathrm{tr}}, \delta), \tag{7.15}$$

$$= P_{\mathrm{Cds}}(t_0) \sum_{N_{\mathrm{tr}}=0}^{\infty} P(N_{\mathrm{tr}}) e^{-k_0 t}\, e^{-k_{\mathrm{tr}} N_{\mathrm{tr}} t} \left\langle e^{-\sum_{i=1}^{N_{\mathrm{tr}}} \delta_i t} \right\rangle, \tag{7.16}$$

$$= P_{\mathrm{Cds}}(t_0)\, e^{-k_0 t} e^{-\langle N_{\mathrm{tr}} \rangle} \sum_{N_{\mathrm{tr}}=0}^{\infty} \frac{[\langle N_{\mathrm{tr}} \rangle e^{-k_{\mathrm{tr}} t} \hat{p}(t)]^{N_{\mathrm{tr}}}}{N_{\mathrm{tr}}!}, \tag{7.17}$$

which upon replacing $P_{\mathrm{Cds}}(t_0)$ with the initial amplitude A yields the final result:

$$P_{\mathrm{Cds}}(t) = A \exp[-k_0 t + \langle N_{\mathrm{tr}} \rangle (e^{-k_{\mathrm{tr}} t} \hat{p}(t) - 1)]. \tag{7.18}$$

To gauge the importance of intrinsic rate fluctuations, we approximate $\hat{p}(t)$ at the level of the second cumulant,

$$\hat{p}(t) \approx e^{\frac{\langle \delta^2 \rangle}{2} t^2}. \tag{7.19}$$

Including $\langle \delta^2 \rangle$ in the model functions leads to a negligible decrease in the reduced chi-square value (2% decrease) without appreciably changing the other fit parameters. Therefore, $\langle \delta^2 \rangle$ is a statistically insignificant parameter and the TA data are insensitive to fluctuations in the intrinsic rates.

7.4.4 Electron-transfer kinetics

The presence of H_2ase introduces ET as an additional pathway by which photoexcited electrons in CdS NRs can decay. Figure 7.6 shows the kinetic traces of CdS–H_2ase complexes with molar ratios of H_2ase:CdS in the range of 0.14:1 to 1.75:1. As the H_2ase:CdS molar ratio increases, the bleach feature of CdS recovers more quickly due to the increasing ET rate.[24] Mixing of CdS NRs and H_2ase to form complexes results in a distribution in the number of H_2ase adsorbed on each NR. At H_2ase:CdS molar ratios close to 1:1, we treat the adsorption events as independent of each other because H_2ase occupies a small fraction of the available surface area.[44] Thus, the number of H_2ase adsorbed on each CdS NR can be described by a Poisson distribution, $P\left(N_{\mathrm{H_2ase}}\right)$. To analyze the TA decays in Figure 7.6, we use a similar treatment as described above to account for the Poisson distributions of both the electron traps and adsorbed electron acceptors. This allows us to determine k_{ET} and the average number of H_2ase moieties adsorbed and capable of accepting an electron, $\langle N_{\mathrm{H_2ase}} \rangle$.

We arrive at the fitting equation by starting with a model for the conditional survival probabilities for photoexcited electrons in CdS NRs with both traps and adsorbed H_2ase moieties, $P_{\mathrm{CdS-H_2ase}}(t, N_{\mathrm{tr}}, N_{\mathrm{H_2ase}})$. The master equation for $P_{\mathrm{CdS-H_2ase}}(t, N_{\mathrm{tr}}, N_{\mathrm{H_2ase}})$ is

$$\begin{aligned} &\frac{dP_{\mathrm{CdS-H_2ase}}\left(t, N_{\mathrm{tr}}, N_{\mathrm{H_2ase}}\right)}{dt} \\ &= -\left(k_0 + k_{\mathrm{tr}} N_{\mathrm{tr}} + k_{\mathrm{ET}} N_{\mathrm{H_2ase}}\right) P_{\mathrm{CdS-H_2ase}}(t, N_{\mathrm{tr}}, N_{\mathrm{H_2ase}}). \end{aligned} \tag{7.20}$$

Just like the model discussed above, the term $k_{\mathrm{ET}} N_{\mathrm{H_2ase}}$ is the probability per unit time to decay to any of the $N_{\mathrm{H_2ase}}$ enzymes on the NR. The solution to this equation is

$$\begin{aligned} &P_{\mathrm{CdS-H_2ase}}(t, N_{\mathrm{tr}}, N_{\mathrm{H_2ase}}) \\ &\quad = P_{\mathrm{CdS-H_2ase}}(t_0, N_{\mathrm{tr}}, N_{\mathrm{H_2ase}}) e^{-\left(k_0 + k_{\mathrm{tr}} N_{\mathrm{tr}} + k_{\mathrm{ET}} N_{\mathrm{H_2ase}}\right)(t - t_0)}. \end{aligned} \tag{7.21}$$

Again, factorizing the initial conditions, $P_{\mathrm{CdS-H_2ase}}(t_0, N_{\mathrm{tr}}, N_{\mathrm{H_2ase}}) = P_{\mathrm{CdS-H_2ase}}(t_0)$. Assuming that the coverage of both enzymes and traps is low and that they do not interact, i.e., each is at a fixed chemical potential, the joint probability factorizes, $P(N_{\mathrm{tr}}, N_{\mathrm{H_2ase}}) = P(N_{\mathrm{tr}})P(N_{\mathrm{H_2ase}})$. Using the same model for each species as above,

$$P(N_{\mathrm{tr}}) = \frac{\langle N_{\mathrm{tr}}\rangle^{N_{\mathrm{tr}}} e^{-\langle N_{\mathrm{tr}}\rangle}}{N_{\mathrm{tr}}!} \tag{7.22}$$

$$P(N_{\mathrm{H_2ase}}) = \frac{\langle N_{\mathrm{H_2ase}}\rangle^{N_{\mathrm{H_2ase}}} e^{-\langle N_{\mathrm{H_2ase}}\rangle}}{N_{\mathrm{H_2ase}}!}. \tag{7.23}$$

Where $\langle N_{\mathrm{H_2ase}}\rangle$ and $\langle N_{\mathrm{tr}}\rangle$ are the average numbers of enzyme attached to the CdS NR and traps in the NR, respectively, at thermal equilibrium. $P_{\mathrm{CdS-H_2ase}}(t)$ is therefore

$$P_{\mathrm{CdS-H_2ase}}(t) = \sum_{N_{\mathrm{H_2ase}}=0}^{\infty} \sum_{N_{\mathrm{tr}}=0}^{\infty} P(N_{\mathrm{H_2ase}})P(N_{\mathrm{tr}})P_{\mathrm{CdS-H_2ase}}(t, N_{\mathrm{tr}}, N_{\mathrm{H_2ase}}) \tag{7.24}$$

$$= P_{\mathrm{CdS-H_2ase}}(t_0)e^{-k_0 t}\left[\sum_{N_{\mathrm{tr}}=0}^{\infty} P(N_{\mathrm{tr}})e^{-k_{\mathrm{tr}}N_{\mathrm{tr}}t}\right]\left[\sum_{N_{\mathrm{H_2ase}}=0}^{\infty} P(N_{\mathrm{H_2ase}})e^{-k_{\mathrm{ET}}N_{\mathrm{H_2ase}}t}\right] \tag{7.25}$$

$$\begin{aligned} &= P_{\mathrm{CdS-H_2ase}}(t_0)e^{-k_0(t-t_0)}\left[\exp\left\{\langle N_{\mathrm{tr}}\rangle\left(e^{-k_{\mathrm{tr}}(t-t_0)} - 1\right)\right\}\right] \\ &\quad \times\left[\exp\left\{\langle N_{\mathrm{H_2ase}}\rangle\left(e^{-k_{\mathrm{ET}}(t-t_0)} - 1\right)\right\}\right] \end{aligned} \tag{7.26}$$

$$\begin{aligned} &= P_{\mathrm{CdS-H_2ase}}(t_0)\exp\left\{-k_0(t-t_0) + \langle N_{\mathrm{tr}}\rangle\left(e^{-k_{\mathrm{tr}}(t-t_0)} - 1\right)\right. \\ &\quad \left. + \langle N_{\mathrm{H_2ase}}\rangle\left(e^{-k_{\mathrm{ET}}(t-t_0)} - 1\right)\right\} \end{aligned} \tag{7.27}$$

We replace $P(t_0)$ in favor of the initial amplitude, A:

$$P_{\mathrm{CdS-H_2ase}}(t) = A\exp\left[-k_0 t + \langle N_{\mathrm{tr}}\rangle(e^{-k_{\mathrm{tr}}t} - 1) + \langle N_{\mathrm{H_2ase}}\rangle(e^{-k_{\mathrm{ET}}t} - 1)\right] \tag{7.28}$$

To minimize the number of adjustable parameters, the fitting of this equation to the kinetic traces of CdS–H2ase complexes was performed by fixing the values of k_0, $\langle N_{\mathrm{tr}}\rangle$ and k_{tr} found from fitting CdS NRs alone to Equation (7.8) (Figure 7.6). This reflects the assumption

that ET introduces another decay pathway without changing the intrinsic CdS parameters in Table 3.1. This assumption is supported by the fact that allowing variation in k_0 and k_{tr} upon addition of H_2ase does not statistically improve the fit. A global fit of Equation (7.28) was performed such that recursive analysis converged upon the optimum value of k_{ET} that fits all four traces containing H_2ase in Figure 7.6 simultaneously while allowing $\langle N_{\mathrm{H_2ase}} \rangle$ to vary.

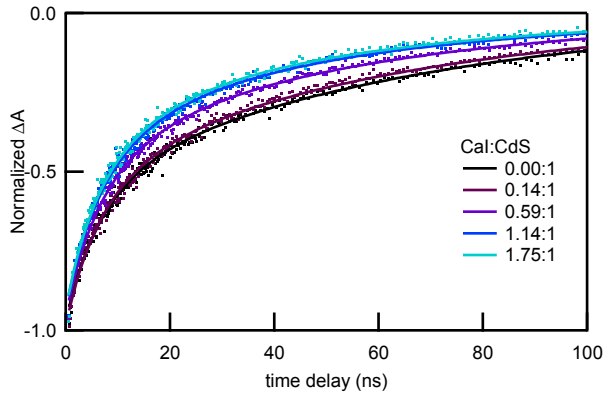

Figure 7.6. TA time traces of CdS–H_2ase complexes. TA kinetic decays of CdS–H_2ase complexes (points) at 470 nm for several ratios of H_2ase:CdS and fit functions from Equation (7.28) (solid lines). The ratios listed are the mixing molar ratios during sample preparation.

The fits of Equation (7.28) to the data are shown as solid lines in Figure 7.6. Extracted global fit parameters for ET are given in the last two columns of Table 3.1. Similar values were obtained when fitting our previously published electron decay kinetics in CdS–H_2ase complexes using Equation (7.8) and Equation (7.28) (Table 7.2). Because of possible variations in the CdS NR interaction with H_2ase, we examined the possibility that there is a distribution in the value of k_{ET}. Using the second cumulant approximation, we included a parameter representing the variance in the values of k_{ET}. A similar derivation as for fluctuations in the trapping rate, as described above, gives

$$P_{\mathrm{CdS-H_2ase}}(t) = A\exp\left\{-k_0 t + \langle N_{\mathrm{tr}}\rangle\left(e^{-k_{\mathrm{tr}}t}\hat{p}_{\mathrm{tr}}(t) - 1\right) + \langle N_{\mathrm{H_2ase}}\rangle\left(e^{-k_{\mathrm{ET}}t}\hat{p}_{\mathrm{ET}}(t) - 1\right)\right\}, \tag{7.29}$$

where $\hat{p}_{\mathrm{tr}}(t)$ and $\hat{p}_{\mathrm{ET}}(t)$ are the moment generating functions for the distributions in trapping and ET rate fluctuations, $p(\delta_{\mathrm{tr}})$ and $p(\delta_{\mathrm{ET}})$, respectively. Using the second cumulant approximation $\hat{p}_{\mathrm{ET}}(t) \approx e^{\langle\delta_{\mathrm{ET}}^2\rangle t^2/2}$, including fluctuations in the rates for ET does not statistically improve the fit (reduced chi-squared decreases by 0.05%), indicating that a model with one representative value of k_{ET} is sufficient to describe the TA data reported here. This implies that, while variations in k_{ET} may exist, they do not make a measurable contribution to the TA decays reported here.

To assess the reproducibility of fit parameters found in this study, we apply our analysis to previously published data on the decay kinetics of CdS–H_2ase complexes.[24] The CdS NRs used for that data set come from the same synthesis batch as the ones used above. The fitting parameters obtained by fitting the data in Figure 7.7 to Equation (7.8) and Equation (7.28) are summarized in Table 7.2. The values of k_0, k_{tr}, and $\langle N_{\mathrm{tr}}\rangle$ in Table 7.2 are consistent with those in Table 3.1 within the 95% confidence integral, indicating that the behavior described here is reproducible for CdS NRs made in the same synthesis. The value of k_{ET} obtained from this data set also agrees with that of the data set in Figure 7.6, within the confidence interval.

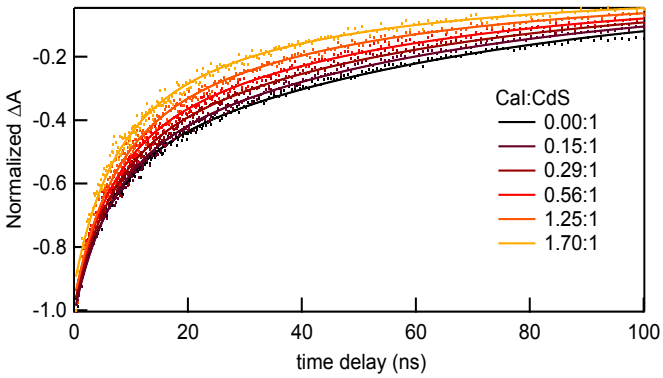

Figure 7.7. TA time traces of second CdS–H_2ase sample. Band gap TA kinetics of CdS–H_2ase complexes for various ratios H_2ase:CdS. The data (dots) with H_2ase are fit (solid lines) with Equation (7.28) by a global fit. Ratios listed are the relative concentrations upon mixing during sample preparation.

Table 7.2. Summary of fitting parameters for second CdS NR sample

H_2ase:CdS molar ratio	k_0 (10^7 s^{-1})[a]	$\langle N_{tr}\rangle$[a]	k_{tr} (10^8 s^{-1})[a]	$\langle N_{H_2ase}\rangle$[b]	k_{ET} (10^7 s^{-1})[b]
0.00:1	1.54 ± 0.08	0.57 ± 0.03	1.1 ± 0.2	–	–
0.15:1	1.54 ± 0.08	0.57 ± 0.03	1.1 ± 0.2	0.17 ± 0.02	2.2 ± 0.3
0.29:1	1.54 ± 0.08	0.57 ± 0.03	1.1 ± 0.2	0.30 ± 0.02	2.2 ± 0.3
0.56:1	1.54 ± 0.08	0.57 ± 0.03	1.1 ± 0.2	0.44 ± 0.03	2.2 ± 0.3
1.25:1	1.54 ± 0.08	0.57 ± 0.03	1.1 ± 0.2	0.70 ± 0.04	2.2 ± 0.3
1.70:1	1.54 ± 0.08	0.57 ± 0.03	1.1 ± 0.2	0.99 ± 0.05	2.2 ± 0.3

[a] Values found by fitting CdS NR kinetic trace (Figure 7.7) according to Equation (7.8).
[b] Result of global fit of data in Figure 7.7 to Equation (7.28) by holding k_0, k_{tr}, and $\langle N_{tr}\rangle$ fixed, defining k_{ET} as a global variable between data sets containing H_2ase and allowing $\langle N_{H_2ase}\rangle$ to vary.
Uncertainties associated with each fit parameter are 95% confidence intervals.

7.4.5 Error analysis for k_0, $\langle N_{tr}\rangle$, k_{tr}, $\langle N_{CdI}\rangle$ and k_{ET}

To determine the fit parameters k_0, $\langle N_{tr}\rangle$, k_{tr}, $\langle N_{H_2ase}\rangle$ and k_{ET} and their uncertainties, we employed the bootstrapping Monte Carlo method.[131] Distributions for model parameters and their correlations come from generating 10,000 synthetic datasets by resampling the original data with replacement and performing nonlinear least squares fits for each set. The fit parameters that

minimize the chi-square value from this process are distributed around the parameters of best fit (Table 3.1). Joint parameter distributions for particular pairs appear in Figure 7.8.

Bootstrapping data indicate strong correlations between fit parameters as one might expect from such a nonlinear, multi-parameter data model. These correlations imply that standard error estimates of each parameter taken individually are insufficient to represent the uncertainties for all parameters simultaneously. The uncertainties reported for the fit parameters in Table 3.1 include covariances between parameters and represent the 95% confidence in the multidimensional parameter space.[131]

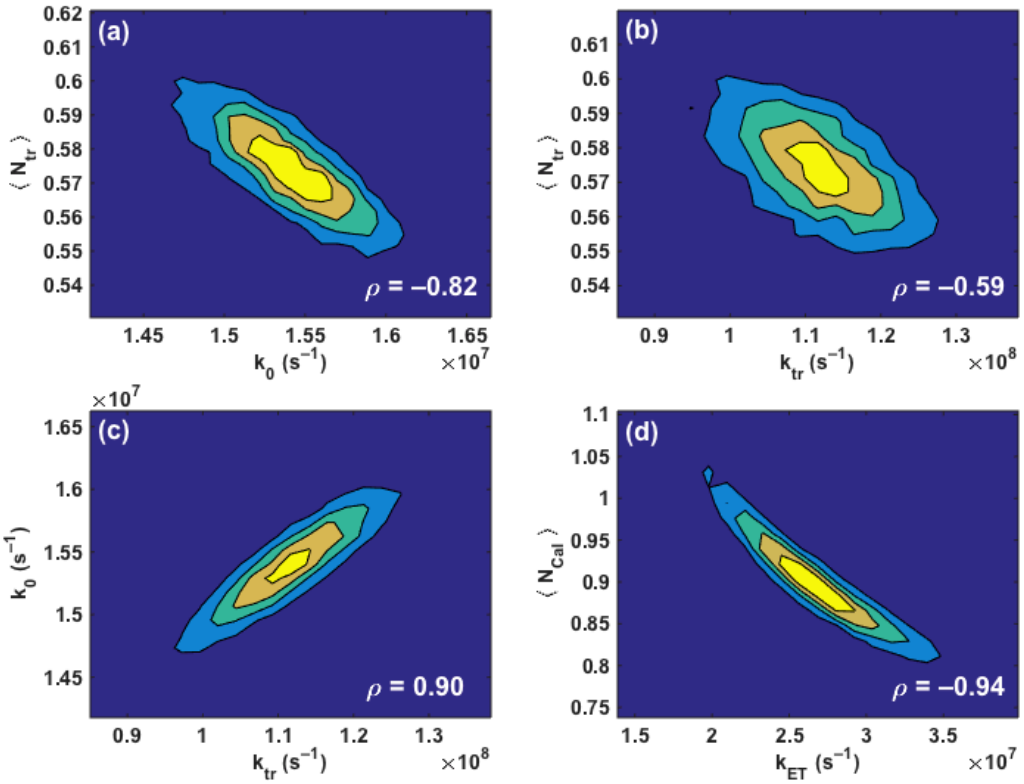

Figure 7.8. Joint probability distributions for parameter pairs generated by bootstrapping Monte Carlo resampling. Parameter distributions are shown pairwise for (a) $\langle N_{\mathrm{tr}} \rangle$ and k_0; (b) $\langle N_{\mathrm{tr}} \rangle$ and k_{tr}; (c) k_{tr} and k_0, and; (d) $\langle N_{\mathrm{H_2ase}} \rangle$ and k_{ET}. The distribution in (d) was produced from the 1.70:1 data set from Table 7.2. Pearson's correlation coefficient for each pair of parameters, ρ, appears in each panel of the figure.

7.4.6 Electron transfer efficiency

The value of k_{ET} (2.4×10^7 s^{-1}) for ET from photoexcited CdS to H_2ase is within an order of magnitude of k_0 and k_{tr} for CdS NRs, resulting in a direct competition between these processes. While k_0 and k_{tr} are properties of CdS NRs, k_{ET} is determined by the electron pathway, which involves electron tunneling for a considerable distance from the NR surface to the distal [FeS] cluster of the enzyme.[24] The values of $\langle N_{H_2ase}\rangle$ in Table 3.1 increase with increasing H_2ase:CdS molar ratios and are consistently smaller than the mixing ratios. This observation may point to the presence of H_2ase adsorbed with orientations that prevent ET and/or to an equilibrium adsorption/desorption process that leaves some H_2ase free in solution.

For each individual CdS–H_2ase complex in the ensemble, competition between the processes described by k_0, k_{tr} and k_{ET} depends on the number of traps and enzymes adsorbed (N_{tr} and N_{H_2ase}). For each CdS–H_2ase complex,

$$QE_{ET} = \frac{k_{ET}N_{H_2ase}}{\left(k_0 + k_{tr}N_{tr} + k_{ET}N_{H_2ase}\right)}. \tag{7.30}$$

For example, in the case of a CdS NR with zero traps and one H_2ase adsorbed, $QE_{ET} = 62\%$, while for a NR with one trap and one H_2ase, $QE_{ET} = 16\%$. Note that dividing the numerator and denominator of this expression by k_0 reveals that QE_{ET} does not depend on the individual values of the intrinsic rates. Rather, it depends only on the ratios k_{ET}/k_0 and k_{tr}/k_0. To understand the contribution of each electron decay process to photochemical H_2 generation in solutions of CdS–H_2ase complexes, it is important to examine the behavior of QE_{ET} for the ensemble sample. This is commonly done using average lifetimes for the nonexponential decays:

$$QE_{ET} = 1 - \frac{\langle\tau_{CdS\text{–}H_2ase}\rangle}{\langle\tau_{CdS}\rangle} = 1 - \frac{\int_0^\infty dt\, P_{CdS\text{–}H_2ase}(t)}{\int_0^\infty dt\, P_{CdS}(t)} = 1 - \frac{\int_0^\infty d(k_0t) P_{CdS\text{–}H_2ase}(k_0t)}{\int_0^\infty d(k_0t) P_{CdS}(k_0t)}. \tag{7.31}$$

In implementing this approach, $P_{\mathrm{CdS}}(t)$ and $P_{\mathrm{CdS\text{–}H_2ase}}(t)$ are the fits of TA kinetics of CdS NRs to Equation (7.8) and CdS–H_2ase complexes to Equation (7.28), respectively.[84] Changing integration variables in the expression for the quantum yield from t to $k_0 t$ as in the second part of Equation (7.31) shows that the quantum yield of electron transfer depends only on the ratio of rate constants, so that there are two degrees of freedom and not three for fixed values of $\langle N_{\mathrm{tr}} \rangle$ and $\langle N_{\mathrm{H_2ase}} \rangle$. That is, $\mathrm{QE_{ET}}(k_0, k_{tr}, k_{ET}) = \mathrm{QE_{ET}}(k_{tr}/k_0, k_{ET}/k_0)$. Figure 7.9 shows $\mathrm{QE_{ET}}(k_{tr}/k_0, k_{ET}/k_0)$, evaluated by numerical integration of Equation (7.31) using the value of $\langle N_{\mathrm{tr}} \rangle$ given in Table 3.1 and $\langle N_{\mathrm{H_2ase}} \rangle = 1$. For this system, $\mathrm{QE_{ET}}$ of the ensemble depends strongly on k_{ET}/k_0 but weakly on k_{tr}/k_0. To further illustrate the behavior of ensemble $\mathrm{QE_{ET}}$, using the values of k_0, $\langle N_{\mathrm{tr}} \rangle$, k_{tr} and k_{ET} given in Table 3.1, the $\mathrm{QE_{ET}}$ would be 41% for $\langle N_{\mathrm{H_2ase}} \rangle = 1$. If $\langle N_{\mathrm{tr}} \rangle = 0$, the $\mathrm{QE_{ET}}$ would only increase to 43%. The small impact that trapping has on $\mathrm{QE_{ET}}$ reflects the fact that $\langle N_{\mathrm{tr}} \rangle$ is already small. Increasing $\langle N_{\mathrm{H_2ase}} \rangle$ above 1 would increase $\mathrm{QE_{ET}}$, but this strategy decreases H_2 production, as we have shown previously.[44] H_2 generation requires transfer of two electrons to the same H_2ase moiety, and if multiple H_2ase are adsorbed on each NR, they compete for the second electron.[24,44] In an ensemble, there is an upper limit on the maximum achievable value of $\mathrm{QE_{ET}}$, $\mathrm{QE_{ET}^{max}}$. For a given $\langle N_{\mathrm{H_2ase}} \rangle$, the fraction of NRs that do not have any H_2ase attached and thus do not undergo ET determines $\mathrm{QE_{ET}^{max}}$. From Poisson statistics, the fraction of NRs with one or more H_2ase adsorbed is $1 - e^{-\langle N_{\mathrm{H_2ase}} \rangle}$. The saturation value is therefore $\mathrm{QE_{ET}^{max}} = 1 - e^{-\langle N_{\mathrm{H_2ase}} \rangle}$. For $\langle N_{\mathrm{H_2ase}} \rangle = 1$, $\mathrm{QE_{ET}^{max}} = 63\%$. The ensemble value of 41% at $\langle N_{\mathrm{H_2ase}} \rangle = 1$ achieved with the rate constants characteristic of our current system is already ~2/3 of $\mathrm{QE_{ET}^{max}}$. Because the most important quantity in determining $\mathrm{QE_{ET}}$ is k_{ET}/k_0, increasing k_{ET}, decreasing k_0, or changing both to increase the ratio increases the quantum efficiency for electron transfer. Figure 7.9b shows the

predicted values of QE_{ET} as a function of k_{ET}/k_0, for fixed values of $\langle N_{tr} \rangle$ and k_{tr} when $\langle N_{H_2ase} \rangle = 1$. The circles in Figure 7.9a and b mark the $QE_{ET} = 41\%$ calculated when the values for all parameters take on those that are measured in this study (Table 3.1). The quantum efficiency saturates to $\approx 63\%$ when $k_{ET}/k_0 \approx 100$. Thus, a relatively modest increase in k_{ET}/k_0 by a factor of 10-100 would be sufficient to approach QE_{ET}^{max}. This could be achieved through synthetic modifications of nanocrystal surface chemistry and band structure. For example, surface-capping ligands can strongly influence ET rates from a nanocrystal to an acceptor.[8] Thus k_{ET} could be increased through ligand manipulation. Alternatively, type-II nanocrystals with long-lived charge separated states could decrease k_0.[113,161]

Finally, we compare a previously reported value of quantum yield of H_2 generation with QE_{ET} of a corresponding ensemble sample of CdS–H_2ase. In our prior work, H_2 quantum yield was 20% for a CdS–H_2ase solution with a CdS:H_2ase molar ratio of 0.67.[44] Interestingly, the value of QE_{ET} with the same value of CdS:H_2ase, obtained by interpolating between data points in Table 3.1, is 21%. This similarity suggests that H_2ase converts electrons from photoexcited CdS NRs into H_2 with close to 100% efficiency and illustrates the remarkable electrocatalytic properties of H_2ase.[214] It also highlights the point that the key to improving H_2 production is in increasing QE_{ET}.

It is important to note that the method of Equation (7.31), which relies on the average lifetimes of nonexponential heterogeneous ensemble decays, is not an exact treatment. The results for QE_{ET} found here should be thought of as approximate values that do not account for competition between ET and NR relaxation at the single-particle level. Calculating QE_{ET} exactly is the subject of Chapter 9.

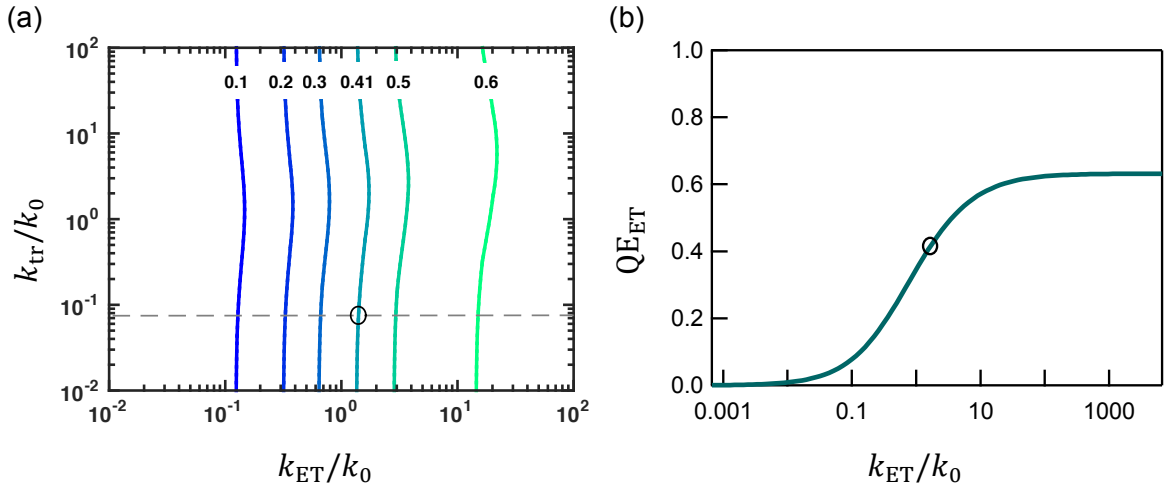

Figure 7.9. Quantum efficiency of electron transfer, QE_{ET}, for $\langle N_{H_2ase}\rangle = 1$. (a) Contour plot of QE_{ET} as a function of k_{tr}/k_0 and k_{ET}/k_0. Contour lines of constant QE_{ET}, where the labels denote the values of the contours, run roughly parallel to the y-axis indicating that the quantum yield for electron transfer depends very weakly on k_{tr}/k_0 when $\langle N_{tr}\rangle$ and $\langle N_{H_2ase}\rangle$ take on the values determined by fits to our data model. The gray dashed line in (a) marks the slice of the data plotted in (b). The circle in both graphs indicates the point in parameter space where the CdS–H_2ase system currently lies. QE_{ET} = 41% when k_0, $\langle N_{tr}\rangle$, k_{tr} and k_{ET} take on the values presented in Table 3.1 ($k_{tr}/k_0 = 7.3$ and $k_{ET}/k_0 = 1.6$). (b) QE_{ET} as a function of k_{ET}/k_0 where k_0, $\langle N_{tr}\rangle$ and k_{tr} values given in Table 3.1. This trace corresponds to the gray dashed line in (a). The circle shows the point where QE_{ET} = 41% ($k_{ET}/k_0 = 1.6$), which is the QE_{ET} we find from the fits to the TA data (Table 3.1).

7.4.7 The quotient method

If the presence of an electron acceptor does not impact the intrinsic relaxation of the donor, as was the case for the CdS–H_2ase system with 3-MPA ligands studied here, then the quotient of the donor–acceptor decay and the donor decay cancels out the donor decay, yielding the isolated charge transfer kinetics. For instance, dividing Equation (7.28) by Equation (7.8) gives

$$\frac{P_{CdS-H_2ase}(t)}{P_{CdS}(t)} = \frac{P_{CdS}(t)f_{ET}(t)}{P_{CdS}(t)} = f_{ET}(t) = A\exp\left[\langle N_{H_2ase}\rangle(e^{-k_{ET}t} - 1)\right]. \quad (7.32)$$

This approach can be applied to extract $\langle N_{H_2ase}\rangle$ and k_{ET} in CdS–H_2ase (Figure 7.10), giving fitted values that are within error of those found when fitting the CdS and CdS–H_2ase decay

traces to Equation (7.8) and then Equation (7.28), respectively. The quotient method can be employed without a physically motivated kinetic model for the donor decay, making it useful for diagnostic purposes when establishing the functional form for decay due to electron transfer as well as a means to study charge transfer kinetics for an unknown, arbitrary donor decay.

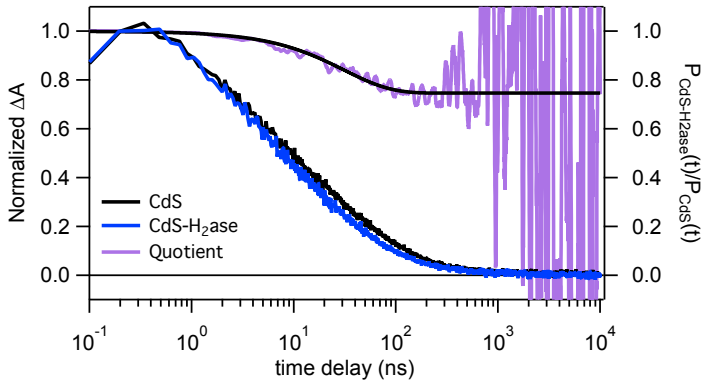

Figure 7.10. Demonstration of the quotient method applied to CdS–H_2ase electron trasnfer kinetics. TA time traces of second CdS–H_2ase sample. Band gap TA kinetics of CdS and CdS–H_2ase complexes are shown, as well as the quotient of the CdS–H_2ase decay trace over the CdS decay trace. The quotient is fit to Equation (7.32).

7.5 Conclusions

In summary, we have shown that a kinetic model that includes distributions in electron traps and adsorbed enzymes describes the kinetics of ET between CdS NRs and H_2ase in the time window of 1–100 ns. The model allows us to determine the intrinsic rate constants for electron-hole recombination, electron trapping, and ET. QE_{ET} depends strongly on the ratio of the rate constants for ET and electron-hole recombination, but only weakly on electron trapping. The maximum QE_{ET} saturates at a value determined by the fraction of NRs with no H_2ase moieties adsorbed. The current CdS–H_2ase system has a QE_{ET} value that is two-thirds of the maximum. The relatively simple model used here captures the essential kinetics of ET and provides guidance on the relevant design parameters that could be manipulated to optimize photochemical redox reactions using nanocrystal-enzyme hybrids.

Chapter 8

The Role of Surface-Capping Ligands in Photoexcited Electron Transfer between CdS Nanorods and [FeFe] Hydrogenase and the subsequent H2 Generation**

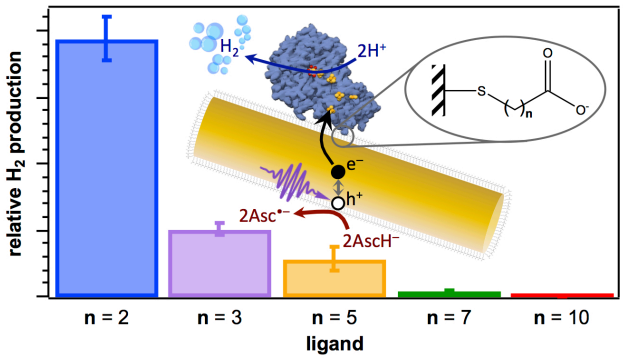

8.1 Abstract

Complexes of CdS nanorods and [FeFe] hydrogenase from *Clostridium acetobutylicum* have been shown to photochemically produce H_2. This study examines the role of the ligands that passivate the nanocrystal surfaces in the electron transfer from photoexcited CdS to hydrogenase and the H_2 generation that follows. We functionalized CdS nanorods with a series of mercaptocarboxylate surface-capping ligands of varying lengths and measured their photoexcited electron relaxation by transient absorption (TA) spectroscopy before and after hydrogenase adsorption. Rate constants for electron transfer from the nanocrystals to the enzyme, extracted by

Adapted with permission from Wilker, M. B.; Utterback, J. K.; Greene, S.; Brown, K. A.; Mulder, D. W.; King, P. W.; Dukovic, G. *J. Phys. Chem. C* **2018, *122*(1), 741-750. Copyright © 2018 American Chemical Society). This publication is based on a previously published thesis chapter: Wilker, M. B. Charge Transfer Dynamics in Complexes of Light-Absorbing CdS Nanorods and Redox Catalysts. *University of Colorado Boulder, Chemistry & Biochemistry Graduate Theses & Dissertations*, **2015**.

modeling of TA kinetics, decrease exponentially with ligand length, suggesting that the ligand layer acts as a barrier to charge transfer and controls the degree of electronic coupling. Relative light-driven H_2 production efficiencies follow the relative quantum efficiencies of electron transfer, revealing the critical role of surface-capping ligands in determining the photochemical activity of these nanocrystal–enzyme complexes. Our results suggest that the H_2 production in this system could be maximized with a choice of a surface-capping ligand that decreases the distance between the nanocrystal surface and the electron injection site of the enzyme.

8.2 Introduction

Architectures that couple cadmium chalcogenide nanocrystals with redox enzymes have emerged as an intriguing strategy to use light to drive multi-electron redox reactions such as proton reduction to H_2, CO_2 reduction to CO, and N_2 fixation to NH_3.[12,24,30,31,44-46,65,99,101,215,216] These systems all operate on a similar general principle: light absorption in the nanocrystal is followed by electron transfer (ET) to the enzyme, which stores and uses the electrons for the multi-electron reduction reaction. Holes are scavenged by sacrificial electron donors, most frequently ascorbate. Because the electrons in the final photochemical product arrive from the nanocrystals, the kinetics of the ET step play a critical role in the overall photochemistry, as we showed in the example of CdS nanorods (NRs) and an [FeFe] hydrogenase (H_2ase).[24,65] In particular, ET competes with electron–hole recombination and electron trapping in the nanocrystal. The interplay of the rates for these processes determines quantum efficiency of ET (QE_{ET}), which in turn defines the upper limit of the overall photochemical efficiency.[24,65,217] In the CdS–H_2ase system, QE_{ET} depends strongly on the ratio of the ET and recombination rate constants such that an order of magnitude change in either variable can alter the end result dramatically.[65] As this

example illustrates, understanding the factors that govern the kinetics of ET and the competing processes in the nanocrystal is critical to controlling light-driven redox chemistry of nanocrystal–enzyme complexes.

In nanocrystal–enzyme architectures in general, and the CdS–H_2ase system in particular, the interface between the light absorber and the catalyst is determined by the capping ligands on the nanocrystal surface. Evidence suggests that CdS–H_2ase complexes form via an electrostatic interaction in which CdS NRs, capped with negatively-charged mercaptopropionate ligands, bind to a positively charged region on H_2ase.[24,30,31,44,65] This biomimetic interaction is analogous to the binding of ferredoxin, the natural electron donor partner of H_2ase,[30,44] allowing the electrons from the nanocrystals to be injected at the same iron-sulfur cluster in both cases.[24,218] The surface-capping ligands may play multiple roles in ET and the overall photochemistry. They enable the solubility of complexes in aqueous buffer and facilitate the electrostatic nanocrystal–enzyme binding via the negative carboxylate groups. Surface-capping ligands also affect the competing relaxation pathways, especially the electron trapping on the nanocrystal surface.[26] Finally, our working model of the nanocrystal–enzyme interaction suggests that the ligands impact the electronic coupling between CdS and the electron injection site of H_2ase.

In this work, we examine how surface-capping ligands on CdS NRs impact ET kinetics and photochemical H_2-production rates. Specifically, we use a sequence of mercaptocarboxylate ligands with varying aliphatic chain lengths while keeping the ligand functional groups that govern the interactions between the nanocrystal and the enzyme constant. To determine the ET rates in each CdS–H_2ase system, we measured the relaxation dynamics of photoexcited electrons in CdS NRs with and without H_2ase using transient absorption (TA) spectroscopy. We analyzed the data using a kinetic model that allowed us to extract the rate constants for electron–hole

recombination, electron trapping, ET, and the average number of enzymes adsorbed, all of which were ligand-dependent. Each sample of CdS NRs capped with a ligand of different length exhibited slightly different photoexcited electron decay kinetics due to the impact of ligands on nanocrystal photophysics. Once mixed with H_2ase, the number of enzymes adsorbed also varied with ligand length. Most notably, the rate constant of ET decreased exponentially with increasing ligand length. This strong dependence suggests that the surface-capping ligands form a bridge between the nanocrystal donor and the enzyme acceptor, consistent with our model of the nanocrystal–enzyme interaction.[44] Similar to other nanocrystal–acceptor systems,[98,219-227] the ligand acts as a bridge with weak electronic coupling that falls off rapidly with distance. We also report a significant decrease in the quantity of photogenerated H_2 as the length of the nanocrystal surface ligand increases. By comparing QE_{ET} with H_2 production, we show that, although not the only factor that determines H_2 production, the competitiveness of ET with the other electron relaxation processes plays a governing role in the photocatalytic efficiency of this system. This, in turn, suggests that ET efficiency could be controlled with judicious choice of surface-capping ligands that enhance both the electronic coupling and enzyme adsorption.

This work represents a close collaboration between the co-authors of the published article on which this chapter is based.[14] Dr. Molly Wilker, who was the lead author on that article, carried out the experimental work, including the nanocrystal synthesis, ligand exchange, TA spectroscopy experiments and H_2-production experiments. An early version of this work appears in Wilker's dissertation,[228] as she graduated before the project was completed. My role was in carrying out the kinetic modeling, analysis of the TA data, error analysis, and QE_{ET} calculations.

8.3 Methods

8.3.1 Nanocrystal preparation and characterization

The seeded synthesis of CdS NRs was adapted from a published procedure and is described in Chapter 2.[46,121] The resulting NRs had average diameters of 3.7 ± 0.3 nm and an average length of 22.6 ± 1.8 nm as determined by measurements of 300 particles in transmission electron microscopy (TEM) images. The molar absorptivity (ε) of the CdS NRs was determined by correlating absorption spectra with Cd^{2+} concentrations determined by elemental analysis (ICP-OES). The estimated value of ε_{350} was 1710 M^{-1} cm^{-1} per Cd^{2+}. The number of Cd^{2+} per NR was estimated from the average NR dimensions. ε_{350} was 8.6 x 10^6 M^{-1} cm^{-1}. The hydrophobic surface-capping ligands on the as-synthesized CdS NRs were replaced with mercaptocarboxylate ligands following the previously reported procedure, and the resulting particles were redispersed in 12.5 mM Tris buffer, pH 7.[44]

The length of each ligand, defined as the distance between the center of the S atom to the center of the furthest O atom in the carboxylate, was estimated based on alkyl chain C–C bond lengths of 1.523 Å, C–C bond lengths of 1.509 Å for the carboxylate carbon, carboxylate $C–O^-$ bond lengths of 1.250 Å, C–S bond lengths of 1.815 Å, C–C–C and C–C–S bond angles of 109.5º, and carboxylate $C–C–O^-$ bond angles of 120º.

8.3.2 H_2ase purification, characterization, and coupling to CdS NRs

The [FeFe] hydrogenase from *Clostridium acetobutylicum* (CaI) was expressed and purified from *Escherichia coli* as previously described with some modifications (Chapter 2).[127] Mixtures of CdS NRs and H_2ase were prepared in buffer (12.5 mM Tris-HCl, 5mM NaCl, 5% glycerol, pH 7) under an anaerobic Ar environment.

8.3.3 Transient absorption spectroscopy

The TA experimental setup was previously described in detail.[116] The samples were prepared and sealed under Ar in airtight 2 mm quartz cuvettes. The CdS NR sample concentration was 800 nM. The samples containing both NRs and H_2ase were mixed in 1:1 molar ratios in buffer C. The samples were pumped at 401 nm. The pump beam diameter was 240 μm and pulse energy was 10 nJ/pulse. The pump power was chosen such that the TA time traces were independent of pump power, indicating that the signal is dominated by NRs with single excitons. The samples were stirred during data collection.

8.3.4 Light-driven H_2 production

Solutions for light-driven H_2 production consisted of 40 nM CdS and 40 nM H_2ase (1:1 molar ratio) with 100 mM ascorbate as a hole scavenger in buffer in 1.5 mL vials sealed with septa. The samples were illuminated with a 405 nm diode laser (Laserglow Technologies) at 12 mW for 10 min. H_2 was detected in the headspace of the vessel by injecting a sample of headspace atmosphere into a gas chromatograph (Agilent Technologies 7820A, molecular sieve 5A column, Ar carrier gas, TCD detector).

8.3.5 Photoluminescence (PL) Spectra of CdS NR samples

PL spectra were obtained at room temperature using a Horiba Jobin Yvon Fluorolog-3 Spectrofluorometer with a 450W xenon arc lamp and a R928P Photomultiplier tube. Samples in 1 cm × 1 cm quartz cuvettes were excited at 350 nm and the emission from 365 nm to 685 nm was recorded at 90° relative to the excitation. PL spectra were corrected for wavelength dependence of the instrument response using a tungsten lamp provided by the manufacturer. CdS NR concentration was 0.18 μM in 12.5 mM Tris-HCl Buffer, pH 7.

8.4 Results

To examine the effect of ligand length on ET kinetics and H_2 production in CdS–H_2ase complexes, CdS NRs with an average diameter of 3.7 ± 0.3 nm and an average length of 22.6 ± 1.8 nm (Figure 8.1) were capped with mercaptocarboxylate surface ligands of the form $HS{-}(CH_2)_{\mathbf{n}}{-}COO^-$ with **n** = 2, 3, 5, and 7. These ligands will be referred to by their **n**-value throughout this chapter. After CdS NR synthesis, the native octadecylphosphonic acid (ODPA) ligands were exchanged with each of these ligands as detailed in the Methods. The ligand exchange to all of the mercaptocarboxylates causes the band edge absorption to shift 2 nm to the blue, but does not significantly alter the shape of the absorption spectrum (Figure 8.2 and Figure 8.3). The blue shift is a signature of the removal of some surface metal ions, which can be displaced as complexes with native ligands during the process of ligand exchange to place thiol ligands on the surface.[28,229-231] The ligand-exchanged particles are soluble in aqueous solutions as the carboxylate end groups are deprotonated at pH 7.[232]

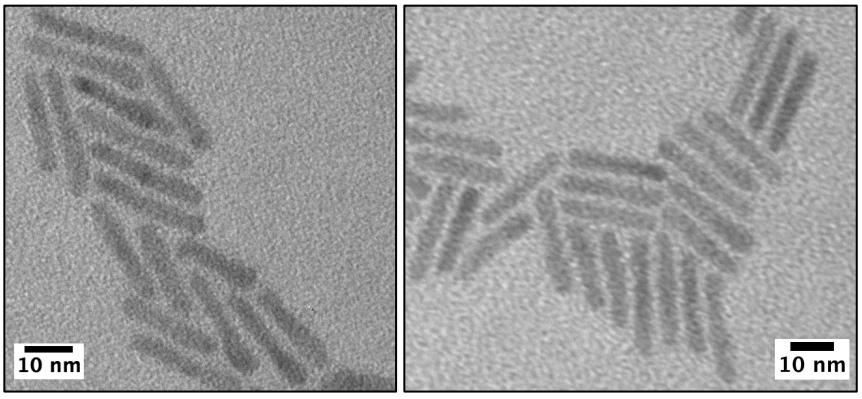

Figure 8.1. TEM images of CdS NRs capped with native ligands.

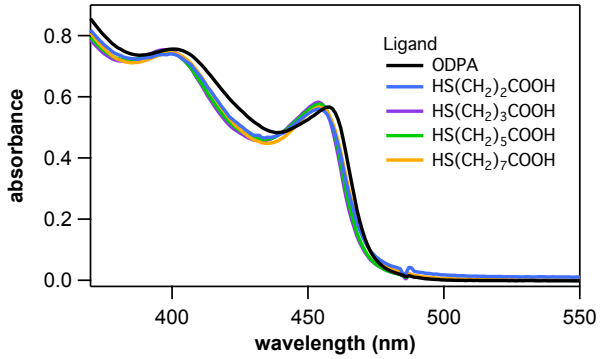

Figure 8.2. Normalized steady-state absorption spectrum of CdS NRs with various surface-capping ligands.

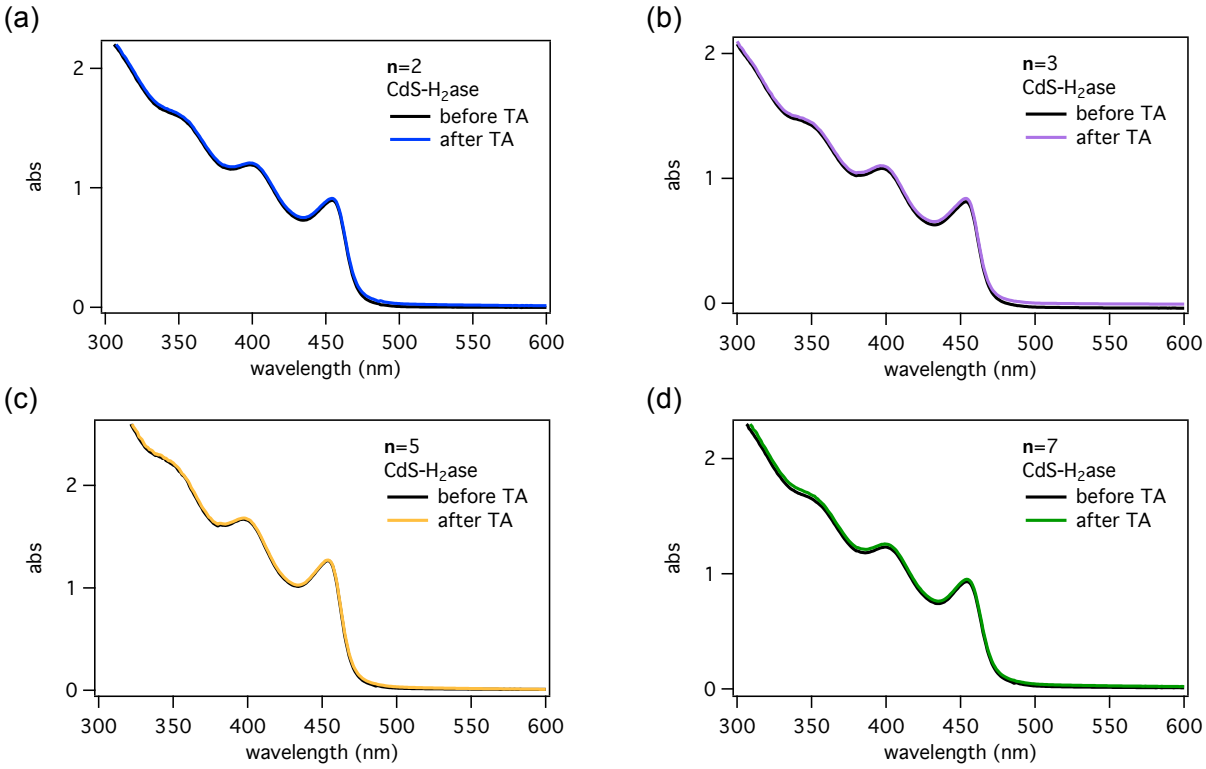

Figure 8.3. Steady state absorption spectra of CdS–H_2ase complexes in buffer solution before and after collecting TA data. The absence of spectral changes demonstrates stability of the complexes in solution throughout the data collection time period.

The steady-state photoluminescence (PL) spectra of photoexcited CdS NRs consist of two distinct emission features—a higher energy peak from band-gap emission and a broad, lower energy peak from trap emission.[233,234] Each of the PL spectra can be fit with three Gaussians (Figure 8.4). Two Gaussians are necessary to fit the band gap PL.[130] This is because of the wider

"bulb" structural feature of these nanorods as well as the "rod" structure.[130] The bulb region has a smaller band gap and therefore a red-shifted peak in the absorption and emission spectra. Wu *et al*. previously showed that band-gap emission can unambiguously be assigned to overlapping rod and bulb emission peaks, and the lower energy bulb peak cannot be attributed to sub-band gap transitions such as an Urbach tail.[130] The third, broad Gaussian fits to the trap emission feature. From the CdS NR PL spectra, we observe that changing the nanocrystal surface ligands causes the relative intensities of the PL peaks to change but their positions and widths are similar from sample to sample (Table 8.1).

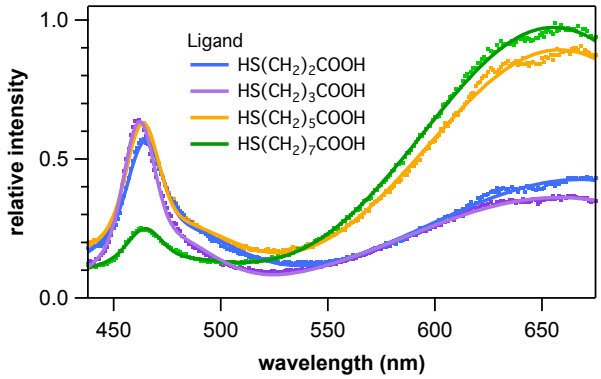

Figure 8.4. Steady state emission from CdS NRs with various ligands after excitation with 350 nm light (dotted lines). The spectra are fit with a sum of three Gaussian peaks (solid lines).

Table 8.1. Fit parameters for the peaks in the PL spectra

Ligand	Feature	A^a	λ_0 (nm)	σ (nm)
n = 2	rod	1.00 ± 0.02	464.6 ± 0.1	7.5 ± 0.1
	bulb	3.87 ± 0.09	470.4 ± 0.4	33.0 ± 0.6
	trap	13.9 ± 0.3	669 ± 2	73 ± 1
n = 3	rod	1.23 ± 0.02	461.8 ±0.1	6.8 ± 0.1
	bulb	2.54 ± 0.07	468.8 ± 0.4	25.0 ± 0.4
	trap	11.6 ± 0.2	658 ± 2	72 ± 1
n = 5	rod	1.11 ± 0.03	463.5 ± 0.1	7.1 ± 0.1
	bulb	4.2 ± 0.1	469.5 ± 0.6	33.9 ± 0.7
	trap	24.7 ± 0.2	658.1 ± 0.6	62.0 ± 0.5
n = 7	rod	0.33 ± 0.03	464.4 ± 0.3	7.4 ± 0.4
	bulb	2.4 ± 0.1	466.2 ± 0.9	37 ± 1
	trap	26.6 ± 0.2	655.4 ± 0.3	61.2 ± 0.4

[a] Amplitudes are normalized relative to rod amplitude of the **n** = 2 ligand.

The sample-to-sample variation in the spectral peak intensity of both band-gap and trap emission indicates that the ligand exchange process introduces small changes to the excited state relaxation. This data suggests that there are differences in the intrinsic excited-state decay kinetics of the CdS nanorods with the varying ligands even before coupling with H_2ase.

Photoluminescence (PL) spectra of all samples have similar band-edge and trap emission peak positions and widths, but their relative intensities vary from sample to sample. This implies variations in the excited-state relaxation of the CdS NRs with the different ligands even before coupling with H_2ase. We examine those differences using TA spectroscopy.

8.4.1 Photoexcited electron relaxation of CdS NRs with varying surface-capping ligands

In order to extract ET kinetics in CdS–H_2ase complexes, we first address the photoexcited electron relaxation in CdS NRs capped with **n** = 2, 3, 5, 7 mercaptocarboxylate ligands with no enzyme present. The relaxation dynamics of similar CdS NRs have been studied extensively by TA spectroscopy.[23,24,35,64,65,130] These studies provide the background for understanding the effects of the varying surface-capping ligands on CdS NR photophysics, and we describe our results in the context of this prior work. It has been shown that samples of CdS NRs contain structures that are not uniform along the rod length.[130] Instead, they contain a wider region, which has been referred to as the "bulb", along the "rod" structure. TA spectra of photoexcited CdS NRs exhibit a transient bleach feature peaked at 457 nm corresponding to the band-edge electron population (Figure 8.5).[23,114] Ultrafast (~200 fs) 401 nm pulses excite primarily the rod population.[130] This process is followed by fast (<1 ps) cooling to the band edge.[23,114] Photoexcited holes rapidly (~1 ps) trap to the NR surface.[23,56] After electron cooling, there is a partial decay of the 457 nm peak and a corresponding growth of a broad bleach feature around 479 nm due to electron localization from the rod to the lower energy bulb (Figure 8.5).[64,130] The

spectral features corresponding to the rod and the bulb are also apparent in the PL spectra (Figure 8.4), as described previously.[130] The timescale (~4 ps) and efficiency (~25%) for electron localization are similar for all four ligands (Figure 8.6). The fraction of CdS NRs that undergo localization are 24%, 25%, 26% and 27% for ligands **n** = 2, 3, 5, and 7, respectively. After this process is complete, the kinetics of the rod and bulb bleach recovery reflect the decay of photoexcited electrons by two pathways: recombination with a trapped hole and electron trapping.[64,130] The rod comprises the vast majority of the particle volume and, given the low enzyme coverage in our study (<1 enzyme per NR), is more relevant for H_2 generation than the minor bulb feature. In Figure 8.7 we show that the bulb feature kinetics are not noticeably affected by the presence of H_2ase in these samples. For this reason, in the remainder of this chapter we focus on the electron decay in the rod on the timescale well after electron localization is complete (>100 ps). We take into account the loss of rod population by transfer to the bulb in the calculation of QE_{ET} (see Discussion).

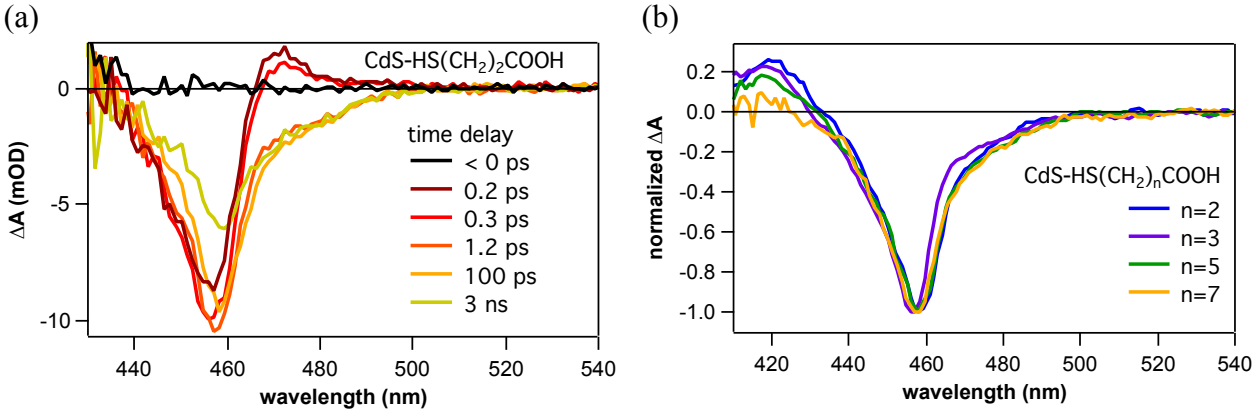

Figure 8.5. Transient absorption spectra of CdS NRs. (a) Transient absorption spectra of CdS NRs with the **n** = 2 ligand at different time delays following 401 nm excitation. The CdS NRs exhibit a strong transient bleach feature at the band gap (457 nm) transition, a bleach feature characteristic of the bulb transitions (479 nm), and a short-lived positive Δ*A* feature at 473 nm. (b) Transient absorption spectra of CdS NRs with each mercaptocarboxylate ligand at 1 ns after 401 nm excitation. Spectra are normalized for comparison.

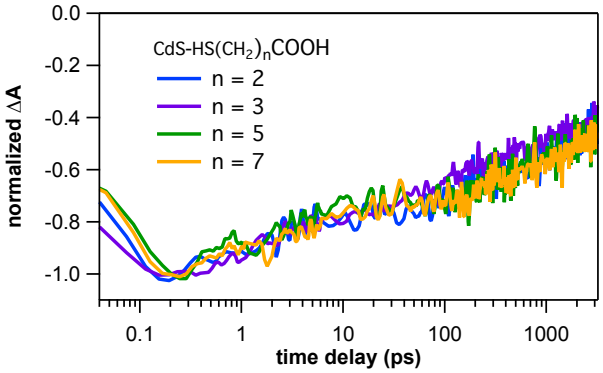

Figure 8.6. TA time traces of the rod signal of CdS NRs with various ligands after 401 nm excitation. Decay traces are shown from 40 fs to 3 ns on a logarithmic time axis and are normalized at 200 fs. Decays of NRs with **n** = 2, 3, 5, and 7 ligands were monitored at 451 nm, 448 nm, 447 nm and 450 nm, respectively.

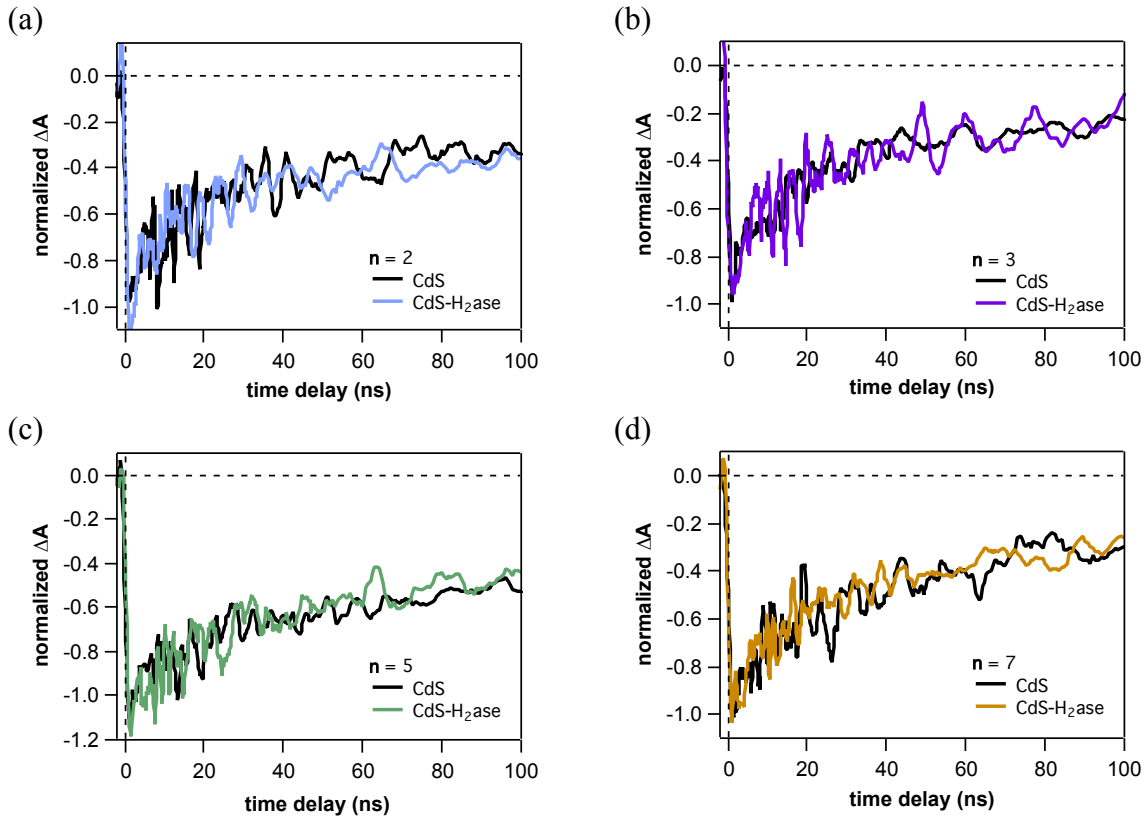

Figure 8.7. TA decay traces of the bulb bleach feature of CdS NRs with and without H_2ase. For each ligand, (a) **n** = 2, (b) **n** = 3, (c) **n** = 5 and (d) **n** = 7, the NRs were excited at 401 nm and the decay traces were normalized at 0.1 ns. CdS and H_2ase were mixed in 1:1 ratio in 12.5 mM Tris-HCl buffer at pH 7 without a sacrificial hole scavenger. CdS–H_2ase decay traces are monitored at the same wavelengths as their corresponding free CdS NR decays (485 nm). Decay traces are smoothed for presentation.

In Figure 8.8, we examine how the rod electrons decay after the localization process is complete in the CdS NR samples with the different mercaptocarboxylate ligands. We monitor wavelengths on the blue side of the bleach peak in order to reduce the contribution from the 479 nm bulb feature.[64] This is important because the bulb feature decays more slowly than the rod, with power-law dynamics at long times, and the contamination from this signal can complicate data analysis.[64] The tradeoff for obtaining a more pure rod signal is that the signal-to-noise ratio is lower than it is at the bleach maximum. The rod bleach decay kinetics in Figure 8.8 vary as a function of ligand, necessitating first an examination of ligand effects on electron relaxation.

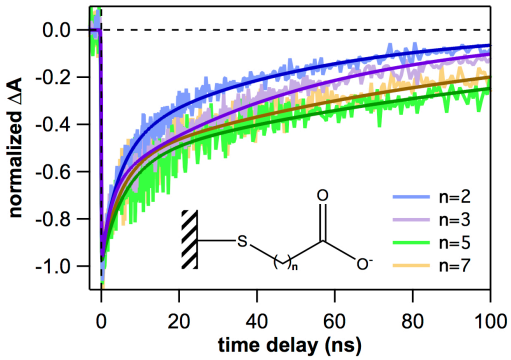

Figure 8.8. Decays of the rod bleach feature in the TA spectra of CdS NRs with various ligands after 401 nm excitation, normalized at 0.3 ns. Decays of NRs with **n** = 2, 3, 5, and 7 ligands were monitored at 451 nm, 448 nm, 447 nm and 450 nm, respectively. Corresponding to fits of Equation (8.1) to the data are shown as darker solid lines of the same color. Fit parameters appear in Table 8.2.

As is common in semiconductor nanocrystal samples,[36,37] the excited electron decays in Figure 8.8 are multi-exponential. The complicated dynamics reflect the sample heterogeneity including a variation in the number of electron trapping sites at the nanocrystal surfaces in the ensemble. We analyze the TA decay traces of CdS NRs with different ligands in Figure 8.8 using a previously described kinetic model that accounts for electron decay by recombination with the

trapped hole and by trapping on the nanocrystal surface. Assuming a Poisson distribution in the trap density leads to an expression with only three kinetic parameters (see Chapter 7):[35,65,84,209]

$$S(t) = A\exp[-k_0 t + \langle N_{\mathrm{tr}}\rangle(e^{-k_{\mathrm{tr}}t} - 1)]. \quad (8.1)$$

In Equation (8.1), A is a normalization constant, k_0 is the rate constant of recombination, $\langle N_{\mathrm{tr}}\rangle$ is the average number of traps in the ensemble, and k_{tr} is the rate constant of electron trapping.

The TA decays of CdS NRs with each of the different mercaptocarboxylate ligands (Figure 8.8) can be fit well using Equation (8.1) convoluted with the instrument response function. Convolution was carried out using an approximate truncated sum form of Equation (8.1), as described in Section 8.4.3 below. Fit parameters appear in Table 8.2. The timescales of electron trapping and recombination are on the order of nanoseconds and tens of nanoseconds, respectively, for these samples. The trap densities are very small ($\langle N_{\mathrm{tr}}\rangle \sim 1$) such that recombination dominates the lifetime. Similar results have been reported for CdS nanocrystals previously.[35,37,65,84] The small number of electron traps suggests effective ligand passivation of the surface cadmium atoms. The values of the decay parameters of CdS NRs with different mercaptocarboxylate ligands all fall within about a factor of two of each other. The fact that all 4 samples can be fit with the same model with only small differences in the resulting parameter values indicates that the photoexcited electrons in CdS NRs with different length ligands decay by the same processes with somewhat different rates. The small differences between the fit parameter values may occur due to variations in surface coverage and ligand packing.

Table 8.2. Electron decay parameters of CdS NRs with different ligands

Ligand	k_0 (s^{-1})	$\langle N_{\mathrm{tr}}\rangle$	k_{tr} (s^{-1})
n = 2	$(2.00 \pm 0.08) \times 10^7$	0.73 ± 0.08	$(1 \pm 2) \times 10^8$
n = 3	$(1.85 \pm 0.03) \times 10^7$	0.44 ± 0.03	$(3.2 \pm 0.6) \times 10^8$
n = 5	$(8.3 \pm 0.8) \times 10^6$	0.59 ± 0.03	$(1.2 \pm 0.0.3) \times 10^8$
n = 7	$(1.02 \pm 0.04) \times 10^7$	0.59 ± 0.04	$(1.7 \pm 0.3) \times 10^8$

8.4.2 Kinetics of ET from CdS NRs to H_2ase

CdS NRs capped with the **n** = 2, 3, 5 and 7 mercaptocarboxylate ligands and H_2ase were mixed in a 1:1 molar ratio, which has been previously determined to be nearly the optimal ratio for H_2 production in this system.[44] The TA experiment isolates the one-electron transfer step from CdS NRs to the H_2ase.[24] Although all the ligands studied have the same functional groups, the differences in aliphatic chain lengths affect ligand hydrophilicity. Increasing ligand length led to decreased colloidal stability of CdS NRs when combined with H_2ase. For this reason, TA data was collected immediately after ligand exchange. Data collection times were limited by the tendency of CdS–H_2ase complexes to precipitate after a period of hours, and shorter collection times were required to avoid changes in the sample during the experiment. The duration of the TA experiment for each sample was chosen such that a comparison of absorption spectra before and after data collection confirmed that samples were stable during the experiment (Figure 8.3). The limits on data collection time also limit the signal-to-noise ratios in the TA data. This is in addition to the signal-to-noise ratio reduction caused by choosing probe wavelengths to the blue of the bleach peak in order to minimize interference from the bulb signal as described above. These limitations on the signal-to-noise ratio in the data are responsible for uncertainties in the values of k_{ET}, as described later in the text. In Figure 8.9, the TA kinetics are smoothed to facilitate comparison of the decays with and without the enzyme. Fitting to the kinetic model described below was performed on the raw data.

The addition of H_2ase introduces ET as an additional pathway by which photoexcited electrons in CdS NRs can decay. As a consequence, the TA bleach feature of CdS NRs with each ligand decays faster in the presence of H_2ase (Figure 8.9). For the **n** = 3, and, to a lesser extent, **n** = 7 ligand, the TA kinetic traces do not change dramatically in the presence of H_2ase, but the

differences are statistically significant (Section 8.4.3). Mixing CdS NRs with H_2ase forms CdS–H_2ase complexes with a distribution in the number of H_2ase moieties adsorbed on a given NR, $N_{\mathrm{H_2ase}}$.[44,65,235] We have previously shown that at low surface coverage, this interaction can be described by a Poisson distribution, characterized by $\langle N_{\mathrm{H_2ase}} \rangle$ as the average number of H_2ase moieties per nanocrystal available to accept electrons in the ensemble.[65] ET can thus be included in the electron decay kinetic model by introducing an additional decay pathway with rate constant k_{ET} and averaging over the number distribution:[45,65,84]

$$S(t) = A \exp\left[-k_0 t + \langle N_{\mathrm{tr}} \rangle (e^{-k_{\mathrm{tr}} t} - 1) + \langle N_{\mathrm{H_2ase}} \rangle (e^{-k_{\mathrm{ET}} t} - 1)\right]. \qquad (8.2)$$

Analysis and fitting of the data in Figure 8.9 to Equation (8.2) is detailed in Section 8.4.3 below. Like Equation (8.1), this equation must be convoluted with the instrument response function in order to account for early time processes. Convolution was carried out using an approximate truncated sum form of Equation (8.2). Fitting of the CdS–H_2ase decay traces in Figure 8.9 was performed by fixing the values of k_0, $\langle N_{\mathrm{tr}} \rangle$ and k_{tr} found from fitting free CdS NRs to Equation (8.1) (Figure 8.8, Table 8.2), allowing only $\langle N_{\mathrm{H_2ase}} \rangle$ and k_{ET} to vary. This reflects the assumption that the presence of adsorbed H_2ase does not measurably affect the intrinsic decay pathways of the NRs and only introduces the ET pathway.[65] To obtain robust estimates of the mean fit parameters and their uncertainties we employed the bootstrapping Monte Carlo method, as detailed in Section 8.4.3 below.[65,131] Fits of Equation (8.2) to the CdS–H_2ase decays are shown in Figure 8.9 and ET fit parameters and their uncertainties are given in Table 8.3.

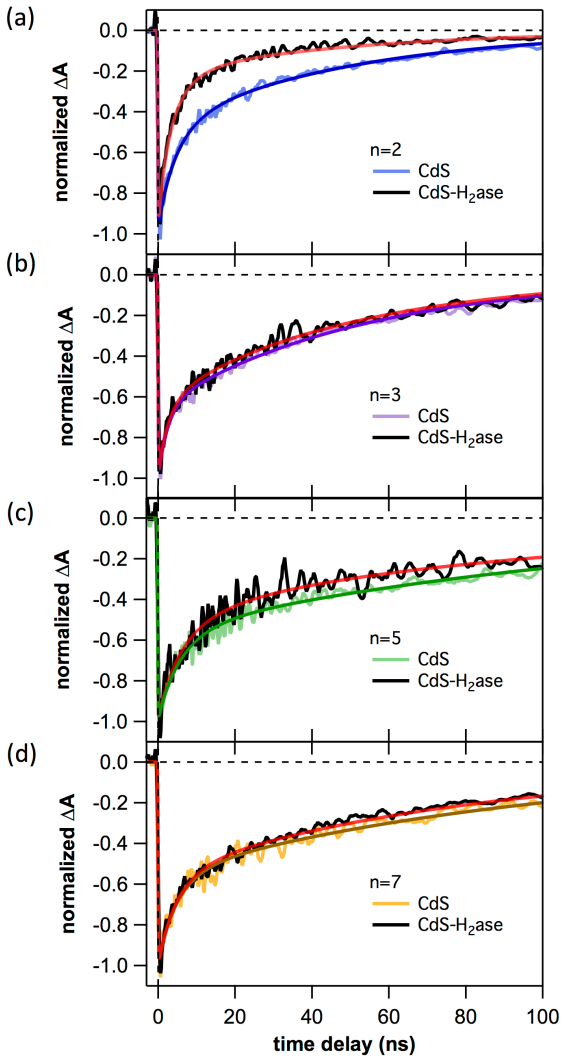

Figure 8.9. Decay traces of the rod bleach feature in the TA spectra of CdS NRs with and without H_2ase for ligands with (a) **n** = 2, (b) **n** = 3, (c) **n** = 5 and (d) **n** = 7, excited at 401 nm and normalized at 0.3 ns. Decays of free CdS NRs are reproduced from Figure 8.8 for each corresponding ligand. CdS–H_2ase decay traces are monitored at the same wavelengths as their corresponding free CdS NR decays from Figure 8.8. The darker solid lines of the same color as the CdS NRs decays correspond to fits to Equation (8.1), reproduced from Figure 8.8, while red lines are fits to Equation (8.2) to CdS–H_2ase decays. ET kinetic parameters appear in Table 8.3.

Table 8.3. Electron transfer parameters for CdS–H_2ase complexes with varying surface-capping ligands

Ligand	$\langle N_{H_2ase} \rangle$	k_{ET} (s^{-1})
n = 2	0.8 ± 0.1	(1.6 ± 0.2) × 10^8
n = 3	0.10 ± 0.03	(6 ± 2) × 10^7
n = 5	0.26 ± 0.06	(3 ± 2) × 10^7
n = 7	0.44 ± 0.06	(6 ± 2) × 10^6

As plotted in Figure 8.9, the kinetic data do not appear to have a clear pattern in the rate of ET with ligand length as the lifetime shortening upon the addition of H_2ase does not seem to change monotonically with ligand. However, fitting to the model of Equation (8.2) allows us to distinguish k_{ET} and the number of H_2ase moieties bound to determine how each quantity varies with ligand length. Both k_{ET} and $\langle N_{H_2ase} \rangle$ determine the rate of ET, but they do not have the same ligand dependence. The value of k_{ET} decreases monotonically with increasing ligand length, from 1.6×10^8 s^{-1} for **n** = 2 to 6×10^6 s^{-1} for **n** = 7. The considerable uncertainties of the extracted k_{ET} values are primarily due to the signal-to-noise ratio of the TA decay traces. In contrast to k_{ET}, $\langle N_{H_2ase} \rangle$, ranging from 0.1 to 0.8, varies for the different ligands with no particular trend. We have already shown in prior work on the **n** = 2 ligand that the value of $\langle N_{H_2ase} \rangle$ is somewhat smaller than 1 when the nanorods and enzyme are mixed in 1:1 ratio.[65] Here we observe that the longer ligands have even less H_2ase adsorbed when mixed at the same ratio.

Figure 8.10 shows the values of k_{ET} as a function of ligand length. We observe strong distance dependence, with k_{ET} decaying significantly as the ligand length increases. Following the common practice when a bridge length in a donor-bridge-acceptor system is varied,[98,221,222,224,226,227,236] we fit the resulting data points to an exponential decay,

$$k_{ET}(d) = k_{ET}(0)e^{-\beta d}, \tag{8.3}$$

where d is the ligand length in Å, $k_{ET}(0)$ is the rate constant when d = 0 (i.e., no ligand between the NR and H_2ase), and β is the electronic decay coefficient describing how k_{ET} decreases with distance. When the data in Figure 8.10 are fit with Equation (8.3), the resulting value of β is 0.66 ± 0.15 $Å^{-1}$ and $k_{ET}(0)$ = (4.8 ± 3.8) × 10^9 s^{-1}. The latter value represents a maximum ET rate constant one can expect to observe in this system in the absence of a ligand. We note, however,

that the uncertainty in this value is large because of the uncertainty in the values of k_{ET} (Table 8.3).

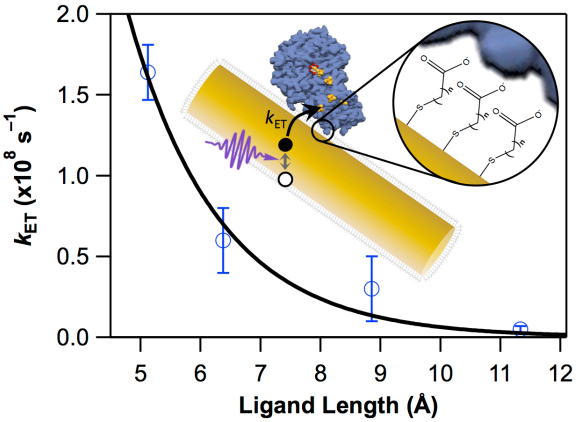

Figure 8.10. Values of k_{ET} from the TA data as a function of ligand length. The solid black line corresponds to a fit to Equation (8.3). Inset: Schematic depiction of the ET process being measured.

8.4.3 Fitting procedure and error analysis

Equations (8.1) and (8.2) were convoluted with a Gaussian IRF in order to fit the rise of the TA bleach signal and decay that occurs on a timescale similar to the ~100 ps IRF. This was especially important for obtaining accurate ET parameters for CdS NRs with **n** = 2 ligands because ET occurs within an order of magnitude of the IRF in that sample. Because Equations (8.1) and (8.2) cannot directly be convoluted with a Gaussian function as written, convolution was carried out in the following way. Equations (8.1) and (8.2) are the simplified versions of the infinite sums that they originate from:[84,209]

$$S(t) = A \sum_{N_{tr}=0}^{\infty} P(N_{tr})\, e^{-(k_0 + N_{tr}k_{tr})t}; \tag{8.4}$$

$$S(t) = A \sum_{N_{H_2ase}=0}^{\infty} \sum_{N_{tr}=0}^{\infty} P(N_{H_2ase}) P(N_{tr})\, e^{-(k_0 + N_{tr}k_{tr} + N_{H_2ase}k_{ET})t}, \tag{8.5}$$

where $P(N) = \langle N \rangle^N \mathrm{e}^{-\langle N \rangle}/N!$ describes the Poisson distribution in the number of electron traps and number of bound H_2ase moieties for a given NR. Equations (8.4) and (8.5) are equivalent to Equations (8.1) and (8.2), respectively. Now, each exponential term of Equations (8.4) and (8.5) can be analytically convoluted with a Gaussian IRF. Due to the linearity of convolution, convolution of Equations (8.4) and (8.5) with a Gaussian IRF results in an infinite sum over convoluted exponentials. Then, in order to carry out fitting, these sums were truncated such that enough terms were included to achieve convergence.

Because the TA decays of CdS NRs with and without enzyme look relatively similar by eye in some of the samples, we performed a chi-squared test to examine whether Equation (8.1) (or Equation (8.4)) can fit the CdS–H_2ase data without the ET component of Equation (8.2) (or Equation (8.5)). When the CdS–H_2ase decay trace is fit with Equation (8.4) and is assumed to have the same decay as the CdS-only trace (Table 8.2), the reduced chi-squared values are unacceptably large, taking on values of 20.77, 1.17, 1.33 and 1.37 for ligands **n** = 2, 3, 5 and 7, respectively. Evaluating the chi-squared distribution to find the probabilities that these values of reduced chi-squared are greater than or equal to the measured values shows that we must reject the null hypothesis of independence at the 1% level for all ligands.[131,237] In other words, for all ligands the disagreement between the CdS and CdS–H_2ase traces is highly significant with a 99% probability of originating from different distributions (due to the additional decay pathway of ET), despite the noise levels. When the ET component is added by fitting the CdS–H_2ase decay traces to Equation (8.5) using the model parameters from Table 8.2 and Table 8.3, the reduced chi-squared values are significantly improved, giving 1.03, 1.02, 1.02 and 1.01 for ligands **n** = 2, 3, 5 and 7, respectively. These values are sufficiently close to 1, according to evaluation of the chi-squared distribution, and indicate good fits.

Fit parameters from Equations (8.4) and (8.5) and their uncertainties were obtained using the bootstrapping Monte Carlo method.[65,131] Data sets were resampled with replacements and fit 10,000 times to give the average and standard deviations of each fit parameter in Table 8.2 and Table 8.3. CdS NR decay traces (Figure 8.8) were first fit to Equation (8.1) in this way to obtain k_0, $\langle N_{\mathrm{tr}} \rangle$ and k_{tr}. Then, CdS–H_2ase decay traces (Figure 8.9) were also fit using the bootstrap Monte Carlo method, while holding the CdS parameters fixed for each corresponding ligand, allowing only $\langle N_{\mathrm{H_2ase}} \rangle$ and k_{ET} to vary. We chose to report standard errors (Table 8.2 and Table 8.3) instead of the asymmetric confidence intervals for simplicity because they are approximately the same for all parameters when evaluated at the 68.3% confidence level.

8.4.4 H_2 production using CdS NRs with varied ligand lengths

Upon illumination with 405 nm light, H_2 production from the CdS–H_2ase complexes with different ligands in the presence of ascorbate as a sacrificial hole scavenger was measured by gas chromatography (Figure 8.11). The steps involved in the photochemical H_2 production reaction are shown in Figure 8.12. After photon absorption, a photoexcited electron transfers to H_2ase and is transported to the active site, which binds a proton, resulting in a reduced protonated enzyme (H_2ase]$^-H^+$).[218] Ascorbate ($AscH^-$) is oxidized by the photoexcited hole to form the ascorbyl radical ($Asc^{\bullet -}$) with a release of a proton.[44,238] This photoexcitation and charge transfer cycle repeats, with the second electron and proton resulting in H_2 generation. The overall reaction is a light-driven oxidation of ascorbate that generates H_2.

In the measurements of photochemical H_2 production in Figure 8.11, concentrations of CdS NRs, H_2ase, and ascorbate, as well as illumination conditions, were the same in all the samples. As in the TA experiments, all samples were mixed in a 1:1 molar ratio and the value of $\langle N_{\mathrm{H_2ase}} \rangle$ may vary between samples. Ascorbate concentrations were in the range where H_2

production no longer depends on the amount of hole scavenger.[44] Illumination times (10 min) were short compared to the timescale on which these systems become inactivated (hours).[44] In the absence of H_2ase, background H_2 production was negligible. Similarly, H_2 was not detectable when the enzyme accepted electrons but the active site was inactivated.[24] We were able to add the **n** = 10 ligand to the dataset in this experiment because it was carried out at lower concentrations than TA experiments and the samples were stable with this longer ligand. Figure 8.11 shows the relative H_2 production as a function of ligand, obtained by dividing the amount of H_2 made by each sample by the amount of H_2 generated from the **n** = 2 sample. Under the same photoexcitation and concentration conditions for each sample, photochemical H_2 production decreases with increasing ligand length. The data points and error bars indicate the mean and standard deviation from three independent measurements. We have repeated this experiment under a variety conditions, using H_2ase samples with various H_2 evolution activity levels. Although the absolute amounts of H_2 produced vary depending on these conditions, the trend of the relative H_2 production level with ligand is robust. For example, Figure 8.13 shows a set of H_2 production experiments with different enzyme and nanocrystal batches.

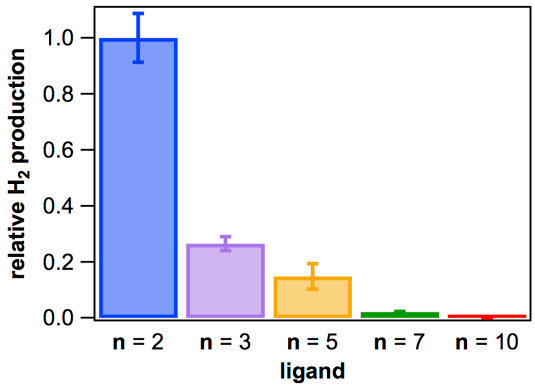

Figure 8.11. Relative photochemical H_2 production as a function of the ligands capping the CdS surface at equal illumination conditions and concentrations of CdS NRs, H_2ase, and ascorbate.

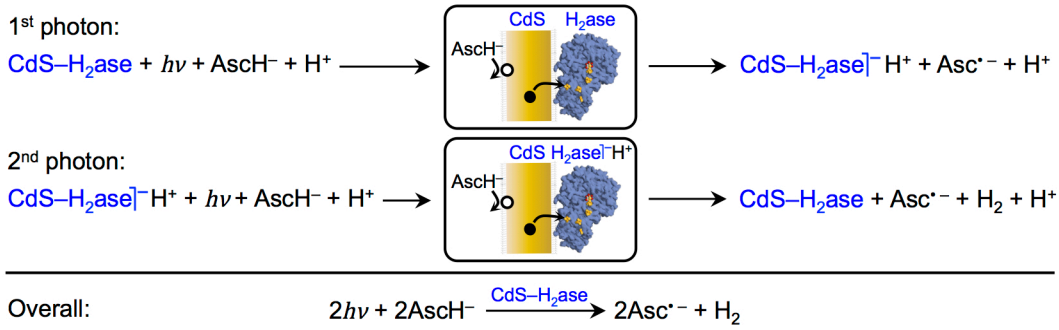

Figure 8.12. Steps involved in the light-driven H_2 production by CdS–H_2ase.

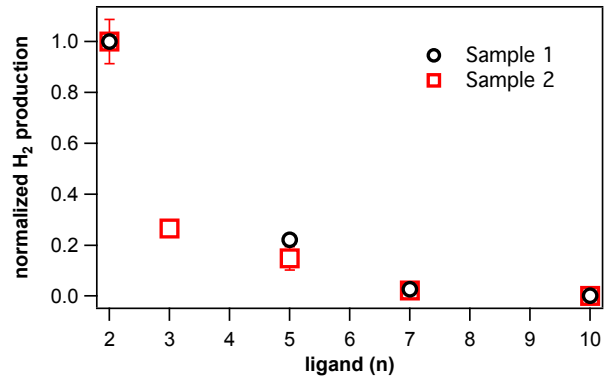

Figure 8.13. Normalized photochemical H_2 production from CdS–H_2ase complexes with varied ligands illuminated with a 405 nm laser at similar incident powers (12–13 mW). The two samples contain both enzymes and nanocrystals originating from different batches.

8.5 Discussion

8.5.1 Kinetics of ET from CdS NRs to H_2ase

Our investigation of the dependence of ET kinetics on the length of the nanocrystal-surface capping ligand is analogous to several previously reported studies of architectures of the donor-bridge-acceptor type that contain semiconductor nanocrystals.[98,219-227,236,239-241] Many of the donor-bridge-acceptor type systems in which aliphatic molecules form a bridge between the donor and acceptor show exponentially decaying ET rate constants with increasing ligand length due to a decrease in the electronic coupling between the donor and acceptor.[223,224,226,227] The

common interpretation of this result is that the bridge imposes a tunneling barrier for electron transfer. Our data in Figure 8.10 are consistent with this interpretation.

Our experiments are also somewhat analogous to a study which used protein film cyclic voltammetry and electrochemical scanning tunneling microscopy to measure the catalytic turnover from H_2ase immobilized onto a self-assembled monolayer of mercaptocarboxylates with varying lengths of aliphatic chain on a Au electrode.[242] The ligands were the same as the ones used in our study. That work showed a clear exponential decay of turnover frequency with increasing ligand length resulting in an electronic decay constant (β) of 0.82 ± 0.16 $Å^{-1}$. From this electrochemical experiment, it was concluded that the catalytic turnover rate was kinetically controlled by ET from the electrode to the enzyme, such that the exponential decay in turnover current is due to the exponential decay in k_{ET}.[242] That experiment differs from our work in that it measures a catalytic current directly, does not have a light-driven component with competing kinetic processes but rather direct electron injection from an electrode, and the mercaptocarboxylate molecules are on a flat Au surface rather than curved CdS surface. Nevertheless, the catalytic current is determined by ET rate and its exponential dependence on ligand length is similar to the k_{ET} behavior that we observe in Figure 8.10. The similarities between our observations and this prior work support our working model of the CdS NR–H_2ase interaction in which the enzyme adsorbs onto the negatively charged layer created by the carboxylate groups, rather than displacing the ligands and adsorbing directly to the nanocrystal surface.[44] We note that photochemical H_2 production is not equivalent to the electrochemical turnover measurement because photochemical H_2 production depends on the efficiency of ET (i.e., competition between ET and other electron decay pathways in CdS), as discussed below, rather than k_{ET} alone.

While it is clear that the dependence of k_{ET} on ligand length is strong, the values of β and $k_{ET}(0)$ that we report here should be taken as approximate. The value of β, 0.66 ± 0.15 Å^{-1}, falls within the uncertainty range of the value measured by the electrochemical experiments described above. The β value we measure is also close to but smaller than the values of β that have been previously measured for ET through saturated alkyl chains (0.79–1.2 Å^{-1}).[224,226,243-248] However, the value of β depends on the relative ligand lengths, which may not be accurately represented by a simple model of fully extended molecules. The ligands may not be perfectly aligned and fully extended at all lengths and the different ligands used here may have different packing efficiencies and ordering on the CdS surface.[224,249-251] The curvature of the NR surface may also change the molecular structure in a manner that is different for each ligand.[251] All these factors affect the effective values of d, and therefore the value of β. Compared to the literature values, our value of β suggests that the ligands create more compressed nanocrystal–enzyme spacing than fully extended and tightly packed ligand layer would create. The value of $k_{ET}(0)$ depends sensitively on the absolute ligand lengths (both the value of β and the exact meaning of $d = 0$) and thus may be subject to significant systematic error. Our reported value for the maximum ET rate in the CdS–H_2ase system should be taken as an estimate and is probably in the range of 10^9–10^{11} s^{-1}.

The strong dependence of the ET rate constant on ligand length provides some guidance for the design of systems that maximize QE_{ET}, which in these systems depends primarily on the ratio of k_{ET} to k_0. This ratio is already such that QE_{ET} is more than 50% of the maximum in the **n** = 2 system.[65] A hundred-fold increase in the ratio of k_{ET} to k_0 would maximize QE_{ET}, provided that electron trapping does not become prominent.[65] The $k_{ET}(0)$ value of 10^9–10^{11} s^{-1} (together with k_0 value of 10^7 s^{-1}) indicates that this can be achieved with the use of very short

ligands that place the nanocrystal surface closer to the electron injection site in the enzyme. Since the CdS–H_2ase complexes rely on the negatively charged surface ligands for solubility, stability, and the electrostatic interaction that mediates binding, ligands cannot be eliminated from the system. However, there have been major developments in the nanocrystal literature specifically concerning ligands that enhance electronic coupling,[252,253] and some of those ligands, provided they are enzyme-compatible, may allow QE_{ET} to be maximized.

8.5.2 Relationship between ET kinetics and H_2 production

Light-driven H_2 production in the CdS–H_2ase system is a multi-step process involving light absorption in CdS, ET to H_2ase, which competes with recombination and trapping, electron transport in the enzyme, and electron donation from ascorbate to CdS.[24,44,65,217] Since H^+ reduction is a two-electron process, this series of charge transport must happen twice in sequence before a H_2 molecule is released. The fact that the H_2 production trend shown in Figure 8.11 demonstrates strong ligand-length dependence suggests that the rate and efficiency of ET play an important role in determining the yield of photodriven H_2 production in the CdS–H_2ase system. In the case of the **n** = 2 ligand, we have previously shown that the quantum yield of H_2 production is similar to the value of QE_{ET}, meaning that the majority of electrons transferred to H_2ase end up in a H_2 molecule.[65] Here, we compare the values of QE_{ET} with relative H_2 production for the samples with **n** = 2, 3, 5, and 7 ligands. QE_{ET} is the fraction of photoexcited electrons that undergo ET in the ensemble rather than decay by processes intrinsic to the CdS NR (i.e., trapping and recombination). In the model of Equation (8.2), the electron population of an individual CdS–H_2ase complex decays with a total rate of $k_0 + N_{\mathrm{tr}}k_{\mathrm{tr}} + N_{\mathrm{H_2ase}}k_{\mathrm{ET}}$. The quantum efficiency of electron transfer for the complex with N_{tr} electron traps and $N_{\mathrm{H_2ase}}$ bound H_2ase moieties is $N_{\mathrm{H_2ase}}k_{\mathrm{ET}}/\left(k_0 + N_{\mathrm{tr}}k_{\mathrm{tr}} + N_{\mathrm{H_2ase}}k_{\mathrm{ET}}\right)$. The total QE_{ET} of the ensemble is

found by summing over the Poisson distributions in both the number of electron traps and H_2ase moieties bound (Equation (8.6)):

$$QE_{ET} = \sum_{N_{H_2ase}=0}^{\infty} \sum_{N_{tr}=0}^{\infty} \frac{\langle N_{H_2ase}\rangle^{N_{H_2ase}} e^{-\langle N_{H_2ase}\rangle}}{N_{H_2ase}!} \frac{\langle N_{tr}\rangle^{N_{tr}} e^{-\langle N_{tr}\rangle}}{N_{tr}!} \frac{N_{H_2ase} k_{ET}}{k_0 + N_{tr} k_{tr} + N_{H_2ase} k_{ET}}. \quad (8.6)$$

Because we assume that non-uniform CdS NRs do not contribute to ET or H_2-production at the low mixing ratios used here, QE_{ET} was adjusted for the fraction of structures in which the electron localizes to the bulb (Figure 8.6). Equation (8.6), after accounting for this adjustment, was used to calculate the QE_{ET} for each ligand using the model parameters listed in Table 8.2 and Table 8.3. Note that these values of QE_{ET} are calculated using the measured values of $\langle N_{H_2ase}\rangle$, which vary among ligands at the 1:1 mixing ratio of CdS NRs to H_2ase. The resulting QE_{ET} values for each ligand, along with relative H_2 production, normalized so that the two match for the **n** = 2 ligand, are plotted in Figure 8.14.

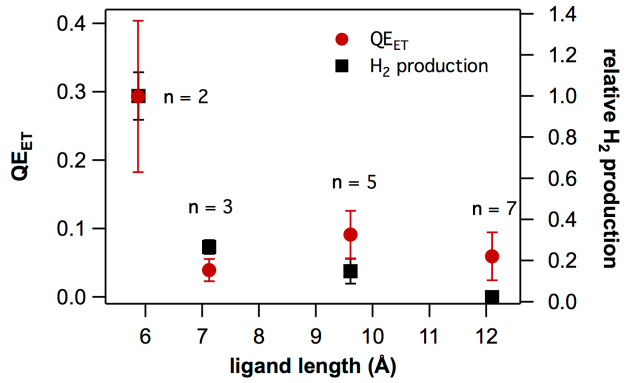

Figure 8.14. QE_{ET} and relative H_2 production as a function of ligand length. Error bars on QE_{ET} values come from error propagation of all input parameters from Table 8.2 and Table 8.3 and their uncertainties. Relative H_2 production values are normalized to match the QE_{ET} for the n = 2 ligand.

The strong dependence and the rapid decay of QE_{ET} with ligand length in Figure 8.14 is a consequence of both the decreasing value of k_{ET} and the changes in the value of $\langle N_{H_2ase}\rangle$, which

is highest for the **n** = 2 sample. It is not clear why the enzyme binding varies from ligand to ligand even though the NRs and H_2ase are always mixed in a 1:1 ratio. We suspect that the differences in the chemical environment (dipole moment, ligand orientation, ligand packing and coverage, etc.) create a complex interplay of factors that contribute to the $\langle N_{\mathrm{H_2ase}} \rangle$ values we measure. The trend of relative H_2 production as a function of ligand length is qualitatively similar to that of the $\mathrm{QE_{ET}}$ (Figure 8.14). This similarity suggests that the combination of both decreasing k_{ET} and varying $\langle N_{\mathrm{H_2ase}} \rangle$ when ligand length changes is also at play in the H_2-production experiments. The implication of this result is that the control and enhancement of H_2-production efficiency will require the increase in k_{ET} as well as control and enhancement of nanocrystal–enzyme binding. We note that, in the hypothetical scenario where each sample in Figure 8.14 were to have the same value of $\langle N_{\mathrm{H_2ase}} \rangle$, $\mathrm{QE_{ET}}$ would have a much weaker dependence on ligand length (Figure 8.15), as discussed below.

Figure 8.14 shows the values of $\mathrm{QE_{ET}}$ for the different mercaptocarboxylate ligand lengths using the values of $\langle N_{\mathrm{H_2ase}} \rangle$ that were extracted from kinetic modeling (Table 8.3). These $\langle N_{\mathrm{H_2ase}} \rangle$ values varied with no particular trend for the different ligands. The resulting decrease of $\mathrm{QE_{ET}}$ with increasing ligand length was thus a product of both k_{ET} decreasing and $\langle N_{\mathrm{H_2ase}} \rangle$ varying. In the hypothetical scenario where all samples have the same $\langle N_{\mathrm{H_2ase}} \rangle$, $\mathrm{QE_{ET}}$ has a much weaker dependence on the ligand length. Figure 8.15 shows the values of $\mathrm{QE_{ET}}$ calculated using Equation (8.6) with the CdS decay and ET parameters from Table 8.2 and Table 8.3, only $\langle N_{\mathrm{H_2ase}} \rangle$ was set equal to 1 for all ligands. The uncertainty of $\langle N_{\mathrm{H_2ase}} \rangle$ was zero by definition. This weak dependence on ligand length in Figure 8.15 stems from the fact that ET is slightly faster than recombination for the three shortest ligands; the $\mathrm{QE_{ET}}$ only begins to fall off significantly for the **n** = 7 ligand.

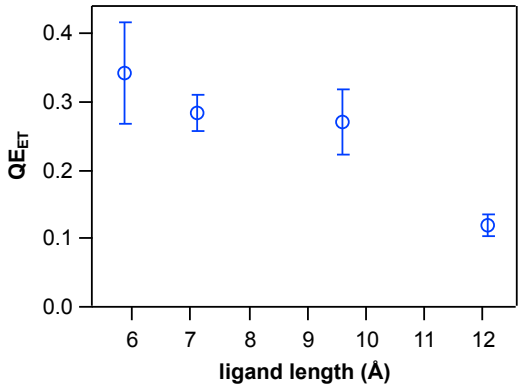

Figure 8.15. QE_{ET} as a function of ligand length when $\langle N_{H_2ase} \rangle$ was set equal to 1 for all ligands. Values were calculated using eq 4 with the CdS decay and ET parameters from Table 8.2 and Table 8.3. Error bars on QE_{ET} values come from standard error propagation of all input parameters and their uncertainties.

Our results support the idea that, although there are multiple steps in H_2 production by CdS–H_2ase complexes, ET is a critical step determining overall photochemical efficiency. This is true provided that sufficient hole scavenger is present and hole removal keeps up with ET.[111,145,146] In systems where ET to the catalyst is fast, such as CdS–Pt, the hole scavenging rate limits the overall H_2 production efficiency.[111,147] In the CdS–H_2ase system, where ET is slower by orders of magnitude, it is easier to reach a regime where hole scavenging is not limiting the overall photochemical activity. We have previously shown that H_2 production in this system depends on ascorbate concentration but reaches a saturation limit where this dependence becomes flat.[44] In the H_2 production data in Figure 8.11, the ascorbate concentration is well past that limit, making ET the key step that determines the overall H_2 production efficiency. The enzyme is excellent at utilizing the electrons it receives from the nanocrystals over a broad range of excitation intensities.[24,44,65] Under the conditions where ET is the efficiency-limiting step for photochemical H_2 production, the key to maximizing the output of the system is in controlling the ratio of ET rate and the rates of the competing relaxation pathways, as described above, as

well as nanocrystal–enzyme binding, both of which can be achieved with judicious choice of surface-capping ligands.

8.6 Conclusions

We have studied the effect of mercaptocarboxylate surface ligands of various lengths on CdS NR excited state dynamics, ET to hydrogenase, and photochemical H_2 production. Rate constants for ET decrease exponentially with ligand length, as observed in other donor-bridge-acceptor systems involving nanocrystals. Quantum efficiencies of ET depend on both k_{ET} and the number of enzymes adsorbed, both of which vary with ligand. H_2 production closely tracks the trends in $\mathrm{QE_{ET}}$, demonstrating the critical role of surface-capping ligands in the photochemical activity of these systems. Our results suggest that using shorter ligands could lead to significant increases in the rate of ET, which would maximize $\mathrm{QE_{ET}}$ of this system and enhance photochemical H_2 generation.

Chapter 9

Modeling quantum efficiency of charge transfer in nanocrystal–acceptor complexes with non-exponential relaxation

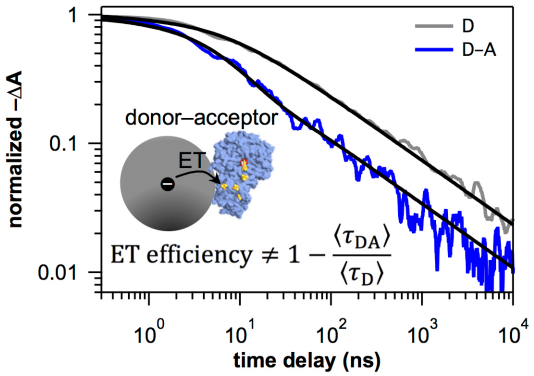

9.1 Abstract

Photoexcited charge transfer from nanocrystals to charge acceptors is a key step for solar energy conversion in semiconductor nanocrystal-based light-harvesting systems. The efficiency of energy conversion is determined by the competition between charge transfer and relaxation within the nanocrystal. Kinetic modeling of experimental data can provide a detailed picture of how excited-state dynamics govern the efficiency of solar energy conversion, leading to insights for the rational design of more efficient systems. However, modeling excited-state relaxation in nanocrystals and charge-transfer kinetics in nanocrystal–acceptor complexes is complicated by the non-exponential decay curves that typically occur in heterogeneous ensemble systems. Average lifetimes do not capture the various decay components and thus can only be used to approximate the efficiency of charge transfer. Because nanocrystals exhibit several heterogeneous relaxation processes on a broad range timescales, we need methods to accurately describe their competition with charge transfer in order to determine charge transfer efficiency

exactly. Here we use transient absorption spectroscopy and kinetic modeling to study electron transfer from CdS NRs to a hydrogenase enzyme and evaluate the impact of nanocrystal morphology. Using kinetic modeling we arrive at an exact expression for calculating the quantum efficiency of charge transfer for a system in which the donors exhibit multi-exponential and power-law decay kinetics. This system offers as a case study for evaluating the impact of non-exponential relaxation on the calculation of charge-transfer efficiency. This approach can be applied to calculate the exact efficiency of charge or energy transfer in any donor–acceptor system that exhibits non-exponential decay due to heterogeneous relaxation.

9.2 Introduction

There has been growing enthusiasm about the potential of using colloidal semiconductor nanocrystals for solar energy conversion in recent decades.[4,5,112] They are exceptionally versatile light absorbers, having tunable electronic structure and surface chemistry.[4,26,32-34] Additionally, quantum confinement and a large surface area-to-volume ratio in nanocrystals leads to enhanced electronic coupling with charge acceptors, increasing the rate and efficiency of charge transfer.[96,254-256] Semiconductor nanocrystals have been successfully employed in solar cells,[4-6] and coupling them to redox catalysts is an emerging strategy for photochemically driving multi-electron redox reactions.[4,7,8,47,107,112,146,148] Nanocrystal–enzyme complexes in particular are capable of selectively performing various light-driven multi-electron redox reactions, including H_2 production, N_2 fixation, and CO_2 reduction.[30,44-46,99,101] In order to convert solar energy into electricity and chemical energy in such systems, photoexcited charge carriers must undergo charge transfer across the nanocrystal–acceptor interface.[4,6,22,36,112,240,253] The efficiency of the energy conversion depends on the competition between this charge transfer and relaxation within

the nanocrystal. Thus charge transfer is a key dynamical step in light-harvesting applications, and understanding the principles that govern the charge transfer efficiency is critical for improving such processes.

Joining time-resolved experiments with kinetic modeling can provide fundamental understanding of the factors that determine charge-carrier dynamics. However, kinetic modeling is often complicated by the fact that photoexcited nanocrystals often exhibit heterogeneous decay and can undergo non-exponential relaxation mechanisms.[36,37,64] Still, much progress has been made towards mapping out the dynamics of carriers in certain semiconductor nanocrystal systems by using kinetic models that ascribe physical meaning to non-exponential decay components. In Cd-chalcogenide nanocrystals, photoexcited electrons and holes can undergo distinct decay pathways; holes trap efficiently on a picosecond timescale while electrons predominately decay by recombination with the trapped hole on a timescale of tens of nanoseconds.[23,26,36,37,52,56-58] Structural heterogeneity, particularly in the number of traps due to the degree of surface passivation, leads to multi-exponential relaxation in ensemble samples.[35] Morphology also plays an important role in carrier dynamics.[33-35] CdS nanorods (NRs) that are non-uniform in width have been shown to exhibit internal carrier localization to regions of larger diameter with lower confinement energy, which introduces additional heterogeneous relaxation components.[130] Further, charge separation can occur intrinsically within such nanostructures when the hole traps and the electron localizes to a different region, and lead to power-law relaxation kinetics.[64] The impact that this charge separation in non-uniform CdS NRs has on charge transfer to surface-bound acceptors has not yet been investigated.

In donor–acceptor systems that are mixed and self assembled, charge transfer is also heterogeneous, introducing an additional layer of multi-exponential decay due to the distribution

in the number of acceptors bound to a particular donor in the ensemble.[65,66,84,136,207,235,257,258] Thus, care must be taken to separate contributions of the number of bound acceptors, the distribution in the number of bound acceptors, and the intrinsic single-acceptor charge transfer rate constant to the total, observed rate constant.[240] This can be achieved through fitting of experimentally measured excited-state decay curves to kinetic models that explicitly account for such distributions in addition to the non-exponential decay of the donor.[65,66,84,136,207,235,257,258]

The internal quantum efficiency of quenching (ϕ_{q}) by a pathway such as electron transfer, hole transfer or energy transfer is a convenient and important measure for evaluating the competition between quenching and excited-state relaxation in donor–acceptor complexes. In nanocrystal–catalyst complexes that carry out multi-electron photochemistry, ϕ_{q} can define the upper limit to the quantum yield of the photochemical reaction and thus the ultimate photochemical activity of the system.[65] The calculation of ϕ_{q} in a system that undergoes non-exponential relaxation is typically carried out using average lifetimes (or average rates) of the donor and donor–acceptor complexes.[259] However, average lifetimes do not necessarily capture the complex behavior of a system,[260] and therefore calculating ϕ_{q} in this way does not always provide an accurate calculation. Moreover, when the donor exhibits a power-law decay, as is the case in some semiconductor systems,[64,143,177,195,196,198,261] ϕ_{q} cannot be calculated by this approach because power laws cannot be described by a characteristic lifetime. Because photoexcited charge carriers in nanocrystals have decay processes on multiple timescales due to population heterogeneity, we need methods to accurately account for their competition with charge transfer.

In this chapter, we investigate the quantum efficiency of electron transfer (ϕ_{ET}) in a system that exhibits multi-exponential and power-law relaxation: CdS NR–hydrogenase (H_2ase)

complexes. We examine the impact of non-uniform morphology and charge separation on electron transfer (ET) in CdS–H_2ase complexes and exactly account for multi-exponential and power-law relaxation when calculating ϕ_{ET}. Transient absorption (TA) spectroscopy is used to probe photoexcited electron dynamics in CdS NRs as well as ET in CdS–H_2ase complexes. The CdS NR sample contains both structures that are uniform and non-uniform in diameter, and we study ET from both regions of the nanostructures. While uniform CdS NRs exhibit multi-exponential decay that is common in heterogeneous nanocrystal samples, photoexcited excitons in non-uniform CdS NRs undergo dissociation, leading to a charge-separated state in which the electron and trapped hole are located in different regions of the nanostructure and display a power-law decay. Kinetic modeling is used to extract the rate constants of ET from both of these electron states and characterize the ensemble distribution in the number of H_2ase moieties bound to each morphological feature. An exact expression for ϕ_{ET} is derived that accurately accounts for the competition between ET and heterogeneous relaxation, including power-law decay, and is used to quantify the efficiency of ET for both uniform and non-uniform CdS NRs with H_2ase. We find that the internal ϕ_{ET} of non-uniform NRs is significantly larger than that of uniform NRs because of the long-lived charge-separated state that intrinsically forms, even though ET occurs with similar rate constants for the two states. However, in the mixed ensemble sample, the two morphologies have nearly equal contributions to the overall ϕ_{ET} due to the balancing out of the different electron relaxation rates with the fraction of NRs that are non-uniform in the sample and the relative acceptor loading on the relevant regions of the nanostructures, which are different because of their relative surface areas. The comparison of uniform and non-uniform NRs provides insights about design principles for optimizing the photochemistry of such nanocrystal–catalyst systems. Such a detailed analysis provides a fundamental understanding of

which processes determine the efficiency of electron transfer and overall photochemical activity of this system. We find that using average lifetimes to calculate ϕ_q can lead to significant error in some cases and therefore caution against such a treatment when an exact approach is possible. CdS–H_2ase is a model system for this study because the excited-state dynamics of CdS NRs are relatively well understood,[23,35,64,130] they exhibit both exponential and power-law relaxation,[64] the TA signal is sensitive only to electrons in the CdS NRs,[23] ET occurs a similar timescale as non-exponential trapping and recombination dynamics.[24,65] This system is of broader interest because it is a model nanocrystal–enzyme system that is capable of photochemically reducing protons to generate H_2.[44] It is critical to have accurate calculations of the ET efficiency in order to guide design principles for more efficient solar energy conversion. This system offers as a case study for evaluating the impact of non-exponential relaxation on the calculation of ϕ_q. The exact expression for ϕ_q that we describe here can be applied to an arbitrary heterogeneous donor decay, and the general approach can be applied to a broad range of systems.

9.3 Methods

9.3.1 Nanocrystal preparation and characterization

We synthesized CdS NRs according to previously published procedures (Chapter 2).[119,120] All experiments were performed on NRs functionalized with 3-mercaptopropionic acid (MPA) suspended in an aqueous buffer solution. Transmission electron micrograph (TEM) samples were prepared by drop-casting as-synthesized NRs onto TEM grids (300 mesh copper grids with carbon film, Electron Microscopy Science). TEM images were taken using a Phillips CM100 TEM at 80 kV with a bottom-mounted 4 megapixel AMT v600 digital camera. The dimensions of the CdS NRs were determined by measuring about 200 particles in TEM using ImageJ

software.[129] UV-visible absorption spectra were recorded at room temperature sealed under Ar in 2 mm quartz cuvettes.

9.3.2 H_2ase purification, characterization, and coupling to CdS NRs

The [FeFe] hydrogenase from *Clostridium acetobutylicum* (CaI) was expressed and purified from *Escherichia coli* as previously described with some modifications (Chapter 2).[127] Mixtures of CdS NRs and H_2ase were prepared in buffer (12.5 mM Tris-HCl, 5mM NaCl, 5% glycerol, pH 7) under an anaerobic Ar environment.

9.3.3 Transient absorption spectroscopy

The TA experimental setup was previously described in detail (Chapter 2).[116] The CdS NR sample used for TA experiments was 730 nM CdS NRs with MPA ligands in 12.5 mM Tris-HCl buffer at pH 7, and the CdS-H_2ase sample additionally contained about 42 mM H_2ase. The samples were sealed under Ar in 2 mm quartz cuvettes equipped with Kontes valves. A magnetic stirrer continuously stirred samples during data collection. The pump power was chosen so as to be in a regime where the CdS NR decay kinetics were independent of pump power, ensuring that the signal originated primarily from NRs excited by single photons.[114] Experiments were conducted at room temperature.

9.4 Results and Discussion

9.4.1 Morphology and excited-state dynamics of CdS NRs

The CdS NRs studied here are 32 ± 6 nm in length and 4.4 ± 0.6 nm in diameter, on average. The native ligands were exchanged for 3-mercaptopropionic acid (3-MPA) and dispersed in aqueous buffer solution. While some CdS NRs made by colloidal synthesis are effectively uniform, some NRs in a sample can have non-uniform diameters along their lengths, manifesting with both

narrow and wide regions referred to as the "rod" and "bulb," respectively. These two morphological features can be seen in the transmission electron microscopy (TEM) images (Figure 9.1a), and are depicted schematically in the inset of Figure 9.1b.[130]

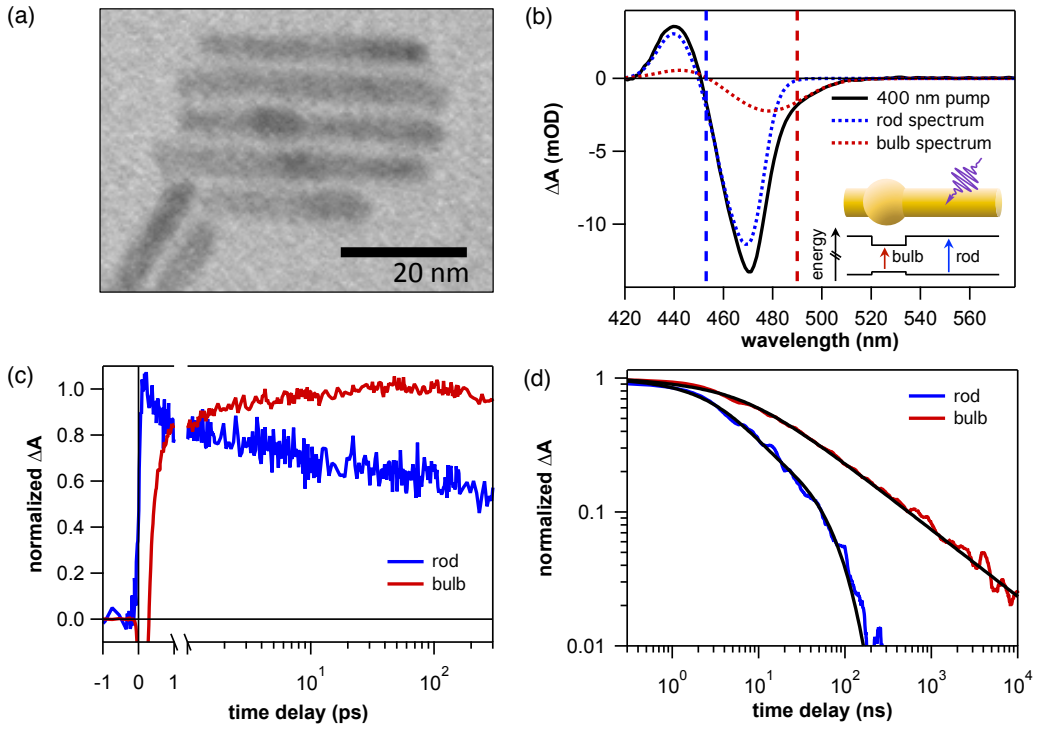

Figure 9.1. Impact of non-uniform morphology on electron dynamics in CdS NRs. (a) Representative TEM image of a CdS NRs showing both uniform and non-uniform NRs. (b) TA spectra of CdS NRs recorded 10 ns after excitation with 400 nm pulses (solid black line), with the fitted rod (dashed blue line) and bulb (dashed red line) spectra. Vertical lines mark 453 nm and 490 nm, the wavelengths that isolate the rod and bulb signals of these CdS NRs, respectively. Inset: Schematic depiction of a non-uniform CdS NR and energy level diagram as a function of position along the NR. 400 nm light primarily excites the rod. The bulb has a larger diameter than the rod, resulting in a lower transition energy. Energy offsets are drawn to scale for 70 meV and 20 meV electron and hole offsets, respectively, which are based on the centers of the rod and bulb bleach peaks. (c) TA time traces from 0 ps to 300 ps (~150 fs instrument response function) of CdS NRs monitored at the rod and bulb transitions, showing population transfer from the rod to the bulb. The traces are plotted on a split time axis that is linear for the first 1 ps and logarithmic thereafter. (d) TA time traces from 300 ps to 10 μs of CdS NRs, normalized at 300 ps, plotted on a log-log scale. The rod decay fits Equation (9.1) with an exponential tail, while the bulb feature fits Equation (9.2) with a $t^{-1/2}$ power-law tail. Fits were performed on raw data and the data were smoothed for presentation only.

We probed the excited-state dynamics of CdS NRs with and without adsorbed H_2ase using TA spectroscopy. The photophysics of CdS NRs have been previously studied in great detail.[23,24,35,64,65,82,84,116,119,130,147] Photoexcitation at 400 nm gives rise to transient bleach peaks (Figure 9.1b), the magnitudes of which (ΔA) are attributed to state filling of the electron in the conduction band states and thus directly probe electron dynamics.[23,114] The non-uniform morphology of CdS NRs has a significant impact on the electronic structure of these nanocrystals. The rod and the bulb of non-uniform NRs can act as two distinct electronic states within the same nanostructure where the bulb has a lower transition energy compared to the rod due to having a lower degree of quantum confinement, producing the two different but overlapping bleach features in the TA spectrum (Figure 9.1b).[130] The individual contributions of the rod and bulb to the TA spectrum after 400 nm excitation, obtaining by fitting,[64] are shown in Figure 9.1b. Wu *et al*. performed a systematic study of the relationship between CdS NR morphology and absorption, emission and TA spectroscopy that supports the assignment of the low-energy spectral feature to the bulb rather than to sub-band gap features such as an Urbach tail.[130] Following previous work,[64] the signals of the rod and bulb are isolated from each other by choosing the probe wavelengths shown in Figure 9.1b.

The dynamics of electrons and holes in uniform and non-uniform CdS NRs have been explored previously. After excitation above the band edge at 400 nm (Figure 9.2), the band-edge bleach features grow in on a <1 ps timescale as the hot photoexcited carriers cool (Figure 9.3). Photoexcited holes in CdS nanocrystals rapidly trap to the surface.[23,26,56,57] The rise of a broadband photoinduced absorption (PA) feature at wavelengths to the red of the band-edge bleach, which has previously been assigned to surface-trapped holes,[23,82] indicates that holes trap with a time constant of 0.60 ± 0.02 ps in our CdS NRs (Figure 9.4). Photoexcitation with 400 nm

light primarily excites the rod rather than the bulb because the rod constitutes a much larger volume fraction of the nanostructures.[64,130] Thus holes are more likely to trap on the rod than the bulb. Electrons in non-uniform NRs localize from the rod to the bulb, giving rise to a partial decay of the rod bleach and a corresponding rise of the bulb bleach (Figure 9.1c).[64,130] The fraction of nanocrystals in which electrons localize, f_{loc}, has been shown to reflect the fraction of nanorods that are non-uniform in the sample.[64] Electron localization constitutes f_{loc} = (47 ± 3)% of the decay, occurs on timescales well beyond that of hole trapping, and is complete by ~100 ps in this sample of CdS NRs. The remaining signal of the rod is dominated by the uniform NRs in the sample.[64] We have previously shown that, in non-uniform NRs, electrons can dissociate from the hole trapped on the rod when they localize to the bulb, resulting in a charge-separated state in which the hole is trapped on the rod while the electron is localized in the bulb.[64] The subsequent decays of electrons in both uniform and non-uniform NRs after localization is complete (Figure 9.1d) are due to relaxation by recombination with a trapped hole or electron trapping, though the charge separation in non-uniform NRs leads to suppressed recombination.

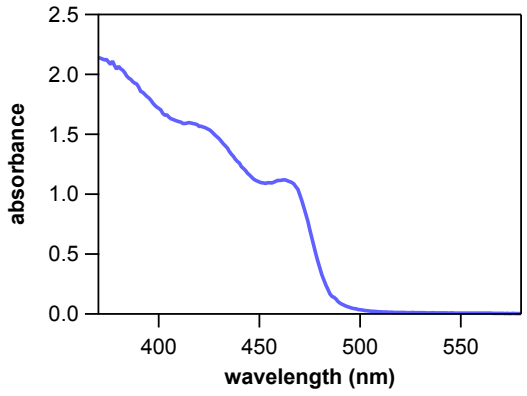

Figure 9.2. UV-visible absorption spectrum of CdS NRs in buffer solution.

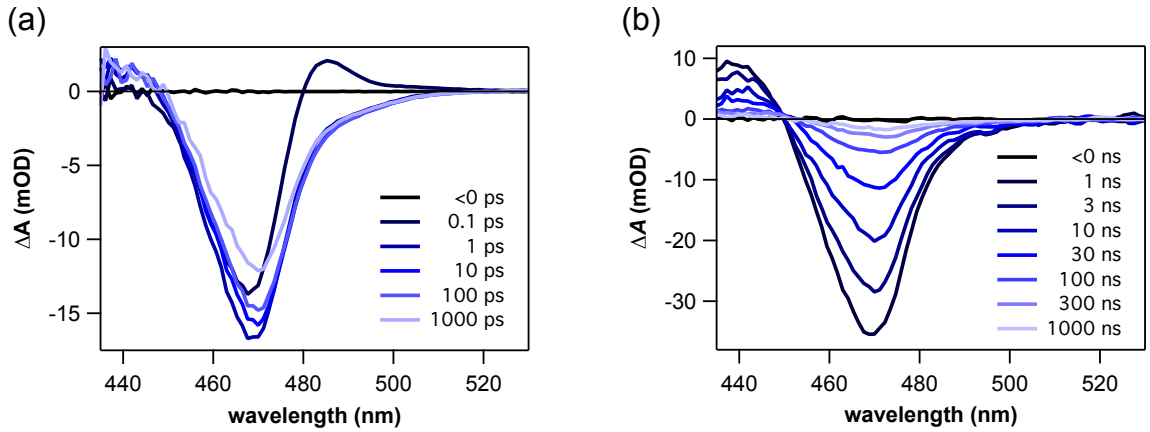

Figure 9.3. TA spectra of CdS NRs after excitation at 400 nm at various time delays. Spectra are shown at selected times between (a) 0.1-1000 ps and (b) 1-1000 ns.

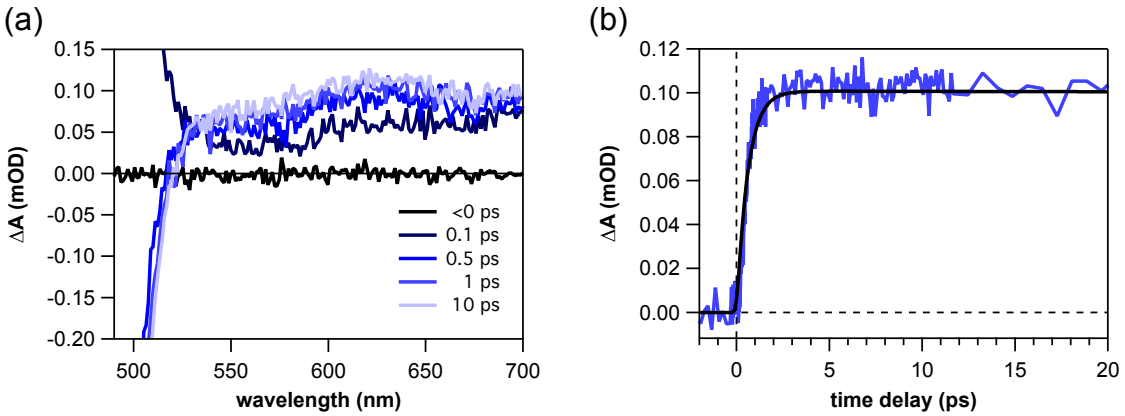

Figure 9.4. TA spectra and formation kinetics of the PA feature in CdS NRs. (a) TA spectra in the region of the PA feature at selected times. (b) TA time trace of the PA feature, averaged over 600-700 nm to improve signal-to-noise ratio, fit to a single exponential rise.

Electrons in the rod and bulb states exhibit distinct recombination dynamics. Figure 9.1d shows the decays of electrons in the rod and bulb states of CdS NRs after electron localization is complete. The relaxation of rod and bulb electrons in similar CdS NRs has previously been described in detail.[64] The decay of electrons in the rod of uniform NRs can be described with a kinetic model that accounts for the exponential decay pathways of recombination and trapping as well as the heterogeneity in the number of trap sites present in a given NR—assumed to be represented by a Poisson distribution:[35,65,84,136]

$$S_{\mathrm{rod}}(t) = A\exp\left[-t/\tau_0 + \langle N_{\mathrm{tr}}\rangle\left(e^{-t/\tau_{\mathrm{tr}}} - 1\right)\right], \quad (9.1)$$

where τ_0 is the time constant of recombination, $\langle N_{\mathrm{tr}}\rangle$ is the average number of electron traps per NR, and τ_{tr} is the time constant of electron trapping. This decay function is multi-exponential in nature, reflecting the heterogeneous distribution in decay rates that occurs due to nanocrystals having different numbers of electron traps. Fitting of the rod decay in Figure 9.1d to Equation (9.1) gives τ_0 = 47 ± 3 ns, $\langle N_{\mathrm{tr}}\rangle$ = 1.16 ± 0.05 and τ_{tr} = 7.4 ± 0.5 ns, consistent with previous reports of CdS nanocrystals.[35,64,65,84] Most importantly, the decay of uniform NRs has an exponential tail due to direct recombination.

Electrons in the bulb of non-uniform NRs are much longer lived than uniform NRs because of the spatial separation between the bulb electron and the rod-trapped hole (Figure 9.1d). In contrast to the exponential recombination in a uniform NR, where the electron and trapped hole are present in the same region of the nanostructure, recombination of the charge-separated electron and hole exhibits a slow $t^{-1/2}$ power-law tail. The decay of this state has been modeled as diffusion-limited recombination of a stationary electron in the bulb and a mobile surface-trapped hole.[64] The survival probability of electrons in non-uniform NRs fits the following equation:

$$S_{\mathrm{bulb}}(t) = A\left[\sqrt{t/\pi\tau}\left(e^{-\tau/t} - 1\right) + \mathrm{erf}\left(\sqrt{\tau/t}\right)\right], \quad (9.2)$$

where τ is a fitting parameter that depends on the initial electron–hole separation and diffusion coefficient of the trapped hole. Fitting Equation (9.2) to the bulb decay in Figure 9.1d gives τ = 15.6 ± 0.3 ns (Figure 9.1d). We note that while the bulb electron decay is parameterized by τ, the power-law tail prevents the decay from being described by a characteristic timescale. As discussed below, the difference in decay dynamics between uniform and non-uniform NRs has a significant impact on the efficiency of ET to adsorbed electron acceptors.

9.4.2 Electron transfer in CdS–H_2ase complexes

To study ET from CdS NRs to H_2ase we focus on nanosecond-TA spectroscopy as this is the time window relevant to ET in CdS–H_2ase complexes with 3-MPA ligands.[14,24,65] The particular H_2ase used here is an [FeFe] hydrogenase from *Clostridium acetobutylicum*. Complexes of CdS NRs and H_2ase form by electrostatic interaction between the negatively charged carboxylate end groups of the 3-MPA ligands and a positively charged region on the surface of the enzyme located near the distal iron-sulfur cluster that acts as the electron-injection site.[24,30,44] In the experiments studied here, the enzyme and nanocrystals were mixed in a 6:1 H_2ase:CdS molar ratio in aqueous buffer solution at pH 7. The presence of H_2ase adsorbed onto the surface of the CdS NRs introduces ET as an additional decay pathway for photoexcited electrons, causing the TA signal of CdS–H_2ase complexes to decay more quickly than that of free CdS NRs (Figure 9.5).[24,65] We find that a new decay component is present in both the rod signal (Figure 9.5a) and bulb signal (Figure 9.5b), indicating that ET occurs from both regions of the NRs.

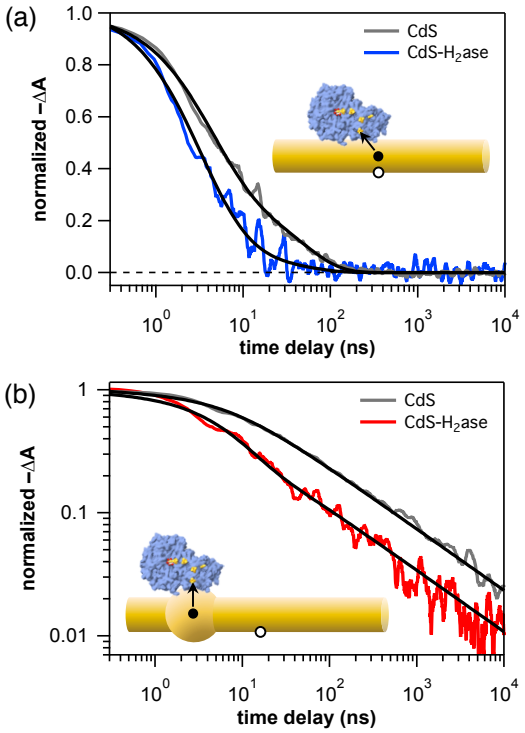

Figure 9.5. Photoexcited electron transfer from the rod and bulb in CdS–H_2ase complexes. TA time traces of the rod (a) and bulb (b) signals in CdS NRs and CdS–H_2ase complexes (6:1 H_2ase:CdS molar ratio) excited at 400 nm from 300 ps to 10 μs, normalized to 1 at 300 ps. The rod decay (a) is shown on a linear-log scale while the bulb decay (b) is shown on log-log scale to emphasize the power-law tail. Insets: Schematic depictions of CdS–H_2ase complexes and the excited state from which ET occurs. In uniform NRs ET occurs from the rod, where the electron is located in the same region of the NR as the trapped hole. In non-uniform NRs ET occurs from the bulb, where the electron is spatially separated from the trapped hole, giving a longer-lived excited state. Fits were performed on raw data and the data were smoothed for presentation only. Decays of free CdS NRs (gray traces) are reproduced from Figure 9.1d.

We have previously studied the kinetics of ET from the rod state in CdS–H_2ase complexes.[65] Mixing of CdS NRs and H_2ase at low H_2ase:CdS ratios in solution results in a Poisson distribution in the number of H_2ase moieties bound and able to accept electrons from a given NR, N_A. The time constant of ET for a single acceptor, τ_{ET} (the reciprocal of the single-acceptor rate constant, $\tau_{ET} = 1/k_{ET}$), is effectively the same for each H_2ase moiety,[65] and the total rate constant of ET in a given complex is proportional to the number of moieties bound, N_A/τ_{ET}. The TA decay of CdS–H_2ase complexes can be described by[65,84,235,258]

$$S_{\mathrm{DA}}(t) = S_{\mathrm{D}}(t)\exp\left[\langle N_{\mathrm{A}}\rangle\left(e^{-t/\tau_{\mathrm{ET}}} - 1\right)\right], \tag{9.3}$$

where $S_{\mathrm{D}}(t)$ is the survival probability of the donor in the absence of the acceptor (i.e., the rod or bulb state of the CdS NRs), $\langle N_{\mathrm{A}}\rangle$ is the average number of H_2ase moieties bound and able to accept electrons from a given electron state, and τ_{ET} is the single-acceptor time constant for ET to each bound acceptor. The use of such a kinetic model allows us to extract the intrinsic time constant of ET per enzyme moiety, separate from the average number of enzymes bound.[65] This kinetic model can be applied to both the rod and bulb states. The existence of a distribution in N_{A} can be seen directly in the bulb decay (Figure 9.5b), which displays both an additional decay component compared to the free CdS bulb decay (due to bulbs with $N_{\mathrm{A}} > 0$) and a persisting power-law tail (due to bulbs with $N_{\mathrm{A}} = 0$). Additionally, we are able to obtain τ_{ET} despite the power-law decay of the bulb, and distinguish electron acceptors available to the spatially distinct electron states. The TA time traces in Figure 9.5 were fit using Equation (9.3) by first establishing $S_{\mathrm{D}}(t)$ for the free CdS NRs as done above (Equation (9.1) and Equation (9.2) for the rod and bulb, respectively), then holding the nanocrystal parameters fixed and fitting the CdS–H_2ase traces to obtain the ET parameters. This model assumes that the binding of H_2ase to the nanocrystal does not affect the intrinsic decay of the nanocrystal, as we have previously demonstrated is the case.[65] The extracted ET parameters appear in Table 8.1.

Table 9.1. Electron transfer parameters for CdS–H_2ase complexes

State	$\langle N_{\mathrm{A}}\rangle$	τ_{ET} (ns)	$\phi_{\mathrm{ET},i}^{N_{\mathrm{A}}=1\,a}$	$\phi_{\mathrm{ET},i}{}^{b}$	$\phi_{\mathrm{ET,tot}}{}^{b}$
rod	1.6 ± 0.3	14 ± 5	41 ± 6 %	21 ± 4 %	37 ± 3 %
bulb	0.74 ± 0.04	11 ± 1	62 ± 2 %	16 ± 2 %	

[a] $N_{\mathrm{A}} = 1$, assumes sample is completely uniform or non-uniform
[b] $\langle N_{\mathrm{A}}\rangle$ from table, f_{loc} = (47 ± 3) %

The value of τ_{ET} for the rod of 14 ± 5 ns is in agreement with previous reports of for the CdS–H_2ase system.[14,24,65] Interestingly, the time constant for ET from the bulb of 11 ± 1 ns is within error of that of the rod. The present experiments do not allow us to identify the individual contributions of driving force, electronic coupling and activation energy that ultimately make the rate constant of ET the same for the rod and bulb. The values of $\langle N_A \rangle$ for the rod and bulb on the other hand are statistically different; the apparent number of H_2ase moieties able to accept electrons is higher for the rod than it is for the bulb by a factor of 2.2 ± 0.4. This can be explained by the relative surface areas of the rod and bulb. In the non-uniform NRs of this sample, the rods make up a larger fraction of the length of the NR while the bulbs are typically shorter (Figure 9.1a). Thus, if a H_2ase moiety adsorbs at a random point along the length of a non-uniform NR, it is most likely to be found along the rod where it would not be available to accept electrons. However, an enzyme on a uniform NR can accept electrons from any position along the structure since the electron is able to explore the entire nanostructure. This hypothesis is supported by TEM measurements, from which we estimate that the surface area of the rod in uniform NRs is 3 ± 1 times larger than that of the bulb in the non-uniform NRs, consistent with the relative values of $\langle N_A \rangle$ for the rod and bulb from Table 8.1. We note that because the bulb makes up only a fraction of the NR surface area, the Poisson distribution may break down at moderate enzyme loading and binding may be better represented with the Binomial distribution.[66,257] However, Equation (9.3) provides an adequate fit to the data and the addition of more fit parameters was unnecessary (Figure 9.5b). With a full description of the kinetics of ET and the CdS NR decay based on physical pictures we are able calculate the exact quantum efficiency of ET and evaluate the impact of the excite-state dynamics in uniform and non-uniform NRs.

9.4.3 Modeling quantum efficiency of quenching for non-exponential relaxation

The quantum efficiency of quenching by a particular pathway (e.g., charge or energy transfer) in donor–acceptor complexes, ϕ_{q}, is typically calculated using average lifetimes (or average rate constants) for both the donor and the donor–acceptor complexes:[259]

$$\phi_{\mathrm{q}} = 1 - \frac{\langle \tau_{\mathrm{DA}} \rangle}{\langle \tau_{\mathrm{D}} \rangle}, \tag{9.4}$$

where $\langle \tau \rangle = \int_0^\infty dt S(t)$ is the amplitude-averaged lifetime of the system that decays with a normalized, non-exponential decay function, $S(t)$.[259] However, systems that decay according to a power law cannot necessarily be described by a characteristic lifetime. In our case, the power-law tail of the bulb decay in the nanocrystals studied here prohibits the approach of Equation (9.4) because a $t^{-1/2}$ power law does not have a finite average lifetime. We note that in any finite system the power-law tail that is exhibited will eventually have a cutoff, ultimately rendering the average lifetime finite. However, we do not observe such behavior on the timescale of our measurement, and because ET is complete before the power law is in CdS–H_2ase, Equation (9.4) would inaccurately return unity quenching efficiency. Furthermore, Equation (9.4) does not always capture the competition between quenching and the various donor decay components in a non-exponential decay because it treats the various distinct decay components as one average. Because kinetic modeling allowed us to extract the time constant of ET as above we are able model and calculate ϕ_{ET} exactly without using average lifetimes.

Here we derive an expression for ϕ_{q} that can be applied to a donor–acceptor system with arbitrary heterogeneous donor decay function. We can obtain the exact expression for ϕ_{q} by simply starting with the definition for the quantum efficiency of a quenching pathway and then using rate equations to find the fraction of excitations that lead to decay by a given quenching

pathway. Let $S_{\mathrm{D}}(t)$ be the function that describes time-dependent population of excited donors in the absence of acceptors, $S_{\mathrm{DA}}(t|N)$ the time-dependent population of excited donors in the presence of N acceptors, and $S_{\mathrm{A}}(t|N)$ be the population of acceptors that have quenched a donor (e.g., by electron, hole or energy transfer). The donor decay, $S_{\mathrm{D}}(t)$, can have an arbitrary functional form in this analysis. We will average over the distribution in N later. The quantum efficiency of quenching is defined as the fraction of excited donors that have been quenched by the acceptors:

$$\phi_{\mathrm{q}}(N) = \frac{\lim_{t\to\infty} S_{\mathrm{A}}(t|N)}{S_{\mathrm{DA}}(0|N)}. \tag{9.5}$$

Moving forward we will take all decay functions to be normalized relative to the initial population of the donor (i.e., $S_{\mathrm{D}}(0) = S_{\mathrm{DA}}(0|N) = 1$) so that Equation (9.5) becomes $\phi_{\mathrm{q}}(N) = \lim_{t\to\infty} S_{\mathrm{A}}(t|N)$, which has a maximum of 1. The acceptor begins unpopulated: $S_{\mathrm{A}}(0|N) = 0$. The definition in Equation (9.5) assumes that there is no decay pathway for the acceptor after quenching. Note that if the acceptor can undergo some subsequent decay, for example by the reverse of the quenching process or internal relaxation, then one could adapt the present analysis to look at a "transient quantum yield" at some intermediate time and incorporate the appropriate terms in the rate equations below.

In this model, the acceptors each quench the donors with a single-acceptor rate constant k_{q}, and the total rate constant of quenching is assumed to increase linearly with the number of acceptors: $k_{\mathrm{q,tot}} = Nk_{\mathrm{q}}$. The rate equation for the growth of the population of product of the quenching pathway in this case is

$$\frac{dS_{\mathrm{A}}(t|N)}{dt} = Nk_{\mathrm{q}}S_{\mathrm{DA}}(t|N). \tag{9.6}$$

Note that $S_{\mathrm{DA}}(t|N)$ itself does not have to obey a simple rate process and can follow a non-exponential decay. The solution to this equation can be written as

$$S_{\mathrm{A}}(t|N) = Nk_{\mathrm{q}} \int_0^t dt' S_{\mathrm{DA}}(t'|N). \tag{9.7}$$

Thus the quantum efficiency of quenching for a donor–acceptor complex that has N acceptors is

$$\phi_{\mathrm{q}}(N) = Nk_{\mathrm{q}} \int_0^\infty dt S_{\mathrm{DA}}(t|N). \tag{9.8}$$

Notice that this is simply the familiar expression for quantum efficiency for a given complex, $\phi_{\mathrm{q}}(N) = Nk_{\mathrm{q}}\langle\tau_{\mathrm{DA}}\rangle(N) = Nk_{\mathrm{q}}/\bar{k}_{\mathrm{DA}}(N)$,[260] where $\langle\tau_{\mathrm{DA}}\rangle(N) = 1/\bar{k}_{\mathrm{DA}}(N) = \int_0^\infty dt S_{\mathrm{DA}}(t|N)$ is the amplitude-averaged lifetime of the donor in the presence of N acceptors. The use of this expression requires there to be a finite average lifetime of a donor in the presence of at least one acceptor, thus it is important to note that the efficiency when there are no acceptors is zero by definition: $\phi_{\mathrm{q}}(N = 0) = 0$. This is the case in our model where there is power-law decay of the donor but exponential ET; the decay $S_{\mathrm{bulb}}(t)e^{-N_{\mathrm{A}}t/\tau_{\mathrm{ET}}}$ has a finite average lifetime for $N_{\mathrm{A}} > 0$ due to the exponential tail imposed by ET.

If there is a distribution in the number of acceptors bound to a given donor, $P(N)$, the total quenching efficiency is found by simply averaging over the distribution of subpopulations in the ensemble:[14,262-264]

$$\phi_{\mathrm{q}} = \sum_N P(N)\phi_{\mathrm{q}}(N). \tag{9.9}$$

In an ensemble measurement we do not necessarily have direct access to $S_{\mathrm{DA}}(t|N)$ or $\phi_{\mathrm{q}}(N)$—we measure the ensemble decay $S_{\mathrm{DA}}(t) = \sum_N P(N)S_{\mathrm{DA}}(t|N)$. Thus, Equation (9.9) requires knowledge of the quenching kinetics that determine $S_{\mathrm{DA}}(t|N)$ and $P(N)$ in order to be evaluated.

In our case, the presence of the acceptors introduces a competing decay pathway for the donors that does not change the intrinsic donor decay: $S_{\mathrm{DA}}(t|N) = S_{\mathrm{D}}(t)e^{-Nk_{\mathrm{q}}t}$ (Equation (9.3)). Additionally, $P(N)$ takes on a Poisson distribution: $P(N) = \langle N\rangle^N e^{-\langle N\rangle}/N!$. In this case, Equation (9.9) simplifies to

$$\phi_{\mathrm{q}} = \langle N\rangle k_{\mathrm{q}} \int_0^\infty dt\, S_{\mathrm{DA}}(t)e^{-k_{\mathrm{q}}t}. \tag{9.10}$$

This equation for ϕ_{q} can be straightforwardly employed by first fitting $S_{\mathrm{D}}(t)$ and $S_{\mathrm{DA}}(t)$ in order to find $\langle N\rangle$ and k_{q}, then simply inserting the measured ensemble decay of the donor–acceptor complex, $S_{\mathrm{DA}}(t)$, and evaluating the integral. An arbitrary empirical model can be used for $S_{\mathrm{D}}(t)$ provided that a kinetic model such as Equation (9.3) can be used to obtain the kinetic parameters of quenching.

Note that Equation (9.10) specifically applies when there is a Poisson distribution in the number of bound acceptors; the expression for ϕ_{q} must be modified when other distributions are used. Here we list the results for the ϕ_{q} expression for three common number distributions: each of the donors has the same number of acceptors, a Poisson distribution, and a binomial distribution. In the following examples we follow the same assumptions above, namely that the donor–acceptor decay for a complex with N acceptors can be described as $S_{\mathrm{DA}}(t|N) = S_{\mathrm{D}}(t)e^{-Nk_{\mathrm{q}}t}$. ϕ_{q} is found by applying Equation (9.8) and Equation (9.9) for different $P(N)$.

In the case where every donor has the same number acceptors bound, the distribution can be written as $P(N') = \delta(N' - N)$. In this case the quantum efficiency of each complex is the same and is given by

$$\phi_{\mathrm{q}}(N) = Nk_{\mathrm{q}} \int_0^\infty dt S_{\mathrm{DA}}(t) = Nk_{\mathrm{q}}\langle\tau_{\mathrm{DA}}\rangle. \tag{9.11}$$

An example of such a scenario is Pt-tipped CdS NRs.[23]

The case of Poisson-distributed quenching was considered in the main text, and averaging over $P(N) = \langle N \rangle^N e^{-\langle N \rangle}/N!$ gives Equation (9.10) from the main text:

$$\phi_{\mathrm{q}} = \langle N \rangle k_{\mathrm{q}} \int_0^\infty dt\, S_{\mathrm{DA}}(t) e^{-k_{\mathrm{q}} t}. \tag{9.12}$$

Finally, in the case where the finite number of acceptor binding sites needs to be accounted for, then the binomial distribution must be used: $P(N) = \binom{N_{\max}}{N} \left(\frac{\langle N \rangle}{N_{\max}}\right)^N \left(1 - \frac{\langle N \rangle}{N_{\max}}\right)^{N_{\max}-N}$, where $\langle N \rangle$ is the average number of acceptors bound per donor and $N_{\max}$ is the total number of available binding sites per donor.[66,257] In this case evaluating Equation (9.9) gives

$$\phi_{\mathrm{q}} = \langle N \rangle k_{\mathrm{q}} \int_0^\infty dt\, S_{\mathrm{DA}}(t) \frac{e^{-k_{\mathrm{q}} t}}{\left(1 - \frac{\langle N \rangle}{N_{\max}}\right) + \frac{\langle N \rangle}{N_{\max}} e^{-k_{\mathrm{q}} t}}. \tag{9.13}$$

Note that the Poisson distribution is a limiting case of the binomial distribution and Equation (9.13) simplifies to Equation (9.12) in the case that $\langle N \rangle$ is small compared to $N_{\max}$.

In the case of electron transfer in the CdS–H_2ase complexes studied here, Equation (9.10) represents the quantum efficiency of electron transfer. Rewriting Equation (9.10) in terms of ET parameters gives

$$\phi_{\mathrm{ET}} = \frac{\langle N_{\mathrm{A}} \rangle}{\tau_{\mathrm{ET}}} \int_0^\infty dt\, S_{\mathrm{DA}}(t) e^{-t/\tau_{\mathrm{ET}}}. \tag{9.14}$$

This integral is finite even when the CdS–H_2ase decay exhibits a power-law tail.

Equation (9.14) was evaluated numerically to calculate the ϕ_{ET} for each electron state of the CdS–H_2ase complexes as well as the ensemble. There are multiple ways to calculate ϕ_{ET} that are useful for evaluating different aspects of this system. For this purpose we define three

different quantum efficiencies: The "ideal quantum efficiency of ET" of each state ($\phi_{\mathrm{ET},i}^{N_\mathrm{A}=1}$, i = rod, bulb), the "ensemble quantum efficiency of ET" of each state ($\phi_{\mathrm{ET},i}$, i = rod, bulb), and the "total ensemble quantum efficiency of ET" ($\phi_{\mathrm{ET,tot}}$). The ideal $\phi_{\mathrm{ET},i}^{N_\mathrm{A}=1}$ considers the hypothetical case where N_A = 1 (no Poisson distribution in the number of bound acceptors) for both the rod and bulb and does not include branching ratio of electron localization, or fraction of non-uniform NRs; it yields the fraction of electrons that undergo ET *after* electron localization is complete as if the sample were completely made up of either uniform or non-uniform NRs. Thus, this quantity represents the internal ET efficiency of uniform or non-uniform NRs, and allows for a more direct comparison of the two morphologies by putting them on equal footing. The ensemble $\phi_{\mathrm{ET},i}$ of each state accounts for the fraction of uniform and non-uniform NRs in the ensemble as well as the different fitted values of $\langle N_\mathrm{A} \rangle$ that occur for the different morphological locations, and thus represents the actual number of photoexcited electrons that transfer to H_2ase via each state in the experimental sample of Figure 9.5. The total ensemble quantum efficiency of system, $\phi_{\mathrm{ET,tot}}$, is the sum of the ensemble $\phi_{\mathrm{ET},i}$ of the rod and the bulb: $\phi_{\mathrm{ET,tot}} = \phi_{\mathrm{ET,rod}} + \phi_{\mathrm{ET,bulb}}$. This quantity reflects how the complete sample actually performs and is directly related to the photochemical activity of the ensemble system.

The values of each version of ϕ_{ET} for CdS–H_2ase are presented in Table 8.1. Despite having similar time constants of ET, the ideal quantum efficiency of ET of the bulb is substantially larger than that of the rod ($\phi_{\mathrm{ET,bulb}}^{N_\mathrm{A}=1}$ = 62% *vs.* $\phi_{\mathrm{ET,rod}}^{N_\mathrm{A}=1}$ = 41%). This difference is due to the bulb electron being in a charge-separated state that is much longer lived than the rod electron in uniform NRs. Not only is the half-life of the bulb larger than that of the rod (16 ns *vs.* 5 ns), but the different functional forms of the two decays play an important role; the slow, distributed decay of the power law in the bulb allows much more opportunity for ET compared

to the steeper decay of the exponential tail in the rod. However, even though $\phi_{\mathrm{ET,bulb}}^{N_\mathrm{A}=1}$ is much larger than $\phi_{\mathrm{ET,rod}}^{N_\mathrm{A}=1}$, the ensemble $\phi_{\mathrm{ET},i}$ values of the rod and bub are the same, within error. This is due to a combination of there being an approximately 50/50 mixture of uniform and non-uniform NRs and the larger surface area of the rod compared to the bulb causing $\langle N_\mathrm{A} \rangle$ to be larger for the uniform NRs. Thus, in the ensemble, the rod and bulb have approximately equal contributions to $\phi_{\mathrm{ET,tot}}$ such that the total fraction of photoexcited electrons that undergo ET via the bulb is no larger than the rod. A total electron transfer efficiency of $\phi_{\mathrm{ET,tot}}$ = 37% in this sample is considerably large and reflects the fact that ET is in direct kinetic competition with the intrinsic relaxation of the CdS NRs.

Note that while the power-law decay of the non-uniform NRs prohibits us from obtaining a lifetime to compare to τ_{ET}, our analysis allowed us to calculate the exact ϕ_{ET}, which serves as a measure of the competitiveness of ET with the nanorod relaxation. Additionally, rather than comparing the average lifetime of the rod decay to τ_{ET}, we again can simply consider ϕ_{ET}. Thus Equation (9.14) (or Equation (9.10)) made it possible to directly compare the ability of the rod and bulb states to deliver electrons to the acceptor, revealing that the bulb is in principle much better. This comparison is not possible using average lifetimes.

Here we examine the differences between the exact calculation of ϕ_{ET} and the use of average lifetimes, using the rod decay of CdS–H_2ase as an example. Equation (9.4) can be applied to calculate ϕ_{ET} for the rod state because its decay is multi-exponential in nature with an exponential tail, and thus has a finite average lifetime. However, the result is notably different than when Equation (9.10) is used. For $N_\mathrm{A} = 1$ (no Poisson distribution in the number of H_2ase moieties bound), Equation (9.4) gives an ideal ET efficiency of 68% for the rod. This is significantly different from the value of 41% obtained when using Equation (9.10) (Table 1). The

difference between Equation (9.4) and Equation (9.10) is illustrated further in Figure 9.6a, which shows the ideal ϕ_{ET} as a function of $k_{\mathrm{ET}} = 1/\tau_{\mathrm{ET}}$ for Poisson-distributed ET. In the case of a single-exponential donor decay, Equation (9.4) and Equation (9.10) are in agreement (Figure 9.6b). The average method of Equation (9.4) overestimates ϕ_{ET} in this case because it treats the donor decay as a single exponential with a lifetime of $\langle\tau_{\mathrm{D}}\rangle$, but this amplitude-weighted lifetime is artificially dominated by the longest-lived component and therefore Equation (9.4) overestimates the quenching efficiency. The origin of the difference in the two expressions is that Equation (9.4) assumes that, even for the subpopulation of complexes with $N_{\mathrm{A}} = 1$ acceptors, the rate constant of quenching is related to the average lifetimes by $k_{\mathrm{q}} = \frac{1}{\langle\tau_{\mathrm{DA}}\rangle} - \frac{1}{\langle\tau_{\mathrm{D}}\rangle}$ (or $\bar{k}_{\mathrm{DA}} = \bar{k}_{\mathrm{D}} + \bar{k}_{\mathrm{q}}$), which is not true for a general non-exponential donor decay. Thus Equation (9.4), which relies on average lifetimes, can only approximate the competitiveness of quenching when the donor exhibits multi-exponential relaxation. In contrast, Equation (9.10), which was derived from the definition of ϕ_{q} and rate equations while accounting for a heterogeneous decay, accounts for competition between quenching and every decay component that leads to non-exponential electron depopulation in the ensemble.

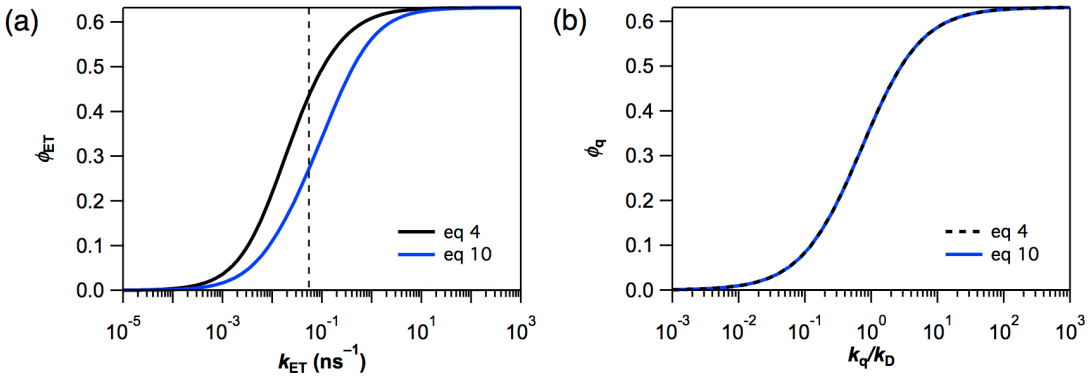

Figure 9.6. Comparison of ϕ_{ET} (or ϕ_q) calculated using average lifetimes (Equation (9.4)) and exactly (Equation (9.10)) as function of quenching rate. (a) The ideal ϕ_{ET} of rod state of uniform in CdS–H_2ase complexes, as a function of $k_{ET} = 1/\tau_{ET}$, calculated by Equation (9.4) and Equation (9.10) for $\langle N_A \rangle = 1$. Electron localization is not considered in this simplified example. For reference, $\bar{k}_D = 1/\langle \tau_D \rangle = 0.055 \pm 0.003$ ns^{-1} for the CdS rod is indicated with a dashed vertical line, and $k_{ET} = 1/\tau_{ET} = 0.07 \pm 0.02$ ns^{-1} for the rod (Table 1). (b) Comparison of ϕ_q calculated using Equation (9.4) and Equation (9.10) for a single exponential donor decay as a function of k_q/k_D, and a Poisson distribution of acceptors with $\langle N_A \rangle = 1$.

Equation (9.10) is an exact expression for calculating ϕ_q that accounts for the competition between quenching and each component of a non-exponential donor decay. In other words, it is the weighted average of the quenching efficiency of all subpopulations in an ensemble. It can be applied for an arbitrary donor decay $S_D(t)$ in which non-exponential relaxation occurs due to a heterogeneous distribution of decay rates in the ensemble. It allowed us to calculate ϕ_{ET} in the CdS–H_2ase complex even when the CdS NRs had a power-law decay, which does not have an average lifetime. However, the model for ϕ_q used here is not without limitations. First, this model assumes that the presence of the acceptor does not influence the intrinsic decay pathways within the donor. The model could in principle be adapted to account for such an effect, but it complicates the derivation and this was not necessary for the CdS–H_2ase system. Secondly, the use of Equation (9.10) requires knowledge of $\langle N \rangle$ and k_q in addition to the empirical decay of the donor–acceptor complex. We were able to obtain these parameters by using a kinetic model for ET (Equation (9.3)) and fitting transient data of the donor with and

without the acceptors present. Finally, this model assumes that all subpopulations are excited with equal probability such that $S_{\mathrm{DA}}(t = 0|N)$ is the same for all N. Physically, this means that the presence of the donor does not affect the likelihood of a particular donor being excited, which we expect to be the case for CdS in the presence of H_2ase because the extinction coefficient of the CdS NRs is much larger than that of H_2ase. While the expression for ϕ_{q} used here is specific to the present sample in these ways, the general approach of deriving ϕ_{q} exactly using rate equations can be applied to a broad range of systems to give an exact calculation as opposed to an approximate average.

9.4.4 Implications and future design

The analysis above allows us to break down ϕ_{ET} into its underlying contributions and informs the rational design of more efficient photochemical systems. The ET efficiency is determined by the competition between ET and electron relaxation within the nanocrystal. In CdS–H_2ase with 3-MPA ligands studied here, ET is in direct competition with recombination, resulting in ET efficiencies close to 50% of the maximum for both uniform and non-uniform CdS NRs. Thus, ϕ_{ET} of the CdS–H_2ase system can be improved by attaining a long-lived electron state the CdS NRs, making ET faster, or both. These changes could be achieved through relatively simple synthetic means.

One way to control the CdS NR relaxation rate is through morphology. Because hole trapping is fast in CdS nanocrystals and the presence of the bulb drives the electron to dissociate from the hole, non-uniform CdS NRs exhibit intrinsic charge separation and have much longer lived states than uniform NRs (Figure 9.1). It follows that a sample made up entirely of non-uniform structures would have a larger ϕ_{ET} than the one studied here, provided that the H_2ase:CdS mixing ratio were optimized for acceptor loading on the bulb. This charge separation

may additionally improve the efficiency of multi-electron redox reactions, which rely on slow recombination of the intermediates due to back-ET and have been shown to be improved by electron–hole charge separation.[47,107,112] Separately, type-II and quasi type-II semiconductor heterostructure nanocrystals, designed to extend nanocrystal lifetimes by reducing wavefunction overlap, could also be used to achieve more efficient ET.[47,113,152,153] However, we recently found that non-uniform CdSe/CdS and ZnSe/CdS dot-in-rod heterostructures in fact exhibited similar dynamics to single-component, non-uniform CdS NRs.[177] Interestingly, electron−hole dissociation between a rod-trapped hole and a bulb-localized electron occurs in all three systems, and that charge-separated state is longer lived than the interfacial state formed by the type-II band alignment. Therefore, such heterostructures would be no more competitive for ET than their single-component counterparts, at least in terms of the excited-state decay rate. However, the seed material can influence the electron state in the bulb and it remains to be seen if such heterostructure nanocrystals also influence the ET rate constant.

The rate constant of ET in CdS–H_2ase complexes may be improved through modifications of surface chemistry. We have previously shown that mercaptocarboxylate surface-capping ligands, such as the 3-MPA ligands used here, present a barrier to ET in CdS–H_2ase.[14] Thus, using different ligands that decrease the CdS–H_2ase distance or otherwise increase the electronic coupling could bring ϕ_{ET} to its maximal value for this system. This maximum would be achieved with a hundred-hold increase in k_{ET} (Figure 9.7), which we showed could be a realistic goal with short ligands.[14] Additionally, having such fast ET would render uniform and non-uniform CdS NRs equally as efficient for ET because ET would easily outcompete recombination in both structures (Figure 9.7). However, charge separation in non-uniform NRs could still impact the overall photochemical activity in this case.

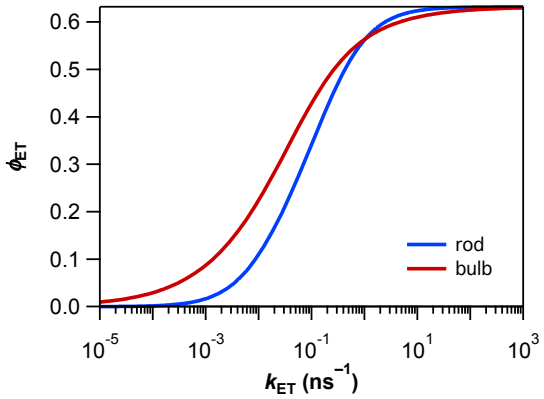

Figure 9.7. Comparison of ϕ_{ET} of rod and bulb in CdS-H_2ase complexes as a function of k_{ET}, calculated using Equation (9.14). Calculations were performed using measured decay parameters of CdS rod and bulb (Figure 9.1 and Figure 9.5) and $\langle N_A \rangle$ was set to 1 for both morphological features for comparison. The range of k_{ET} values represent hypothetical values of the ET rate constant in the CdS-H_2ase system. The value of $k_{ET} = 1/\tau_{ET}$ in this system is 0.07 ± 0.02 ns^{-1} for the rod and 0.09 ± 0.01 ns^{-1} for the bulb (Table 8.1).

Finally, we note that increasing $\langle N_A \rangle$ would also increase ϕ_{ET} but can be disadvantageous for multi-electron photochemistry because multiple acceptors compete for electrons.[110] Indeed, the optimal H_2ase loading for H_2 production in the CdS–H_2ase system with 3-MPA ligands was found to be near $\langle N_A \rangle = 1$.[44] However, this limitation is defined by rates of back-ET and hole scavenging and could potentially be avoided.

9.5 Conclusions

CdS–H_2ase is a system that exemplifies the need to exactly model the competition between quenching and heterogeneous multi-timescale donor relaxation in order to accurately calculate ϕ_q. Average lifetimes led to inaccurate results that did not capture the contributions of fast decay components in the CdS NR donor and moreover could not be used for power-law donor decay. Thus care must be taken when describing non-exponential excited-state decays with average decay parameters. Modeling the relationship between ET and nanocrystal relaxation led to a

quantitative understanding of the factors that determined ϕ_{ET} for CdS NR–H_2ase complexes and provided guidance for future design. The efficiency of ET in CdS NR–H_2ase complexes could be improved either by utilizing intrinsic charge separation in a completely non-uniform CdS NR sample or by increasing the rate of ET via surface modifications. Non-exponential decay curves are ubiquitous in semiconductor nanocrystals, and while the expression for ϕ_q derived here is specific to a Poisson distribution of quenchers, the general approach of deriving ϕ_q from its definition and rate equations is relatively simple and can be applied to a large range of systems on a case-by-case basis. We advocate for an exact treatment of calculating quenching efficiencies in donor–acceptor systems when possible, cautioning that the use of average lifetimes can lead to significant errors when non-exponential relaxation occurs in the ensemble.

Chapter 10

Summary and Conclusion

The work presented in this dissertation described investigations of the excited-state dynamics of semiconductor nanocrystals, focusing on the discovery of trapped-hole diffusion in CdS and CdSe nanorods as well as the modeling of electron-transfer kinetics in nanocrystal–acceptor complexes. Together, the combination of experimental measurements, theoretical modeling and data analysis reported here provide detailed conceptual and quantitative pictures of carrier dynamics these systems.

Part I covered research efforts to elucidate the dynamics of photoexcited charge carriers that are trapped at defect sites on nanocrystal surfaces. The main contribution of that series of studies was the discovery of evidence that trapped holes on the surfaces of CdS and CdSe nanocrystals are not stationary, but instead are mobile on timescales relevant to other excited-state relaxation processes such as recombination and photochemistry. Chapter 3 explained in detail how we arrived at the picture that trapped holes diffuse among sulfur sites on the surfaces of CdS nanorods. Chapters 4 and 5 expanded upon that original study, showing that the same phenomenon occurs in other related materials, including CdSe/CdS and ZnSe/CdS dot-in-rod heterostructures as well as CdSe nanorods. Together, those studies suggest that trapped-hole diffusion is a general phenomenon in Cd-chalcogenide nanocrystals, but one that is normally obscured due to spatial overlap of the electron and trapped hole. However, as the evidence for this phenomenon was indirect, we considered alternative interpretations of the experimental observations. As explained in Chapter 6, this was accomplished with a temperature dependence study of CdS and CdSe nanorods, which ruled out alternative mechanisms for the observed

dynamics, making the evidence for trapped-hole diffusion much more robust. In sum, this work provides a fundamentally different view of the behavior of trapped holes in these materials, as the conventional picture was that charge carriers become immobile once they have trapped. The ability of trapped holes to diffuse on nanocrystal surfaces may have wide-ranging consequences for the photophysics and photochemistry of CdS- and CdSe-based optoelectronic devices.

Part II presented work to explain the nonexponential kinetics of charge transfer in nanocrystal–acceptor complexes in terms of simple analytical models. Chapter 7 described transient absorption measurements of electron transfer from photoexcited CdS nanorods to hydrogenase enzyme, showing that the microscopic rate constant and quantum efficiency of electron transfer can be obtained by accounting for the distributions in the numbers of electron traps and enzymes adsorbed. In Chapter 8 we established the impact of surface-capping ligands on electron transfer and subsequent H_2 production in CdS nanorod–hydrogenase complexes. Chapter 9 provided an exact calculation of charge-transfer efficiency in heterogeneous nanocrystal–acceptor complexes, showing that the use average rate constants can lead to significant errors. Additionally, relating back to Part I of this dissertation, Chapter 9 demonstrated the benefit of charge separation followed by trapped-hole diffusion-limited recombination in CdS nanorods, as the resulting state is exceptionally long-lived, improving the efficiency of charge extraction by making charge transfer more competitive with recombination. The relatively simple models developed in Part II capture the essential kinetics of electron transfer and provide guidance on the relevant design parameters that could be controlled to optimize photochemical redox reactions using nanocrystal–enzyme hybrids. Together, those chapters showed that kinetic modeling of ultrafast spectroscopy experiments on heterogeneous

systems can yield deep insights about the microscopic processes underlying the behavior of complex systems.

In the research presented in this dissertation I sought to perform experiments and data analysis guided by physical models in order to gain new insights about the excited-state dynamics CdS and CdSe nanorods, an important class of semiconductor nanocrystals. It was my hope to cast the complex photophysical and photochemical behavior of these materials in terms of relatively simple physical pictures. The power of theoretical modeling is to take the observations of experiments and reveal physical insights that deepen our scientific understanding and provide predictive abilities that can be used to develop practical applications. This body of work extends our fundamental understanding of the behavior of trapped holes at the surfaces of Cd-chalcogenide nanocrystals as well as electron-transfer kinetics in nanocrystal–acceptor complexes. Ultimately, this dissertation comprises advances in the basic science that, in the future, may provide important insights that inform the design of solar energy harvesting systems.

References

1. Ekimov, A. I.; Onushchenko, A. A., Quantum size effect in 3-dimensional microscopic semiconductor crystals. *J. Exp. Theor. Phys. Lett.,* **1981,** *34*, 345.
2. Kuno, M., *Introductory Nanoscience: Physical and Chemical Concepts*. Garland Science: New York, **2012**.
3. Rossetti, R.; Nakahara, S.; Brus, L. E., Quantum Size Effects in the Redox Potentials, Resonance Raman-Spectra, and Electronic-Spectra of CdS Crystallites in Aqueous-Solution. *J. Chem. Phys.,* **1983,** *79*, 1086-1088.
4. Kamat, P. V., Quantum dot solar cells. Semiconductor nanocrystals as light harvesters. *J. Phys. Chem. C,* **2008,** *112*, 18737-18753.
5. Talapin, D. V.; Lee, J. S.; Kovalenko, M. V.; Shevchenko, E. V., Prospects of Colloidal Nanocrystals for Electronic and Optoelectronic Applications. *Chem. Rev.,* **2010,** *110*, 389-458.
6. Nozik, A. J.; Beard, M. C.; Luther, J. M.; Law, M.; Ellingson, R. J.; Johnson, J. C., Semiconductor Quantum Dots and Quantum Dot Arrays and Applications of Multiple Exciton Generation to Third-Generation Photovoltaic Solar Cells. *Chem. Rev.,* **2010,** *110*, 6873-6890.
7. Han, Z. J.; Qiu, F.; Eisenberg, R.; Holland, P. L.; Krauss, T. D., Robust photogeneration of H_2 in water using semiconductor nanocrystals and a nickel catalyst. *Science,* **2012,** *338*, 1321-1324.
8. Wilker, M. B.; Schnitzenbaumer, K. J.; Dukovic, G., Recent Progress in Photocatalysis Mediated by Colloidal II-VI Nanocrystals. *Isr. J. Chem.,* **2012,** *52*, 1002-1015.
9. West, J. L.; Halas, N. J., Engineered nanomaterials for biophotonics applications: Improving sensing, imaging, and therapeutics. *Annu. Rev. Biomed. Eng.,* **2003,** *5*, 285-292.
10. Bruchez, M.; Moronne, M.; Gin, P.; Weiss, S.; Alivisatos, A. P., Semiconductor nanocrystals as fluorescent biological labels. *Science,* **1998,** *281*, 2013-2016.
11. Grimme, R. A.; Lubner, C. E.; Bryant, D. A.; Golbeck, J. H., Photosystem I/Molecular Wire/Metal Nanoparticle Bioconjugates for the Photocatalytic Production of H2. *J. Am. Chem. Soc.,* **2008,** *130*, 6308-6309.

12. Kornienko, N.; Sakimoto, K. K.; Herlihy, D. M.; Nguyen, S. C.; Alivisatos, A. P.; Harris, C. B.; Schwartzberg, A.; Yang, P., Spectroscopic Elucidation of Energy Transfer in Hybrid Inorganic–Biological Organisms for Solar-to-Chemical Production. *Proc. Natl. Acad. Sci. U.S.A.,* **2016,** *113*, 11750-11755.
13. Krause, M. M.; Mooney, J.; Kambhampati, P., Chemical and Thermodynamic Control of the Surface of Semiconductor Nanocrystals for Designer White Light Emitters. *ACS Nano,* **2013,** *7*, 5922-5929.
14. Wilker, M. B.; Utterback, J. K.; Greene, S.; Brown, K. A.; Mulder, D. W.; King, P. W.; Dukovic, G., Role of Surface-Capping Ligands in Photoexcited Electron Transfer between CdS Nanorods and [FeFe] Hydrogenase and the Subsequent H-2 Generation. *J. Phys. Chem. C,* **2018,** *122*, 741-750.
15. Yetisen, A. K.; Coskun, A. F.; England, G.; Cho, S. Y.; Butt, H.; Hurwitz, J.; Kolle, M.; Khademhosseini, A.; Hart, A. J.; Folch, A.; Yun, S. H., Art on the Nanoscale and Beyond. *Advanced Materials,* **2016,** *28*, 1724-1742.
16. Liu, C., *The Three-Body Problem*. Tor Books: New York, **2016**.
17. Climate Change 2016: The Physical Science Basis. Intergovernmental Panel on Climate Change. **2016**.
18. Withagen, C., Pollution and Exhaustibility of Fossil-Fuels. *Resour. Energy Econ.,* **1994,** *16*, 235-242.
19. Kampa, M.; Castanas, E., Human health effects of air pollution. *Environ. Pollut.,* **2008,** *151*, 362-367.
20. Lewis, N. S.; Crabtree, G.; Nozik, A. J.; Wasielewski, M. R.; Alivisatos, P.; Kung, H.; Tsao, J.; Chandler, E.; Walukiewicz, W.; Spitler, M.; Ellingson, R.; Overend, R.; Mazer, J.; Gress, M.; Horwitz, J.; Ashton, C.; Herndon, B.; Shapard, L.; Nault, R. M., Basic research needs for solar energy utilization: report of the basic energy sciences workshop on solar energy utilization, April 18-21, 2005. US Department of Energy, Office of Basic Energy Science: 2005.
21. Blankenship, R. E.; Tiede, D. M.; Barber, J.; Brudvig, G. W.; Fleming, G.; Ghirardi, M.; Gunner, M. R.; Junge, W.; Kramer, D. M.; Melis, A.; Moore, T. A.; Moser, C. C.; Nocera, D. G.; Nozik, A. J.; Ort, D. R.; Parson, W. W.; Prince, R. C.; Sayre, R. T., Comparing

Photosynthetic and Photovoltaic Efficiencies and Recognizing the Potential for Improvement. *Science,* **2011,** *332*, 805-809.

22. Semonin, O. E.; Luther, J. M.; Choi, S.; Chen, H. Y.; Gao, J. B.; Nozik, A. J.; Beard, M. C., Peak external photocurrent quantum efficiency exceeding 100% via MEG in a quantum dot solar cell. *Science,* **2011,** *334*, 1530-1533.
23. Wu, K.; Zhu, H.; Liu, Z.; Rodriguez-Cordoba, W.; Lian, T., Ultrafast charge separation and long-lived charge separated state in photocatalytic CdS-Pt nanorod heterostructures. *J. Am. Chem. Soc.,* **2012,** *134*, 10337-40.
24. Wilker, M. B.; Shinopoulos, K. E.; Brown, K. A.; Mulder, D. W.; King, P. W.; Dukovic, G., Electron transfer kinetics in CdS nanorod–[FeFe]-hydrogenase complexes and implications for photochemical H_2 generation. *J. Am. Chem. Soc.,* **2014,** *136*, 4316-4324.
25. Yu, W. W.; Qu, L.; Guo, W.; Peng, X., Experimental determination of the extinction coefficient of CdTe, CdSe, and CdS nanocrystals. *Chem. Mater.,* **2003,** *15*, 2854-2860.
26. Peterson, M. D.; Cass, L. C.; Harris, R. D.; Edme, K.; Sung, K.; Weiss, E. A., The role of ligands in determining the exciton relaxation dynamics in semiconductor quantum dots. *Annu. Rev. Phys. Chem.,* **2014,** *65*, 317-339.
27. Nag, A.; Kovalenko, M. V.; Lee, J.-S.; Liu, W.; Spokoyny, B.; Talapin, D. V., Metal-free Inorganic Ligands for Colloidal Nanocrystals: S2-, HS-, Se2-, HSe-, Te2-, HTe-, TeS32-, OH-, and NH2- as Surface Ligands. *J. Am. Chem. Soc.,* **2011,** *133*, 10612-10620.
28. Anderson, N. C.; Hendricks, M. P.; Choi, J. J.; Owen, J. S., Ligand Exchange and the Stoichiometry of Metal Chalcogenide Nanocrystals: Spectroscopic Observation of Facile Metal-Carboxylate Displacement and Binding. *J. Am. Chem. Soc.,* **2013,** *135*, 18536-18548.
29. Yun, H. J.; Paik, T.; Edley, M. E.; Baxter, J. B.; Murray, C. B., Enhanced Charge Transfer Kinetics of CdSe Quantum Dot-Sensitized Solar Cell by Inorganic Ligand Exchange Treatments. *ACS Appl. Mater. Inter.,* **2014,** *6*, 3721-3728.
30. Brown, K. A.; Dayal, S.; Ai, X.; Rumbles, G.; King, P. W., Controlled Assembly of Hydrogenase-CdTe Nanocrystal Hybrids for Solar Hydrogen Production. *J. Am. Chem. Soc.,* **2010,** *132*, 9672-9680.
31. Brown, K. A.; Song, Q.; Mulder, D. W.; King, P. W., Diameter Dependent Electron Transfer Kinetics in Semiconductor-Enzyme Complexes. *ACS Nano,* **2014,** *8*, 10790-10798.

32. Bawendi, M. G.; Steigerwald, M. L.; Brus, L. E., The quantum mechanics of larger semiconductor clusters ("quantum dots"). *Annu. Rev. Phys. Chem.,* **1990,** *41*, 477-496.
33. Peng, X. G.; Manna, L.; Yang, W. D.; Wickham, J.; Scher, E.; Kadavanich, A.; Alivisatos, A. P., Shape control of CdSe nanocrystals. *Nature,* **2000,** *404*, 59-61.
34. Burda, C.; Chen, X. B.; Narayanan, R.; El-Sayed, M. A., Chemistry and properties of nanocrystals of different shapes. *Chem. Rev.,* **2005,** *105*, 1025-1102.
35. Sadhu, S.; Patra, A., Relaxation Dynamics of Anisotropic Shaped CdS Nanoparticles. *J. Phys. Chem. C,* **2011,** *115*, 16867-16872.
36. Jones, M.; Scholes, G. D., On the use of time-resolved photoluminescence as a probe of nanocrystal photoexcitation dynamics. *J. Mater. Chem.,* **2010,** *20*, 3533-3538.
37. Knowles, K. E.; McArthur, E. A.; Weiss, E. A., A Multi-Timescale Map of Radiative and Nonradiative Decay Pathways for Excitons in CdSe Quantum Dots. *ACS Nano,* **2011,** *5*, 2026-2035.
38. Scholes, G. D.; Rumbles, G., Excitons in nanoscale systems (vol 5, pg 683, 2006). *Nat. Mater.,* **2006,** *5*, 920-920.
39. Brus, L. E., Electron Electron and Electron-Hole Interactions in Small Semiconductor Crystallites - the Size Dependence of the Lowest Excited Electronic State. *J. Chem. Phys.,* **1984,** *80*, 4403-4409.
40. Mohamed, M. B.; Burda, C.; El-Sayed, M. A., Shape dependent ultrafast relaxation dynamics of CdSe nanocrystals: Nanorods vs nanodots. *Nano Lett.,* **2001,** *1*, 589-593.
41. Dabbousi, B. O.; Rodriguez-Viejo, J.; Mikulec, F. V.; Heine, J. R.; Mattoussi, H.; Ober, R.; Jensen, K. F.; Bawendi, M. G., (CdSe)ZnS core-shell quantum dots: Synthesis and characterization of a size series of highly luminescent nanocrystallites. *J. Phys. Chem. B,* **1997,** *101*, 9463-9475.
42. Wang, P.; Klein, C.; Humphry-Baker, R.; Zakeeruddin, S. M.; Gratzel, M., A high molar extinction coefficient sensitizer for stable dye-sensitized solar cells. *Journal of the American Chemical Society,* **2005,** *127*, 808-809.
43. Duonghong, D.; Ramsden, J.; Gratzel, M., Dynamics of Interfacial Electron-Transfer Processes in Colloidal Semiconductor Systems. *J. Am. Chem. Soc.,* **1982,** *104*, 2977-2985.

44. Brown, K. A.; Wilker, M. B.; Boehm, M.; Dukovic, G.; King, P. W., Characterization of photochemical processes for H2 production by CdS nanorod-[FeFe] hydrogenase complexes. *J. Am. Chem. Soc.,* **2012,** *134*, 5627-36.

45. Brown, K. A.; Harris, D. F.; Wilker, M. B.; Rasmussen, A.; Khadka, N.; Hamby, H.; Keable, S.; Dukovic, G.; Peters, J. W.; Seefeldt, L. C.; King, P. W., Light-driven dinitrogen reduction catalyzed by a CdS:nitrogenase MoFe protein biohybrid. *Science,* **2016,** *352*, 448-450.

46. Brown, K. A.; Wilker, M. B.; Boehm, M.; Hamby, H.; Dukovic, G.; King, P. W., Photocatalytic Regeneration of Nicotinamide Cofactors by Quantum Dot-Enzyme Biohybrid Complexes. *ACS Catal.,* **2016,** *6*, 2201-2204.

47. Zhu, H.; Song, N.; Lv, H.; Hill, C. L.; Lian, T., Near Unity Quantum Yield of Light-Driven Redox Mediator Reduction and Efficient H2 Generation Using Colloidal Nanorod Heterostructures. *J. Am. Chem. Soc.,* **2012,** *134*, 11701-11708.

48. Klimov, V. I.; McBranch, D. W., Femtosecond 1P-to-1S electron relaxation in strongly confined semiconductor nanocrystals. *Phys. Rev. Lett.,* **1998,** *80*, 4028-4031.

49. Guyot-Sionnest, P.; Wehrenberg, B.; Yu, D., Intraband relaxation in CdSe nanocrystals and the strong influence of the surface ligands. *J. Phys. Chem.,* **2005,** *123*.

50. Bockelmann, U.; Bastard, G., Phonon-Scattering and Energy Relaxation in 2-Dimensional, One-Dimensional, and Zero-Dimensional Electron Gases. *Phys. Rev. B,* **1990,** *42*, 8947-8951.

51. Tsui, E. Y.; Carroll, G. M.; Miller, B.; Marchioro, A.; Gamelin, D. R., Extremely Slow Spontaneous Electron Trapping in Photodoped n-Type CdSe Nanocrystals. *Chem. Mater.,* **2017,** *29*, 3754-3762.

52. Keene, J. D.; McBride, J. R.; Orfield, N. J.; Rosenthal, S. J., Elimination of Hole-Surface Overlap in Graded CdSxSe1-x Nanocrystals Revealed by Ultrafast Fluorescence Upconversion Spectroscopy. *ACS Nano,* **2014,** *8*, 10665-73.

53. Underwood, D. F.; Kippeny, T.; Rosenthal, S. J., Ultrafast carrier dynamics in CdSe nanocrystals determined by femtosecond fluorescence upconversion spectroscopy. *J. Phys. Chem. B,* **2001,** *105*, 436-443.

54. Garrett, M. D.; Dukes, A. D.; McBride, J. R.; Smith, N. J.; Pennycook, S. J.; Rosenthal, S. J., Band edge recombination in CdSe, CdS and CdSxSe1-x alloy nanocrystals observed by

ultrafast fluorescence upconversion: The effect of surface trap states. *J. Phys. Chem. C,* **2008,** *112*, 12736-12746.

55. Garrett, M. D.; Bowers, M. J.; McBride, J. R.; Orndorff, R. L.; Pennycook, S. J.; Rosenthal, S. J., Band edge dynamics in CdSe nanocrystals observed by ultrafast fluorescence upconversion. *J. Phys. Chem. C,* **2008,** *112*, 436-442.
56. Klimov, V. I.; Schwarz, C. J.; McBranch, D. W.; Leatherdale, C. A.; Bawendi, M. G., Ultrafast dynamics of inter- and intraband transitions in semiconductor nanocrystals: Implications for quantum-dot lasers. *Phys. Rev. B,* **1999,** *60*, R2177-R2180.
57. Klimov, V.; Bolivar, P. H.; Kurz, H., Ultrafast carrier dynamics in semiconductor quantum dots. *Phys. Rev. B,* **1996,** *53*, 1463-1467.
58. McArthur, E. A.; Morris-Cohen, A. J.; Knowles, K. E.; Weiss, E. A., Charge Carrier Resolved Relaxation of the First Excitonic State in CdSe Quantum Dots Probed with Near-Infrared Transient Absorption Spectroscopy. *J. Phys. Chem. B,* **2010,** *114*, 14514-14520.
59. Burda, C.; Link, S.; Mohamed, M.; El-Sayed, M., The relaxation pathways of CdSe nanoparticles monitored with femtosecond time-resolution from the visible to the IR: Assignment of the transient features by carrier quenching. *J. Phys. Chem. B,* **2001,** *105*, 12286-12292.
60. Li, X.; Feng, D. H.; Tong, H. F.; Jia, T. Q.; Deng, L.; Sun, Z. R.; Xu, Z. Z., Hole Surface Trapping Dynamics Directly Monitored by Electron Spin Manipulation in CdS Nanocrystals. *J. Phys. Chem. Lett.,* **2014,** *5*, 4310-4316.
61. Klimov, V. I.; McBranch, D. W.; Leatherdale, C. A.; Bawendi, M. G., Electron and hole relaxation pathways in semiconductor quantum dots. *Phys. Rev. B,* **1999,** *60*, 13740-13749.
62. Wuister, S. F.; Donega, C. D.; Meijerink, A., Influence of thiol capping on the exciton luminescence and decay kinetics of CdTe and CdSe quantum. *J. Phys. Chem. B,* **2004,** *108*, 17393-17397.
63. Wuister, S. F.; van Houselt, A.; de Mello Donegá, C.; Vanmaekelbergh, D.; Meijerink, A., Temperature Antiquenching of the Luminescence from Capped CdSe Quantum Dots. *Angew. Chem. Int. Edit.,* **2004,** *43*, 3029-3033.
64. Utterback, J. K.; Grennell, A. N.; Wilker, M. B.; Pearce, O.; Eaves, J. D.; Dukovic, G., Observation of trapped-hole diffusion on the surfaces of CdS nanorods. *Nat. Chem.,* **2016,** *8*, 1061-1066.

65. Utterback, J. K.; Wilker, M. B.; Brown, K. A.; King, P. W.; Eaves, J. D.; Dukovic, G., Competition between electron transfer, trapping, and recombination in CdS nanorod-hydrogenase complexes. *Phys. Chem. Chem. Phys.,* **2015,** *17*, 5538-5542.

66. Morris-Cohen, A. J.; Vasilenko, V.; Amin, V. A.; Reuter, M. G.; Weiss, E. A., Model for Adsorption of Ligands to Colloidal Quantum Dots with Concentration-Dependent Surface Structure. *ACS Nano,* **2012,** *6*, 557-565.

67. Brus, L., Electronic Wave-Functions in Semiconductor Clusters - Experiment and Theory. *J. Phys. Chem.,* **1986,** *90*, 2555-2560.

68. Jasieniak, J.; Mulvaney, P., From Cd-rich to Se-rich–the manipulation of CdSe nanocrystal surface stoichiometry. *J. Am. Chem. Soc.,* **2007,** *129*, 2841-8.

69. Gomez-Campos, F. M.; Califano, M., Hole Surface Trapping in CdSe Nanocrystals: Dynamics, Rate Fluctuations, and Implications for Blinking. *Nano Lett.,* **2012,** *12*, 4508-4517.

70. Krause, M. M.; Kambhampati, P., Linking surface chemistry to optical properties of semiconductor nanocrystalsl. *Phys. Chem. Chem. Phys.,* **2015,** *17*, 18882-18894.

71. Busby, E.; Anderson, N. C.; Owen, J. S.; Sfeir, M. Y., Effect of Surface Stoichiometry on Blinking and Hole Trapping Dynamics in CdSe Nanocrystals. *J. Phys. Chem. C,* **2015,** *119*, 27797-27803.

72. Gao, Y.; Peng, X. G., Photogenerated Excitons in Plain Core CdSe Nanocrystals with Unity Radiative Decay in Single Channel: The Effects of Surface and Ligands. *J. Am. Chem. Soc.,* **2015,** *137*, 4230-4235.

73. Kilina, S. V.; Tamukong, P. K.; Kilin, D. S., Surface Chemistry of Semiconducting Quantum Dots: Theoretical Perspectives. *Acc. Chem. Res.,* **2016,** *49*, 2127-2135.

74. Houtepen, A. J.; Hens, Z.; Owen, J. S.; Infante, I., On the Origin of Surface Traps in Colloidal II-VI Semiconductor Nanocrystals. *Chem. Mater.,* **2017,** *29*, 752-761.

75. Hill, N. A.; Whaley, K. B., A Theoretical-Study of the Influence of the Surface on the Electronic-Structure of Cdse Nanoclusters. *J. Chem. Phys.,* **1994,** *100*, 2831-2837.

76. Wei, H. H. Y.; Evans, C. M.; Swartz, B. D.; Neukirch, A. J.; Young, J.; Prezhdo, O. V.; Krauss, T. D., Colloidal semiconductor quantum dots with tunable surface composition. *Nano Lett.,* **2012,** *12*, 4465-4471.

77. Knowles, K. E.; Tice, D. B.; McArthur, E. A.; Solomon, G. C.; Weiss, E. A., Chemical Control of the Photoluminescence of CdSe Quantum Dot-Organic Complexes with a Series of Para-Substituted Aniline Ligands. *J. Am. Chem. Soc.,* **2010,** *132*, 1041-1050.

78. Kilina, S. V.; Neukirch, A. J.; Habenicht, B. F.; Kilin, D. S.; Prezhdo, O. V., Quantum Zeno Effect Rationalizes the Phonon Bottleneck in Semiconductor Quantum Dots. *Phys. Rev. Lett.,* **2013,** *110*.

79. Mooney, J.; Krause, M. M.; Saari, J. I.; Kambhampati, P., Challenge to the deep-trap model of the surface in semiconductor nanocrystals. *Phys. Rev. B,* **2013,** *87*.

80. Jones, M.; Lo, S. S.; Scholes, G. D., Quantitative modeling of the role of surface traps in CdSe/CdS/ZnS nanocrystal photoluminescence decay dynamics. *Proc. Natl. Acad. Sci. U.S.A.,* **2009,** *106*, 3011-3016.

81. Mooney, J.; Krause, M. M.; Saari, J. I.; Kambhampati, P., A microscopic picture of surface charge trapping in semiconductor nanocrystals. *J. Chem. Phys.,* **2013,** *138*, 204705.

82. Wu, K.; Du, Y.; Tang, H.; Chen, Z.; Lian, T., Efficient extraction of trapped holes from colloidal CdS nanorods. *J. Am. Chem. Soc.,* **2015,** *137*, 10224-30.

83. Olshansky, J. H.; Balan, A. D.; Ding, T. X.; Fu, X.; Lee, Y. V.; Alivisatos, A. P., Temperature-Dependent Hole Transfer from Photoexcited Quantum Dots to Molecular Species: Evidence for Trap-Mediated Transfer. *ACS Nano,* **2017,** *11*, 8346-8355.

84. Sadhu, S.; Tachiya, M.; Patra, A., A Stochastic Model for Energy Transfer from CdS Quantum Dots/Rods (Donors) to Nile Red Dye (Acceptors). *J. Phys. Chem. C,* **2009,** *113*, 19488-19492.

85. Tarafder, K.; Surendranath, Y.; Olshansky, J. H.; Alivisatos, A. P.; Wang, L. W., Hole Transfer Dynamics from a CdSe/CdS Quantum Rod to a Tethered Ferrocene Derivative. *J. Am. Chem. Soc.,* **2014,** *136*, 5121-5131.

86. Cohn, A. W.; Schimpf, A. M.; Gunthardt, C. E.; Gamelin, D. R., Size-Dependent Trap-Assisted Auger Recombination in Semiconductor Nanocrystals. *Nano Lett.,* **2013,** *13*, 1810-1815.

87. Sippel, P.; Albrecht, W.; Mitoraj, D.; Eichberger, R.; Hannappel, T.; Vanmaekelbergh, D., Two-Photon Photoemission Study of Competing Auger and Surface-Mediated Relaxation of Hot Electrons in CdSe Quantum Dot Solids. *Nano Lett.,* **2013,** *13*, 1655-1661.

88. Efros, A. L.; Nesbitt, D. J., Origin and control of blinking in quantum dots. *Nat. Nanotechnol.,* **2016,** *11*, 661-671.

89. Wu, K. F.; Hill, L. J.; Chen, J. Q.; McBride, J. R.; Pavlopolous, N. G.; Richey, N. E.; Pyun, J.; Lian, T. Q., Universal Length Dependence of Rod-to-Seed Exciton Localization Efficiency in Type I and Quasi-Type II CdSe@CdS Nanorods. *ACS Nano,* **2015,** *9*, 4591-4599.

90. Klimov, V. I.; Mikhailovsky, A. A.; Xu, S.; Malko, A.; Hollingsworth, J. A.; Leatherdale, C. A.; Eisler, H. J.; Bawendi, M. G., Optical gain and stimulated emission in nanocrystal quantum dots. *Science,* **2000,** *290*, 314-317.

91. Kambhampati, P., Hot Exciton Relaxation Dynamics in Semiconductor Quantum Dots: Radiationless Transitions on the Nanoscale. *J. Phys. Chem. C,* **2011,** *115*, 22089-22109.

92. Talapin, D. V.; Rogach, A. L.; Kornowski, A.; Haase, M.; Weller, H., Highly luminescent monodisperse CdSe and CdSe/ZnS nanocrystals synthesized in a hexadecylamine-trioctylphosphine oxide-trioctylphospine mixture. *Nano Lett.,* **2001,** *1*, 207-211.

93. Bryant, G. W.; Jaskolski, W., Surface effects on capped and uncapped nanocrystals. *J. Phys. Chem. B,* **2005,** *109*, 19650-19656.

94. Mahler, B.; Spinicelli, P.; Buil, S.; Quelin, X.; Hermier, J. P.; Dubertret, B., Towards non-blinking colloidal quantum dots. *Nat. Mater.,* **2008,** *7*, 659-664.

95. Kovalenko, M. V.; Scheele, M.; Talapin, D. V., Colloidal Nanocrystals with Molecular Metal Chalcogenide Surface Ligands. *Science,* **2009,** *324*, 1417-1420.

96. Zhu, H. M.; Song, N. H.; Lian, T. Q., Controlling Charge Separation and Recombination Rates in CdSe/ZnS Type I Core-Shell Quantum Dots by Shell Thicknesses. *J. Am. Chem. Soc.,* **2010,** *132*, 15038-15045.

97. Jiang, Z. J.; Kelley, D. F., Hot and Relaxed Electron Transfer from the CdSe Core and Core/Shell Nanorods. *J. Phys. Chem. C,* **2011,** *115*, 4594-4602.

98. Ding, T. X.; Olshansky, J. H.; Leone, S. R.; Alivisatos, A. P., Efficiency of Hole Transfer from Photoexcited Quantum Dots to Covalently Linked Molecular Species. *J. Am. Chem. Soc.,* **2015,** *137*, 2021-2029.

99. Greene, B. L.; Joseph, C. A.; Maroney, M. J.; Dyer, R. B., Direct Evidence of Active-Site Reduction and Photodriven Catalysis in Sensitized Hydrogenase Assemblies. *J. Am. Chem. Soc.,* **2012,** *134*, 11108-11111.

100. Hamon, C.; Ciaccafava, A.; Infossi, P.; Puppo, R.; Even-Hernandez, P.; Lojou, E.; Marchi, V., Synthesis and enzymatic photo-activity of an O-2 tolerant hydrogenase-CdSe@CdS quantum rod bioconjugate. *Chem. Commun.,* **2014,** *50*, 4989-4992.
101. Chaudhary, Y. S.; Woolerton, T. W.; Allen, C. S.; Warner, J. H.; Pierce, E.; Ragsdale, S. W.; Armstrong, F. A., Visible light-driven CO2 reduction by enzyme coupled CdS nanocrystals. *Chem. Commun.,* **2012,** *48*, 58-60.
102. Parkin, A.; Seravalli, J.; Vincent, K. A.; Ragsdale, S. W.; Armstrong, F. A., Rapid and efficient electrocatalytic CO2/CO interconversions by Carboxydothermus hydrogenoformans CO dehydrogenase I on an electrode. *J. Am. Chem. Soc.,* **2007,** *129*, 10328-10329.
103. Woolerton, T. W.; Sheard, S.; Chaudhary, Y. S.; Armstrong, F. A., Enzymes and bio-inspired electrocatalysts in solar fuel devices. *Energ. Environ. Sci.,* **2012,** *5*, 7470-7490.
104. Chen, X. B.; Shen, S. H.; Guo, L. J.; Mao, S. S., Semiconductor-based Photocatalytic Hydrogen Generation. *Chem. Rev.,* **2010,** *110*, 6503-6570.
105. Maeda, K.; Domen, K., Photocatalytic Water Splitting: Recent Progress and Future Challenges. *J. Phys. Chem. Lett.,* **2010,** *1*, 2655-2661.
106. Caputo, J. A.; Frenette, L. C.; Zhao, N.; Sowers, K. L.; Krauss, T. D.; Weix, D. J., General and Efficient C-C Bond Forming Photoredox Catalysis with Semiconductor Quantum Dots. *J. Am. Chem. Soc.,* **2017,** *139*, 4250-4253.
107. Amirav, L.; Alivisatos, A. P., Photocatalytic hydrogen production with tunable nanorod heterostructures. *J. Phys. Chem. Lett.,* **2010,** *1*, 1051-1054.
108. Amirav, L.; Alivisatos, A. P., Luminescence Studies of Individual Quantum Dot Photocatalysts. *J. Am. Chem. Soc.,* **2013,** *135*, 13049-13053.
109. Kalisman, P.; Nakibli, Y.; Amirav, L., Perfect Photon-to-Hydrogen Conversion Efficiency. *Nano Lett.,* **2016,** *16*, 1776-1781.
110. Nakibli, Y.; Kalisman, P.; Amirav, L., Less Is More: The Case of Metal Cocatalysts. *J. Phys. Chem. Lett.,* **2015,** *6*, 2265-2268.
111. Wu, K.; Chen, Z.; Lv, H.; Zhu, H.; Hill, C. L.; Lian, T., Hole removal rate limits photodriven H2 generation efficiency in CdS-Pt and CdSe/CdS-Pt semiconductor nanorod-metal tip heterostructures. *J. Am. Chem. Soc.,* **2014,** *136*, 7708-16.

112. Wu, K. F.; Lian, T. Q., Quantum confined colloidal nanorod heterostructures for solar-to-fuel conversion. *Chem. Soc. Rev.,* **2016,** *45*, 3781-3810.
113. Zhu, H. M.; Lian, T. Q., Wavefunction engineering in quantum confined semiconductor nanoheterostructures for efficient charge separation and solar energy conversion. *Energ. Environ. Sci.,* **2012,** *5*, 9406-9418.
114. Klimov, V. I., Spectral and dynamical properties of multilexcitons in semiconductor nanocrystals. *Annu. Rev. Phys. Chem.,* **2007,** *58*, 635-673.
115. Berera, R.; van Grondelle, R.; Kennis, J. T. M., Ultrafast transient absorption spectroscopy: principles and application to photosynthetic systems. *Photosynth. Res.,* **2009,** *101*, 105-118.
116. Tseng, H. W.; Wilker, M. B.; Damrauer, N. H.; Dukovic, G., Charge Transfer Dynamics between Photoexcited CdS Nanorods and Mononuclear Ru Water-Oxidation Catalysts. *J. Am. Chem. Soc.,* **2013,** *135*, 3383-3386.
117. Klimov, V. I., Optical nonlinearities and ultrafast carrier dynamics in semiconductor nanocrystals. *J. Phys. Chem. B,* **2000,** *104*, 6112-6123.
118. Wu, K.; Zhu, H.; Lian, T., Ultrafast exciton dynamics and light-driven H2 evolution in colloidal semiconductor nanorods and Pt-tipped nanorods. *Acc. Chem. Res.,* **2015,** *48*, 851-9.
119. Peng, P.; Sadtler, B.; Alivisatos, A. P.; Saykally, R. J., Exciton dynamics in CdS-Ag_2S nanorods with tunable composition probed by ultrafast transient absorption spectroscopy. *J. Phys. Chem. C,* **2010,** *114*, 5879-5885.
120. Robinson, R. D.; Sadtler, B.; Demchenko, D. O.; Erdonmez, C. K.; Wang, L. W.; Alivisatos, A. P., Spontaneous superlattice formation in nanorods through partial cation exchange. *Science,* **2007,** *317*, 355-358.
121. Carbone, L.; Nobile, C.; De Giorgi, M.; Sala, F. D.; Morello, G.; Pompa, P.; Hytch, M.; Snoeck, E.; Fiore, A.; Franchini, I. R.; Nadasan, M.; Silvestre, A. F.; Chiodo, L.; Kudera, S.; Cingolani, R.; Krahne, R.; Manna, L., Synthesis and Micrometer-Scale Assembly of Colloidal CdSe/CdS Nanorods prepared by a Seeded Growth Approach. *Nano Lett.,* **2007,** *7*, 2942-2950.
122. Peterson, M. D.; Jensen, S. C.; Weinberg, D. J.; Weiss, E. A., Mechanisms for adsorption of methyl viologen on CdS quantum dots. *ACS Nano,* **2014,** *8*, 2826-2837.

123. Hines, M. A.; Guyot-Sionnest, P., Bright UV-Blue Luminescent Colloidal ZnSe Nanocrystals. *J. Phys. Chem. B,* **1998,** *102*, 3655-3657.

124. Hewa-Kasakarage, N. N.; Kirsanova, M.; Nemchinov, A.; Schmall, N.; El-Khoury, P. Z.; Tarnovsky, A. N.; Zamkov, M., Radiative Recombination of Spatially Extended Excitons in (ZnSe/CdS)/CdS Heterostructured Nanorods. *J. Am. Chem. Soc.,* **2009,** *131*, 1328-1334.

125. Huang, J.; Kovalenko, M. V.; Talapin, D. V., Alkyl Chains of Surface Ligands Affect Polytypism of CdSe Nanocrystals and Play an Important Role in the Synthesis of Anisotropic Nanoheterostructures. *J. Am. Chem. Soc.,* **2010,** *132*, 15866-15868.

126. Lee, D.; Kim, W. D.; Lee, S.; Bae, W. K.; Lee, S.; Lee, D. C., Direct Cd-to-Pb Exchange of CdSe Nanorods into PbSe/CdSe Axial Heterojunction Nanorods. *Chem. Mater.,* **2015,** *27*, 5295-5304.

127. King, P. W.; Posewitz, M. C.; Ghirardi, M. L.; Seibert, M., Functional studies of [FeFe] hydrogenase maturation in an Escherichia coli biosynthetic system. *J. Bacteriol.,* **2006,** *188*, 2163-2172.

128. Bradford, M. M., Rapid and Sensitive Method for Quantitation of Microgram Quantities of Protein Utilizing Principle of Protein-Dye Binding. *Anal. Biochem.,* **1976,** *72*, 248-254.

129. Schneider, C. A.; Rasband, W. S.; Eliceiri, K. W., NIH Image to ImageJ: 25 years of image analysis. *Nat. Methods,* **2012,** *9*, 671-675.

130. Wu, K.; Rodriguez-Cordoba, W.; Lian, T., Exciton localization and dissociation dynamics in CdS and CdS-Pt quantum confined nanorods: effect of nonuniform rod diameters. *J. Phys. Chem. B,* **2014,** *118*, 14062-9.

131. Press, W. H.; Teukolsky, S. A.; Vetterling, W. T.; Flannery, B. P., *Numerical Recipes: The Art of Scientific Computing*. 3rd ed.; Cambridge University Press: Cambridge, **2007**.

132. Madelung, O., *Semiconductors—Basic Data*. 2nd ed.; Springer: Berlin, 1996.

133. Wu, K. F.; Rodriguez-Cordoba, W. E.; Liu, Z.; Zhu, H. M.; Lian, T. Q., Beyond Band Alignment: Hole Localization Driven Formation of Three Spatially Separated Long-Lived Exciton States in CdSe/CdS Nanorods. *ACS Nano,* **2013,** *7*, 7173-7185.

134. Sacra, A.; Norris, D. J.; Murray, C. B.; Bawendi, M. G., Stark spectroscopy of CdSe nanocrystallites - the significance of transition linewidths. *J. Chem. Phys.,* **1995,** *103*, 5236-5245.

135. Infelta, P. P.; Gratzel, M.; Thomas, J. K., Luminescence decay of hydrophobic molecules solubilized in aqueous micellar systems. A kinetic model. *J. Phys. Chem.,* **1974,** *78*, 190-195.

136. Tachiya, M., Application of a generating function to reaction knetics in micelles. Kinetics of quenching of luminescent probes in micelles. *Chem. Phys. Lett.,* **1975,** *33*, 289-292.

137. Redner, S., *A guide to first-passage processes*. Cambridge University Press: Cambridge, **2001**.

138. Kuno, M.; Fromm, D. P.; Hamann, H. F.; Gallagher, A.; Nesbitt, D. J., Nonexponential "blinking" kinetics of single CdSe quantum dots: A universal power law behavior. *J. Chem. Phys.,* **2000,** *112*, 3117-3120.

139. Tang, J.; Marcus, R. A., Mechanisms of fluorescence blinking in semiconductor nanocrystal quantum dots. *J. Chem. Phys.,* **2005,** *123*, 054704.

140. Frantsuzov, P.; Kuno, M.; Janko, B.; Marcus, R. A., Universal emission intermittency in quantum dots, nanorods and nanowires. *Nature Phys.,* **2008,** *4*, 519-522.

141. Einstein, A., The motion of elements suspended in static liquids as claimed in the molecular kinetic theory of heat. *Ann. Phys.,* **1905,** *17*, 549-560.

142. Nakade, S.; Kambe, S.; Kitamura, T.; Wada, Y.; Yanagida, S., Effects of lithium ion density on electron transport in nanoporous TiO_2 electrodes. *J. Phys. Chem. B,* **2001,** *105*, 9150-9152.

143. Nelson, J.; Chandler, R. E., Random walk models of charge transfer and transport in dye sensitized systems. *Coordin. Chem. Rev.,* **2004,** *248*, 1181-1194.

144. Acharya, K. P.; Khnayzer, R. S.; O'Connor, T.; Diederich, G.; Kirsanova, M.; Klinkova, A.; Roth, D.; Kinder, E.; Imboden, M.; Zamkov, M., The Role of Hole Localization in Sacrificial Hydrogen Production by Semiconductor-Metal Heterostructured Nanocrystals. *Nano Lett.,* **2011,** *11*, 2919-2926.

145. Berr, M. J.; Wagner, P.; Fischbach, S.; Vaneski, A.; Schneider, J.; Susha, A. S.; Rogach, A. L.; Jackel, F.; Feldmann, J., Hole scavenger redox potentials determine quantum efficiency and stability of Pt-decorated CdS nanorods for photocatalytic hydrogen generation. *Appl. Phys. Lett.,* **2012,** *100*, 223903.

146. Simon, T.; Bouchonville, N.; Berr, M. J.; Vaneski, A.; Adrovic, A.; Volbers, D.; Wyrwich, R.; Doblinger, M.; Susha, A. S.; Rogach, A. L.; Jackel, F.; Stolarczyk, J. K.; Feldmann, J.,

Redox shuttle mechanism enhances photocatalytic H_2 generation on Ni-decorated CdS nanorods. *Nat. Mater.,* **2014,** *13*, 1013-1018.

147. Berr, M. J.; Vaneski, A.; Mauser, C.; Fischbach, S.; Susha, A. S.; Rogach, A. L.; Jackel, F.; Feldmann, J., Delayed Photoelectron Transfer in Pt-Decorated CdS Nanorods under Hydrogen Generation Conditions. *Small,* **2012,** *8*, 291-297.
148. Yehezkeli, O.; de Oliveira, D. R. B.; Cha, J. N., Electrostatically assembled CdS-Co_3O_4 nanostructures for photo-assisted water oxidation and photocatalytic reduction of dye molecules. *Small,* **2015,** *11*, 668-674.
149. Duan, L. L.; Bozoglian, F.; Mandal, S.; Stewart, B.; Privalov, T.; Llobet, A.; Sun, L. C., A molecular ruthenium catalyst with water-oxidation activity comparable to that of photosystem II. *Nat. Chem.,* **2012,** *4*, 418-423.
150. Hines, M. A.; Guyot-Sionnest, P., Synthesis and characterization of strongly luminescing ZnS-Capped CdSe nanocrystals. *J. Phys. Chem.,* **1996,** *100*, 468-471.
151. Peng, X. G.; Schlamp, M. C.; Kadavanich, A. V.; Alivisatos, A. P., Epitaxial growth of highly luminescent CdSe/CdS core/shell nanocrystals with photostability and electronic accessibility. *J. Am. Chem. Soc.,* **1997,** *119*, 7019-7029.
152. Kim, S.; Fisher, B.; Eisler, H. J.; Bawendi, M., Type-II quantum dots: CdTe/CdSe(core/shell) and CdSe/ZinTe(core/shell) heterostructures. *J. Am. Chem. Soc.,* **2003,** *125*, 11466-11467.
153. Lo, S. S.; Mirkovic, T.; Chuang, C. H.; Burda, C.; Scholes, G. D., Emergent properties resulting from type-II band alignment in semiconductor nanoheterostructures. *Advanced Materials,* **2011,** *23*, 180-97.
154. Li, J. J.; Wang, Y. A.; Guo, W. Z.; Keay, J. C.; Mishima, T. D.; Johnson, M. B.; Peng, X. G., Large-scale synthesis of nearly monodisperse CdSe/CdS core/shell nanocrystals using air-stable reagents via successive ion layer adsorption and reaction. *J. Am. Chem. Soc.,* **2003,** *125*, 12567-12575.
155. Steckel, J. S.; Zimmer, J. P.; Coe-Sullivan, S.; Stott, N. E.; Bulovic, V.; Bawendi, M. G., Blue luminescence from (CdS)ZnS core-shell nanocrystals. *Angew. Chem. Int. Edit.,* **2004,** *43*, 2154-2158.

156. Dorfs, D.; Franzl, T.; Osovsky, R.; Brumer, M.; Lifshitz, E.; Klar, T. A.; Eychmueller, A., Type-I and type-II nanoscale heterostructures based on CdTe nanocrystals: A comparative study. *Small,* **2008,** *4*, 1148-1152.

157. Kumar, S.; Jones, M.; Lo, S. S.; Scholes, G. D., Nanorod heterostructures showing photoinduced charge separation. *Small,* **2007,** *3*, 1633-1639.

158. He, J.; Zhong, H. Z.; Scholes, G. D., Electron-Hole Overlap Dictates the Hole Spin Relaxation Rate in Nanocrystal Heterostructures. *Phys. Rev. Lett.,* **2010,** *105*.

159. Zhu, H.; Song, N.; Rodriguez-Cordoba, W.; Lian, T., Wave function engineering for efficient extraction of up to nineteen electrons from one CdSe/CdS quasi-type II quantum dot. *J. Am. Chem. Soc.,* **2012,** *134*, 4250-7.

160. Zhu, H. M.; Chen, Z. Y.; Wu, K. F.; Lian, T. Q., Wavelength dependent efficient photoreduction of redox mediators using type II ZnSe/CdS nanorod heterostructures. *Chem. Sci.,* **2014,** *5*, 3905-3914.

161. Zhu, H. M.; Song, N. H.; Lian, T. Q., Wave Function Engineering for Ultrafast Charge Separation and Slow Charge Recombination in Type II Core/Shell Quantum Dots. *J. Am. Chem. Soc.,* **2011,** *133*, 8762-8771.

162. Chuang, C. H.; Doane, T. L.; Lo, S. S.; Scholes, G. D.; Burda, C., Measuring Electron and Hole Transfer in Core/Shell Nanoheterostructures. *ACS Nano,* **2011,** *5*, 6016-6024.

163. Chen, C. Y.; Cheng, C. T.; Yu, J. K.; Pu, S. C.; Cheng, Y. M.; Chou, P. T.; Chou, Y. H.; Chiu, H. T., Spectroscopy and femtosecond dynamics of type-II CdSe/ZnTe core-shell semiconductor synthesized via the CdO precursor. *J. Phys. Chem. B,* **2004,** *108*, 10687-10691.

164. Ning, Z. J.; Tian, H. N.; Yuan, C. Z.; Fu, Y.; Qin, H. Y.; Sun, L. C.; Agren, H., Solar cells sensitized with type-II ZnSe-CdS core/shell colloidal quantum dots. *Chem. Commun.,* **2011,** *47*, 1536-1538.

165. Lupo, M. G.; Della Sala, F.; Carbone, L.; Zavelani-Rossi, M.; Fiore, A.; Luer, L.; Polli, D.; Cingolani, R.; Manna, L.; Lanzani, G., Ultrafast Electron-Hole Dynamics in Core/Shell CdSe/CdS Dot/Rod Nanocrystals. *Nano Lett.,* **2008,** *8*, 4582-4587.

166. Steiner, D.; Dorfs, D.; Banin, U.; Della Sala, F.; Manna, L.; Millo, O., Determination of Band Offsets in Heterostructured Colloidal Nanorods Using Scanning Tunneling Spectroscopy. *Nano Lett.,* **2008,** *8*, 2954-2958.

167. Sitt, A.; Sala, F. D.; Menagen, G.; Banin, U., Multiexciton Engineering in Seeded Core/Shell Nanorods: Transfer from Type-I to Quasi-type-II Regimes. *Nano Lett.,* **2009,** *9*, 3470-3476.

168. Luo, Y.; Wang, L. W., Electronic Structures of the CdSe/CdS Core-Shell Nanorods. *ACS Nano,* **2010,** *4*, 91-98.

169. Raino, G.; Stoferle, T.; Moreels, I.; Gomes, R.; Kamal, J. S.; Hens, Z.; Mahrt, R. F., Probing the Wave Function Delocalization in CdSe/CdS Dot-in-Rod Nanocrystals by Time- and Temperature-Resolved Spectroscopy. *ACS Nano,* **2011,** *5*, 4031-4036.

170. She, C. X.; Demortiere, A.; Shevchenko, E. V.; Pelton, M., Using Shape to Control Photoluminescence from CdSe/CdS Core/Shell Nanorods. *J. Phys. Chem. Lett.,* **2011,** *2*, 1469-1475.

171. Smith, E. R.; Luther, J. M.; Johnson, J. C., Ultrafast Electronic Delocalization in CdSe/CdS Quantum Rod Heterostructures. *Nano Lett.,* **2011,** *11*, 4923-4931.

172. Sitt, A.; Hadar, I.; Banin, U., Band-gap engineering, optoelectronic properties and applications of colloidal heterostructured semiconductor nanorods. *Nano Today,* **2013,** *8*, 494-513.

173. Borys, N. J.; Walter, M. J.; Huang, J.; Talapin, D. V.; Lupton, J. M., The role of particle morphology in interfacial energy transfer in CdSe/CdS heterostructure nanocrystals. *Science,* **2010,** *330*, 1371-1374.

174. Müller, J.; Lupton, J. M.; Lagoudakis, P. G.; Schindler, F.; Koeppe, R.; Rogach, A. L.; Feldmann, J.; Talapin, D. V.; Weller, H., Wave function engineering in elongated semiconductor nanocrystals with heterogeneous carrier confinement. *Nano Lett.,* **2005,** *5*, 2044-2049.

175. Park, Y. S.; Bae, W. K.; Baker, T.; Lim, J.; Klimov, V. I., Effect of Auger Recombination on Lasing in Heterostructured Quantum Dots with Engineered Core/Shell Interfaces. *Nano Lett.,* **2015,** *15*, 7319-7328.

176. Mauser, C.; Da Como, E.; Baldauf, J.; Rogach, A. L.; Huang, J.; Talapin, D. V.; Feldmann, J., Spatio-temporal dynamics of coupled electrons and holes in nanosize CdSe-CdS semiconductor tetrapods. *Phys. Rev. B,* **2010,** *82*.

177. Grennell, A. N.; Utterback, J. K.; Pearce, O. M.; Wilker, M. B.; Dukovic, G., Relationships between Exciton Dissociation and Slow Recombination within ZnSe/CdS and CdSe/CdS Dot-in-Rod Heterostructures. *Nano Lett.,* **2017,** *17*, 3764-3774.

178. Grennell, A. N. Photophysics and Electron Transfer Dynamics of Type-II and Quasi Type-II Heterostructure Nanocrystals. University of Colorado Boulder, Chemistry & Biochemistry Graduate Theses & Dissertations, 2017.

179. Talapin, D. V.; Nelson, J. H.; Shevchenko, E. V.; Aloni, S.; Sadtler, B.; Alivisatos, A. P., Seeded growth of highly luminescent CdSe/CdS nanoheterostructures with rod and tetrapod morphologies. *Nano Lett.,* **2007,** *7*, 2951-2959.

180. O'connor, T.; Panov, M. S.; Mereshchenko, A.; Tarnovsky, A. N.; Lorek, R.; Perera, D.; Diederich, G.; Lambright, S.; Moroz, P.; Zamkov, M., The Effect of the Charge-Separating Interface on Exciton Dynamics in Photocatalytic Colloidal Heteronanocrystals. *ACS Nano,* **2012,** *6*, 8156-8165.

181. Ivanov, S. A.; Piryatinski, A.; Nanda, J.; Tretiak, S.; Zavadil, K. R.; Wallace, W. O.; Werder, D.; Klimov, V. I., Type-II core/shell CdS/ZnSe nanocrystals: Synthesis, electronic structures, and spectroscopic properties. *J. Am. Chem. Soc.,* **2007,** *129*, 11708-11719.

182. Nemchinov, A.; Kirsanova, M.; Hewa-Kasakarage, N. N.; Zamkov, M., Synthesis and characterization of type IIZnSe/CdS core/shell nanocrystals. *J. Phys. Chem. C,* **2008,** *112*, 9301-9307.

183. Ben-Shahar, Y.; Scotognella, F.; Waiskopf, N.; Kriegel, I.; Dal Conte, S.; Cerullo, G.; Banin, U., Effect of Surface Coating on the Photocatalytic Function of Hybrid CdS-Au Nanorods. *Small,* **2015,** *11*, 462-471.

184. Crooker, S. A.; Barrick, T.; Hollingsworth, J. A.; Klimov, V. I., Multiple temperature regimes of radiative decay in CdSe nanocrystal quantum dots: Intrinsic limits to the dark-exciton lifetime. *Appl. Phys. Lett.,* **2003,** *82*, 2793-2795.

185. Khon, E.; Lambright, K.; Khnayzer, R. S.; Moroz, P.; Perera, D.; Butaeva, E.; Lambright, S.; Castellano, F. N.; Zamkov, M., Improving the Catalytic Activity of Semiconductor Nanocrystals through Selective Domain Etching. *Nano Lett.,* **2013,** *13*, 2016-2023.

186. Cline, R. P.; Utterback, J. K.; Strong, S. E.; Dukovic, G.; Eaves, J. D., On the Nature of Trapped-Hole States in CdS Nanocrystals and the Mechanism of their Diffusion. *J. Phys. Chem. Lett.,* **2018,** *9*, 3532-3537.

187. Creti, A.; Anni, M.; Zavelani-Rossi, M.; Lanzani, G.; Leo, G.; Della Sala, F.; Manna, L.; Lomascolo, M., Ultrafast carrier dynamics in core and core/shell CdSe quantum rods: Role of the surface and interface defects. *Phys. Rev. B,* **2005,** *72*.

188. Jiang, Z. J.; Kelley, D. F., Role of Surface States in the Exciton Dynamics in CdSe Core and Core/Shell Nanorods. *J. Phys. Chem. C,* **2010,** *114*, 17519-17528.

189. Sagarzazu, G.; Inoue, K.; Saruyama, M.; Sakamoto, M.; Teranishi, T.; Masuo, S.; Tamai, N., Ultrafast dynamics and single particle spectroscopy of Au-CdSe nanorods. *Phys. Chem. Chem. Phys.,* **2013,** *15*, 2141-2152.

190. Zhu, H. M.; Lian, T. Q., Enhanced Multiple Exciton Dissociation from CdSe Quantum Rods: The Effect of Nanocrystal Shape. *J. Am. Chem. Soc.,* **2012,** *134*, 11289-11297.

191. Yang, Y.; Wu, K. F.; Chen, Z. Y.; Jeong, B. S.; Lian, T. Q., Competition of branch-to-core exciton localization and interfacial electron transfer in CdSe tetrapods. *Chem. Phys.,* **2016,** *471*, 32-38.

192. Yu, P.; Wen, X. M.; Lee, Y. C.; Lee, W. C.; Kang, C. C.; Tang, J., Photoinduced Ultrafast Charge Separation in Plexcitonic CdSe/Au and CdSe/Pt Nanorods. *J. Phys. Chem. Lett.,* **2013,** *4*, 3596-3601.

193. Le Thomas, N.; Herz, E.; Schops, O.; Woggon, U.; Artemyev, M. V., Exciton fine structure in single CdSe nanorods. *Phys. Rev. Lett.,* **2005,** *94*.

194. Carslaw, H. S.; Jaeger, J. C., *Conduction of Heat in Solids*. 2nd ed.; Oxford University Press: Amen House, London, E.C.4, **1959**.

195. Kern, S. J.; Sahu, K.; Berg, M. A., Heterogeneity of the Electron-Trapping Kinetics in CdSe Nanoparticles. *Nano Lett.,* **2011,** *11*, 3493-3498.

196. Rabouw, F. T.; Kamp, M.; van Dijk-Moes, R. J. A.; Gamelin, D. R.; Koenderink, A. F.; Meijerink, A.; Vanmaekelbergh, D., Delayed Exciton Emission and Its Relation to Blinking in CdSe Quantum Dots. *Nano Lett.,* **2015,** *15*, 7718-7725.

197. Christians, J. A.; Leighton, D. T.; Kamat, P. V., Rate limiting interfacial hole transfer in Sb2S3 solid-state solar cells. *Energ. Environ. Sci.,* **2014,** *7*, 1148-1158.

198. Rabouw, F. T.; van der Bok, J. C.; Spinicelli, P.; Mahler, B.; Nasilowski, M.; Pedetti, S.; Dubertret, B.; Vanmaekelbergh, D., Temporary Charge Carrier Separation Dominates the Photoluminescence Decay Dynamics of Colloidal CdSe Nanoplatelets. *Nano Lett.,* **2016,** *16*, 2047-2053.

199. Kuno, M.; Fromm, D. P.; Hamann, H. F.; Gallagher, A.; Nesbitt, D. J., "On"/"off" fluorescence intermittency of single semiconductor quantum dots. *J. Chem. Phys.,* **2001,** *115*, 1028-1040.

200. Stefani, F. D.; Hoogenboom, J. P.; Barkai, E., Beyond quantum jumps: Blinking nanoscale light emitters. *Physics Today,* **2009,** *62*, 34-39.

201. Rudin, S.; Reinecke, T. L.; Segall, B., Temperature-Dependent Exciton Linewidths in Semiconductors. *Phys. Rev. B,* **1990,** *42*, 11218-11231.

202. Mack, T. G.; Jethi, L.; Kambhampati, P., Temperature Dependence of Emission Line Widths from Semiconductor Nanocrystals Reveals Vibronic Contributions to Line Broadening Processes. *J. Phys. Chem. C,* **2017,** *121*, 28537-28545.

203. Utterback, J. K.; Hamby, H.; Pearce, O.; Eaves, J. D.; Dukovic, G., Trapped-hole diffusion in photoexcited CdSe nanorods. *J. Phys. Chem. C,* **2018**, *122*, 16974-16982.

204. Chestnoy, N.; Harris, T. D.; Hull, R.; Brus, L. E., Luminescence and photophysics of CdS semiconductor clusters - the nature of the emitting electronic state. *J. Phys. Chem.,* **1986,** *90*, 3393-3399.

205. Baker, D. R.; Kamat, P. V., Tuning the emission of CdSe quantum dots by controlled trap enhancement. *Langmuir,* **2010,** *26*, 11272-11276.

206. van Driel, A. F.; Nikolaev, I. S.; Vergeer, P.; Lodahl, P.; Vanmaekelbergh, D.; Vos, W. L., Statistical analysis of time-resolved emission from ensembles of semiconductor quantum dots: Interpretation of exponential decay models. *Phys. Rev. B,* **2007,** *75*, 035329.

207. Huang, J. E.; Huang, Z. Q.; Jin, S. Y.; Lian, T. Q., Exciton Dissociation in CdSe Quantum Dots by Hole Transfer to Phenothiazine. *J. Phys. Chem. C,* **2008,** *112*, 19734-19738.

208. Infelta, P. P.; Gratzel, M.; Thomas, J. K., Luminescence Decay of Hydrophobic Molecules Solubilized in Aqueous Micellar Systems - Kinetic-Model. *J. Phys. Chem.,* **1974,** *78*, 190-195.

209. Tachiya, M., Application of a Generating Function to Reaction-Kinetics in Micelles - Kinetics of Quenching of Luminescent Probes in Micelles. *Chem. Phys. Lett.,* **1975,** *33*, 289-292.

210. Beane, G. A.; Morfa, A. J.; Funston, A. M.; Mulvaney, P., Defect-Mediated Energy Transfer between ZnO Nanocrystals and a Conjugated Dye. *J. Phys. Chem. C,* **2012,** *116*, 3305-3310.

211. Sadhu, S.; Patra, A., A Brief Overview of Some Physical Studies on the Relaxation Dynamics and Forster Resonance Energy Transfer of Semiconductor Quantum Dots. *Chemphyschem,* **2013,** *14*, 2641-2653.

212. Morris-Cohen, A. J.; Frederick, M. T.; Cass, L. C.; Weiss, E. A., Simultaneous Determination of the Adsorption Constant and the Photoinduced Electron Transfer Rate for a Cds Quantum Dot-Viologen Complex. *J. Am. Chem. Soc.,* **2011,** *133*, 10146-10154.

213. VanKampen, N. G., Stochastic Processes in Physics and Chemistry, 3rd Edition. *Stochastic Processes in Physics and Chemistry, 3rd Edition,* **2007**, 1-463.

214. Vincent, K. A.; Parkin, A.; Armstrong, F. A., Investigating and exploiting the electrocatalytic properties of hydrogenases. *Chem. Rev.,* **2007,** *107*, 4366-4413.

215. Burai, T. N.; Panay, A. J.; Zhu, H. M.; Lian, T. Q.; Lutz, S., Light-Driven, Quantum Dot-Mediated Regeneration of FMN To Drive Reduction of Ketoisophorone by Old Yellow Enzyme. *ACS Catal.,* **2012,** *2*, 667-670.

216. Sakimoto, K. K.; Wong, A. B.; Yang, P., Self-Photosensitization of Nonphotosynthetic bacteria for Solar-to-Chemical Production. *Science,* **2016,** *351*, 74-77.

217. Simon, T.; Carlson, M. T.; Stolarczyk, J. K.; Feldmann, J., Electron Transfer Rate vs Recombination Losses in Photocatalytic H2 Generation on Pt-Decorated CdS Nanorods. *ACS Energy Lett.,* **2016,** *1*, 1137-1142.

218. Ratzloff, M. W.; Wilker, M. B.; Mulder, D. W.; Lubner, C. E.; Hamby, H.; Brown, K. A.; Dukovic, G.; King, P. W., Activation Thermodynamics and H/D Kinetic Isotope Effect of the Hox to HredH+ Transition in [FeFe] Hydrogenase. *J. Am. Chem. Soc.,* **2017,** *139*, 12879-12882.

219. Lawless, D.; Kapoor, S.; Meisel, D., Bifunctional Capping of CdS Nanoparticles and Bridging to TiO2. *J. Phys. Chem.,* **1995,** *99*, 10329-10335.

220. Bakkers, E. P. A. M.; Roest, A. L.; Marsman, A. W.; Jenneskens, L. W.; de Jong-van Steensel, L. I.; Kelly, J. J.; Vanmaekelbergh, D., Characterization of Photoinduced Electron Tunneling in Gold/SAM/Q-CdSe Systems by Time-Resolved Photoelectrochemistry. *J. Phys. Chem. B,* **2000,** *104*, 7266-7272.

221. Adams, D. M.; Brus, L.; Chidsey, C. E. D.; Creager, S.; Creutz, C.; Kagan, C. R.; Kamat, P. V.; Lieberman, M.; Lindsay, S.; Marcus, R. A.; Metzger, R. M.; Michel-Beyerle, M. E.; Miller, J. R.; Newton, M. D.; Rolison, D. R.; Sankey, O.; Schanze, K. S.; Yardley, J.; Zhu,

X. Y., Charge Transfer on the Nanoscale: Current Status. *J. Phys. Chem. B,* **2003,** *107*, 6668-6697.

222. Dibbell, R. S.; Youker, D. G.; Watson, D. F., Excited-State Electron Transfer from CdS Quantum Dots to TiO2 Nanoparticles via Molecular Linkers with Phenylene Bridges. *J. Phys. Chem. C,* **2009,** *113*, 18643-18651.
223. Dibbell, R. S.; Watson, D. F., Distance-Dependent Electron Transfer in Tethered Assemblies of CdS Quantum Dots and TiO2 Nanoparticles. *J. Phys. Chem. C,* **2009,** *113*, 3139-3149.
224. Tagliazucchi, M.; Tice, D. B.; Sweeney, C. M.; Morris-Cohen, A. J.; Weiss, E. A., Ligand-Controlled Rates of Photoinduced Electron Transfer in Hybrid CdSe Nanocrystal/Poly(viologen) Films. *ACS Nano,* **2011,** *5*, 9907-9917.
225. Hyun, B. R.; Bartnik, A. C.; Sun, L. F.; Hanrath, T.; Wise, F. W., Control of Electron Transfer from Lead-Salt Nanocrystals to TiO2. *Nano Lett.,* **2011,** *11*, 2126-2132.
226. Wang, H.; McNellis, E. R.; Kinge, S.; Bonn, M.; Canovas, E., Tuning Electron Transfer Rates through Molecular Bridges in Quantum Dot Sensitized Oxides. *Nano Lett.,* **2013,** *13*, 5311-5315.
227. Hines, D. A.; Forrest, R. P.; Corcelli, S. A.; Kamat, P. V., Predicting the Rate Constant of Electron Tunneling Reactions at the CdSe–TiO2 Interface. *J. Phys. Chem. B,* **2015,** *119*, 7439-7446.
228. Wilker, M. B. Charge Transfer Dynamics in Complexes of Light-Absorbing CdS Nanorods and Redox Catalysts. University of Colorado Boulder, Chemistry & Biochemistry Graduate Theses & Dissertations, 2015.
229. Goodwin, E. D.; Diroll, B. T.; Oh, S. J.; Paik, T.; Murray, C. B.; Kagan, C. R., Effects of Post-Synthesis Processing on CdSe Nanocrystals and Their Solids: Correlation between Surface Chemistry and Optoelectronic Properties. *J. Phys. Chem. C,* **2014,** *118*, 27097-27105.
230. Shakeri, B.; Meulenberg, R. W., A Closer Look into the Traditional Purification Process of CdSe Semiconductor Quantum Dots. *Langmuir,* **2015,** *31*, 13433-13440.
231. Knauf, R. R.; Lennox, J. C.; Dempsey, J. L., Quantifying Ligand Exchange Reactions at CdSe Nanocrystal Surfaces. *Chem. Mater.,* **2016,** *28*, 4762-4770.

232. Dai, Z.; Ju, H., Effect of Chain Length on the Surface Properties of [omega]-Carboxy Alkanethiol Self-Assembled Monolayers. *Phys. Chem. Chem. Phys.,* **2001,** *3*, 3769-3773.
233. Saunders, A. E.; Ghezelbash, A.; Sood, P.; Korgel, B. A., Synthesis of high aspect ratio quantum-size CdS nanorods and their surface-dependent photoluminescence. *Langmuir,* **2008,** *24*, 9043-9049.
234. Kambhampati, P., On the kinetics and thermodynamics of excitons at the surface of semiconductor nanocrystals: Are there surface excitons? *Chem. Phys.,* **2015,** *446*, 92-107.
235. Leng, H. X.; Loy, J.; Amin, V.; Weiss, E. A.; Pelton, M., Electron Transfer from Single Semiconductor Nanocrystals to Individual Acceptor Molecules. *ACS Energy Lett.,* **2016,** *1*, 9-15.
236. Anderson, N. A.; Lian, T. Q., Ultrafast Electron Transfer at the Molecule-Semiconductor Nanoparticle Interface. *Annu. Rev. Phys. Chem.,* **2005,** *56*, 491-519.
237. Taylor, J., *Introduction to error analysis: The study of uncertainties in physical measurements*. 2nd ed.; University Science Books: Sausalito, CA, **1997**.
238. Warren, J. J.; Mayer, J. M., Tuning of the Thermochemical and Kinetic Properties of Ascorbate by Its Local Environment: Solution Chemistry and Biochemical Implications. *J. Am. Chem. Soc.,* **2010,** *132*, 7784-7793.
239. Pernik, D. R.; Tvrdy, K.; Radich, J. G.; Kamat, P. V., Tracking the Adsorption and Electron Injection Rates of CdSe Quantum Dots on TiO2: Linked versus Direct Attachment. *J. Phys. Chem. C,* **2011,** *115*, 13511-13519.
240. Knowles, K. E.; Peterson, M. D.; McPhail, M. R.; Weiss, E. A., Exciton Dissociation within Quantum Dot-Organic Complexes: Mechanisms, Use as a Probe of Interfacial Structure, and Applications. *J. Phys. Chem. C,* **2013,** *117*, 10229-10243.
241. Bakkers, E. P. A. M.; Marsman, A. W.; Jenneskens, L. W.; Vanmaekelbergh, D., Distance-Dependent Electron Transfer in Au/Spacer/Q-CdSe Assemblies. *Angew. Chem. Int. Edit.,* **2000,** *39*, 2297-2299.
242. Madden, C.; Vaughn, M. D.; Díez-Pérez, I.; Brown, K. A.; King, P. W.; Gust, D.; Moore, A. L.; Moore, T. A., Catalytic Turnover of [FeFe]-Hydrogenase Based on Single-Molecule Imaging. *J. Am. Chem. Soc.,* **2012,** *134*, 1577-1582.
243. Wold, D. J.; Haag, R.; Rampi, M. A.; Frisbie, C. D., Distance Dependence of Electron Tunneling through Self-Assembled Monolayers measured by Conducting Probe Atomic

Force Microscopy: Unsaturated versus Saturated Molecular Junctions. *J. Phys. Chem. B,* **2002,** *106*, 2813-2816.

244. Smalley, J. F.; Finklea, H. O.; Chidsey, C. E. D.; Linford, M. R.; Creager, S. E.; Ferraris, J. P.; Chalfant, K.; Zawodzinsk, T.; Feldberg, S. W.; Newton, M. D., Heterogeneous Electron-Transfer Kinetics for Ruthenium and Ferrocene Redox Moieties through Alkanethiol Monolayers on Gold. *J. Am. Chem. Soc.,* **2003,** *125*, 2004-2013.
245. Holmlin, R. E.; Haag, R.; Chabinyc, M. L.; Ismagilov, R. F.; Cohen, A. E.; Terfort, A.; Rampi, M. A.; Whitesides, G. M., Electron Transport through Thin Organic Films in Metal-Insulator-Metal Junctions based on Self-Assembled Monolayers. *J. Am. Chem. Soc.,* **2001,** *123*, 5075-5085.
246. Bumm, L. A.; Arnold, J. J.; Dunbar, T. D.; Allara, D. L.; Weiss, P. S., Electron Transfer through Organic Molecules. *J. Phys. Chem. B,* **1999,** *103*, 8122-8127.
247. Weber, K.; Hockett, L.; Creager, S., Long-range Electronic Coupling between Ferrocene and Gold in Alkanethiolate-Based Monolayers on Electrodes. *J. Phys. Chem. B,* **1997,** *101*, 8286-8291.
248. Wang, W.; Lee, T.; Reed, M. A., Elastic and Inelastic Electron Tunneling in Alkane Self-Assembled Monolayers. *J. Phys. Chem. B,* **2004,** *108*, 18398-18407.
249. Hostetler, M. J.; Stokes, J. J.; Murray, R. W., Infrared Spectroscopy of Three-Dimensional Self-Assembled Monolayers: N-alkanethiolate Monolayers on Gold Cluster Compounds. *Langmuir,* **1996,** *12*, 3604-3612.
250. Ghorai, P. K.; Glotzer, S. C., Molecular Dynamics Simulation Study of Self-Assembled Monolayers of Alkanethiol Surfactants on Spherical Gold Nanoparticles. *J. Phys. Chem. C,* **2007,** *111*, 15857-15862.
251. Love, C. J.; Estroff, L. A.; Kriebel, J. K.; Nuzzo, R. G.; Whitesides, G. M., Self-Assembled Monolayers of Thiolates on Metals as a Form of Nanotechnology. *Chem. Rev.,* **2005,** *105*, 1103-1169.
252. Brutchey, R. L.; Hens, Z.; Kovalenko, M. V., Surface Chemistry of Colloidal Semiconductor Nanocrystals: Organic, Inorganic and Hybrid. In *Chemistry of Organo-Hybrids: Synthesis and Characterization of Functional Nano-Objects*, Charleux, B.; Coperet, C.; Lacote, E., Eds. John Wiley & Sons: New York, 2015.

253. Harris, R. D.; Homan, S. B.; Kodaimati, M.; He, C.; Nepomnyashchii, A. B.; Swenson, N. K.; Lian, S. C.; Calzada, R.; Weiss, E. A., Electronic Processes within Quantum Dot-Molecule Complexes. *Chem. Rev.,* **2016,** *116*, 12865-12919.

254. Tisdale, W. A.; Zhu, X. Y., Artificial atoms on semiconductor surfaces. *Proc. Natl. Acad. Sci. U.S.A.,* **2011,** *108*, 965-970.

255. Schnitzenbaumer, K. J.; Dukovic, G., Chalcogenide-Ligand Passivated CdTe Quantum Dots Can Be Treated as Core/Shell Semiconductor Nanostructures. *J. Phys. Chem. C,* **2014,** *118*, 28170-28178.

256. Xiong, W.; Hickstein, D. D.; Schnitzenbaumer, K. J.; Ellis, J. L.; Palm, B. B.; Keister, K. E.; Ding, C. Y.; Miaja-Avila, L.; Dukovic, G.; Jimenez, J. L.; Murnane, M. M.; Kapteyn, H. C., Photoelectron Spectroscopy of CdSe Nanocrystals in the Gas Phase: A Direct Measure of the Evanescent Electron Wave Function of Quantum Dots. *Nano Lett.,* **2013,** *13*, 2924-2930.

257. Tachiya, M., Kinetics of Quenching of Luminescent Probes in Micellar Systems. II. *J. Phys. Chem.,* **1982,** *76*, 340-348.

258. Song, N. H.; Zhu, H. M.; Jin, S. Y.; Zhan, W.; Lian, T. Q., Poisson-Distributed Electron-Transfer Dynamics from Single Quantum Dots to C60 Molecules. *ACS Nano,* **2011,** *5*, 613-621.

259. Lakowicz, J. R., *Principles of Fluorescence Spectroscopy*. Springer: New York, **2006**.

260. Sillen, A.; Engelborghs, Y., The correct use of "average" fluorescence parameters. *Photochem. Photobiol.,* **1998,** *67*, 475-486.

261. Ravensbergen, J.; Abdi, F. F.; van Santen, J. H.; Frese, R. N.; Dam, B.; van de Krol, R.; Kennis, J. T. M., Unraveling the Carrier Dynamics of BiVO4: A Femtosecond to Microsecond Transient Absorption Study. *J. Phys. Chem. C,* **2014,** *118*, 27793-27800.

262. Medintz, I. L.; Mattoussi, H., Quantum dot-based resonance energy transfer and its growing application in biology. *Phys. Chem. Chem. Phys.,* **2009,** *11*, 17-45.

263. Beane, G.; Boldt, K.; Kirkwood, N.; Mulvaney, P., Energy Transfer between Quantum Dots and Conjugated Dye Molecules. *J. Phys. Chem. C,* **2014,** *118*, 18079-18086.

264. Pons, T.; Medintz, I. L.; Wang, X.; English, D. S.; Mattoussi, H., Solution-phase single quantum dot fluorescence resonance energy transfer. *J. Am. Chem. Soc.,* **2006,** *128*, 15324-15331.